Aidan Grummer

Candidate

Physics and Astronomy

Department

This dissertation is approved, and it is acceptable in quality and form for publication:

Approved by the Dissertation Committee:

Sally Seidel , Chairperson

Rouzbeh Allahverdi

Francis-Yan Cyr-Racine

Alessandro Cerri

CERN-THESIS-2021-057
02/12/2021

A Search for New Physics in $B_{(s)} \to \mu^+\mu^-$ Decays Using Multivariate Data Analysis, and Development of Particle Detection Technology with Silicon Pixel Detectors

by

Aidan Kelly Grummer

B.S., Physics, University of New Mexico, 2014
M.S., Physics, University of New Mexico, 2016

DISSERTATION

Submitted in Partial Fulfillment of the
Requirements for the Degree of

Doctor of Philosophy
Physics

The University of New Mexico

Albuquerque, New Mexico

May 2021

Dedication

This dissertation is dedicated to my parents and my brother - who have lovingly supported me in all of my goals. This work is also dedicated to my Uncle Larry and Aunt Sara in Geneva and my Uncle Larry and Aunt Garner in Los Altos who inspire me to be better every day.

Acknowledgments

First and foremost I would like to thank my advisor, Sally Seidel, for her incredible support of this research and for the many opportunities she has provided to me. Thank you to Martin Hoeferkamp, Konstantin Toms, and Iskander Ibragimov for the many useful conversations and guidance throughout this project. I am thankful for the help I received from Alex Cerri, Ben Nachman, Matt McCulloch, and Charlie Young. I am also very thankful for the many friends and colleagues I have gained during this time.

I am grateful to the funding agencies that have allowed me to carry out this research: the US Department of Energy (DOE), the National Science Foundation (NSF), and the National Aeronautics and Space Administration (NASA). I was awarded a year-long research grant by the Office of Science Graduate Student Research Program (SCGSR) which allowed me the valuable experience of working at the SLAC National Accelerator Laboratory. I was selected by the New Mexico Space Grant Consortium (NMSG) to receive the Graduate Research Fellowship, twice, which has allowed me to extend the bounds of my research. I am grateful to have had the opportunity to work in the fantastic facilities provided by CERN and ATLAS. I am also very appreciative of opportunities to use the irradiation facility LANSCE at Los Alamos National Laboratory and the Gamma Irradiation Facility at Sandia National Laboratories.

A Search for New Physics in $B_{(s)} \to \mu^+\mu^-$ Decays Using Multivariate Data Analysis, and Development of Particle Detection Technology with Silicon Pixel Detectors

by

Aidan Kelly Grummer

B.S., Physics, University of New Mexico, 2014
M.S., Physics, University of New Mexico, 2016

Ph.D., Physics, University of New Mexico, 2021

Abstract

A suite of linked research projects is undertaken, combining a search for phenomena beyond the Standard Model of particle physics, development of new instruments for greater precision in detecting fundamental particles, and tracking and understanding the effect upon the detectors of the radiation that is an indelible element of their operating environment. Data recorded by the ATLAS Detector at CERN are employed in a search for evidence of undiscovered particles contributing to the rate of decays of B^0 and B_s^0 mesons to dimuon final states. New applications of machine learning techniques are implemented to separate this signal from its many backgrounds. That analysis is combined with a highly sensitive evaluation of the effects of radiation damage already received by the ATLAS Pixel Detector and a comparison of

these data to a detailed model of radiation damage. A complementary thrust of this effort involves development of new devices and techniques for monitoring radiation fluences and calibrating particle physics detectors in a high radiation field. Finally, a comprehensive program for quality assurance of the ATLAS upgrade inner tracker modules and staves is being developed and applied to components assembled at SLAC laboratory, including electrical and mechanical tests.

Contents

List of Figures **xiii**

List of Tables **xlvi**

1 Introduction **1**

1.1 Overview 1

1.2 The Standard Model 3

1.3 The Large Hadron Collider 5

1.3.1 Introduction to the Large Hadron Collider 5

1.3.2 Energy and Luminosity 6

1.4 The ATLAS Experiment 8

1.4.1 The ATLAS Detector 8

1.4.2 The Pixel Detector 11

1.5 ATLAS Experiment Upgrades 15

1.6 Irradiation Facilities 16

1.7 Prelude 18

2 B^0 and B_s^0 Meson Decays to Two Muons **20**

2.1 Introduction to the $B^0 \to \mu^+\mu^-$ and $B_s^0 \to \mu^+\mu^-$ Analysis 20

2.2 ATLAS Data and Simulation Samples 24

2.3 Data Selection 27

2.4 Background Composition 33

2.5 Hadron Misidentification 36

2.6 Continuum Background Reduction via Multivariate Analysis 38

2.6.1 Discriminating Variables 38

2.6.2 Training, Testing, and Implementation Strategy 40

2.6.3 BDT Configuration 43

2.6.4 Final BDT Output 43

2.7 Data–Simulation Comparisons 52

2.8 $B^+ \to J/\psi K^+$ Yield Extraction 56

2.9 Evaluation of the $B^+ \to J/\psi\, K^+$ to $B^0_{(s)} \to \mu^+\mu^-$ Efficiency Ratio . . 59

2.10 Extraction of the Signal Yield 62

2.10.1 Signal and Background Model 63

2.10.2 Relative Signal Efficiency Between BDT Bins 65

2.10.3 Systematic Uncertainties in the Fit 66

2.10.4 Results of the Signal Yield Extraction 68

2.11 Branching Fraction Extraction 70

2.12 Combination with the Run 1 Result 74

2.13 Conclusions for the 2015-2016 Dataset Combined with Run 1 Results 76

2.14 Combination of ATLAS, CMS and LHCb Results 76

2.15 Modified Procedure and Analysis of the Full Run 2 Statistics 82

2.15.1 Motivation for Improvement of Analysis Techniques 83

2.15.2 Improvements to the Reconstruction Procedures of B Meson Isolation Variables 85

2.15.3 Assessment of the Isolation Variables in the Re-processed 2015-2016 Dataset 103

2.15.4 Improvements in BDT Performance 110

3 Analysis of Leakage Current in ATLAS Pixel Detector 117

3.1 Introduction to the Pixel Detector Leakage Current Analysis 117

3.2 Measurement Subsystems 120

3.3 Details of the Measurement 121

3.4 Details of Luminosity Accumulation 123

3.5 Hamburg Model Predictions 124

3.6 Precision and Systematic Uncertainties 127

3.7 Leakage Current Results 130

3.7.1 Leakage Current versus Axial Position 133

3.7.2 Leakage Current versus Azimuthal Angle 136

3.7.3 Leakage Current on the Disks 137

3.8 Sensitivity to the Effective Silicon Band Gap Energy Value 143

3.9 Determination of the Optimal Value of Effective Band Gap Energy with Irradiated Silicon Sensors in the ATLAS Pixel Detector 145

3.10 Comparisons of Measured and Predicted Fluence 150

3.11 Lifetime Projections 156

3.12 Summary and Conclusions of the Leakage Current Analysis 159

4 Quality Assurance of the Next Generation ATLAS Detector 160

4.1 Inner Tracker (ITk) Overview 160

4.2 Contribution to Detector Construction 161

4.3 Adhesive Introduction 163

4.4 Irradiations 164

4.5 Adhesive Mixing 169

4.6 Adhesive Deposition Patterns 179

4.7 Robot-Controlled Adhesive Deposition 181

4.8 Module Placement Fixture 185

4.9 Robot Module Placement 185

4.10 Module-to-Framework Loading Strategy 187

4.11 Prototype Assembly 197

4.12 Preparations for Correcting Loading Mistakes 203

4.13 Coordinate Measuring Machine 205

4.14 Thermal Conductivity 211

5 New Technologies for Particle Physics Applications 212

5.1 A Radiation Tolerant Light Pulser for Particle Physics Applications . 213

5.1.1 Pulser Design 213

5.1.2 Characterization 214

5.1.3 Proton Irradiations 216

5.1.4 Gamma Irradiations 216

5.1.5 Pulser Operational Results 219

5.2 Application of p-i-n Photodiodes to Charged Particle Fluence Measurements Beyond 10^{15} $n_{\mathrm{eq}}/\mathrm{cm}^2$ 221

5.2.1 Introduction to Beam Fluence Monitoring with p-i-n Photodiodes 221

5.2.2 Irradiation of the Diodes 223

5.2.3 Pulse Width Optimization 224

5.2.4 Systematic Uncertainties 227

5.2.5 Amplitude of the Pulsed Current 227

5.2.6 Conclusions From the p-i-n Photodiode Irradiation Studies . . 228

5.3 Application of 3D Diodes to Charged Beam Profile Measurement . . 228

5.3.1 Introduction to Beam Monitoring with 3D Diodes 229

5.3.2 The Positioners 229

5.3.3 The Beam Monitor 233

5.3.4 P-i-n diodes 233

5.3.5 3D diodes 233

5.3.6 Diode Array Readout 234

5.3.7 The Cooling System 237

5.3.8 Operational Experience and Conclusions 240

5.4 The Hamburg Model of Depletion Voltage 243

5.4.1 The Hamburg Model: Depletion Voltage in n-type Sensors . . 243

5.4.2 The Hamburg Model for p-type Sensors 246

5.5 Simulation of Silicon Sensor Characteristics Under Extra-Terrestrial Radiation Conditions 248

5.5.1 Simulation Model and Sensor Types 248

5.5.2 Environmental Conditions for the Simulation 250

5.5.3 Simulation Results 257

5.5.4 Results, Uncertainties, and Discussion 259

A $B^0_{(s)} \to \mu^+\mu^-$ Analysis - Variable Distributions in the Signal Channel 263

References 278

List of Figures

1.1 Large Hadron Collider complex. The top ring is the LHC at which is installed the ATLAS Detector. The original diagram can be found in Reference [118]. 6

1.2 The ATLAS Detector [33]. 9

1.3 The Magnet System [33]. 10

1.4 The barrel region of ATLAS Inner Detector depicting the Pixel, SCT and TRT subsystems. The image includes the innermost layer of the Pixel Detector (IBL). This image was originally published in [33]. . 11

1.5 The Inner Detector showing the barrel regions of the Pixel Detector and SCT and one side of the endcap regions of the Pixel, SCT and TRT subsystems. The image includes the innermost layer of the Pixel Detector (IBL). This image (excluding IBL) was originally published in [33]. 12

1.6 Calorimeter System [33]. 12

1.7 The Muon Spectrometer [33, 180]. 13

1.8 ATLAS Pixel Detector [18]. 13

1.9 (Left) planar and (right) 3D silicon sensor geometries. These diagrams were originally published in [66]. 14

1.10 LHC and HL–LHC energy and luminosity schedule [54]. 16

1.11 Layout of ITk pixel barrel layers and disks (red) and strip layers and disks (blue) [12]. 17

1.12 LANSCE proton beam line facility. This image can found in [130]. . 18

2.1 Diagrams of the $B_s^0 \to \mu^+\mu^-$ decay. (Left) Direct flavor-changing neutral currents are forbidden in the Standard Model. (Middle) The box diagram and (right) penguin diagram represent higher order flavor-changing neutral currents and are allowed in the Standard Model but occur with a low probability. These diagrams were originally published in [60]. 21

2.2 Two possible decay mode diagrams for $B_s^0 \to \mu^+\mu^-$ occurring in theories beyond the Standard Model. Here the X represents an undiscovered particle. These diagrams were originally published in [60]. 22

2.3 Diagram of sideband regions. 26

2.4 (Left) stability of the $B^0_{(s)} \to \mu^+\mu^-$ sidebands yield and (right) the $B^+ \to J/\psi\, K^+$ signal yield for the 2015 and 2016 data-taking periods. For $B^+ \to J/\psi\, K^+$, the *Delayed* stream was activated from the run 302956 in the Period D of 2016, therefore the period D has been split into two parts: 16D_mainonly, with the data available only in the *Main* stream and 16D_delayed, with the data from the *Delayed* stream. The integrated luminosity of the $B^0_{(s)} \to \mu^+\mu^-$ and $B^+ \to J/\psi\, K^+$ samples is overlaid and is reported with the axis on the right. The errors on the yield are calculated by adding the error on the number of events and the error on the luminosity in quadrature. The error on the luminosity is 2.2% [16, 39]. 31

2.5 (Left) variable distribution of ΔR_{flight} for the ATLAS data-taking periods in 2015 and 2016. (Right) The ΔR_{flight} distribution across longer data collection periods in 2015 and 2016 defined between technical stops and machine development stops. An auxiliary comparison is made to the ΔR_{flight} distribution in (green line) the $b\bar{b} \to \mu^+\mu^- X$ background MC sample. 32

2.6 Illustration of the difference between a signal $B^0_{(s)} \to \mu^+\mu^-$ event and the dominant combinatoric background. 33

2.7 (a) Dimuon invariant mass distribution for the partially reconstructed background (as categorized in Section 2.4), from simulation, before the final selection against continuum is applied but after all other requirements. The different components are shown as stacked histograms, normalized according to world-averaged measured branching fractions. The SM expectations for the $B^0_{(s)} \to \mu^+\mu^-$ signals are also shown for comparison. Continuum background is not included here. (b) Invariant mass distribution of the $B^0_{(s)} \to hh'$ peaking background components after the complete signal selection is applied. The $B^0_s \to \pi^+\pi^-$ and $B^0 \to K^+K^-$ contributions are negligible on this scale. In both plots the vertical dashed lines indicate the blinded analysis region. Distributions are normalized to the expected yield for the integrated luminosity of 26.3 fb^{-1}. These figures were originally published in [29]. 35

2.8 Correlation matrix of analysis variables for (left) signal Monte Carlo and (right) dimuon sideband datasets before the BDT output variable is used for data selection. 40

2.9 Distributions in (left) p_{T}^B and (right) L_{xy} of the sample splitting investigations to check for biases in the BDT training samples; both the (top) signal MC and (bottom) sideband data samples are compared. 42

2.10 The BDT variable for the BDT trained with sample 1 and tested on sample 2 for (left) the full range of the BDT variable and (right) a magnified range with the vertical axis in log scale. 48

2.11 The BDT variable for the BDT trained with sample 2 and tested on sample 3 for (left) the full range of the BDT variable and (right) a magnified range with the vertical axis in log scale. 48

2.12 The BDT variable for the BDT trained with sample 3 and tested on sample 1 for (left) the full range of the BDT variable and (right) a magnified range with the vertical axis in log scale. 49

2.13 (Left) Comparison of the ROC curves for the Run 2 BDT and the Run 1 BDT applied to Run 1 and Run 2 Data. (Right) The ROC comparisons are also performed in a magnified range of the background efficiency versus signal efficiency in log scale. The ROCs are evaluated on the high-mass data sideband. Errors on the background efficiency values are represented by shaded error bands. 49

2.14 (Left) Comparison of ROC curves for the three Run 2 BDTs and the Run 1 BDT applied to Run 1 data and Run 2 data. (Right) The ROC comparisons are also performed in a magnified range of the background efficiency versus signal efficiency in log scale. The ROCs are evaluated on the high-mass data sideband (the evaluation dataset). Errors on the background efficiency values are represented by shaded bands. 50

2.15 The sideband data (black dots), $b\bar{b} \rightarrow \mu^+\mu^- X$ (green line) and $B^0_{(s)} \rightarrow \mu^+\mu^-$ (red shaded area) MC distributions of the B_{iso} variable in three pileup bins: (upper left) nPV ≤ 11, (upper right) $11 <$ nPV ≤ 15, and (lower) nPV > 15. 51

2.16 BDT output distribution for the signal and background events after the preliminary selection and before applying any reweighting to the BDT input variables: (a) simulation distributions for $B_s^0 \to \mu^+\mu^-$ signal, continuum, partially reconstructed $b \to \mu^+\mu^- X$ events and B_c decays; (b) dimuon sideband candidates (which also include prompt contributions, mainly at lower BDT values and not simulated in the continuum MC sample), compared with the continuum MC sample and the simulated signal. All distributions are normalized to unity in (a) and to data sidebands in (b). 52

2.17 Correlation matrix of analysis variables for (left) signal Monte Carlo and (right) dimuon sideband datasets after the BDT output variable is used for data selection. 53

2.18 Data and continuum MC distributions of the (left) $|\alpha_{\rm 2D}|$ and (right) $\ln(\chi^2_{\mu,\rm xPV})$ variables (defined in Table 2.2). The points correspond to the sideband data, while the continuous-line histogram corresponds to the continuum MC distribution, normalized to the number of data events. The filled-area histogram shows the signal MC distribution for comparison. The bottom panels report the data/MC ratio, magnified in order to highlight discrepancies in the region that is most relevant for the analysis. 54

2.19 Data and MC distributions in $B^+ \to J/\psi\, K^+$ events for the discriminating variables: (a) $|\alpha_{\rm 2D}|$, (b) $\ln\left(\chi^2_{\rm PV,DV\,\mathit{xy}}\right)$ and (c) $I_{0.7}$. The variable $I_{0.7}$ is also shown in (d) for $B^0_s \to J/\psi\,\phi$ events. The points correspond to the sideband-subtracted data, while the line corresponds to the MC distribution, normalized to the number of data events. The highest bin in (c) and (d) accounts for the events with $I_{0.7} = 1$. The bottom panels report the data/MC ratio, magnified in order to highlight discrepancies in the region that is most relevant for the analysis. These figures were originally published in [29]. . . 55

2.20 Result of the fit to the $J/\psi K^+$ invariant mass distribution for all B^+ candidates in half of the data events. The various components of the spectrum are described in the text. The panel at the bottom of the plot shows the bin-by-bin pulls for the fit, where the pull is defined as the difference between the data point and the value obtained from the fit function, divided by the error from the fit. This figure was originally published in [29]. 57

2.21 Dimuon invariant mass distribution for the B^0_s and B^0 signals from simulation. The results of the double-Gaussian fits are overlaid. The two distributions are normalized to the SM prediction for the expected yield with an integrated luminosity of 26.3 fb^{-1}. This figure was originally published in [29]. 64

2.22 BDT value distributions in data and MC simulation for (a) $B^+ \to J/\psi\, K^+$, (b) $B_s^0 \to J/\psi\, \phi$. The MC samples are normalized to the number of data events passing the signal reference BDT selection (Section 2.6). Figure (c) illustrates the BDT output for the $B_s^0 \to \mu^+\mu^-$ signal, with the dashed histogram illustrating the effect of the linear reweighting on the BDT output discussed in the text. The vertical dashed lines correspond to the boundaries of the BDT intervals used in the $B_{(s)}^0 \to \mu^+\mu^-$ signal fit. These figures were originally published in [29]. 67

2.23 Dimuon invariant mass distributions in the unblinded data, in the four intervals of BDT output. Superimposed is the result of the maximum-likelihood fit. The total fit is shown as a continuous line, with the dashed lines corresponding to the observed signal component, the $b \to \mu^+\mu^- X$ background, and the continuum background. The signal components are grouped in one single curve, including both the $B_s^0 \to \mu^+\mu^-$ and the (negative) $B^0 \to \mu^+\mu^-$ component. The curve representing the peaking $B_{(s)}^0 \to hh'$ background lies very close to the horizontal axis in all BDT bins. These figures were originally published in [29]. 69

2.24 (a) Likelihood contours for the simultaneous fit to $\mathcal{B}(B_s^0 \to \mu^+\mu^-)$ and $\mathcal{B}(B^0 \to \mu^+\mu^-)$, for values of $-2\Delta\ln(\mathcal{L})$ equal to 2.3, 6.2 and 11.8. The SM prediction with uncertainties is indicated. (b) Neyman contours in the $\mathcal{B}(B_s^0 \to \mu^+\mu^-)$–$\mathcal{B}(B^0 \to \mu^+\mu^-)$ plane for 68.3%, 95.5% and 99.7% coverage. At each $-2\Delta\ln(\mathcal{L})$ or coverage value, the inner contours are statistical uncertainty only, while the outer ones include statistical and systematic uncertainties. The construction of these contours makes use of both the dimuon (26.3 fb^{-1}) and the reference channel (15.1 fb^{-1}) datasets. These figures were originally published in [29]. 73

2.25 Likelihood contours for the combination of the Run 1 and 2015–2016 Run 2 results (shaded areas). The contours are obtained from the combined likelihoods of the two analyses, for values of $-2\Delta\ln(\mathcal{L})$ equal to 2.3, 6.2 and 11.8. The empty contours represent the result from 2015–2016 Run 2 data alone. The SM prediction with uncertainties is indicated. This figure was originally published in [29]. 75

2.26 (Upper) The two-dimensional likelihood contours of the branching ratio results for the $B_s^0 \to \mu^+\mu^-$ and $B^0 \to \mu^+\mu^-$ decays for the three experiments and their combination. (Lower) The two-dimensional likelihood contours for the branching ratios of the combined results. Both plots are compared to the current SM prediction, shown with the red cross. The published results from ATLAS, CMS and LHCb experiments are detailed in References [29, 61, 122]. These figures were originally published in [38]. 80

2.27 The negative log-likelihood fit values of the LHC experiments combination results for (left) $\mathcal{B}(B_s^0 \to \mu^+\mu^-)$ and (right) $\mathcal{B}(B^0 \to \mu^+\mu^-)$ compared to the SM and its uncertainty (red line and band, respectively). The published results from ATLAS, CMS and LHCb experiments are detailed in References [29, 61, 122]. These figures were originally published in [38]. 81

2.28 The negative log-likelihood, $-2\Delta\ln\mathcal{L}$, for the ratio of the $B^0 \to \mu^+\mu^-$ and $B_s^0 \to \mu^+\mu^-$ branching fractions of the LHC experiments combination results. The results are compared to the SM and its uncertainty (red line and band, respectively) The published results from ATLAS, CMS and LHCb experiments are detailed in References [29, 61, 122]. This figure was originally published in [38]. 82

2.29 Comparison of the signal to background separation power (defined in Equation 2.2) for the analysis variables in the Run 1 and Run 2 data. Use of the term separation in the axis label implies separation power. Two variables had better separation power in the Run 1, B isolation and Distance of closest approach for a track to the primary vertex of the B meson decay. 84

2.30 Mean number of proton-proton interactions per bunch crossing, μ, in the Run 2 data [10]. 87

2.31 Number of primary vertices of single data runs: run 302393 (2016), run 339849 (2017), and run 358096 (2018). The distributions are compared to the number of primary vertices in the full 2015-2016 dataset, the LHC Run 1 dataset, and the simulated datasets MC16a, MC16d and MC16e. The number of primary vertices − 1 is plotted here to match the Run 1 computation choice. 88

2.32 The number of hits in the Inner Detector systems in 2017 run 339849 under different hit selection criteria. The hit distributions for (a) the IBL, (b) the Pixel Detector, and (c) the SCT Detector are investigated separately. 90

2.33 B_{iso} variable distributions for five track selection criteria described in the text for (left) the 2017 run 339849 sideband data and (right) the corresponding MC16d dataset. 94

2.34 (Left) the B_{iso} ROC performance and (right) ROC acceptance curves using the 2017 run 339849 sideband data for the background sample and the corresponding MC16d dataset for the signal sample. 94

2.35 Pileup binned comparisons of the B_{iso} variable constructions described in the text. Each comparison is made for a selected range of $\langle\mu\rangle$ values; the comparisons, (a), (b), (c) and (d), are ordered in increasing pileup. The pileup selections are described in the text. . . 96

2.36 $\text{DOCA}_{\text{xtrk}}$ variable distributions for four track selection criteria described in the text for (left) the 2017 run 339849 sideband data and (right) the corresponding MC16d dataset. 97

2.37 (Left) The $\text{DOCA}_{\text{xtrk}}$ ROC performance and (right) ROC acceptance curves using the 2017 run 339849 sideband data for the background sample and the corresponding MC16d dataset for the signal sample. 98

2.38 Pileup binned comparisons of the $\text{DOCA}_{\text{xtrk}}$ variable constructions described in the text. Each comparison is made for a selected range of $\langle\mu\rangle$ values; the comparisons, (a), (b), (c) and (d), are ordered in increasing pileup. The pileup selections are described in the text. . . 99

2.39 $N_{\text{xtrk}}^{\text{close}}$ variable distributions for four track selection criteria described in the text for (left) the 2017 run 339849 sideband data and (right) the corresponding MC16d dataset. 100

2.40 (Left) The $N_{\text{xtrk}}^{\text{close}}$ ROC performance and (right) ROC acceptance curves using the 2017 run 339849 sideband data for the background sample and the corresponding MC16d dataset for the signal sample. 101

2.41 Pileup binned comparisons of the $N_{\text{xtrk}}^{\text{close}}$ variable constructions described in the text. Each comparison is made for a selected range of $\langle\mu\rangle$ values; the comparisons, (a), (b), (c) and (d), are ordered in increasing pileup. The pileup selections are described in the text. . . 102

2.42 The sideband yield (of candidates) per data-taking period in the 2015 and 2016 data-taking years. The luminosity is overlaid and is reported with the axis on the right. 104

2.43 Subset of the variable distribution visualizations from the validation study of the re-processed 2015-2016 sideband dataset (new nTuples) compared to the original 2015-2016 sideband dataset (old nTuples). The ratio of distributions in the new and old nTuples is shown in the bottom panels. The ratio axis is magnified to reveal that the new and old nTuples are identical within error. The Monte Carlo distributions are also shown in the main panels as a subsidiary comparison, demonstrating the difference between signal and background. . . . 105

2.44 (Left) The full ROC curve and (right) the magnified ROC acceptance for the **Custom TVA**, **Loose TVA**, **As in Run 1**, **As in 2015-2016**, and **Run 1** B_{iso} variable constructions. 106

2.45 The magnified ROC acceptance curves for the **Custom TVA**, **Loose TVA**, **As in Run 1**, **As in 2015-2016**, and **Run 1** (left) negative muon and (right) positive muon isolation variable constructions. 107

2.46 (Left) The full ROC curve and (right) the magnified ROC acceptance for the **Custom TVA**, **Loose TVA**, **As in 2015-2016**, and **Run 1** $\mathrm{DOCA}_{\mathrm{xtrk}}$ constructions. 107

2.47 (Left) The full ROC curve and (right) the magnified ROC acceptance for the **Custom TVA**, **Loose TVA**, **As in 2015-2016**, and **Run 1** $N_{\mathrm{xtrk}}^{\mathrm{close}}$ variable constructions. 108

2.48 The separation power of the analysis variables in the new Run 2 datasets is compared to the separation power in the old Run 2 datasets. Use of the term separation in the axis label implies separation power. 109

2.49 The separation power of the analysis variables in the new Run 2 datasets is compared to the separation power in the Run 1 datasets. Use of the term separation in the axis label implies separation power. 110

2.50 ROC comparison of four BDTs, each trained with 15 input variables: 12 nominal analysis variables and a unique set of three isolation variables. The BDTs compared here are selected based on the consistency in the definitions of the three isolation variables. 111

2.51 ROC comparison of four BDTs, each trained with 15 input variables: 12 nominal analysis variables and a unique set of three isolation variables. Two of the BDTs compared here are selected based on the highest separation power of the three variables, the other two are the best performing BDTs selected based on the consistency in the definitions of the three isolation variables. 112

2.52 ROC acceptance curves for BDTs trained with and without pileup used as an input variable. The BDTs are trained with **Custom TVA** isolation variables and the 12 other nominal input variables. One includes $\langle\mu\rangle$ as an additional input variable and one includes nPV. . 113

2.53 Efficiencies for the pileup variable μ for three BDT selections: (top left) 54% signal efficiency, (top right) 36% signal efficiency or (bottom) 18% signal efficiency in the signal MC sample. A horizontal line indicates 54%, 36% and 18% signal efficiency in each plot, respectively. 115

2.54 Efficiencies for B_{iso} with BDT selection at 18% signal efficiency. The efficiencies are computed (left) before and (right) after a selection of $\langle\mu\rangle > 25$ is applied. Horizontal lines in the upper plots indicate 18% signal efficiency. 116

3.1 The positions of monitored modules in ϕ and r on the barrel layers. Between 4 and 10 modules are monitored at each location indicated in the figures. 119

3.2 The positions of monitored modules in ϕ on the disks side A (left) and side C (right). The modules on each disk are centered at a radial distance: 119.2 mm. 120

3.3 Luminosity accumulated by ATLAS during LHC Run 2. 123

3.4 Simulated n_{eq} fluence shown as a function of the radial and longitudinal distance from the geometric center of the detector for a one-quarter slice through the ATLAS FLUKA geometry. This figure was originally published in [18]. 127

3.5 Applied fluence for the B-Layer, Layer-1, Layer-2, and the Disks, calculated by the FLUKA factors shown in Figure 3.4 and summarized in Table 3.1. PYTHIA8 is used for particle production, MSTW2008LO parton distribution functions [138] and the A2 tune [31] are used for input to the FLUKA simulation. 128

3.6 Average measured leakage current of a representative sample of modules in the ATLAS Pixel Detector barrel layers over the full period of operation. The scaled prediction from the Hamburg Model is also shown. 132

3.7 Ratios of the B-Layer and Layer-1 leakage current data to Layer-2 leakage current for the LHC Run 2 period of ATLAS operation. . . 134

3.8 B-Layer, Layer-1, and Layer-2 leakage current data binned in z (the axis along the beam line) measured at four values of integrated luminosity using single module precision with the HVPP4 subsystem and multiple module precision with the module power supply subsystem. The scaled Hamburg Model prediction is also shown. Missing HVPP4 data are due to temporary power shutdowns. Twenty to twenty-two modules are included in each power supply bin for the B-Layer and twelve to sixteen modules are included in each power supply bin for Layer-1 and Layer-2. 135

3.9 Average measured leakage current of a representative sample of modules on the B-Layer binned in ϕ for the LHC Run 2 period of operation. 136

3.10 Ratios of the various ϕ binned leakage current data on the B-Layer with respect to the $225^\circ < \phi < 315^\circ$ bin for the LHC Run 2 period of operation. 137

3.11 Average measured leakage current of a representative sample of modules on Layer-1 binned in ϕ for the LHC Run 2 period of operation. 137

3.12 Ratios of the various ϕ binned leakage current data on Layer-1 with respect to the $225^\circ < \phi < 315^\circ$ bin for the LHC Run 2 period of operation. 138

3.13 Average measured leakage current of a representative sample of modules on Layer-2 binned in ϕ for the LHC Run 2 period of operation. 138

3.14 Ratios of the various ϕ binned leakage current data on Layer-2 with respect to the $225^\circ < \phi < 315^\circ$ bin for the LHC Run 2 period of operation. 139

3.15 Average measured leakage current of a representative sample of modules in the ATLAS Pixel Detector disks on side A for the LHC Run 2 period of operation. The scaled Hamburg Model prediction is also shown. 140

3.16 Ratios of Disk-1A and Disk-2A leakage current data to Disk-3A leakage current data for the LHC Run 2 period of operation. Also shown are the ratios of the Disk-1 and Disk-2 unscaled Hamburg Model predictions to the Disk-3 unscaled Hamburg Model prediction. 141

3.17 Average measured leakage current of a representative sample of modules in the ATLAS Pixel Detector disks on side C for the LHC Run 2 period of operation. The scaled Hamburg Model prediction is also shown. 141

3.18 Ratios of Disk-1C and Disk-2C leakage current data to Disk-3C leakage current data for the LHC Run 2 period of operation. Also shown are the ratios of the Disk-1 and Disk-2 unscaled Hamburg Model predictions to the Disk-3 unscaled Hamburg Model prediction. 142

3.19 Several predictions of leakage current were generated, all normalized to 0 °C, each using a different value of E_{eff}. The leakage current data were also normalized to 0 °C and analyzed once with each unique value of E_{eff}. The value of E_{eff} is used in the temperature normalization step. Three pairs of leakage current data and predictions with the Hamburg Model, with three E_{eff} values used to analyze them are shown here. Leakage current are compared to a Hamburg Model prediction using 3 different values of E_{eff}. 144

3.20 Leakage current data at various temperatures for a module in the IBL. Data were collected (left) in Feb. 2018 and (right) in May 2019. The temperature of each module is shown in the top panel. 145

3.21 Leakage current data at various temperatures for the (top left) *B*-Layer, (top right) Layer-1, and (bottom) Layer-2. Data were collected in May 2019. The temperature of each module is shown in the top panel. 146

3.22 Leakage current data at various temperatures for the (top left) Disk-1, (top right) Disk-2, and (bottom) Disk-3. Data were collected in May 2019. The temperature of each module is shown in the top panel. 147

3.23 The χ^2 distribution is computed for a module (left) in the IBL and (right) for a module in the *B*-Layer. 147

3.24 (left) Leakage current is analyzed for one module in the IBL and (right) one module in the B-Layer. The leakage current is corrected for temperature using the optimal E_{eff} value for the module. The optimal E_{eff} value for each module is shown in the legend of the figure. The temperature of each module is shown in the top panel. 148

3.25 Summary of the optimal E_{eff} study process. 149

3.26 Average values of the optimal E_{eff} study for each layer and disk of the Pixel Detector, binned in z. 149

3.27 The χ^2 figure of merit in the E_{eff} and temperature offset phase space is investigated. 150

3.28 Comparisons of fluence predictions by PYTHIA8 + FLUKA for the full period of operation, the fluence predicted by PYTHIA8 + GEANT4 in Run 2 and PYTHIA8 + FLUKA in Run 1, and the fluence determined from leakage current data combined with predictions by the Hamburg Model, for the B-Layer, Layer-1, and Layer-2. The horizontal bars on the fluence points determined from leakage current data combined with predictions by the Hamburg Model reflect the bin ranges. 152

3.29 Comparison of fluence predictions by PYTHIA8 + FLUKA to the fluence determined from leakage current data combined with predictions by the Hamburg Model, for the disks. 153

3.30 (Top) The leakage current at the end of Run 2 and (bottom) the fluence rate as a function of z for the entire silicon-based ATLAS inner detector. These figures were originally published in Reference [27]. . 154

3.31 (Top) The leakage current at the end of Run 2 and (bottom) the fluence rate as a function of radius for the entire silicon-based ATLAS inner detector. The size of the horizontal bands on the simulation is chosen to aid the comparison with data - the actual radial uncertainty from the finite size of the sensors is comparable to the marker sizes. These figures were originally published in Reference [27]. . . . 155

3.32 (a) The projection of leakage current levels through LHC Run 3. The simulation of Runs 1 and 2 use the temperature recorded in the *B*-Layer bin overlapping the interaction point, $(-13.3 < z < 1.0)$ cm. Leakage current data in this bin are also shown. The temperature normalization is applied using the operating temperature of the sensors (which is roughly -12 $^{\circ}$C). The volume normalizations are removed so that the leakage current projections represent the leakage current per module. The power supply and services limitations on leakage current is 2 mA per module and in the projection scenarios shown here the leakage current will remain below this limit. (b) The projected temperature levels throughout the long shutdown and the LHC Run 3 operations for three scenarios are shown as a function of date. 158

4.1 (Left) diagram of the ATLAS ITk layout [32] and (right) image of a stave prototype. 162

4.2 Schematic of the single module geometry layout (not to scale). The silicon sensor is operated throughout the front end electronics (ASIC) and power is supplied and data are transfered through the flexible electronics. The modules are attached to the local supports (staves and disks) with a thermally conductive and radiation hard adhesive. For optimal thermal performance, the thickness of the adhesive is required to be 100 micrometers. 163

4.3 (Left) Diagram of a lap joint used for stress versus strain measurements. Adhesive is shown in red and the two surfaces shown in grey are pulled in the direction of the arrows. (Right) Aluminum bars that could be used for this purpose are cut to identical lengths and sanded down where the adhesive may be applied. 165

4.4 Zwick/Roell Z050 machine used for measuring stress versus strain of irradiated samples at CERN. 165

4.5 Apparent stress versus strain of unnirradiated Araldite 2011 samples [77]. 166

4.6 Apparent stress versus strain of Araldite 2011 samples irradiated with a dose of 2 MGy [77]. 166

4.7 Apparent stress versus strain of Araldite 2011 samples irradiated with a dose of 7 MGy [77]. 167

4.8 Apparent stress versus strain of SE4445 samples irradiated with a dose of 5 MGy [77]. 167

4.9 Apparent stress versus strain of SE4445 samples irradiated with a dose of 7 MGy [77]. 168

4.10 Apparent stress versus strain of SE4445 samples irradiated with a dose of 10 MGy [77]. 168

4.11 Materials for mixing Araldite 2011 into a 5 ml syringe. 170

4.12 Setup for manual mixing of SE4445. 171

4.13 (Left) Extension of the helical SE4445 mixing tube was investigated, using a lathe. (Right) the extended tube is longer and has a smaller inner diameter compared to the commercially available option. . . . 173

4.14 The SE4445 mixing station. 174

4.15 The warm-up curve of the freezer after a power cut is represented by the black data points. Two warm-up curves after aluminum blocks were inserted into the freezer, while the power was still on, are represented in the red and blue crosses. 175

4.16 Vacuum chamber used for de-airing the SE4445 syringes. (Left) The contents of the vacuum chamber are visible through the the top view of the vacuum chamber. (Middle) Two syringes of SE4445 are de-aired at a time. (Right) The vacuum pressure of 28 inHg is applied to the chamber. 176

4.17 (Left) The concept of the planetary, centrifugal mixer involves rotation of the mixing material around two axes [134]. (Right) The SpeedMixer allows for streamlined use with display screen controls and programmable settings. 177

4.18 Illustration of the sequence of mixing SE4445 with a centrifugal, planetary mixer. 177

4.19 Illustration of the sequence involved in transfer of SE4445 from the mixing cup to syringe, demonstration. 178

4.20 Simulation of liquid pattern spreading in two dimensions. Full coverage of the rectangular surface is achievable with such an initial dispensed pattern. Image was originally published in [117]. 179

4.21 SE4445 adhesive samples using the star pattern. Samples spread between the two surfaces. 180

4.22 Adhesive testing station in the clean room at SLAC, including a Nordson Robot Machine and a fluid dispenser. The computer used for controlling these instruments is to the left of the image (not pictured). 182

4.23 The custom syringe holder for the Nordson Robot, (left) top view and (right) front view. 182

4.24 Image of four adhesive samples between two glass plates. 183

4.25 Adhesive samples deposited on a glass base plate. The (left) view from the front of glass and (right) through the back of the glass are important for characterizing the SE4445 spread. The adhesive pattern is investigated (top samples) without a cover glass placed on the pattern and (bottom samples) with a cover glass placed on top of the pattern. 183

4.26 Image of a back-lit adhesive sample. 184

4.27 SE4445 samples on carbon fiber. 184

4.28 The placement fixture fabricated with Lexan is used for testing of cover glass placements. 186

4.29 Design of a production single module fixture [139]. 186

4.30 (Left) A cover-glass slide is picked up using the robot arm and (middle) placed on an adhesive sample. (Right) A pressure application device prototype. 187

4.31 Loading strategy for the inner ring of a coupled disk. The procedures are described in the text. The Araldite is applied first, then sets of three SE4445 adhesive patterns are applied and the modules are placed with the placement fixture. Dispensed Araldite and SE4445 are represented by the purple and orange patterns, the future and present module locations are outlined, and the applied fixture is represented by the semi-transparent boxes. The figures and patterns are not drawn to scale and are for illustrative purposes only. 190

4.32 Loading strategy for the first four quad modules in the outer ring of the disk. The procedures are described in the text. The Araldite is applied first, then the SE4445 adhesive patterns are applied and the modules are placed with the placement fixture in sets of two modules at a time. Dispensed Araldite and SE4445 are represented by the purple and orange patterns, the future and present module locations are outlined, and the applied fixture is represented by the semi-transparent boxes. The figures and patterns are not drawn to scale and are for illustrative purposes only. 194

4.33 Loading strategy for the second four quad modules in the outer ring of the disk. The procedures are described in the text. The Araldite is applied first, then the SE4445 adhesive patterns are applied and the modules are placed with the placement fixture in sets of two modules at a time. Dispensed Araldite and SE4445 are represented by the purple and orange patterns, the future and present module locations are outlined, and the applied fixture is represented by the semi-transparent boxes. The figures and patterns are not drawn to scale and are for illustrative purposes only. 195

4.34 Loading strategy for the last two quad modules in the outer ring of the disk. The procedures are described in the text. The Araldite is applied first, then the SE4445 adhesive patterns are applied and the modules are placed with the placement fixture. Dispensed Araldite and SE4445 are represented by the purple and orange patterns, the future and present module locations are outlined, and the applied fixture is represented by the semi-transparent boxes. The figures and patterns are not drawn to scale and are for illustrative purposes only. 196

4.35 (Left and middle) Solder wicks and a silicon heater are held in place with a custom aluminum fixture. (Middle) The fixture is placed on a hot plate, where solder is applied between the heater and the solder wick. 197

4.36 A fully assembled platinum coated silicon heater with solder-attached leads. 198

4.37 A holding fixture used for loading a stavelet. 199

4.38 The robot module loading station. An empty stavelet held in the loading fixture is being prepared for the loading demonstration. . . 200

4.39 The stavelet loading procedures are to (upper left) apply Araldite 2011 pattern for one sensor, (upper right) apply SE4445 adhesive pattern for one sensor, (lower left) pick up the sensor from the holding fixture, and (lower right) place the sensor on the adhesive pattern. . . 201

4.40 Four fully assembled stavelet prototypes. 201

4.41 Adhesive deposition in the pattern of a coupled ring disk. 202

4.42 ATLAS IBL loading mistakes [14]. 203

4.43 Modules can be (left) removed from the carbon fiber framework using a thin metal wire and (right) the adhesive residue can be cleaned with isopropyl alcohol. 204

4.44 The CMM measurement setup. 205

4.45 (Left) A three-dimensional printed model of a coupled disk, in front of the CMM. The model disk is used for preparing the CMM measurements code that will be used during the production of the ITk parts. (Right) The CMM can be controlled with the hand-held controls or through computer numeric control. 206

4.46 The coordinate system of a disk is set with three measurements on the disk. 207

4.47 Measurement graphics generated by the CMM software can be customized to provide information to a parts database and allow for in-situ quality control (go or no-go) information to the user during production. 209

4.48 A measurement with the CMM optical probe. (Right) The optical probe camera takes an image from a precisely known position and (left) transfers the image to a computer for viewing and processing. 210

4.49 The touch probe is used for some thickness measurements of the adhesive samples between glass and carbon fiber. 210

4.50 Infrared image of samples over a heat source. 211

5.1 Pulser circuit design and fabricated board. Images originally published in [88]. 214

5.2 Experimental setup. This image was originally published in [88]. . 215

5.3 Pulse width output using input voltages of $V_{\mathrm{IN}} = 3.5$ V and $V_{\mathrm{IN}} = 10$ V. 215

5.4 Pulse width of pulser before and after proton irradiation to fluences of 1.5×10^{13} and 6.7×10^{13} 800-MeV p/cm^2. 217

5.5 Pulse amplitude of pulser before and after proton irradiation to fluences of 1.5×10^{13} and 6.7×10^{13} 800-MeV p/cm^2. 217

5.6 Pulse amplitude of pulser before and after gamma irradiation to doses up to 5 MGy. 218

5.7 Pulse width of pulser before and after gamma irradiation to doses up to 5 MGy. 218

5.8 Forward current versus forward voltage measurements of LED465E components, with and without applied irradiations. 220

5.9 Measured I_{C} versus applied V_{BE} of NPN Transistor BFR93A with constant $V_{\mathrm{CE}} = 2$ V, with and without applied irradiations. 220

5.10 Linear relation between forward voltage and applied particle fluence [155]. 222

5.11 Front and back sides of the p-i-n diode array used for real time fluence measurements. 222

5.12 The experimental setup inside the LANSCE Irradiation Hall is shown here. The p-i-n diode board arrays together with other samples to be irradiated, included aluminum foil dosimeters, are placed in the Lexan holding box. The 800 MeV proton beam is directed through the center of the box and the diodes arrays and other samples are aligned to intersect the beam. 223

5.13 Real time fluence measurements are made with the p-i-n diode board arrays in the LANSCE proton beam. The fluence contours accumulated with the p-i-n diode arrays reflect the areas in the proton beam that received higher or lower total dose. Displayed together, the fluence measurements from the diodes in the array can reconstruct a profile of the beam. The upstream beam profile is shown on the left and a downstream beam profile is shown on the right. 224

5.14 Forward voltage versus fluence data and linear fit [151]. The fitted line is used for calibration of the p-i-n diode array real time fluence measurements. 225

5.15 (Left) Measurement setup in the UNM laboratory. (Right) Measurement setup diagram. The diagram was originally published in [101]. 225

5.16 Diode forward voltage versus time, for a p–i–n diode irradiated to a fluence of 2.1×10^{15} $n_{\mathrm{eq}}/\mathrm{cm}^2$ at 20 °C, observed for pulse widths of 372 ms (a), 50 ms (b), and 5 ms (c). 226

5.17 Diode forward voltage as a function of applied fluence, for three choices of applied current amplitude. The vertical error bars indicate the combined uncertainties related to temperature variation during the irradiation process, current pulse width, and sourcemeter precision. The horizontal error bars indicate the uncertainty deriving from counting statistics on calibration foils in the gamma spectrometer. 227

5.18 The positioning system, showing seven horizontal translation stages with attached sample boxes and a manifold that allows differential air pressure to be applied selectively to either end of each translation piston. During operation, the actual length of the plastic tubing between manifold and stages would be much greater - typically tens of meters, in order to allow personnel to operate the manifold outside of a radiation zone in which the translation stages are enclosed. This image was originally published in [102]. 230

5.19 A sample box with gas flow port in the lid. This image was originally published in [102]. 231

5.20 (left) Top view and (right) side view of the removable slotted insert that can be positioned at the base of a sample box to allow the sample to be oriented at an angle with respect to the beam axis. This image was originally published in [102]. 232

5.21 The combined vertical-horizontal translation stage. This image was originally published in [102]. 232

5.22 The 3D diode array on a printed circuit board. This image was originally published in [102]. 235

5.23 Electrical circuit for the 3D diode array readout. This image was originally published in [102]. 235

5.24 The 800 MeV proton beam profile, imaged using the p-i-n diode array. (Lower left) The recorded pulse height (or voltage) versus position, projected in the y-direction; (Lower right) The recorded pulse height versus position, projected in the x-direction; (Upper right) three-dimensional reconstruction of the pulse height recorded as a function of x- and y-positions; (Upper left) contour plot of pulse height in the x-y plane, with black dots indicating the locations of the centers of the diodes. 236

5.25 The 800 MeV proton beam profile, imaged using the 3D diode array. (Lower left) the recorded leakage current versus position, projected in the y-direction; (Lower right) the recorded leakage current versus position, projected in the x-direction; (Upper left) three-dimensional reconstruction of the leakage current recorded as a function of x- and y-positions; (Upper right) contour plot of leakage current in the x-y plane, with black dots indicating the locations of the centers of the active diodes. 239

5.26 The PID temperature control system. This image was originally published in [102]. 240

5.27 Temperature recorded in the sample box located 30 m from the Norhof dewar, as a function of time after the cooling process was started. Temperature was measured with two sensors, a thermocouple and an RTD. 241

5.28 A composite of images of the instrument, including prototypes, photographed over several years during irradiation campaigns at LANSCE. 241

5.29 The NIEL scaling hypothesis [176]. 249

5.30 Stopping power for protons applied to silicon, from [46]. 252

5.31 Proton fluence applied per day as a function of proton kinetic energy. 253

5.32 Average daily proton fluence, in 1-MeV-neutron equivalent per area, as a function of proton kinetic energy. 253

5.33 Predicted change in leakage current density as a function of (left) integrated charged hadron fluence and (right) time in Earth-years, in both the n-type and p-type silicon sensors, normalized to 294 K. 258

5.34 Depletion voltage as a function of (left) integrated charged particle fluence, and (right) time in Earth-years, for an oxygenated n-type silicon sensor of depletion depth 250 μm. 258

5.35 Several simulations of depletion voltage as a function of (left) integrated charged particle fluence, and (right) time in Earth-years, for a p-type silicon sensor of depletion depth 40 μm. 260

A.1 Distributions of the variables (left) p_{T}^{B} and (right) $\ln(\chi^2_{\mathrm{PV,DV}\,xy})$ in the sideband data, the $b\bar{b} \to \mu^+\mu^- X$ MC sample and the signal MC sample. For each comparison the ratio of the distributions in the sideband data and the $b\bar{b} \to \mu^+\mu^- X$ MC sample is shown in the lower panel. 264

A.2 Distributions of the variables (top left) ΔR_{flight} and (top right) $|\alpha_{\text{2D}}|$ and (bottom) IP_B^{3D} in the sideband data, the $b\bar{b} \to \mu^+\mu^- X$ MC sample and the signal MC sample. For each comparison the ratio of the distributions in the sideband data and the $b\bar{b} \to \mu^+\mu^- X$ MC sample is shown in the lower panel. 265

A.3 Distributions of the variables (top left) L_{xy} and (top right) the respective error and (bottom) significance in the sideband data, the $b\bar{b} \to \mu^+\mu^- X$ MC sample and the signal MC sample. For each comparison the ratio of the distributions in the sideband data and the $b\bar{b} \to \mu^+\mu^- X$ MC sample is shown in the lower panel. 266

A.4 Distributions of the variables (top left) $\text{DOCA}_{\mu\mu}$, (top right) $|\Delta\phi_{\mu\mu}|$, and (bottom) $P_{\text{L}}^{\text{min}}$ in the sideband data, the $b\bar{b} \to \mu^+\mu^- X$ MC sample and the signal MC sample. For each comparison the ratio of the distributions in the sideband data and the $b\bar{b} \to \mu^+\mu^- X$ MC sample is shown in the lower panel. 267

A.5 Distributions of the variables (left) $|d_0|^{\text{min}}$-sig. and (right) $|d_0|^{\text{max}}$-sig. in the sideband data, the $b\bar{b} \to \mu^+\mu^- X$ MC sample and the signal MC sample. For each comparison the ratio of the distributions in the sideband data and the $b\bar{b} \to \mu^+\mu^- X$ MC sample is shown in the lower panel. 268

A.6 Distributions of the variables (top left) $|d_0|^{\text{min}}$, (top right) $|d_0|^{\text{max}}$, (bottom left) $|d_0|^{\text{min}}$ error and (bottom right) $|d_0|^{\text{max}}$ error in the sideband data, the $b\bar{b} \to \mu^+\mu^- X$ MC sample and the signal MC sample. For each comparison the ratio of the distributions in the sideband data and the $b\bar{b} \to \mu^+\mu^- X$ MC sample is shown in the lower panel. 269

A.7 Distributions of the variables (top left) η_{μ_1} error, (top right) $p_{\mathrm{T}}^{\mu_1}$, (bottom left) η_{μ_2} and (bottom right) $p_{\mathrm{T}}^{\mu_2}$ in the sideband data, the $b\bar{b} \to \mu^+\mu^- X$ MC sample and the signal MC sample. For each comparison the ratio of the distributions in the sideband data and the $b\bar{b} \to \mu^+\mu^- X$ MC sample is shown in the lower panel. 270

A.8 Distributions of the variables (top left) B_{iso}, (top right) number of tracks in the B_{iso} cone, (bottom left) $\mathrm{DOCA}_{\mathrm{xtrk}}$ and (bottom right) $N_{\mathrm{xtrk}}^{\mathrm{close}}$ in the sideband data, the $b\bar{b} \to \mu^+\mu^- X$ MC sample and the signal MC sample. For each comparison the ratio of the distributions in the sideband data and the $b\bar{b} \to \mu^+\mu^- X$ MC sample is shown in the lower panel. 272

A.9 Distributions of the variable $\chi^2_{\mu,\mathrm{xPV}}$ in the sideband data, the $b\bar{b} \to \mu^+\mu^- X$ MC sample and the signal MC sample. For each comparison the ratio of the distributions in the sideband data and the $b\bar{b} \to \mu^+\mu^- X$ MC sample is shown in the lower panel. 273

A.10 Distributions of the variables (left) $\langle\mu\rangle$ and (right) nPV in the sideband data, the $b\bar{b} \to \mu^+\mu^- X$ MC sample and the signal MC sample. For each comparison the ratio of the distributions in the sideband data and the $b\bar{b} \to \mu^+\mu^- X$ MC sample is shown in the lower panel. . 274

A.11 Distributions of the variables (left) η^B and (right) the z position of the B primary vertex in the sideband data, the $b\bar{b} \to \mu^+\mu^- X$ MC sample and the signal MC sample. For each comparison the ratio of the distributions in the sideband data and the $b\bar{b} \to \mu^+\mu^- X$ MC sample is shown in the lower panel. 275

A.12 Distributions of the variables (left) the difference in η of the two muons in the B candidate and (right) the opening angle $\Delta R_{\mu\mu}$ between the two muons in the B candidate in the sideband data, the $b\bar{b} \to \mu^+\mu^- X$ MC sample and the signal MC sample. For each comparison the ratio of the distributions in the sideband data and the $b\bar{b} \to \mu^+\mu^- X$ MC sample is shown in the lower panel. 275

A.13 Distributions of the variables (left) B invariant mass and (right) corresponding error in the sideband data, the $b\bar{b} \to \mu^+\mu^- X$ MC sample and the signal MC sample. For each comparison the ratio of the distributions in the sideband data and the $b\bar{b} \to \mu^+\mu^- X$ MC sample is shown in the lower panel. 276

A.14 Distributions of the variables (left) proper decay time of the B candidate and (right) corresponding significance in the sideband data, the $b\bar{b} \to \mu^+\mu^- X$ MC sample and the signal MC sample. For each comparison the ratio of the distributions in the sideband data and the $b\bar{b} \to \mu^+\mu^- X$ MC sample is shown in the lower panel. 277

List of Tables

2.1 Loose analysis selections applied to $B^0_{(s)} \to \mu^+\mu^-$ data, $B^0_{(s)} \to \mu^+\mu^-$ signal Monte Carlo, and $b\bar{b} \to \mu^+\mu^- X$. 30

2.2 Description of the 15 input variables used in a BDT classifier to discriminate between signal and continuum background. When the BDT classifier is applied to $B^+ \to J/\psi\, K^+$ and $B^0_s \to J/\psi\, \phi$ candidates, the variables related to the decay products of the B mesons refer only to the muons from the decay of the J/ψ. Horizontal lines distinguish the groups (a), (b), (c) and (d) respectively, as described in the text. For category (c), additional tracks are required to have $p_{\rm T} > 500$ MeV. 39

2.3 Training, testing, and evaluation of the 3 BDTs. Each data sample contains 1/3 of the sideband data and 1/3 of the signal MC. For the evaluation sample, 1/3 of the signal MC and only the high-mass sideband of the collision data are used. 41

2.4 Configuration parameters of the BDT. 44

2.5 The BDT 1 ranking of input variable importance compared with the signal and background separation power of each variable as calculated by TMVA. Use of the term separation in the table heading implies separation power. 45

2.6 The BDT 2 ranking of input variable importance compared with the signal and background separation power of each variable as calculated by TMVA. Use of the term separation in the table heading implies separation power. Similar orders of variable importance are seen for each BDT training. 46

2.7 The BDT 3 ranking of input variable importance compared with the signal and background separation power of each variable as calculated by TMVA. Use of the term separation in the table heading implies separation power. Similar orders of variable importance are seen for each BDT training. 47

2.8 Summary of the uncertainties in R_{ε}. This table was originally published in [29]. 61

2.9 Breakdown of the expected systematic uncertainties in $\mathcal{B}(B^0_{(s)} \to \mu^+\mu^-)$. The measurements are dominated by statistical uncertainty, followed by the systematic uncertainty from the fit. The latter is dominated by contributions from the mass scale uncertainty and the parameterization of the $b \to \mu^+\mu^- X$ background. The statistical uncertainties reported here are obtained from the maximization of the fit likelihood and are meant only as a reference for the relative scale uncertainties. This table was originally published in [29]. . . . 72

3.1 Fluence values simulated using the ATLAS FLUKA simulation package for three center-of-mass (C.O.M.) energies. The units of the values in the table are 10^{11} n_{eq} /cm^2 per fb^{-1}. 126

3.2 Summary of the contributing and total measurement uncertainties. The current precision and temperature precision are the statistical uncertainties. The hardware and temperature offset uncertainties are the systematic uncertainties. 130

3.3 Summary of the contributing and total uncertainties for the Hamburg Model. The temperature offset uncertainty does not apply during periods when the power and cooling of the detector are off. The scale factor fit is determined using the statistical uncertainties of Table 3.2. 130

3.4 Summary of the contributing and total uncertainties for the combined model and data fluence measurement. The abbreviation SFF refers to the scale factor fit uncertainty and Lumi. refers to the luminosity uncertainty. The temperature offset uncertainty does not apply during periods when the power and cooling of the detector are off. The scale factor fit is determined using the statistical uncertainties of Table 3.2. The fluence measurement uses data from the power supply subsystem. 131

3.5 Barrel Layer scale factors. The bin limits are determined by the paired module powering scheme. Each bin is defined based on the center location of the modules that are included in the bin; one centimeter is added to or subtracted from the center location in defining the bin limits to include the center position of all modules in the bin. 133

3.6 Disk scale factors. 139

4.1 The key properties of SE4445 and Araldite 2011 as described in the manufacturers' data sheets. 164

4.2 Measurements of a model of a disk performed with the CMM. Trials 1 to 3 are performed using the same program, one after another, to check the repeatability of the measurements. The same measurements of the model disk in Trial 4, marked with an asterisk, are performed with twice as many points per measurement. 208

4.3 Measurements of a model of a Disk performed with the CMM. The same measurements as in Table 4.2 are performed after removing and re-placing the Disk in the holding position. Measurements in Trial 4, marked with an asterisk, are performed with twice as many points per measurement. 209

5.1 Sources of uncertainty in the 3D diode array measurement. 237

5.2 Norhof parameters applied to achieve a -10 °C atmosphere in a few-liter sample box served by a 30 m insulated transfer hose, in a nominally 25 °C experimental hall. 240

5.3 Predicted peak leakage current density and final depletion voltage for silicon sensors operating in the Martian environment for a duration of 28.2 Earth-years, including a safety factor of 1.5 applied to current. The predicted depletion voltage for p-type sensors assuming incomplete initial acceptor removal is shown in parentheses. The 10.5% uncertainty on the leakage current corresponds to contributions from the scale factor fit and the precision by which the temperature is known. The uncertainty on the depletion voltage, due to uncertainties on the Hamburg Model parameters, is taken to be 20%. 261

Chapter 1

Introduction

1.1 Overview

In this dissertation a set of linked research projects focused on the key areas most useful for advancing the search for phenomena beyond those described by the most successful model in physics are presented. The primary goal of this work is to probe this physics model, commonly referred to as the Standard Model. A brief introduction to the Standard Model is provided in the following section. Some of the largest facilities in the world are required to investigate the smallest known pieces of our universe; this is due to the extremely high energies required to resolve distances characteristic of the smallest structures and the short particle lifetimes. In this dissertation those facilities that are employed most importantly are the Large Hadron Collider (LHC), the ATLAS detector, and the irradiation facilities at Los Alamos National Laboratory (LANSCE) and at Sandia National Laboratories (GIF).

Data collected with the ATLAS detector from proton collisions produced by the Large Hadron Collider from 2010 through 2016 are used to make measurements of a

rare and long sought after particle transition: a B^0 (or B_s^0) meson decaying to two muons. The results of this measurement, presented in Chapter 2, reveal the most stringent experimental constraint to date. The production of these data comes at a cost in the form of damage caused from very high radiation environments at the heart of the ATLAS detector - the same particles that provide signals of physics phenomena also cause damage to the detector. In the interest of prolonged use of the detector, detailed monitoring and modeling of this radiation is presented in Chapter 3. Though careful monitoring can help prolong the life of the presently installed detector it becomes clear that within the next decade it will no longer meet the needs of the experiment. This is due, in no small part, to the planned upgrade of the LHC to the High Luminosity LHC (HL-LHC). The unprecedented volume of data provided by the LHC will be increased ten-fold with the HL-LHC and with those data will come an increased radiation environment. Plans and techniques for constructing the ATLAS detector upgrade are presented in Chapter 4. Further work has also been undertaken in the development of new radiation hard technologies, described in Chapter 5 - these studies will be useful for the development of future particle physics and space exploration experiments.

Some of the content of Chapter 2 has previously been published in [29]. Section 2.14 has previously been published in [38]. Some of Chapter 3 has previously been published in [18]. Section 5.1 has previously been published in [88]. Section 5.2 has previously been published in [101]. Section 5.3 has previously been published in [102]. Section 5.5 is soon to appear in a special issue of "Frontiers in Physics, section Radiation Detectors and Imaging."

1.2 The Standard Model

The broad category of the research presented in this dissertation is elementary particle physics, the science that investigates the fundamental fields of nature. The edifice that describes much of that topic is the Standard Model, but it is insufficient. In order to elucidate the insufficiencies that motivate this research, some aspects of the Standard Model are described here.

The Standard Model is a physical model that joins all of the experimentally observed particles into a single framework [74, 84, 90, 98, 164, 178, 181]. These particles can be described by their empirical properties. There are two types of fundamental particles in the model: fermions and bosons. Each fundamental particle has a property called spin; fermions are half-integer spin particles that obey Fermi-Dirac statistics and the Pauli Exclusion Principle while bosons are integer spin particles that obey Bose-Einstein statistics. The fundamental particles also have the properties rest mass and charge, although some of the particles have a rest mass of zero and some have an electric charge of zero. The rest mass is described by the relation to rest energy, namely energy divided by the speed of light squared. An unbound, free particle has a discrete, integer value of charge which can be neutral, positive, or negative. It is possible for particles to have fractional charge; these particles have only been realized in bound states with other particles such that the total charge of the bound state has an integer value.

There are two types of experimentally confirmed bosons in the Standard Model: vector bosons and a scalar boson. The vector bosons are the force carriers and the observed vector bosons describe three of the four fundamental interactions. The fundamental forces are electromagnetism, the weak nuclear force, the strong nuclear force, and gravity. The vector bosons are the photon which is the electromagnetic force carrier, the $W^{\pm}$ and Z bosons which are the weak force carriers, and the

gluons which are the strong nuclear force carriers. The Higgs boson is a scalar boson responsible for giving all other elementary particles mass.

There are two families of fermions: leptons and quarks. There are six known leptons - the electron, the muon, the tau (in increasing order of mass) and the three corresponding neutrinos of the same names. The doublet of each neutrino and the lepton with the corresponding name is called a generation, and so there are three known generations of leptons. There are also six known quarks. Quarks are never observed in isolation; they are typically in bound states of two or three quarks (although, recent experimental results [44, 124, 126, 150] have indicated bound states of four quarks and of five quarks). Quarks in a bound state are called hadrons, bound states of a quark and an anti-quark are called mesons and bound states of three quarks are called baryons. Quarks have fractional charge (with denominator 3) and hadrons have integer charge. The six quarks making up three generations (with increasing mass) are called: up and down, charm and strange, top and bottom. Every fermion has an associated anti-fermion. The anti-fermion has the same properties as the fermion but has the opposite sign in some quantum numbers such as electric charge, lepton number and baryon number. Quarks have an additional property called color charge, which can take the state red, green, blue, anti-red, anti-green, and anti-blue. All hadrons are color neutral.

The Standard Model has been extremely successful in predicting the properties of the fundamental particles, but there are properties of the universe that it does not describe. Some of the major open issues include: There is more matter that anti-matter in the universe - this is called the matter antimatter asymmetry problem [7, 55, 72]. The Standard Model does not describe gravity and a fundamental force carrier for the gravitational interaction has not been observed. There is no explanation in the Standard Model to account for the existence of three (and only three) generations of leptons. Cosmology has indicated that there is a large fraction

of the matter in the universe that does not interact with the electromagnetic force (called dark matter) [83, 163, 185]; this matter is not described by the Standard Model. Cosmology has also determined that there is a large amount of dark energy in the universe that is needed for explaining the expansion of the universe [153, 160]; this energy is not described by the Standard Model.

The overarching goal of this thesis work is to resolve some of the problems in the Standard Model. Any significant deviations from Standard Model predictions could arise in models involving non-Standard Model heavy particles, such as those predicted in the Minimal Supersymmetric Standard Model [40, 57, 58, 92, 104] and in extensions such as Minimal Flavor Violation [50, 65], Two-Higgs-Doublet Models [57], and others [69, 89].

1.3 The Large Hadron Collider

The analysis that is described in Chapter 2, and that directly probes the Standard Model, was conducted in a unique environment, the only environment where this study could possibly have been carried out. This environment was achieved with the high energy proton collisions produced with the Large Hadron Collider.

1.3.1 Introduction to the Large Hadron Collider

The Large Hadron Collider [53] is a high energy particle accelerator and collider that hosts four major experiments: ATLAS [33], CMS [63], LHCb [125], and ALICE [5], and several smaller experiments: TOTEM [173], MoEDAL [141, 142], and LHCf [127]. The LHC has successfully delivered physics data to the experiments in two runs from 2010 to 2018.

The CERN accelerator complex is shown in Figure 1.1. Electrons are stripped from hydrogen atoms and the resulting protons are inserted to the LINAC2. The protons are accelerated through a chain of accelerator devices starting with the LINAC2, passing through the Proton Synchrotron Booster (PSB), the Proton Synchrotron (PS) and the Super Proton Synchrotron (SPS). The protons are inserted to the two beam pipes of the LHC from the SPS. The protons in each beam pipe are made to accelerate in opposite directions and are brought together at four interaction points, corresponding to the locations of the four experiments.

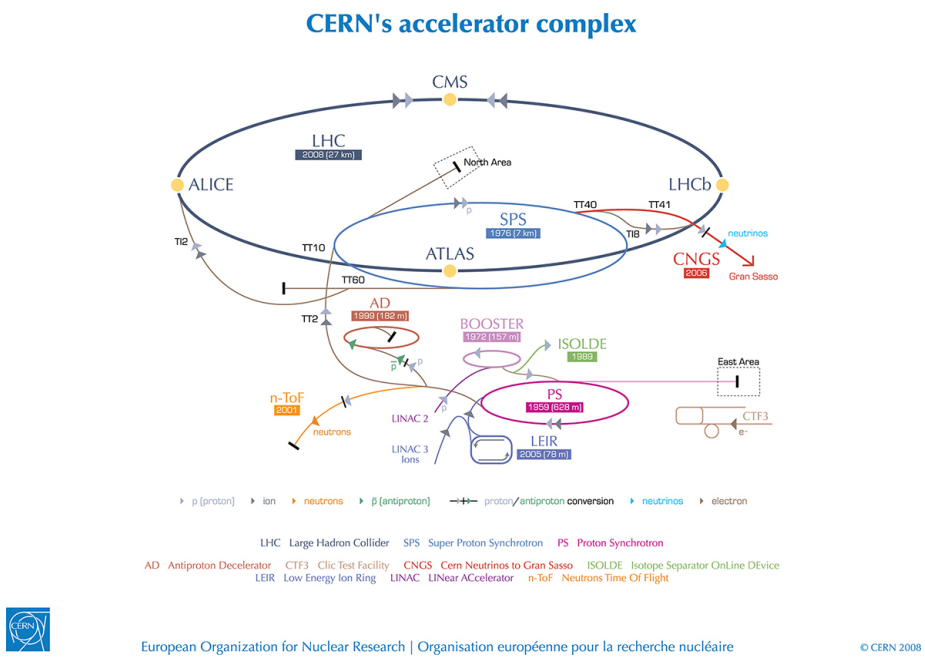


Figure 1.1: Large Hadron Collider complex. The top ring is the LHC at which is installed the ATLAS Detector. The original diagram can be found in Reference [118].

1.3.2 Energy and Luminosity

The LHC has achieved unprecedented success in terms of collisions at high center-of-mass energies and the quantity of data collected (integrated luminosity); these

are the two parameters most often cited for quantifying particle colliders [97]. The definitions of these two parameters are provided in this section.

The center-of-mass energy of two colliding particles can be computed using the energy-momentum four-vector $\mathbf{p} = (E, \overrightarrow{p})$. For one particle with mass m traveling with momentum $\overrightarrow{p}$ (using natural units, i.e. $c = 1$):

$$\mathbf{p}^2 = E^2 - \overrightarrow{p}^2 = m^2. \tag{1.1}$$

For two colliding particles, with mass m_1 and m_2, traveling with momentum $\overrightarrow{p}_1$ and $\overrightarrow{p}_2$, the center-of-mass energy can be written as:

$$(\mathbf{p}_1 + \mathbf{p}_1)^2 = E_{cm}^2 = s = (E_1 + E_2)^2 - (\overrightarrow{p}_1 + \overrightarrow{p}_2)^2. \tag{1.2}$$

The term s is introduced here as the standard notation [91, 133]. Taking the collision point to be in the laboratory frame, $\overrightarrow{p}_1 = -\overrightarrow{p}_2$, and the center-of-mass energy is simply:

$$\sqrt{s} = E_1 + E_2. \tag{1.3}$$

The first run of the LHC (LHC Run 1) was between the years 2010 and 2012. In 2010 and 2011, the LHC operated at a center-of-mass energy $\sqrt{s} = 7$ TeV. In 2012, the center-of-mass energy was $\sqrt{s} = 8$ TeV. LHC Run 2 was during the years of 2015 to 2018 and the center-of-mass energy during LHC Run 2 was $\sqrt{s} = 13$ TeV.

The luminosity is the measurement of the number of collisions that can be produced in a detector per cm^2 and per second. The luminosity is the proportionality constant between the rate of events (or collisions) and the cross section of the event:

$$\frac{dN}{dt} = \mathcal{L}\sigma_N. \tag{1.4}$$

In e^+e^- colliders the luminosity can be determined using a process with a well defined cross section. Typically, the Bhabha scattering process ($e^+e^- \rightarrow e^+e^-$) would be

used. For a hadron collider there is no corresponding process with a well known cross section. For the LHC, the parameters of the beam can be used to determine luminosity. As is shown in [97], the luminosity can be determined from the cross sections of the colliding proton beams (σ_x and σ_y), the number of protons per bunch (N_1 and N_2), the number of bunches (N_b), and the revolution frequency of protons in the collider ring (f):

$$\mathcal{L} = \frac{N_1 N_2 f N_b}{4\pi\sigma_x\sigma_y}. \tag{1.5}$$

Further details on the luminosity determination in the ATLAS experiment can be found in [16], with the techniques described therein (using van der Meer scans and dedicated luminosity detectors) the luminosity can be determined within a few percent.

1.4 The ATLAS Experiment

The experiment described in Chapter 2 was carried out using the ATLAS Detector. The "A Toroidal LHC ApparatuS" (ATLAS) experiment is one of two general purpose experiments on the LHC ring, the other being the Compact Muon Solenoid (CMS).

1.4.1 The ATLAS Detector

The ATLAS Detector is shown in Figure 1.2. The Pixel Detector is at the heart of ATLAS, closest to the interaction point of the LHC proton beams, just over 3 cm from the LHC beam pipe. The Muon chambers surround the rest of the detector and span 44 m and cover 25 m in height.

The ATLAS coordinate system is a right-handed coordinate system with the x-axis pointed toward the center of the LHC ring and the z-axis pointed along the LHC

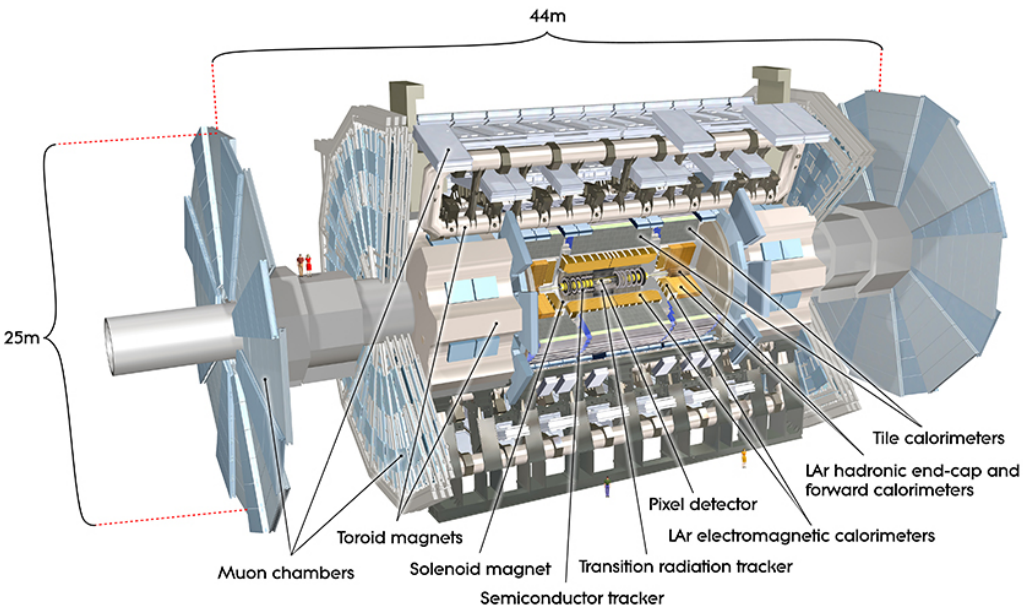


Figure 1.2: The ATLAS Detector [33].

beam line. The azimuthal angle, ϕ, is measured from the x-axis around the beam line. The polar angle is often reported as pseudorapidity, η, where

$$\eta = -\ln(\tan(\theta/2)). \tag{1.6}$$

The ATLAS Detector consists of many layers of state-of-the-art particle detectors. ATLAS features a unique hybrid system of four large superconducting magnets. This magnetic system is 22 m in diameter and 26 m in length, with a stored energy of 1.6 GJ. The magnet system is shown in Figure 1.3. It is made up of a central solenoid, a barrel toroid and two endcap toroids. The ATLAS Inner Detector is designed to provide hermetic and robust pattern recognition, excellent momentum resolution and both primary and secondary vertex measurements for charged tracks above a given momentum in the x-y, transverse plane (p_{T}) threshold (nominally 0.5 GeV) and within the pseudorapidity range $|\eta| < 2.5$. Approximately 1000 particles will emerge from the collision point every 25 ns within $|\eta| < 2.5$, creating a

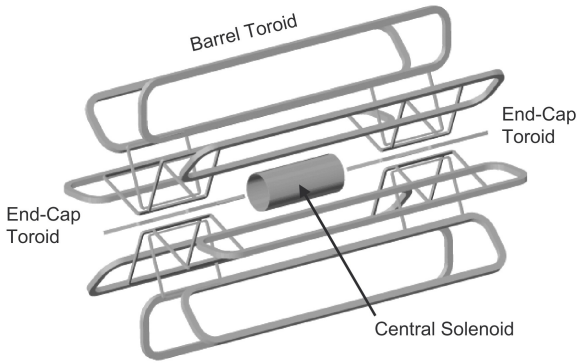


Figure 1.3: The Magnet System [33].

very large track density in the detector. To achieve the momentum and vertex resolution requirements imposed by the benchmark physics processes [33], high-precision measurements must be made with fine detector granularity. The Inner Detector (Figure 1.4) is designed to have superb tracking resolution; it is made up of three systems: the Pixel Detector, the Semiconductor Tracker (SCT), and the Transition Radiation Tracker (TRT). Between LHC Run 1 and Run 2 the Insertable B-Layer was installed as the closest pixel layer to the beam line. The Pixel Detector [1] is discussed in detail in Section 1.4.2. The SCT [23] is a silicon strip detector and is made up of over four thousand two sided modules arranged in four barrel layers and 2×9 disks. The TRT is a drift tube tracker [36]. The basic element of the TRT is a polyimide drift tube, also referred to as a straw tube, with a diameter of 4 mm. The layout of the Inner Detector can be seen in Figures 1.4 and 1.5. The precision electromagnetic calorimeters are lead-liquid argon detectors with absorbers and electrodes. For the outer hadronic calorimeter, the sampling medium consists of scintillator tiles and the absorber medium is steel. A diagram of the calorimeters is shown in Figure 1.6.

The muon spectrometer forms the outer part of the ATLAS Detector and is designed to detect charged particles exiting the barrel and endcap calorimeters and to measure their momentum in the pseudorapidity range $|\eta| < 2.7$. The Muon

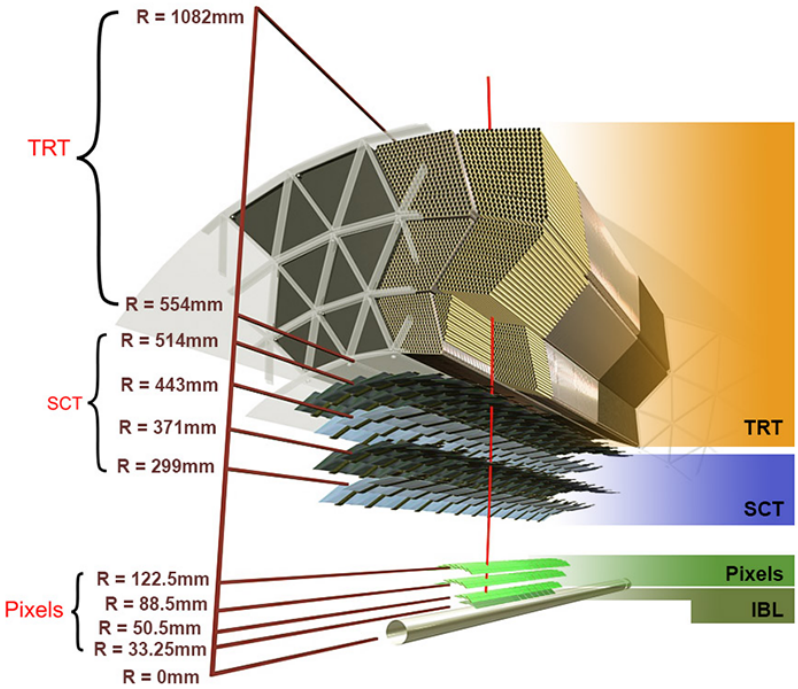


Figure 1.4: The barrel region of ATLAS Inner Detector depicting the Pixel, SCT and TRT subsystems. The image includes the innermost layer of the Pixel Detector (IBL). This image was originally published in [33].

Spectrometer is shown in Figure 1.7.

For data collected during the LHC Run 2, the ATLAS Detector uses a two-level trigger system, consisting of a hardware-based first-level (L1) trigger and a software-based high-level trigger (HLT).

1.4.2 The Pixel Detector

The Pixel Detector is arranged in four barrel layers and 2×3 disks surrounding the proton-proton interaction point (see Figure 1.8); it is the closest ATLAS subsystem to the interaction point. The Insertable *B*-Layer (IBL), illustrated in Figure 1.8, is positioned at a radius of 33.25 mm from the LHC proton beam line. The study

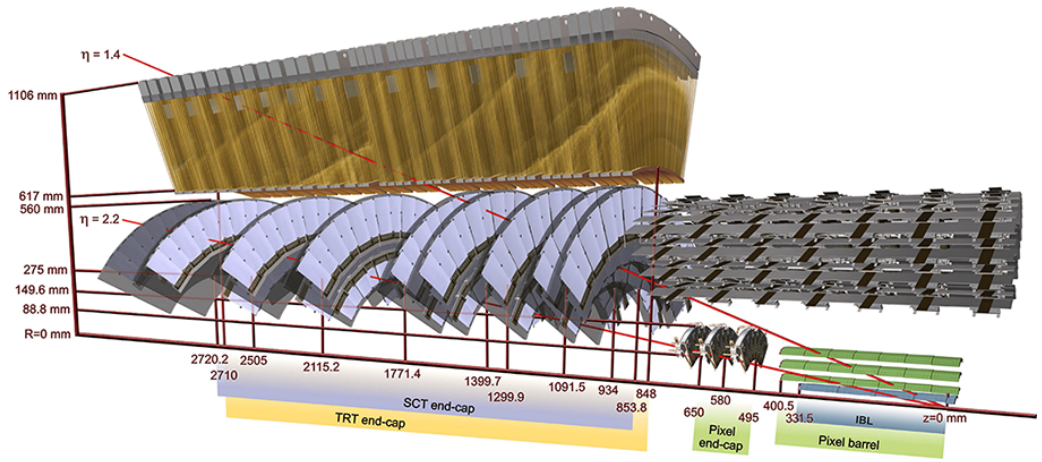


Figure 1.5: The Inner Detector showing the barrel regions of the Pixel Detector and SCT and one side of the endcap regions of the Pixel, SCT and TRT subsystems. The image includes the innermost layer of the Pixel Detector (IBL). This image (excluding IBL) was originally published in [33].

presented in Chapter 3 focuses on the outermost barrel layers and disks of the Pixel Detector. The three barrel layers used in the study are listed in increasing radius r from the beam line: the B-Layer is placed at $r = 50.5$ mm, Layer-1 at 88.5 mm, and

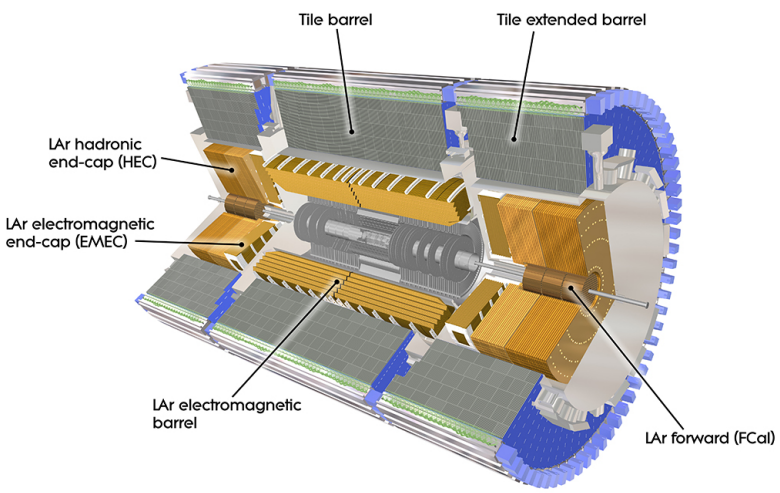


Figure 1.6: Calorimeter System [33].

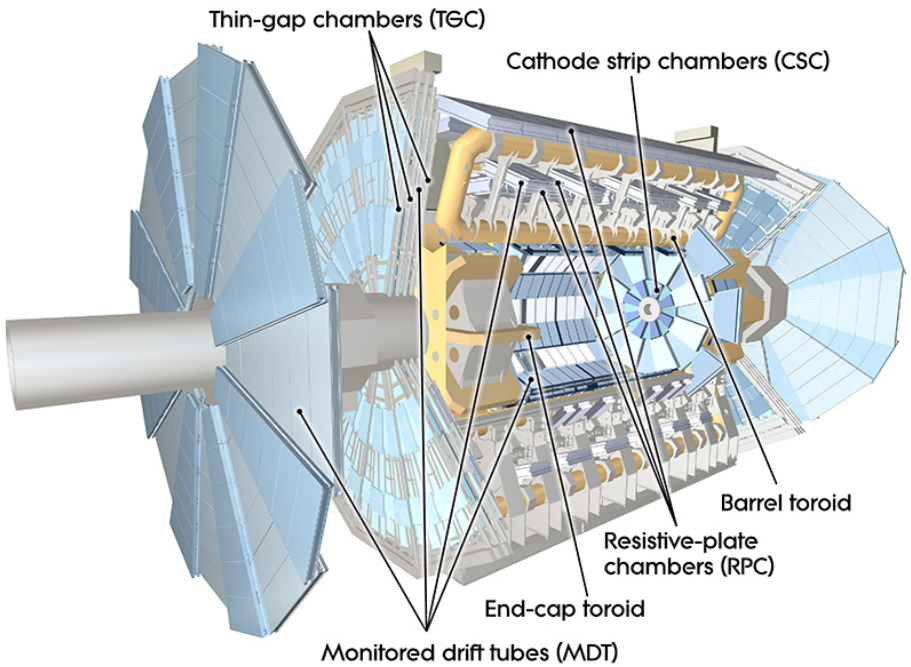


Figure 1.7: The Muon Spectrometer [33, 180].

Layer-2 at 122.5 mm.

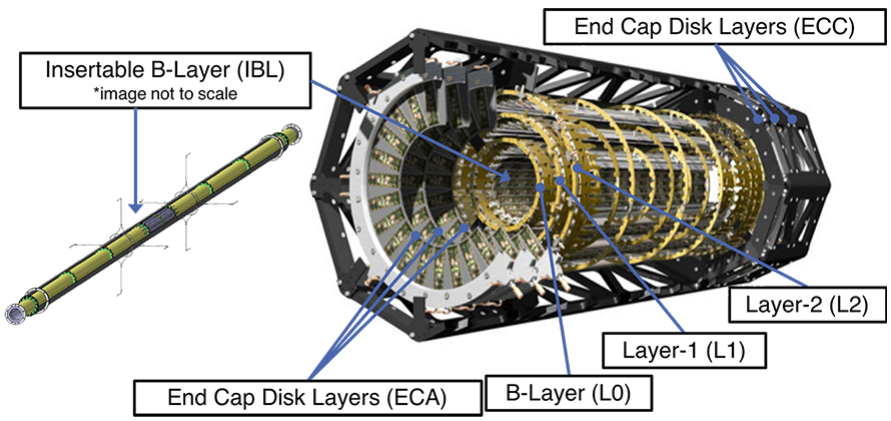


Figure 1.8: ATLAS Pixel Detector [18].

All three barrel layers have the same dimensions along the beam line axis, z = ± 380 mm, where z is measured from the interaction point, and they cover the

full azimuthal angle, ϕ. The disks are located at $z = \pm 495$ mm, ± 580 mm, and ± 650 mm and named Disk-1, Disk-2, and Disk-3, respectively. The modules on the disks have an inner radius of 8.88 cm and an outer radius of 14.96 cm. The barrel layers are comprised of 1456 silicon modules, and disks add an additional 288 modules. Each module includes a pixel sensor with an active surface area of 6.08 $\times$ 1.64 cm^2, fabricated on (252.5 $\pm$ 2.8) μm thick n-type bulk. The sensor is made by implanting highly doped p-type (p^+) and highly doped n-type (n^+) material on opposite surfaces of the bulk. These planar sensors operate with n^+ implants on the read-out side, where the front end electronics read out the signal, and the p-n junction on the back side. Details of the pixel sensor geometry and layout can be found in [1, 8].

A diagram of the planar sensor geometry can be seen in Figure 1.9 (left). Another geometry, called 3D, is shown in Figure 1.9 (right). These are presently operating [2] in the ATLAS Pixel IBL, and they are proposed [32] for future tracking upgrades as well. The 3D sensors contain n^+ and p^+ columnar implants in the silicon bulk and are more radiation hard due to smaller inter-electrode spacing.

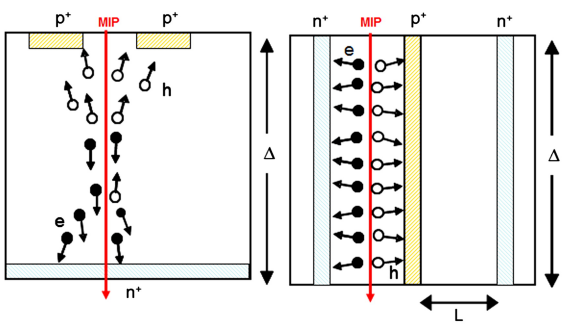


Figure 1.9: (Left) planar and (right) 3D silicon sensor geometries. These diagrams were originally published in [66].

1.5 ATLAS Experiment Upgrades

The analysis of unprecedented amounts of data described in Chapter 2 reveals a tension with the Standard Model, and as such, more data will be required to investigate the predictions of the Standard Model with more statistical power.

The LHC will undergo a major upgrade within the next decade to increase its luminosity by a factor of five beyond its design value and the integrated luminosity by a factor of ten. As a highly complex and optimized machine, an upgrade of the LHC must be carefully studied and requires about ten years to implement. The novel machine configuration, called the High Luminosity LHC (HL-LHC), will rely on a number of innovative technologies, representing exceptional technological challenges, such as cutting-edge 11–12 Tesla superconducting magnets, very compact superconducting cavities for beam rotation with ultra-precise phase control, new technology for beam collimation and 300-meter-long high-power superconducting links with negligible energy dissipation [162]. The nominal HL-LHC upgrade schedule is shown in Figure 1.10. The HL-LHC installations are expected to progress in the mid-2020's and operation will begin before the end of the decade.

The increase in luminosity and discovery potential that will be provided by the HL-LHC generates the need for an upgraded ATLAS detector. An ambitious plan to construct the largest silicon tracking device ever built is underway in the form of the ATLAS tracker upgrade, called the Inner Tracker (ITk) [32]. The ITk will comprise two sub-systems - the Strip Detector surrounding the Pixel Detector. The various layers of the ITk are shown in Figure 1.11, for a cross-section of one quadrant - where the interaction point of the crossing proton beams is located at z = 0 mm and r = 0 mm. The Strip Detector (shown in blue in Figure 1.11) will be made of four barrel layers and six endcap disks covering up to $|\eta| < 2.7$. The Pixel Detector (shown in red in Figure 1.11) will consists of five layers in the central region and ring-shaped

endcaps further from the interaction point, covering out to $|\eta| < 4$. The outer three

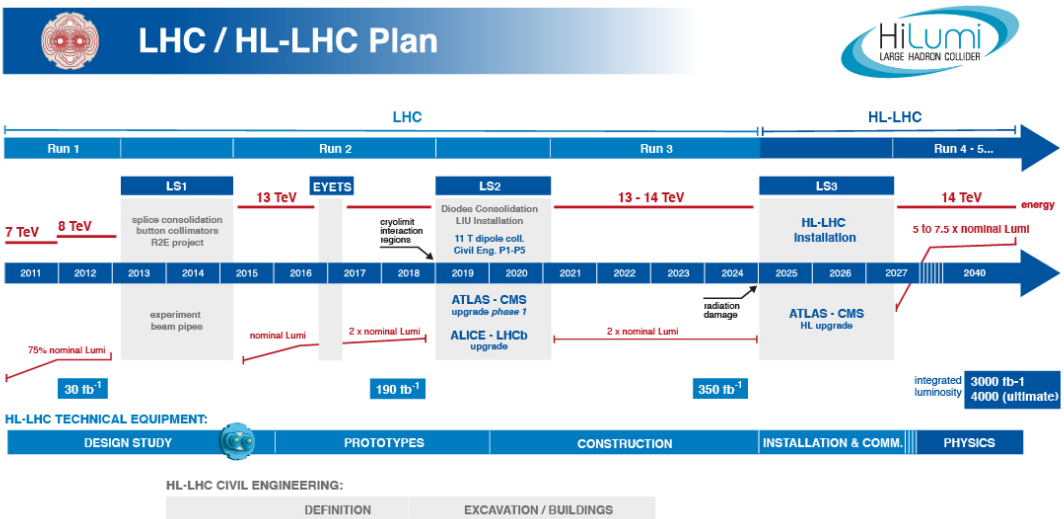


Figure 1.10: LHC and HL–LHC energy and luminosity schedule [54].

layers of the Pixel Detector are designed to operate for the full HL-LHC data-taking period; the innermost two layers of the detector will be replaced around halfway through the HL-LHC design lifetime. The ITk Pixel Detector will be instrumented with new sensors and readout electronics to provide improved tracking performance and radiation hardness compared to the current Pixel Detector. Sensors will be read out by new ASICs based on the chip developed by the RD53 Collaboration [157, 158]. Both 3D and planar sensor technologies will be implemented in the Pixel Detector, together with the module concept to be implemented in the ITk pixel system.

1.6 Irradiation Facilities

In order to understand the consequences of the high radiation environment in the ATLAS Detector, and will be present in the upgraded detector, large, technologically advanced facilities are required for controlled environment replication and device

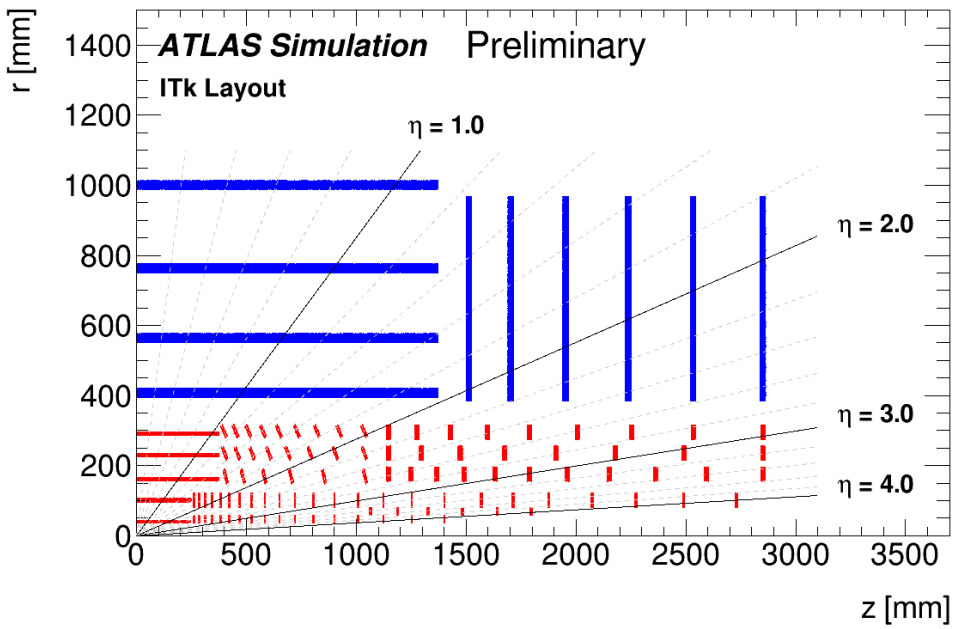


Figure 1.11: Layout of ITk pixel barrel layers and disks (red) and strip layers and disks (blue) [12].

testing.

The Neutron and Nuclear Science Research Facility (WNR) at Los Alamos National Laboratory provides neutron and proton beams and detector arrays for basic, applied, industrial, and defense-related research. Target 2 is housed in the Blue Room in MPF-7 at LANSCE and provides experimenters direct access to the LANSCE proton beam. The Blue Room is a domed room with a diameter of 40 feet. The main floor of the Blue Room is constructed primarily of aluminum and elevated 20 feet above the basement floor to minimize neutron wall return for experiments sensitive to such effects. The proton beam enters the Blue Room from the northeast and then exits to the southwest on its way to Target 4. During Target 2 operations, the beam line is removed in the middle of the Blue Room and experiments are installed at the center of the room in the path of the beam. Target 2 can use either

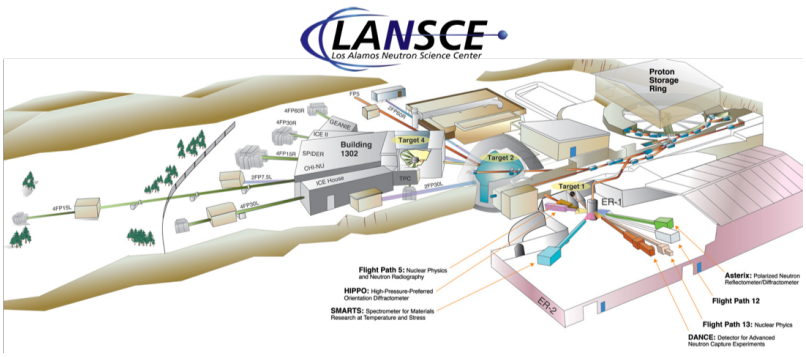


Figure 1.12: LANSCE proton beam line facility. This image can found in [130].

the LANSCE linac beam directly, or the high peak intensity stacked beam from the Proton Storage Ring (PSR). The linac beam to the Blue Room can normally be run at up to 80 nA with substructure available for experiments that require it. Normal linac operations provide 800 MeV protons, but the facility is capable of delivering protons with energy from 200 MeV to 800 MeV. The PSR beam can run from pulse-on-demand up to 40 Hz, and up to 1 A average current. PSR beam pulse intensity can be as high as a few 10^{13} protons/pulse.

The Gamma Irradiation Facility (GIF) at Sandia National Laboratories provides high-fidelity simulation of nuclear radiation environments for materials and component testing. The GIF can produce a wide range of gamma radiation environments (from 10^{-3} to over 10^{3} rad/second) using cobalt-60 sources, and can irradiate objects as small as electronic components and as large as an Abrams M1 tank. The GIF provides in-cell dry irradiations in three test cells and in-pool submerged irradiations.

1.7 Prelude

The work described in the following chapters is based in the theoretical framework and experimental facilities thus far presented. What will manifest is a collection of

carefully selected and interconnected projects that support the prime goal of extending the knowledge of physics through precision testing of the Standard Model. Such an ambition requires advanced statistical tools and applications which were previously undeveloped. Since more statistics is critical to the success of this mission, more data must be collected. To do so in reasonable time frames, a natural consequence is an unprecedented and harsh radiation environment. Such an environment has an adverse impact on the ability for high energy physics experiments to operate with high efficiency, and so careful attention is spent on radiation monitoring and modeling. Nonetheless, the natural increase in radiation, alongside a need for increased precision, to explore extremely large data sets, requires the construction of new particle detection devices. These topics are developed in the pages that follow.

Chapter 2

B^0 and B_s^0 Meson Decays to Two Muons

2.1 Introduction to the $B^0 \to \mu^+\mu^-$ and $B_s^0 \to \mu^+\mu^-$ Analysis

In the analysis of the data collected with the ATLAS Detector in 2015 and 2016 (2015+2016), a measurement of the branching ratio of $B_s^0 \to \mu^+\mu^-$ and an upper limit of the branching ratio of $B^0 \to \mu^+\mu^-$ have been achieved[1] [29]. A combination of these results with similar studies performed with the CMS and LHCb experiments is accomplished. Finally, the development of improved techniques with direct applications for the analysis of the full LHC Run 2 data (data collected in 2015 through 2018 with the ATLAS Detector) is presented.

Flavor-changing neutral-current processes are highly suppressed in the Standard

[1]The notation $B_{(s)}^0 \to \mu^+\mu^-$ will be used to reference both decay channels.

Model (SM). The $B^0_{(s)} \to \mu^+\mu^-$ decays are ultra rare B meson decays. The B meson decays primarily through the $b \to c$ quark transition, producing a charm (D) meson among the final state particles [49, 171]. The branching fractions of the decays $B^0_{(s)} \to \mu^+\mu^-$ are, in addition, helicity suppressed in the SM. Theoretical uncertainties in the calculation of the $B^0_s \to \mu^+\mu^-$ and $B^0 \to \mu^+\mu^-$ branching fractions have been reduced as a result of progress in lattice QCD [76, 80, 82, 103, 105], in the calculation of electroweak effects at next-to-leading order [48], and in the calculation of QCD effects at next-to-next-to-leading order [96]. The most current SM prediction is:

$$\mathcal{B}(B^0_s \to \mu^+\mu^-) = (3.66 \pm 0.14) \times 10^{-9}$$
$$\mathcal{B}(B^0 \to \mu^+\mu^-) = (1.03 \pm 0.05) \times 10^{-10}\,.$$

The direct flavor-changing neutral current process is forbidden in the Standard Model. Higher order processes are allowed in the Standard Model, but are highly suppressed. Two such processes are shown in the two diagrams of Figure 2.1. Extensions of the Standard Model containing new particles could contribute to the branching fractions of $B^0_{(s)} \to \mu^+\mu^-$. Two possible decay modes mediated by one or more undiscovered particles are shown in Figure 2.2.

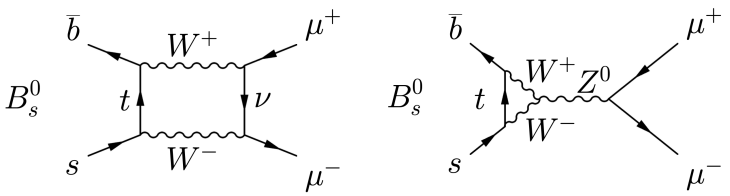


Figure 2.1: Diagrams of the $B^0_s \to \mu^+\mu^-$ decay. (Left) Direct flavor-changing neutral currents are forbidden in the Standard Model. (Middle) The box diagram and (right) penguin diagram represent higher order flavor-changing neutral currents and are allowed in the Standard Model but occur with a low probability. These diagrams were originally published in [60].

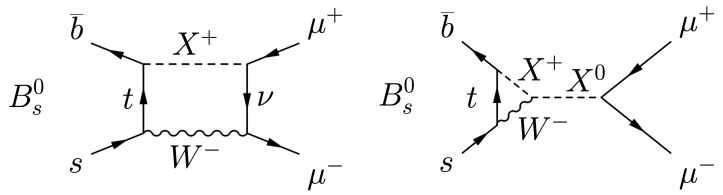


Figure 2.2: Two possible decay mode diagrams for $B_s^0 \to \mu^+\mu^-$ occurring in theories beyond the Standard Model. Here the X represents an undiscovered particle. These diagrams were originally published in [60].

Due to cancellation of several common factors, the ratio $\mathcal{R}$ of the $B^0 \to \mu^+\mu^-$ and $B_s^0 \to \mu^+\mu^-$ branching fractions is predicted with lower uncertainties than those of the individual branching fractions. The predicted ratio is $\mathcal{R} = 0.0281 \pm 0.0016$ [45]. Earlier predictions of the branching fractions [52] are used for comparison to some of the results presented in this chapter (results prior to Section 2.14): $\mathcal{B}(B_s^0 \to \mu^+\mu^-) = (3.65 \pm 0.23) \times 10^{-9}$ and $\mathcal{B}(B^0 \to \mu^+\mu^-) = (1.06 \pm 0.09) \times 10^{-10}$. The smallness and precision of these predicted branching fractions provide a favorable environment for observing contributions from new physics - as described in the introduction chapter of this thesis.

The CMS and LHCb collaborations reported the observation of $B_s^0 \to \mu^+\mu^-$ [62, 121] and evidence of $B^0 \to \mu^+\mu^-$ with combined values $\mathcal{B}(B_s^0 \to \mu^+\mu^-) = \left(2.8^{+0.7}_{-0.6}\right) \times 10^{-9}$ and $\mathcal{B}(B^0 \to \mu^+\mu^-) = \left(3.9^{+1.6}_{-1.4}\right) \times 10^{-10}$ [60]. The LHCb Collaboration updated its Run 1 result with part of the data collected in Run 2, measuring $\mathcal{B}(B_s^0 \to \mu^+\mu^-) = \left(3.0 \pm 0.6^{+0.3}_{-0.2}\right) \times 10^{-9}$ (where the first uncertainty is statistical and the second systematic) and determining $\mathcal{B}(B^0 \to \mu^+\mu^-) < 3.4 \times 10^{-10}$ at 95% confidence level (CL) [122]. ATLAS has measured, with the Run 1 dataset [28], $\mathcal{B}(B_s^0 \to \mu^+\mu^-) = \left(0.9^{+1.1}_{-0.8}\right) \times 10^{-9}$, while setting an upper limit on $B^0 \to \mu^+\mu^-$ of 4.2×10^{-10} at 95% CL.

The result of a search for $B_s^0 \to \mu^+\mu^-$ and $B^0 \to \mu^+\mu^-$ decays is performed using pp collision data corresponding to an effective integrated luminosity of 26.3 fb^{-1},

collected at 13 TeV center-of-mass energy during the first two years of the LHC Run 2 data-taking period using the ATLAS detector. The analysis strategy follows the approach employed in the previous ATLAS measurement [28], but uses data collected with one rather than three separate sets of trigger thresholds, applies standard ATLAS muon selection criteria (Section 2.3) rather than a dedicated muon multivariate discriminant, and employs an improved statistical treatment of the result (Section 2.10).

The notation used throughout this chapter refers to the combination of processes and their charge-conjugates, unless otherwise specified. The $B_s^0 \to \mu^+\mu^-$ and $B^0 \to \mu^+\mu^-$ branching fractions are measured relative to the reference decay mode $B^+ \to J/\psi(\to \mu^+\mu^-)K^+$ which is abundant and has a well-measured branching fraction $\mathcal{B}(B^+ \to J/\psi\, K^+) \times \mathcal{B}(J/\psi \to \mu^+\mu^-)$. The $B^0 \to \mu^+\mu^-$ ($B_s^0 \to \mu^+\mu^-$) branching fraction can be extracted as:

$$\begin{aligned}\mathcal{B}(B^0_{(s)} \to \mu^+\mu^-) &= \frac{N_{d(s)}}{\varepsilon_{\mu^+\mu^-}} \times \left[\mathcal{B}(B^+ \to J/\psi\, K^+) \times \mathcal{B}(J/\psi \to \mu^+\mu^-)\right] \frac{\varepsilon_{J/\psi K^+}}{N_{J/\psi K^+}} \times \frac{f_u}{f_{d(s)}} \\ &= N_{d(s)} \frac{\mathcal{B}(B^+ \to J/\psi\, K^+) \times \mathcal{B}(J/\psi \to \mu^+\mu^-)}{\mathcal{D}_{\text{ref}}} \times \frac{f_u}{f_{d(s)}}\,, \end{aligned} \tag{2.1}$$

where N_d (N_s) is the $B^0 \to \mu^+\mu^-$ ($B_s^0 \to \mu^+\mu^-$) signal yield, $N_{J/\psi K^+}$ is the $B^+ \to J/\psi\, K^+$ reference channel yield, $\varepsilon_{\mu^+\mu^-}$ and $\varepsilon_{J/\psi K^+}$ are the corresponding values of acceptance times efficiency (measured in fiducial regions defined in Section 2.9), and f_u/f_d (f_u/f_s) is the ratio of the hadronization probabilities of a b-quark into B^+ and B^0 (B_s^0). In the quantity $\mathcal{D}_{\text{ref}} = N_{J/\psi K^+} \times (\varepsilon_{\mu^+\mu^-}/\varepsilon_{J/\psi K^+})$, the ε ratio takes into account relative differences in efficiencies, integrated luminosities and the trigger selections used for the signal and the reference modes. Signal and reference channel events are selected with similar dimuon triggers. One half of the reference channel sample is used to determine the normalization and the other half is used to tune the kinematic distributions of simulated events.

The event selection uses variables related to the B candidate decay time, thus

introducing a dependence of the efficiency on the signal lifetime. The relation between the measured branching fraction and the corresponding value at production is established assuming the decay time distribution predicted in the SM, where the decay occurs mainly through the heavy eigenstate $B^0_{(s),\mathrm{H}}$ of the $B^0_{(s)}$–$\overline{B}^0_{(s)}$ system. Some models of new physics [51, 70] predict modifications to the decay time distribution of $B_s^0 \to \mu^+\mu^-$ and a comparison with the experimental result requires a correction to the ratio of the time-integrated efficiencies entering $\mathcal{D}_{\mathrm{ref}}$.

2.2 ATLAS Data and Simulation Samples

The total effective integrated luminosity used in the analysis of the 2015+2016 data amounts to 26.3 fb^{-1} for the signal channel ($B^0_{(s)} \to \mu^+\mu^-$) and 15.1 fb^{-1} for the reference channel ($B^+ \to J/\psi\, K^+$). These totals reflect the implementation for trigger prescale factors - factors that reduce the rate at which data are collected and limit the total amount of data stored for further analysis. Prescale factors are implemented to optimize the use of available resources. Further discussion of the prescales used in this analysis is in Section 2.3.

Samples of simulated Monte Carlo (MC) events are used for training and validation of the multivariate analysis, for the determination of the efficiency ratios, and for developing the procedure used to determine the signal. Exclusive MC samples were produced for the signal channels $B_s^0 \to \mu^+\mu^-$ and $B^0 \to \mu^+\mu^-$, the reference channel $B^+ \to J/\psi\, K^+$ ($J/\psi \to \mu^+\mu^-$), and the control channel $B_s^0 \to J/\psi\,\phi$ ($J/\psi \to \mu^+\mu^-$, $\phi \to K^+K^-$). The control channel is used for cross-checking the analysis procedures and results. In addition, background studies employ MC samples of inclusive $b\bar{b} \to \mu^+\mu^- X$ decays, exclusive samples of $B_s^0 \to K^-\mu^+\nu$, $B^0 \to \pi^-\mu^+\nu$, $\Lambda_b \to p\mu^-\overline{\nu}$, $B^0_{(s)} \to hh'$ decays with $h^{(\prime)}$ being a charged pion or kaon, and inclusive decays $B \to J/\psi X$ as well as the exclusive $B^+ \to J/\psi\,\pi^+$ decay.

Most of the dimuon candidates in the data sample originate from the decays of hadrons produced in the hadronization of $b\bar{b}$ pairs. The inclusive $b\bar{b} \to \mu^+\mu^- X$ MC sample used to describe this background requires the presence of two muons in the final state, with both muons originating from the $b\bar{b}$ decay chain. The size of this sample is equivalent to roughly three times the integrated luminosity of the data.

The MC samples were generated with Pythia 8 [165]. The ATLAS detector and its response were simulated using Geant4 [4, 34]. Additional pp interactions in the same and nearby bunch crossings (pileup) are included in the simulation. Muon reconstruction and triggering efficiencies are corrected in the simulated samples using data-driven scale factors. The scale factors for the trigger efficiencies are obtained by comparing data and simulation efficiencies determined with a tag-and-probe method on inclusive prompt and non-prompt J/ψ candidates. This procedure yields scale factors as a function of the muon transverse momentum and pseudorapidity, which are applied throughout the analysis [17]. Reconstruction and selection efficiencies are obtained from simulation and similarly corrected according to data-driven comparisons. In addition to these efficiency corrections, simulated events are reweighted to reproduce the pileup multiplicity observed in data, and according to the equivalent integrated luminosity associated with each trigger selection.

Using the iterative reweighting method described in Reference [26], the simulated samples of the exclusive decays considered are adjusted with two-dimensional data-driven weights (DDW) to correct for the differences between simulation and data observed in the B meson transverse momentum and pseudorapidity distributions. DDW obtained from $B^+ \to J/\psi\, K^+$ decays are used to correct the simulation samples in the signal and reference channels. DDW obtained from the $B_s^0 \to J/\psi\, \phi$ control channel are found to agree with those from $B^+ \to J/\psi\, K^+$, showing that the same corrections are applicable to B_s^0 and B^0 decays.

Residual differences between data and simulation studied in the $B^+ \to J/\psi\, K^+$

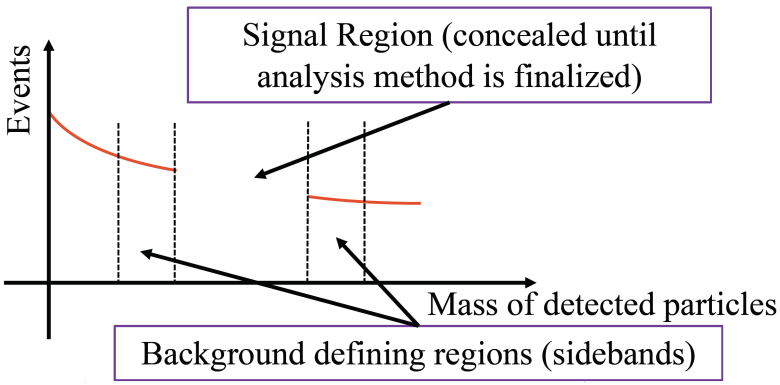


Figure 2.3: Diagram of sideband regions.

and $B_s^0 \to J/\psi\,\phi$ signals are treated as sources of systematic uncertainty in the evaluation of the signal efficiency, as discussed in Section 2.9. The only exception to this treatment is the B meson isolation ($B_{\rm iso}$ in Section 2.6 and Table 2.2), where residual differences are used to reweight the signal MC events and the corresponding uncertainties are propagated to account for residual systematic uncertainty effects.

Similarly to the exclusive decays, the kinematic distributions of the inclusive $b\bar{b} \to \mu^+\mu^- X$ MC sample are reweighted with corrections obtained from dimuon invariant mass sidebands in data. A signal region is defined as the invariant mass range in which the mass of the signal is expected to be observed. In this blind analysis, the signal region is concealed until all analysis procedures, described in the following sections, are finalized. After the analysis procedures are determined, the signal region is revealed and the signal extraction performed. Characterization of background events must be made outside of the signal region. The sideband regions are defined to have close enough proximity to the $B_{(s)}^0 \to \mu^+\mu^-$ signal to contain background events similar to those in the signal region. An illustration of the signal and sideband regions is shown in Figure 2.3. In this analysis the signal region is defined as the dimuon invariant mass range [5166.0–5526.0] MeV. The left sideband is the dimuon invariant mass range [4766.0–5166.0] MeV and the right sideband is

[5526.0–5966.0] MeV. For the reference and control channels, the signal region is [5180–5380] ([5297–5437]) MeV for $B^+ \to J/\psi\, K^+$ ($B_s^0 \to J/\psi\, \phi$) and the left and right sidebands used for background subtraction are [4930–5180] ([5050–5297]) MeV and [5380–5630] ([5437–5650]) MeV, respectively.

2.3 Data Selection

A first-level (L1) dimuon trigger [24] selects events by requiring that one muon has $p_{\mathrm{T}} > 4$ GeV and the other has $p_{\mathrm{T}} > 6$ GeV. A full track reconstruction of the muon candidates is performed by the high-level trigger, where an additional loose selection is imposed on the dimuon invariant mass $m_{\mu\mu}$, accepting candidates in the range 4 GeV to 8.5 GeV. Due to the increased pileup in 2016 data, an additional selection was added at this trigger stage, requiring the vector from the primary vertex to the dimuon vertex to have a positive component (L_{xy}) along the dimuon's transverse momentum direction. The effect of this selection is accounted for in the analysis but has no consequence since stricter requirements are applied in the full event selection (see Section 2.6).

The signal channel, the reference channel $B^+ \to J/\psi\, K^+$ and the control channel $B_s^0 \to J/\psi\phi$ were selected with trigger prescale factors that vary during the data-taking period. In the 36.2 fb^{-1} of data analyzed, the prescaling of the trigger averages to a reduction by a factor of 1.4. The resulting effective integrated luminosity for the signal sample is 26.3 fb^{-1}. For the reference and control channels an effective integrated luminosity of 15.1 fb^{-1} was collected due to a prescale of 2.4. These effects are taken into account in the extraction of the signal branching fraction, through the ε factors in Equation 2.1.

Using information from the full offline reconstruction, a preliminary selection is performed on candidates for $B_{(s)}^0 \to \mu^+\mu^-$, $B^+ \to J/\psi\, K^+ \to \mu^+\mu^- K^+$ and B_s^0

$\to J/\psi\phi \to \mu^+\mu^- K^+K^-$ decays. In the ID system, muon candidates are required to have at least one measured hit in the Pixel Detector and two measured hits in the Semiconductor Tracker. They are also required to be reconstructed in the MS, and to have $|\eta| < 2.5$. The offline muon pair must pass the $p_{\mathrm{T}} > 4$ GeV and $p_{\mathrm{T}} > 6$ GeV requirements imposed by the trigger. Furthermore, the muon candidates are required to fulfill *tight* muon quality criteria [22]; this requirement is relaxed to *loose* for the hadron misidentification studies in Section 2.5. Kaon candidates must satisfy similar requirements in the ID, except for a looser requirement of $p_{\mathrm{T}} > 1$ GeV and *loose* track requirements are applied.

The computed B meson properties are based on a decay vertex fitted to two, three or four tracks, depending on the decay process to be reconstructed. The B candidates are required to have a χ^2 per degree of freedom below 6 for the fit to the B vertex, and below 10 for the fit to the $J/\psi \to \mu^+\mu^-$ vertex. The selections $2915 < m(\mu^+\mu^-) < 3275$ MeV and $1005 < m(K^+K^-) < 1035$ MeV are applied to the $J/\psi \to \mu^+\mu^-$ and the $\phi \to K^+K^-$ vertices, respectively. In the fits to the $B^+ \to J/\psi\, K^+$ and $B_s^0 \to J/\psi\, \phi$ channels, the reconstructed dimuon mass is constrained to the world average J/ψ mass [171].

Reconstructed B candidates are retained if they satisfy $p_{\mathrm{T}}^B > 8.0$ GeV and $|\eta^B| < 2.5$. The invariant mass of each B candidate is calculated using muon trajectories measured by combining the information from the ID and MS to improve upon the mass resolution obtained from ID information only [19].

The coordinates of primary vertices (PV) are obtained from charged-particle tracks not used in the decay vertices, and that are constrained to the luminous region of the colliding beams in the transverse plane. The matching of a B candidate to a PV is made by extrapolating the candidate's trajectory to the point of closest approach to the beam axis, and choosing the PV with the smallest distance along z. Simulation shows that this method matches the correct vertex with a probability

above 99% for all relevant pileup conditions.

To reduce the large background in the $B^0_{(s)} \to \mu^+\mu^-$ channel before applying the final selection based on multivariate classifiers, a loose collinearity requirement is applied between the momentum of the B candidate ($\overrightarrow{p}^B$) and the vector from the PV to the decay vertex ($\overrightarrow{\Delta x}$). The absolute value of the azimuthal angle α_{2D} between these two vectors is required to be smaller than 1.0 radians. The combination $\Delta R_{\text{flight}} = \sqrt{{\alpha_{\text{2D}}}^2 + (\Delta\eta)^2}$, where $\Delta\eta$ is the difference in pseudorapidity, is required to satisfy $\Delta R_{\text{flight}} < 1.5$.

A summary of the selection criteria described above is provided in Table 2.1. The mass of the B meson is calculated from the mass of the paired muons. The μ_{lead} is the leading muon in p_{T} and μ_{trail} is the trailing muon in p_{T}. The tight muon track selections ensure that the muons are not misidentified and suppress the $B \to hh$ background. The additional selections are all kinematic and reduce the background in the $B^0_{(s)} \to \mu^+\mu^-$ channel.

After the preliminary selection, approximately 3.5×10^6 candidates are found in the $B^0_{(s)} \to \mu^+\mu^-$ fit region, with about 1.0×10^6 falling in the blinded range [5166, 5526] MeV.

Following selection and processing of the data, a validation campaign is undertaken to ensure the quality of the data. The sideband data are separated into ATLAS data-taking periods and the distributions of the reconstructed variables are investigated to identify possible systematic changes. The data collection periods are designed such that they represent data with a coherent configuration of the detector and the trigger. Any significant changes to either the detector configuration or calibration or to the trigger result in the definition of a new period.

The stability of the yield during the 2015 and 2016 data collection period is investigated in two data samples: B^+ signal and $B^0_{(s)} \to \mu^+\mu^-$ sidebands. In each

Category	Candidate Event Selection Criteria
Mass Window Cut	$m_{B(\mu\mu)} > 4766.0$ MeV $m_{B(\mu\mu)} < 5966.0$ MeV
Blind Cut	$m_{B(\mu\mu)} \leq 5166.0$ MeV or $m_{B(\mu\mu)} \geq 5526.0$ MeV
Trigger Cut	Event in HLT Trigger Event in L1 Trigger Trigger_Matched == true
Muon Tight Cut	μ_{lead} isTight == true μ_{trail} isTight == true
Muon Conditions Cut	μ_{lead} accept == true μ_{trail} accept == true μ_{lead} isCombinedMuon == true μ_{trail} isCombinedMuon == true
Muon Kinematics Cuts	$p_T^{\mu_{trail}} > 4000$ MeV $\lvert\eta_{\mu_{trail}}\rvert < 2.5$ $p_T^{\mu_{lead}} > 6000$ MeV $\lvert\eta_{\mu_{lead}}\rvert < 2.5$
B Fit Cut	$B_{fit}\ \chi^2/NDF < 6.0$
B Kinematics Cuts	$p_T^B > 8000$ MeV $\lvert\eta_{\mathrm{B}}\rvert < 2.5$
Additional Cuts	$L_{xy} > 0.0$ $\lvert\alpha_{2D}\rvert < 1.0$ $\Delta R < 1.5$

Table 2.1: Loose analysis selections applied to $B^0_{(s)} \to \mu^+\mu^-$ data, $B^0_{(s)} \to \mu^+\mu^-$ signal Monte Carlo, and $b\bar{b} \to \mu^+\mu^- X$.

case the yield is corrected for trigger prescales and based exclusively on the triggers selected for the data analysis. Figure 2.4 shows the $B^0_{(s)} \to \mu^+\mu^-$ sidebands (left) and $B^+ \to J/\psi\, K^+$ signal event yields in data (right), as a function of ATLAS data-

taking period (the period names follow a letter scheme, i.e. Period A, Period B, Period C, etc., and reset back to A each year). The $B^0_{(s)} \to \mu^+\mu^-$ sideband yield is approximately stable along the data-taking period.

The $B^+ \to J/\psi\, K^+$ yield is obtained - in each period - as the number of B^+ signal events[2], divided by the period-integrated luminosity for the corresponding high level trigger[3]. The signal yield is overall stable and reasonably flat.

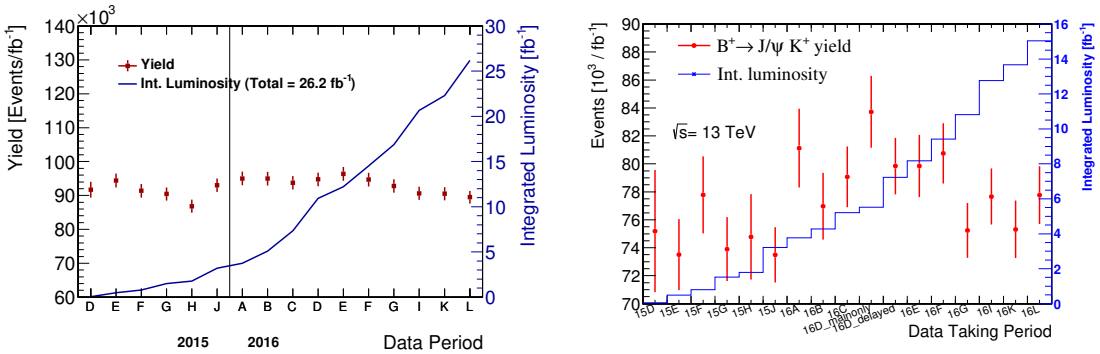


Figure 2.4: (Left) stability of the $B^0_{(s)} \to \mu^+\mu^-$ sidebands yield and (right) the $B^+ \to J/\psi\, K^+$ signal yield for the 2015 and 2016 data-taking periods. For $B^+ \to J/\psi\, K^+$, the *Delayed* stream was activated from the run 302956 in the Period D of 2016, therefore the period D has been split into two parts: 16D_mainonly, with the data available only in the *Main* stream and 16D_delayed, with the data from the *Delayed* stream. The integrated luminosity of the $B^0_{(s)} \to \mu^+\mu^-$ and $B^+ \to J/\psi\, K^+$ samples is overlaid and is reported with the axis on the right. The errors on the yield are calculated by adding the error on the number of events and the error on the luminosity in quadrature. The error on the luminosity is 2.2% [16, 39].

Systematic changes to the reconstructed variable distributions are, in general, not expected. Figure 2.5 (left) shows the distribution of the variable ΔR_{flight} (defined above) for the ATLAS data-taking periods in 2015 and 2016. Every relevant analysis variable is investigated and the variable distributions are compared across each

[2]This number is extracted using a binned maximum likelihood fit similar to the one used in the data-MC comparisons for $B^+ \to J/\psi\, K^+$ described in Section 2.7.

[3]The ATLAS high level trigger tag is HLT_mu6_mu4_bJpsimumu_XXX.

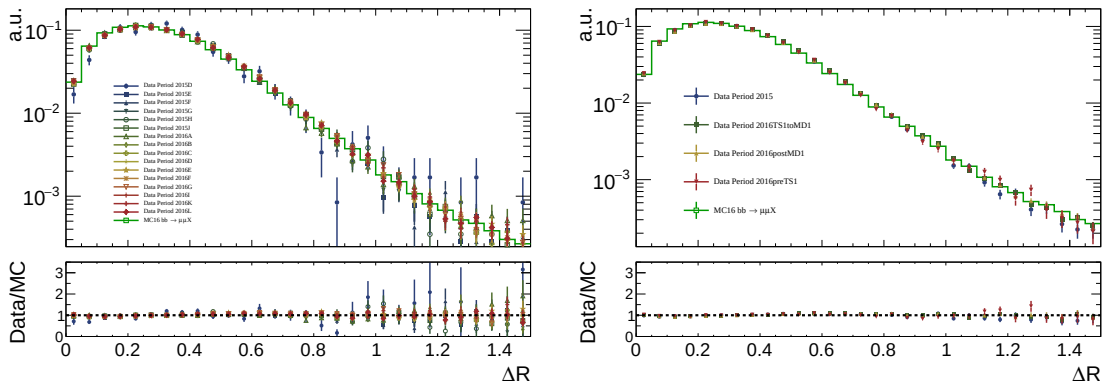


Figure 2.5: (Left) variable distribution of ΔR_{flight} for the ATLAS data-taking periods in 2015 and 2016. (Right) The ΔR_{flight} distribution across longer data collection periods in 2015 and 2016 defined between technical stops and machine development stops. An auxiliary comparison is made to the ΔR_{flight} distribution in (green line) the $b\bar{b} \to \mu^+\mu^- X$ background MC sample.

data-taking period, similar to the distribution comparisons in Figure 2.5 (left). No significant systematic shifts are observed between the ATLAS data-taking periods. Some fluctuations are observed in the 2015 period D due to low statistics.

The data are separated into longer time periods, defined between the expected technical stops and machine development stops. These define the coarse data-taking periods. An example of the visualizations performed for the study of the coarse data-taking periods is shown in Figure 2.5 (right). No significant systematic shifts are observed between the coarse data-taking periods, with the exception of the impact parameters to the primary vertex of the tracks forming the B candidate, in the transverse plane. The smaller and larger impact parameters are labeled as d_0^{min} and d_0^{max} respectively. A minor shift is observed in these variables due to alignment between the innermost Pixel Detector layer IBL and the rest of the detector. These discrepancies are included in systematic uncertainties on the final signal yield extraction.

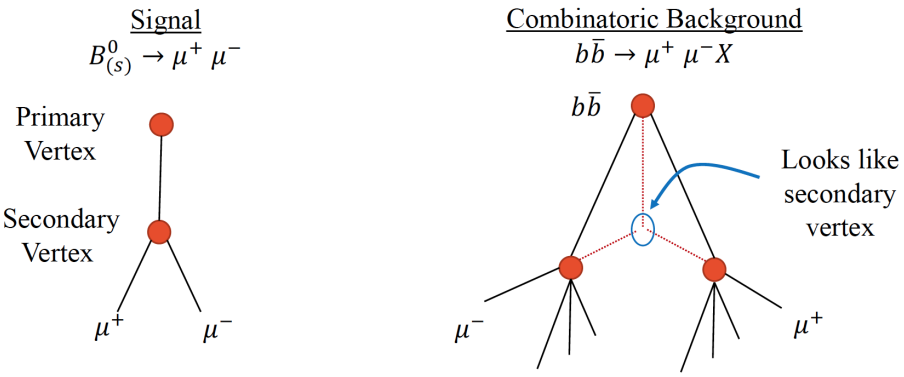


Figure 2.6: Illustration of the difference between a signal $B^0_{(s)} \to \mu^+\mu^-$ event and the dominant combinatoric background.

2.4 Background Composition

The background to the $B^0_{(s)} \to \mu^+\mu^-$ signal originates from three main sources:

Continuum background, the dominant combinatorial component, which consists of muons originating from uncorrelated hadron decays and is characterized by a weak dependence on the dimuon invariant mass;

Partially reconstructed decays, where one or more of the final-state particles (X) in a b-hadron decay is not reconstructed, causing these candidates to accumulate in the low dimuon invariant mass sideband (this background includes a significant contribution from semileptonic decays where one of the muons is a misidentified hadron, discussed below);

Peaking background, due to $B^0_{(s)} \to hh'$ decays, with both hadrons misidentified as muons.

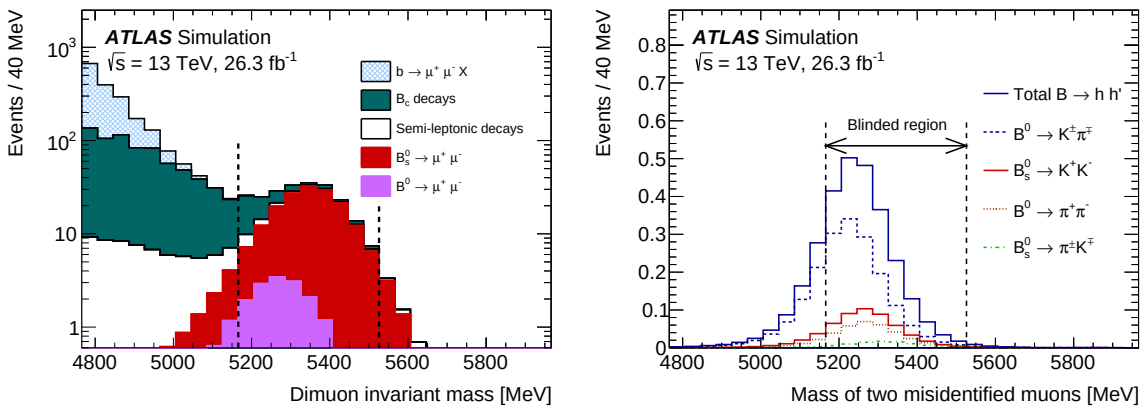
The continuum background consists mainly of muons produced independently in the fragmentation and decay chains of a b-quark and a $\bar{b}$-quark. It is studied in the signal mass sidebands, and it is found to be well described by the inclusive $b\bar{b} \to \mu^+\mu^- X$ MC sample. An illustration is provided in Figure 2.6 to show the difference between a signal event and a background-like event.

The partially reconstructed decays consist of several topologies: (a) *same-side* combinatorial background from decay cascades ($b \to c\mu^-\overline{\nu} \to s(d)\mu^+\mu^-\nu\overline{\nu}$); (b) *same-vertex* background from B decays containing a muon pair (e.g. $B^0 \to K^{*0}\mu^+\mu^-$ or $B \to J/\psi\mu^+X \to \mu^+\mu^-\mu^+X$); (c) B_c^+ decays (e.g. $B_c^+ \to J/\psi\mu^+\nu \to \mu^+\mu^-\mu^+\nu$); (d) semileptonic b-hadron decays where a final-state hadron is misidentified as a muon. The remainder of this chapter implicitly excludes categories (c) and (d) when referring to partially reconstructed or $b \to \mu^+\mu^-X$ decays, since these categories are treated separately.

The $b\bar{b} \to \mu^+\mu^-X$ MC sample is used to investigate the background composition after the analysis selection. All backgrounds in this sample have a dimuon invariant mass distribution mainly below the mass range considered in this analysis, with a high-mass tail extending through the signal region. The simulation does not contemplate sources other than muons from $b\bar{b}$ decays: $c\bar{c}$ and prompt contributions are not included[4]. All possible origins of two muons in the $b\bar{b}$ decay tree are, however, analyzed, after classification into the mutually exclusive continuum and partially reconstructed categories described above. This sample is used only to identify suitable functional models for the corresponding background components, and as a benchmark for these models. No shape or normalization constraints are derived from this simulation. This makes the analysis largely insensitive to mismatches between background simulation and data.

The semileptonic decays with final-state hadrons misidentified as muons consist mainly of three-body charmless decays $B^0 \to \pi^-\mu^+\nu$, $B_s^0 \to K^-\mu^+\nu$ and $\Lambda_b \to p\mu^-\overline{\nu}$ in which the tail of the invariant mass distribution extends into the signal region. Due to branching fractions of the order of 10^{-6}, this background is not large, and is further reduced by the muon identification requirements, discussed in Section 2.5.

[4]These sources are suppressed by the final analysis selections introduced in Section 2.6. Potential residual contributions are found to be consistent with the continuum background models used in the final fit (Section 2.10.1), where systematic uncertainties for background model inconsistencies between data and MC are taken into account (Section 2.10.3).



(a) (b)

Figure 2.7: (a) Dimuon invariant mass distribution for the partially reconstructed background (as categorized in Section 2.4), from simulation, before the final selection against continuum is applied but after all other requirements. The different components are shown as stacked histograms, normalized according to world-averaged measured branching fractions. The SM expectations for the $B^0_{(s)} \to \mu^+\mu^-$ signals are also shown for comparison. Continuum background is not included here. (b) Invariant mass distribution of the $B^0_{(s)} \to hh'$ peaking background components after the complete signal selection is applied. The $B^0_s \to \pi^+\pi^-$ and $B^0 \to K^+K^-$ contributions are negligible on this scale. In both plots the vertical dashed lines indicate the blinded analysis region. Distributions are normalized to the expected yield for the integrated luminosity of 26.3 fb^{-1}. These figures were originally published in [29].

The MC invariant mass distributions of these partially reconstructed decay topologies are shown together with the SM signal predictions in Figure 2.7(a) after applying the preliminary selection criteria described in Section 2.3.

Finally, the peaking background is due to $B^0_{(s)} \to hh'$ decays containing two hadrons misidentified as muons. The distributions in Figure 2.7(b), obtained from simulation, show that these decays populate the signal region. This component is further discussed in Section 2.5.

2.5 Hadron Misidentification

In the preliminary selection, muon candidates are formed from the combination of tracks reconstructed independently in the ID and MS. The performance of the muon reconstruction in ATLAS is presented in Reference [22]. Additional studies were performed to evaluate the amount of background related to hadrons erroneously identified as muons.

Detailed simulation studies were performed for the $B^0_{(s)} \to hh'$ channel with a full GEANT4-based simulation [4] of all systems of the ATLAS detector. The vast majority of background events from particle misidentification are due to decays in flight of kaons and pions, in which the muon receives most of the energy of the parent meson. Hence this background is generally related to true muons measured in the MS, but not produced promptly in the decay of a B meson.

The muon candidate is required to pass *tight* muon requirements in the preliminary selection, which are based on the profile of energy deposits in the calorimeters as well as on tighter ID–MS matching criteria than those used for the *loose* requirements. Two-body B decays in control regions show that *tight* selections have, relative to the *loose* counterpart, an average hadron misidentification probability reduced by a factor of 0.39 with a muon reconstruction efficiency of 90%. The resulting final value of the misidentification probability is 0.08% for kaons and 0.1% for pions. Efficiencies and fake rates are relative to the analysis preselections, including tracking but excluding any muon requirement.

The background due to $B^0_{(s)} \to hh'$, with double misidentification of hh' as $\mu^+\mu^-$, has a reconstructed invariant mass distribution that peaks at 5240 MeV, close to the B^0 mass, and is effectively indistinguishable from the B^0 signal (see Figure 2.7(b)). The expected number of peaking-background events can be estimated in a way anal-

ogous to that for the signal, from the number of observed $B^+ \to J/\psi\, K^+$ events using Equation 2.1, after taking into account the expected differences from muon identification variables and trigger selections. World average [171] values for the branching fractions of B^0 and B_s^0 into $K\pi$, KK and $\pi\pi$ are used, together with the hadron misidentification probabilities obtained from simulation. This results in 2.7 ± 1.3 total expected peaking-background events, after the reference multivariate selection.[5]

When selecting *loose* muons and inverting the additional requirements imposed in the *tight* muon selection, the number of events containing real muons is substantially reduced, while the number of peaking-background events is approximately two times larger than in the sample obtained with the nominal selection. A fit to data for this background-enhanced sample returns 6.8 ± 3.7 events, which translates into a peaking-background yield in the signal region of 2.9 ± 2.0 events when taking into account the relative rejection of the muon quality selections. The predicted yield is in good agreement with the simulation.

Besides the peaking background, the *tight* muon selection also reduces the semileptonic contributions with a single misidentified hadron. Simulation yields 30 ± 3 events expected from the $B^0 \to \pi^- \mu^+ \nu$ and $B_s^0 \to K^- \mu^+ \nu$ channels in the final sample, with a distribution kinematically constrained to be mostly below the signal region. The $\Lambda_b \to p \mu^- \overline{\nu}$ contribution is negligible due to the smaller production cross section and the low rate at which protons fake muons.

[5]This selection, corresponding to 54% signal efficiency, was also applied to derive all other quantities quoted in this Section and includes a selection against the $\mu^+\mu^-$ continuum background based on the boosted decision tree (BDT) discussed in Section 2.6.

2.6 Continuum Background Reduction via Multivariate Analysis

A multivariate analysis (MVA) strategy, implemented as a boosted decision tree (BDT) classifier, is employed to enhance the signal relative to the continuum background. The BDT is implemented using the TMVA [100] package of ROOT. After discussion of the individual variables, details of training and testing of the classifier are provided. This is followed by an evaluation of the BDT performance. The terms training, testing (equivalently, validation) and evaluation refer to distinct steps in procedures of implementing the BDT classifier and will be discussed in detail below.

2.6.1 Discriminating Variables

Fifteen physical input variables are used to obtain the signal-to-background discriminator. The fifteen variables used are summarized in Table 2.2 along with a short description of each variable. The discriminating variables can be classified into four categories: (a) B meson variables, related to the reconstruction of the decay vertex and to the collinearity between $\overrightarrow{p}^B$ and the flight vector between the production and decay vertices $\overrightarrow{\Delta x}$; (b) variables describing the muons that form the B meson candidate; (c) variables related to the isolation of the B candidate within the event; and (d) a variable used to indicate the degree of compatibility of a muon in the B candidate originating somewhere else in the event. The selection of the variables aims to maximize the discrimination power of the classifier without introducing significant dependence on the invariant mass of the muon pair.

The same discriminating variables were used in the previous analysis based on the full Run 1 dataset [28]. The removal of individual variables was explored to simplify the BDT input, however, this results inevitably in a significant reduction of the BDT

Variable	Description
$p_{\rm T}^B$	Magnitude of the B candidate transverse momentum $\overrightarrow{p_{\rm T}}^B$.
$\chi^2_{\rm PV,DV}\ _{xy}$	Compatibility of the separation $\overrightarrow{\Delta x}$ between production (i.e. associated PV) and decay (DV) vertices in the transverse projection: $\overrightarrow{\Delta x}_{\rm T}\cdot\Sigma^{-1}_{\overrightarrow{\Delta x}_{\rm T}}\cdot\overrightarrow{\Delta x}_{\rm T}$, where $\Sigma_{\overrightarrow{\Delta x}_{\rm T}}$ is the covariance matrix.
$\Delta R_{\rm flight}$	Three-dimensional angular distance between $\overrightarrow{p}^B$ and $\overrightarrow{\Delta x}$: $\sqrt{{\alpha_{\rm 2D}}^2+(\Delta\eta)^2}$
$\lvert\alpha_{\rm 2D}\rvert$	Absolute value of the angle in the transverse plane between $\overrightarrow{p_{\rm T}}^B$ and $\overrightarrow{\Delta x}_{\rm T}$.
L_{xy}	Projection of $\overrightarrow{\Delta x}_{\rm T}$ along the direction of $\overrightarrow{p}^B_{\rm T}$: $(\overrightarrow{\Delta x}_{\rm T}\cdot\overrightarrow{p_{\rm T}}^B)/\lvert\overrightarrow{p_{\rm T}}^B\rvert$.
${\rm IP}_B^{\rm 3D}$	Three-dimensional impact parameter of the B candidate to the associated PV.
${\rm DOCA}_{\mu\mu}$	Distance of closest approach (DOCA) of the two tracks forming the B candidate (three-dimensional).
$\Delta\phi_{\mu\mu}$	Azimuthal angle between the momenta of the two tracks forming the B candidate.
$\lvert d_0\rvert^{\rm max}$-sig.	Significance of the larger absolute value of the impact parameters to the PV of the tracks forming the B candidate, in the transverse plane.
$\lvert d_0\rvert^{\rm min}$-sig.	Significance of the smaller absolute value of the impact parameters to the PV of the tracks forming the B candidate, in the transverse plane.
$P_{\rm L}^{\rm min}$	The smaller of the projected values of the muon momenta along $\overrightarrow{p_{\rm T}}^B$.
$B_{\rm iso}$	Isolation variable defined as ratio of $\lvert\overrightarrow{p_{\rm T}}^B\rvert$ to the sum of $\lvert\overrightarrow{p_{\rm T}}^B\rvert$ and the transverse momenta of all additional tracks contained within a cone of size $\Delta R=\sqrt{(\Delta\phi)^2+(\Delta\eta)^2}=0.7$ around the B direction. Only tracks matched to the same PV as the B candidate are included in the sum.
${\rm DOCA}_{\rm xtrk}$	DOCA of the closest additional track to the decay vertex of the B candidate. Only tracks matched to the same PV as the B candidate are considered.
$N_{\rm xtrk}^{\rm close}$	Number of additional tracks compatible with the decay vertex (DV) of the B candidate with $\ln(\chi^2_{\rm xtrk,DV})<1$. Only tracks matched to the same PV as the B candidate are considered.
$\chi^2_{\mu,\rm xPV}$	Minimum χ^2 for the compatibility of a muon in the B candidate with any PV reconstructed in the event.

Table 2.2: Description of the 15 input variables used in a BDT classifier to discriminate between signal and continuum background. When the BDT classifier is applied to $B^+\to J/\psi\,K^+$ and $B_s^0\to J/\psi\,\phi$ candidates, the variables related to the decay products of the B mesons refer only to the muons from the decay of the J/ψ. Horizontal lines distinguish the groups (a), (b), (c) and (d) respectively, as described in the text. For category (c), additional tracks are required to have $p_{\rm T}>500$ MeV.

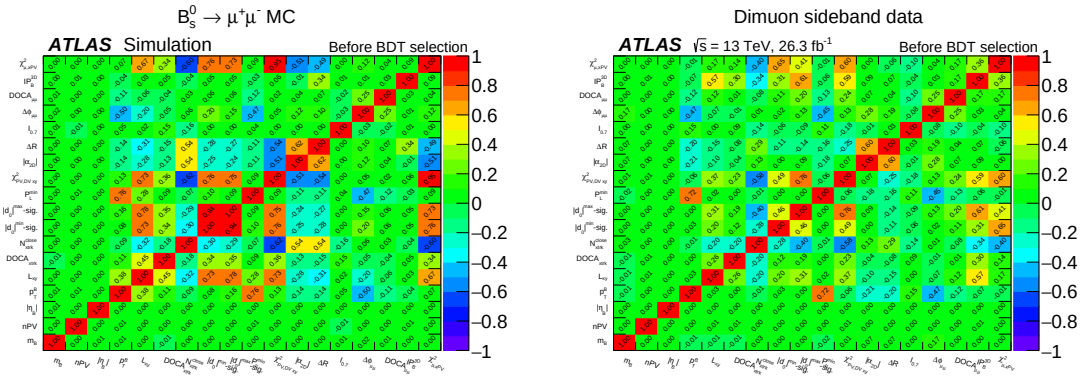


Figure 2.8: Correlation matrix of analysis variables for (left) signal Monte Carlo and (right) dimuon sideband datasets before the BDT output variable is used for data selection.

discrimination power. The proper decay time ($c\tau$) has also been investigated, but due to significant correlations with the variables $\chi^2_{\mathrm{PV,DV}\,xy}$ and L_{xy}, it is excluded from the BDT. To minimize the dependence of the classifier on the effects of pileup, the additional tracks considered to compute the variables B_{iso}, $\mathrm{DOCA}_{\mathrm{xtrk}}$ and $N^{\mathrm{close}}_{\mathrm{xtrk}}$ are required to be compatible with the primary vertex matched to the dimuon candidate.

The correlations among the discriminating variables are studied in the MC samples for signal and continuum background discussed in Section 2.2, and in data from the sidebands of the $\mu^+\mu^-$ invariant mass distribution. The correlation matrices can be seen in Figure 2.8. There are significant linear correlations among the variables $\chi^2_{\mathrm{PV,DV}\,xy}$, L_{xy}, $|d_0|^{\mathrm{max}}$-sig., $|d_0|^{\mathrm{min}}$-sig. and $\chi^2_{\mu,\mathrm{xPV}}$. The variables $\mathrm{IP}_B^{\mathrm{3D}}$, $\mathrm{DOCA}_{\mu\mu}$ and B_{iso} have negligible correlation with any of the others used in the classifier.

2.6.2 Training, Testing, and Implementation Strategy

The simulated signal sample and the data from the dimuon invariant mass sideband regions are used for training and testing the classifier. As discussed in Section 2.2,

simulated signal samples are corrected for muon reconstruction efficiency differences between simulation and data, and reweighted according to the distributions of p_{T} and $|\eta|$ of the dimuon and of the pileup observed in data.

Sideband data and the signal MC data are used for the BDT training and optimization. The samples are each subdivided into three randomly selected separate and equally populated subsamples used in turn to train and validate the selection efficiency of three independent BDTs. The resulting BDTs are found to produce results that are statistically compatible, and are combined in one single classifier in such a way that each BDT is applied only to the part of the data sample not involved in the BDT training.

It is important to use statistically independent samples for each of these three steps. In order to utilize the full datasets, a rotation strategy is implemented. The sample rotation strategy is summarized in Table 2.3.

An investigation is performed comparing the BDT discriminating variable distributions in each sample, for the signal MC and the sideband data. The examples shown in Figure 2.9 are selected from the distributions of the analysis variables. The sample splitting does not introduce any bias in the selection.

BDT Label	Trained	Tested	Evaluated
BDT 1	Sample 1	Sample 2	Sample 3
BDT 2	Sample 2	Sample 3	Sample 1
BDT 3	Sample 3	Sample 1	Sample 2

Table 2.3: Training, testing, and evaluation of the 3 BDTs. Each data sample contains 1/3 of the sideband data and 1/3 of the signal MC. For the evaluation sample, 1/3 of the signal MC and only the high-mass sideband of the collision data are used.

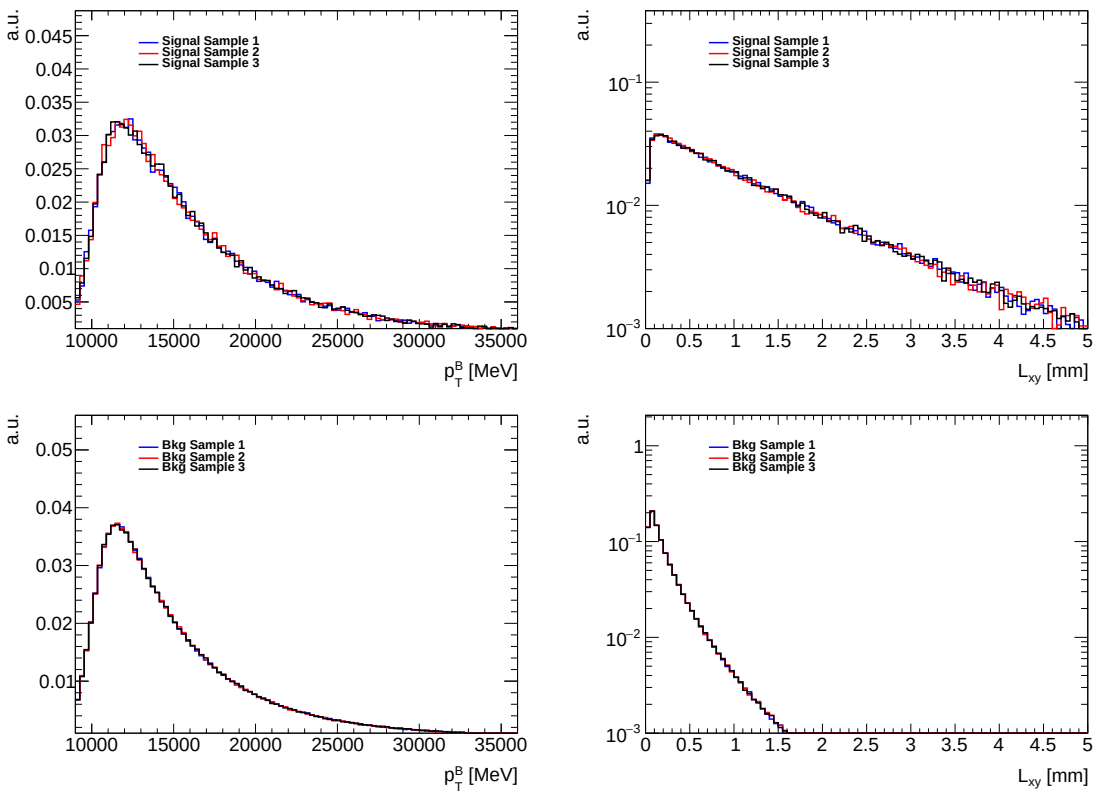


Figure 2.9: Distributions in (left) p_{T}^{B} and (right) L_{xy} of the sample splitting investigations to check for biases in the BDT training samples; both the (top) signal MC and (bottom) sideband data samples are compared.

After the three BDTs are trained and tested, they are evaluated on a third independent dataset which contains 1/3 of the signal MC and only the high-mass sideband of the collision data. The low-mass sideband is excluded from the evaluation procedure since it is contaminated with partially reconstructed decays. The evaluation samples are investigated separately and then together, always enforcing the requirement that the BDT is applied to data that are statistically independent of its training and testing samples.

2.6.3 BDT Configuration

The optimal values for the configuration parameters *MinNodeSize* and *AdaBoostBeta* are found with the help of a grid scan using background rejection at 36% signal efficiency on the Receiver Operating Characteristic (ROC) curve as the figure of merit for classifier performance. The *MaxDepth* parameter is also studied in this way; for this parameter, the performance of the classifier improves with increasing *MaxDepth*, whereas the discrepancy between its performances on the training and testing samples, accessed by the Kolmogorov-Smirnov test [113], becomes larger, leading to the over-training. Over-training occurs when the model has too many fitted parameters and does not generalize well to a larger dataset. In order not to compromise the generality of the classifier, the value $MaxDepth = 4$ is chosen. The value of *NTrees* is chosen to be large enough to allow the training to converge. The choice of other parameters does not have significant impact on the training result. The final choice of the configuration parameters of the BDT, as used by TMVA, is shown in Table 2.4.

2.6.4 Final BDT Output

The BDT importance values are provided by the TMVA output, they take into account how often the variables are used to split decision tree nodes, a weighting at each split occurrence by the separation gain-squared it has achieved and the number of events in the node [100]. The importance of each variable in training BDT 1 is given in Table 2.5 and compared to the separation power of the signal and background. The separation power is a function of two PDF distributions and is greater when the distributions have less overlap. Separation power is defined as:

$$\langle S^2 \rangle = \frac{1}{2} \int \frac{\left(\hat{y}_S(y) - \hat{y}_B(y)\right)^2}{\hat{y}_S(y) + \hat{y}_B(y)} dy \tag{2.2}$$

Parameter	Value	Description
NTrees	500	Number of decision trees used during BDT training.
MinNodeSize	0.2[%]	Minimum number of events used in each node in the decision tree.
MaxDepth	4	Maximum number of decision levels per tree.
BoostType	AdaBoost	Adaptive Boosting algorithm implemented.
AdaBoostBeta	0.5	Learning rate for the AdaBoost algorithm, implemented as an exponent to the boosting weight.
UseBaggedBoost	True	Use only a random (bagged) subsample of all events for growing the trees in each iteration.
BaggedSampleFraction	0.6	Size of bagged event sample relative to original size of the data sample.
SeparationType	GiniIndex	The Gini Index is used as the separation criterion for signal and background classification.
nCuts	100	The granularity over the variable range used for determining the cut value at the decision node.
NormMode	EqualNumEvents	The sum of all weighted signal training events equals the sum of all weights of the background training events.

Table 2.4: Configuration parameters of the BDT.

where $\hat{y}_S(y)$ and $\hat{y}_B(y)$ are the signal and background PDFs, respectively, as defined in [93, 100]. As a first order approximation, higher separation power of a given variable corresponds to higher BDT importance. This intuition is not always realized, however, because correlation between variables will lead the BDT to prefer other, less separated variables in order to increase the final signal-to-background discrimination power. The importance and separation power tables of the other two BDTs are

Variable	Imp. Rank	Importance	Sep. Rank	Separation
ΔR	1	0.11780	1	0.59710
$\lvert\alpha_{2D}\rvert$	2	0.11570	2	0.57890
B Isolation ($I^B_{0.7}$)	3	0.09715	7	0.36160
$\ln(\chi^2_{\mu,xPV})$	4	0.08314	3	0.44190
$\ln(\chi^2_{xy})$	5	0.07723	9	0.30730
$\lvert\Delta\phi_{\mu\mu}\rvert$	6	0.06692	15	0.02661
p_T^B	7	0.06338	13	0.04200
N_{trk}^{clos}	8	0.05866	4	0.42660
$\mathrm{DOCA}_{\mu\mu}$	9	0.05599	12	0.08282
$d^0_{max,sig}$	10	0.05087	10	0.17080
$\lvert IP_B^{3D}\rvert$	11	0.05032	11	0.15100
P_L^{min}	12	0.04700	14	0.03469
L_{xy}	13	0.04241	6	0.38910
$\mathrm{DOCA}_{xtrk,loose,pt>0.5}$	14	0.03732	8	0.31300
$d^0_{min,sig}$	15	0.03611	5	0.39140

Table 2.5: The BDT 1 ranking of input variable importance compared with the signal and background separation power of each variable as calculated by TMVA. Use of the term separation in the table heading implies separation power.

provided in Tables 2.6 and 2.7, showing values similar to those in Table 2.5.

Since individual muons in the signal decay are fairly well separated, isolation variables of individual muon candidates have also been investigated in the BDT training. However, they are excluded from the final training because they are shown to be highly correlated with the B isolation variable B_{iso} and did not improve the BDT performance as a result.

Figure 2.10 (left) shows the test for over-training of BDT 1, where the BDT outputs for training and testing samples are shown, confirming that the BDT is not over-trained as the training and testing samples are in good agreement with each other. In Figure 2.10 (right) the plot is magnified to show the upper tail of the

Variable	Imp. Rank	Importance	Sep. Rank	Separation
ΔR	1	0.11210	1	0.59830
$\lvert\alpha_{2D}\rvert$	2	0.11160	2	0.57890
B Isolation ($I^B_{0.7}$)	3	0.09587	7	0.36200
$\ln(\chi^2_{\mu,xPV})$	4	0.09386	3	0.43950
$\ln(\chi^2_{xy})$	5	0.07944	9	0.30520
$\lvert\Delta\phi_{\mu\mu}\rvert$	6	0.06463	15	0.02697
p_T^B	7	0.05780	13	0.04302
$\lvert IP_B^{3D}\rvert$	8	0.05628	11	0.14910
N_{trk}^{clos}	9	0.05540	4	0.42560
$\mathrm{DOCA}_{\mu\mu}$	10	0.05470	12	0.08036
L_{xy}	11	0.05308	6	0.38570
$d^0_{max,sig}$	12	0.04772	10	0.16850
P_L^{min}	13	0.04544	14	0.03507
$d^0_{min,sig}$	14	0.03779	5	0.38930
$\mathrm{DOCA}_{xtrk,loose,pt>0.5}$	15	0.03431	8	0.32220

Table 2.6: The BDT 2 ranking of input variable importance compared with the signal and background separation power of each variable as calculated by TMVA. Use of the term separation in the table heading implies separation power. Similar orders of variable importance are seen for each BDT training.

background sample in the signal extraction region. Similar results for BDT 2 and BDT 3 can be seen in Figures 2.11 and 2.12. While some structure may be observed in the linear scale figures, the BDT regions used in the remainder of the analysis are far to the right of this structure and no dependence on this shape is carried through.

Figure 2.13 contains the final BDT performance via the ROC curve and the comparison with the BDT used in the Run 1 analysis [30]. The ROC curve of the BDT used in the 2012 analysis applied to the 2015 and 2016 high-mass sideband data is also compared in this figure. There is a large increase in BDT performance compared to the BDT used in 2012 applied to the same data. However there is

Variable	Imp. Rank	Importance	Sep. Rank	Separation
ΔR	1	0.12130	1	0.60000
$\lvert\alpha_{2D}\rvert$	2	0.11090	2	0.57570
B Isolation ($I^B_{0.7}$)	3	0.09922	7	0.36650
$\ln(\chi^2_{xy})$	4	0.08526	9	0.30630
$\ln(\chi^2_{\mu,xPV})$	5	0.08429	3	0.44070
$\lvert\Delta\phi_{\mu\mu}\rvert$	6	0.06827	15	0.02672
p_T^B	7	0.05925	13	0.04204
N_{trk}^{clos}	8	0.05722	4	0.42590
$\mathrm{DOCA}_{\mu\mu}$	9	0.05282	12	0.08507
$d^0_{max,sig}$	10	0.05091	10	0.17020
$\lvert IP_B^{3D}\rvert$	11	0.04972	11	0.15060
P_L^{min}	12	0.04763	14	0.03403
L_{xy}	13	0.04072	6	0.38690
$d^0_{min,sig}$	14	0.04055	5	0.39130
$\mathrm{DOCA}_{xtrk,loose,pt>0.5}$	15	0.03193	8	0.32260

Table 2.7: The BDT 3 ranking of input variable importance compared with the signal and background separation power of each variable as calculated by TMVA. Use of the term separation in the table heading implies separation power. Similar orders of variable importance are seen for each BDT training.

some degradation in the performance of the Run 2 BDT with respect to the Run 1 BDT trained and evaluated on Run 1 data. This degradation provides motivation for improved analysis techniques for studying the full Run 2 dataset and is discussed in depth in Section 2.15.

An investigation is performed on the pileup dependence of the BDT discriminating variables. The datasets are separated into three pileup bins and each variable is investigated separately. The pileup bins are created so that approximately the same number of signal MC events are in each signal bin. The bins are defined based on the number of primary vertices (nPV) as nPV ≤ 11, $11 <$ nPV ≤ 15, and nPV > 15. Due to the increased pileup (and PV pileup density) in Run 2 the variables

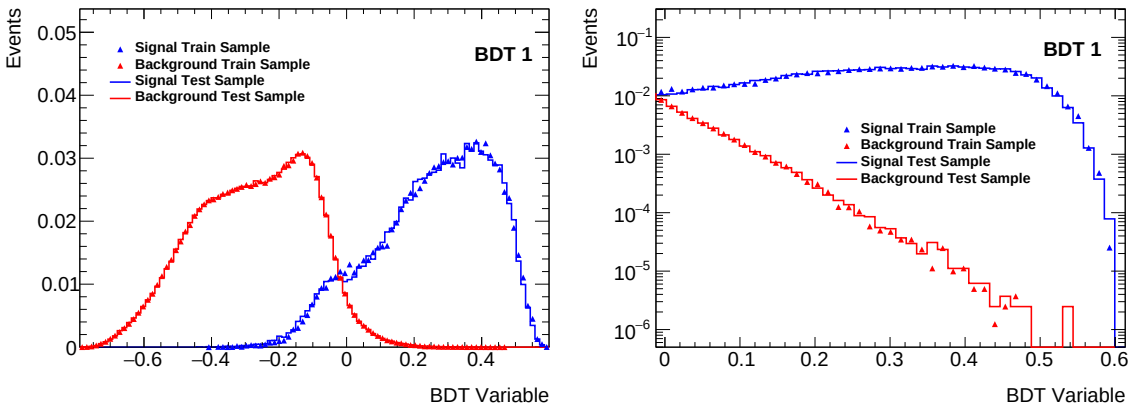


Figure 2.10: The BDT variable for the BDT trained with sample 1 and tested on sample 2 for (left) the full range of the BDT variable and (right) a magnified range with the vertical axis in log scale.

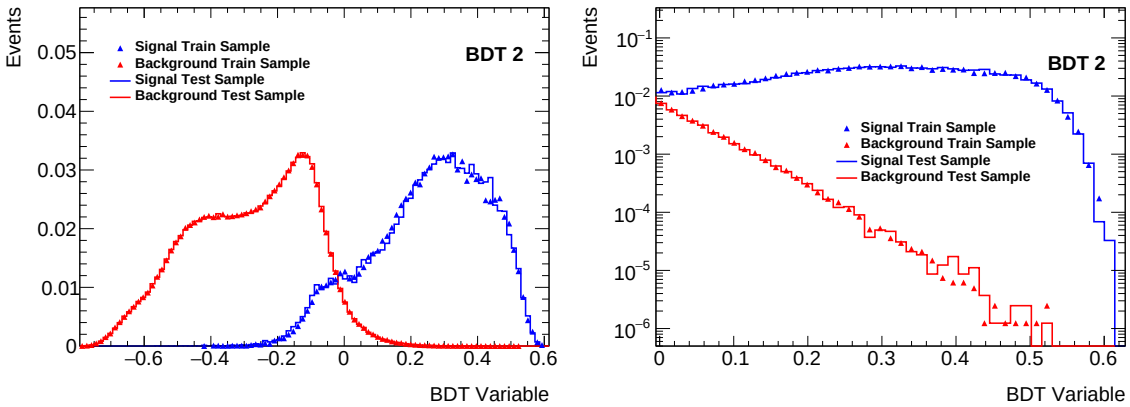


Figure 2.11: The BDT variable for the BDT trained with sample 2 and tested on sample 3 for (left) the full range of the BDT variable and (right) a magnified range with the vertical axis in log scale.

related to the isolation of the B meson vertices show a dependence on pileup. This dependence is demonstrated in Figure 2.15 for the B_{iso} discriminating variable.

The pileup-related degradation is confirmed in a similar study concerning the $B^+ \to J/\psi K^+$ data. Systematic uncertainties due to the residual pileup dependence

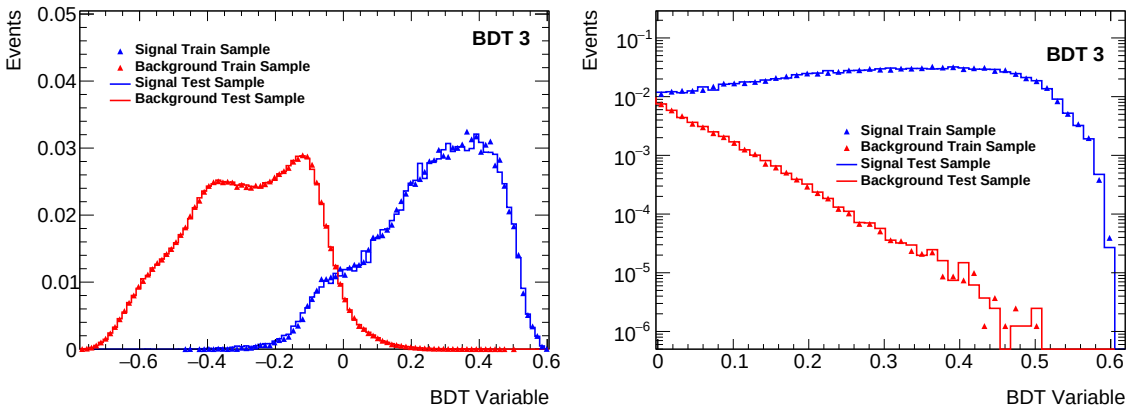


Figure 2.12: The BDT variable for the BDT trained with sample 3 and tested on sample 1 for (left) the full range of the BDT variable and (right) a magnified range with the vertical axis in log scale.

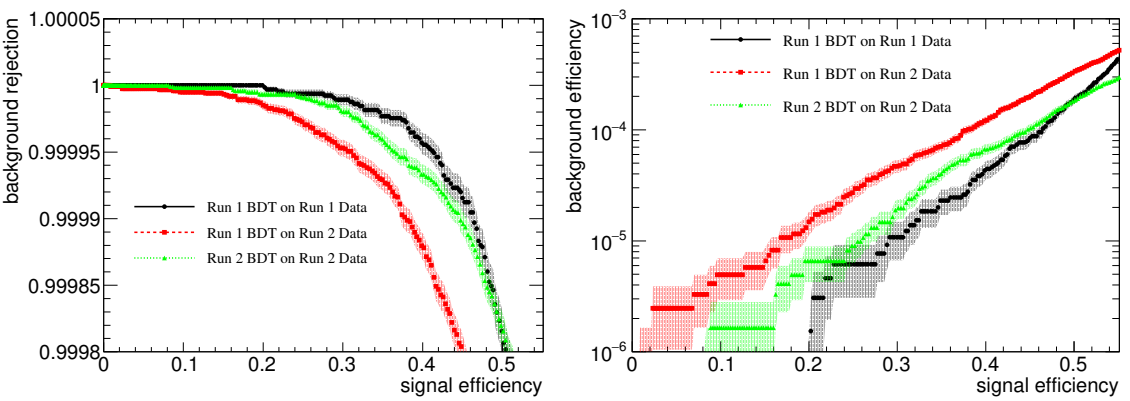


Figure 2.13: (Left) Comparison of the ROC curves for the Run 2 BDT and the Run 1 BDT applied to Run 1 and Run 2 Data. (Right) The ROC comparisons are also performed in a magnified range of the background efficiency versus signal efficiency in log scale. The ROCs are evaluated on the high-mass data sideband. Errors on the background efficiency values are represented by shaded error bands.

of the BDT response are included in the evaluation of the relative signal and reference channel efficiencies.

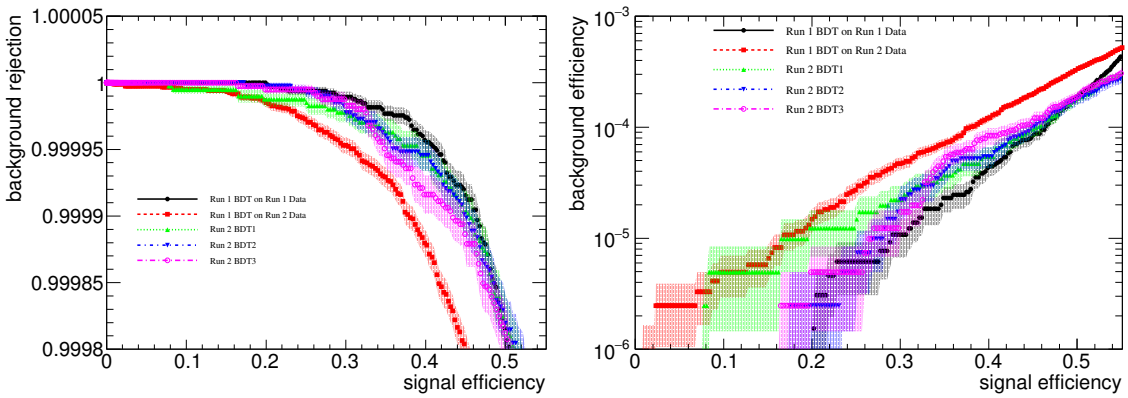


Figure 2.14: (Left) Comparison of ROC curves for the three Run 2 BDTs and the Run 1 BDT applied to Run 1 data and Run 2 data. (Right) The ROC comparisons are also performed in a magnified range of the background efficiency versus signal efficiency in log scale. The ROCs are evaluated on the high-mass data sideband (the evaluation dataset). Errors on the background efficiency values are represented by shaded bands.

Figure 2.16 shows the distribution of the BDT output variable for simulated signal and backgrounds, separately for continuum background and partially reconstructed events. Also shown is the BDT distribution for dimuon candidates from the sidebands of the invariant mass distribution in data. The BDT output was found not to have any significant correlation with the dimuon invariant mass. The correlation matrices of the analysis variables for the simulated signal and sideband data are shown after the BDT selection in Figure 2.17. The dimuon mass variable is also included in this comparison for verification of negligible correlation with the analysis variables.

The final selection requires a BDT output value larger than 0.1439, corresponding to signal and continuum background efficiencies of 72% and 0.3% respectively. The analysis uses all candidates after this selection; however, accepted events with BDT values close to the selection threshold are effectively only constraining the background

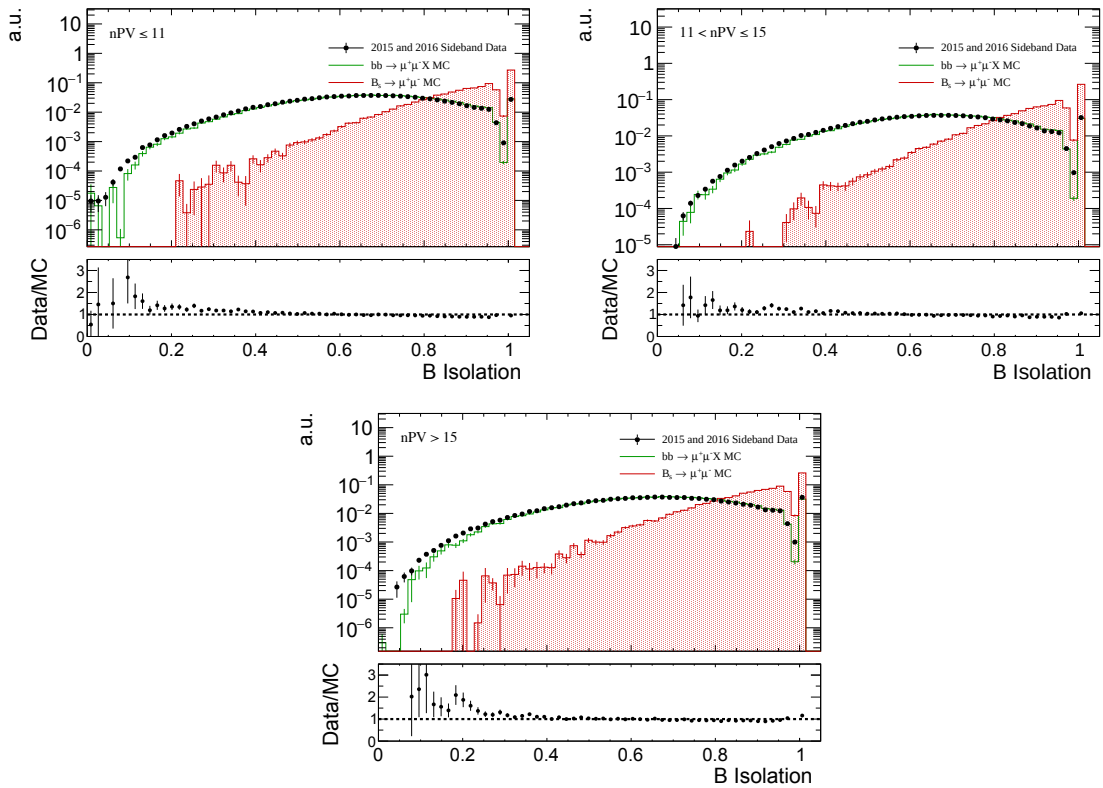
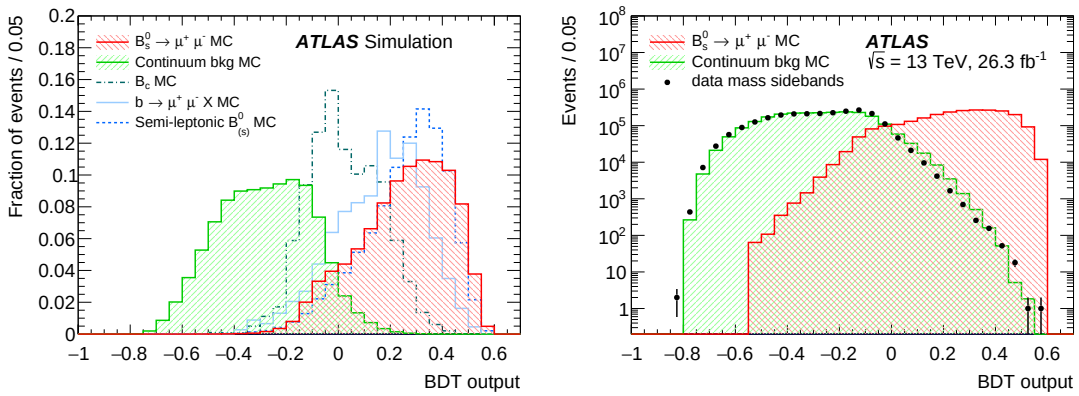


Figure 2.15: The sideband data (black dots), $b\bar{b} \to \mu^+\mu^- X$ (green line) and $B^0_{(s)} \to \mu^+\mu^-$ (red shaded area) MC distributions of the B_{iso} variable in three pileup bins: (upper left) nPV ≤ 11, (upper right) $11 <$ nPV ≤ 15, and (lower) nPV > 15.

models.[6] For this reason, signal and reference channel yields and efficiencies are measured relative to the *signal reference* selection discussed in Section 2.9, while the events in the final selection with lower BDT values are used to improve the background modeling.

After the BDT evaluation, three regions of interest are defined by selections on the signal efficiency. The boundaries of these regions correspond to BDT values of

[6]The $B^0_{(s)} \to \mu^+\mu^-$ signal fit was found to be insensitive to the signal for candidates with BDT output value smaller than 0.2455 (corresponding to 54% and 0.03% efficiencies for signal and background respectively).



(a) (b)

Figure 2.16: BDT output distribution for the signal and background events after the preliminary selection and before applying any reweighting to the BDT input variables: (a) simulation distributions for $B_s^0 \to \mu^+\mu^-$ signal, continuum, partially reconstructed $b \to \mu^+\mu^- X$ events and B_c decays; (b) dimuon sideband candidates (which also include prompt contributions, mainly at lower BDT values and not simulated in the continuum MC sample), compared with the continuum MC sample and the simulated signal. All distributions are normalized to unity in (a) and to data sidebands in (b).

0.2455 (54% signal efficiency), 0.3312 (36% signal efficiency) and 0.4163 (18% signal efficiency).

2.7 Data–Simulation Comparisons

Despite the lack of correlation between the BDT variable and the candidates' invariant mass, the change in relative contribution of different background components as a function of the BDT output can produce a variation of the background shape in separate BDT bins. The shape parameters and normalizations of the backgrounds are for this reason determined purely from data: the $b\bar{b} \to \mu^+\mu^- X$ MC simulation is not used for BDT training, computation of efficiencies or normalization purposes.

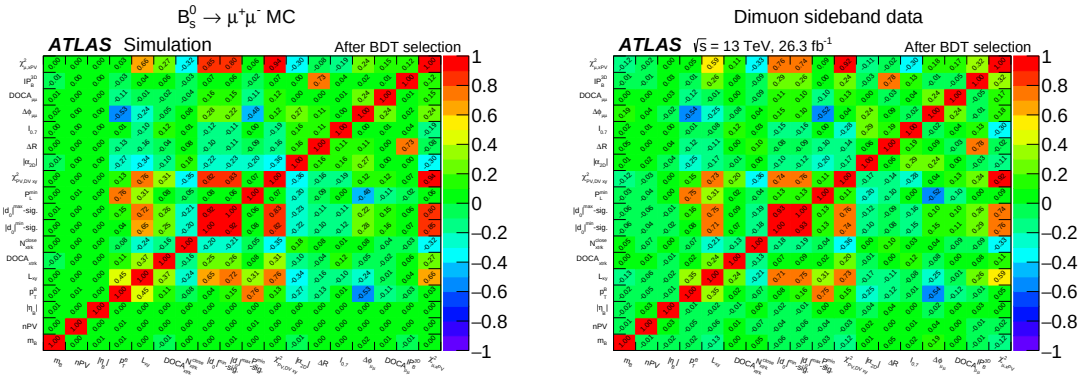


Figure 2.17: Correlation matrix of analysis variables for (left) signal Monte Carlo and (right) dimuon sideband datasets after the BDT output variable is used for data selection.

The only role of the $b\bar{b} \to \mu^+\mu^- X$ MC is the validation of the functional forms employed to parameterize the backgrounds on data, as discussed in Section 2.10.1. The dependence of the background parameterization on the BDT output variable was investigated in data and shown to be consistent with simulation, even for lower BDT values where prompt backgrounds contribute significantly. This observation is supported by the fair agreement of the BDT input variables distribution between the simulated $b\bar{b} \to \mu^+\mu^- X$ background and what is observed on data sidebands.

The shapes of the discriminating variables for the combinatorial background are compared between the $b\bar{b} \to \mu^+\mu^- X$ MC sample and the $B^0_{(s)} \to \mu^+\mu^-$ data sidebands. The $b\bar{b} \to \mu^+\mu^- X$ MC sample is reweighted on the number of reconstructed primary vertices and absolute muon reconstruction efficiencies. A selection of $L_{\rm xy} > 0.3$ mm [7] has been applied to the samples to suppress prompt components. After this selection the $b\bar{b} \to \mu^+\mu^- X$ MC sample has been reweighted to reproduce faithfully the data sidebands on $p_{\rm T}^B$, η^B and $N_{0.7}^{trks}$ (the number of tracks - excluding the B candidate's muon tracks - contained within a cone of size

[7] See Table 2.2 for exact definition of the variables.

$\Delta R = \sqrt{(\Delta\phi)^2 + (\Delta\eta)^2} = 0.7$ around the B direction, and used in the computation of B_{iso}). The reweighting is performed simultaneously on all three variables, using a gradient boosted reweighting technique [161]. Figure 2.18 shows the distributions of two of the highest-ranked discriminating variables with the gradient boosted reweighting included. The distributions shown in Figure 2.18 are selected from the set of relevant analysis variable distributions provided in Appendix A. These distributions show an overall qualitative agreement between data sidebands and $b\bar{b} \to \mu^+\mu^- X$ MC events. The $b\bar{b} \to \mu^+\mu^- X$ MC is used to test and understand the composition of the background components entering the signal region during the extraction of the $B^0_{(s)} \to \mu^+\mu^-$ signal yields.

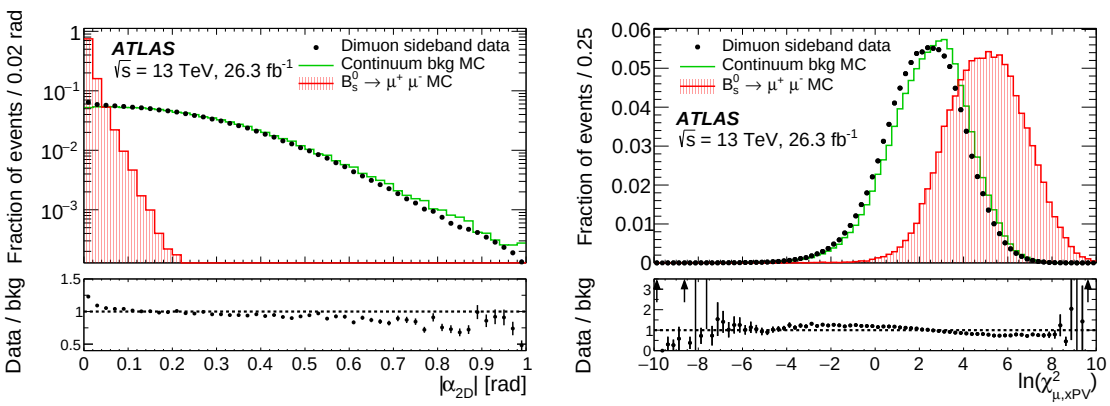


Figure 2.18: Data and continuum MC distributions of the (left) $|\alpha_{\text{2D}}|$ and (right) $\ln(\chi^2_{\mu,\text{xPV}})$ variables (defined in Table 2.2). The points correspond to the sideband data, while the continuous-line histogram corresponds to the continuum MC distribution, normalized to the number of data events. The filled-area histogram shows the signal MC distribution for comparison. The bottom panels report the data/MC ratio, magnified in order to highlight discrepancies in the region that is most relevant for the analysis.

The distributions of the discriminating variables are also used to compare simulation and data in the $B^+ \to J/\psi\, K^+$ and $B^0_s \to J/\psi\, \phi$ samples. To perform these comparisons, for each variable the contribution of the background is subtracted from

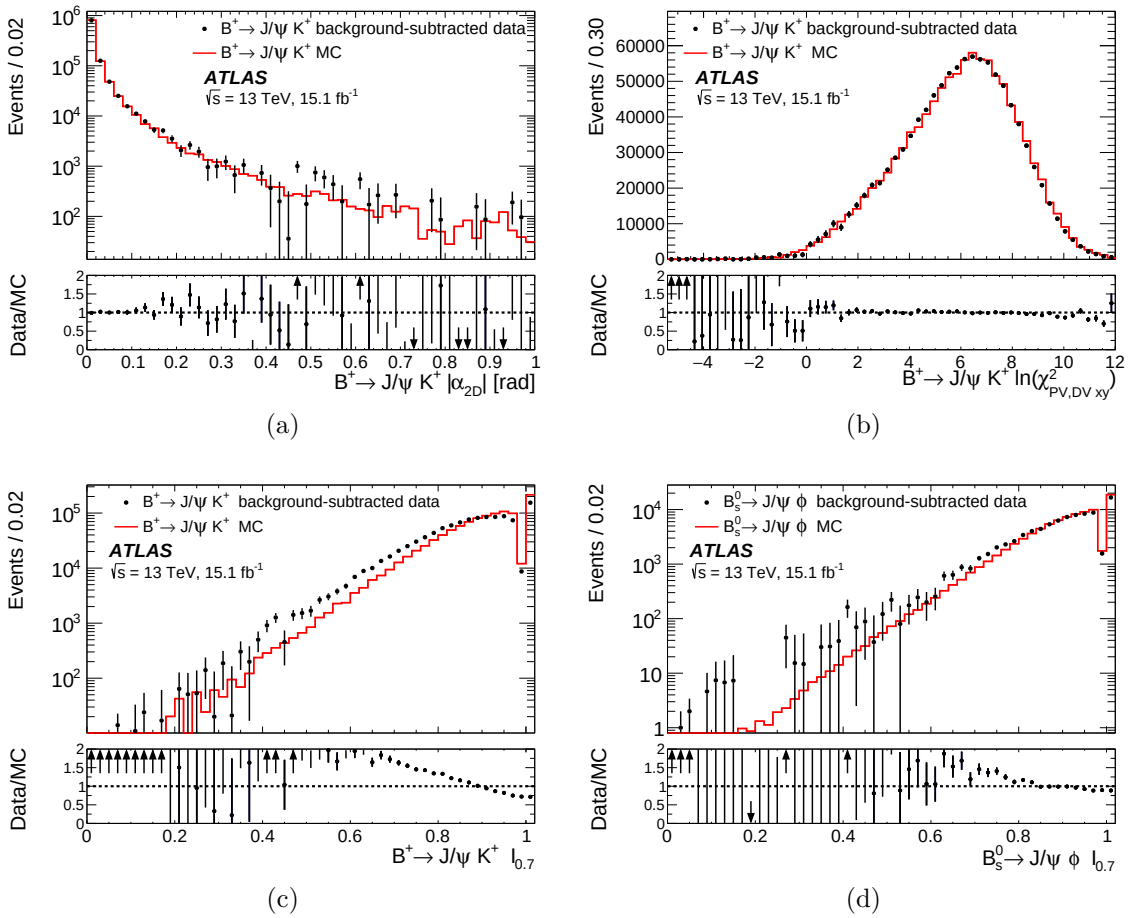


Figure 2.19: Data and MC distributions in $B^+ \to J/\psi\, K^+$ events for the discriminating variables: (a) $|\alpha_{2\mathrm{D}}|$, (b) $\ln\left(\chi^2_{\mathrm{PV,DV}\,xy}\right)$ and (c) $I_{0.7}$. The variable $I_{0.7}$ is also shown in (d) for $B_s^0 \to J/\psi\,\phi$ events. The points correspond to the sideband-subtracted data, while the line corresponds to the MC distribution, normalized to the number of data events. The highest bin in (c) and (d) accounts for the events with $I_{0.7} = 1$. The bottom panels report the data/MC ratio, magnified in order to highlight discrepancies in the region that is most relevant for the analysis. These figures were originally published in [29].

the $B^+ \to J/\psi\, K^+$ ($B_s^0 \to J/\psi\,\phi$) signal. For this purpose, a maximum-likelihood fit is performed to the invariant mass distribution, separately in bins of rapidity and transverse momentum. The fit model used is simpler than the one employed for

the extraction of the B^+ signal for normalization as described in Section 2.8, but is sufficient for the purpose discussed here.

Figure 2.19 shows examples of the distributions of the discriminating variables obtained from data and simulation for the reference samples. Observed differences are used to estimate systematic uncertainties on the efficiency ratio $R_\varepsilon = \varepsilon(B^+ \to J/\psi\, K^+)/\varepsilon(B^0_{(s)} \to \mu^+\mu^-)$ with the procedure described in Section 2.9. The discrepancy visible for the isolation variable $I_{0.7}$ in the $B^+ \to J/\psi\, K^+$ channel is the most significant among all variables and both reference channels.

2.8 $B^+ \to J/\psi K^+$ Yield Extraction

The reference channel yield is extracted with an unbinned extended maximum-likelihood fit to the $J/\psi K^+$ invariant mass distribution. The functional forms used to model both the signal and the backgrounds are obtained from studies of MC samples. All the yields are extracted from the fit to data, while the shape parameters are determined from a simultaneous fit to data and MC samples. Free parameters are introduced for the mass scale and mass resolution to accommodate data–MC differences. The best-fit values indicate a negligibly poorer resolution and a mass shift at the level of 2 MeV.

The fit includes four components: $B^+ \to J/\psi\, K^+$ decays, Cabibbo-suppressed $B^+ \to J/\psi\, \pi^+$ decays in the right tail of the main peak, partially reconstructed B decays (PRD) where one or more of the final-state particles are missing, and the non-resonant background composed mostly of $b\bar{b} \to J/\psi X$ decays. All components other than the last one have shapes constrained by MC simulation as described below, with the data fit including an additional Gaussian convolution to account for possible data–MC discrepancies in mass scale and resolution. The shape of the $B^+ \to J/\psi\, K^+$ mass distribution is parameterized using a Johnson S_U function [108,

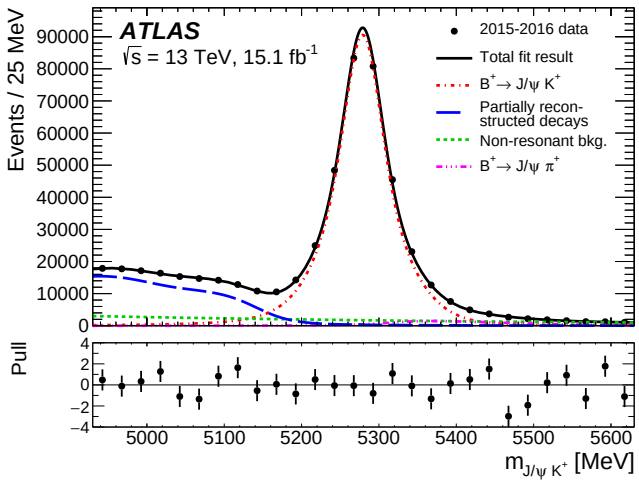


Figure 2.20: Result of the fit to the $J/\psi K^+$ invariant mass distribution for all B^+ candidates in half of the data events. The various components of the spectrum are described in the text. The panel at the bottom of the plot shows the bin-by-bin pulls for the fit, where the pull is defined as the difference between the data point and the value obtained from the fit function, divided by the error from the fit. This figure was originally published in [29].

109]. The Johnson S_U function is given as:

$$p(y) = \frac{\delta}{\sqrt{2\pi}} \frac{1}{\sqrt{y^2+1}} \exp[-\frac{1}{2}\{\gamma + \delta \log[y + \sqrt{y^2+1}]\}^2],$$

where

$$y = \frac{x-\xi}{\lambda},$$

and the parameters to be fit are δ, γ, ξ, and λ. The final $B^+ \to J/\psi\, K^+$ yield includes the contribution from radiative effects (i.e. where photons are emitted from the B decay products). The $B^+ \to J/\psi\, \pi^+$ decays are modeled by the sum of a Johnson S_U function and a Gaussian function, where all parameters except the normalization are determined from the simulation. The decay modes contributing to the PRD are classified in simulation on the basis of their mass dependence. Each of the three resulting categories contributes to the overall PRD shape with combinations of Fermi–Dirac [73, 79] and exponential functions, contributing differently

in the low-mass region. Their shape parameters are determined from simulation. Finally, the non-resonant background is modeled with an exponential function with the shape parameter extracted from the fit. The normalization of each component is unconstrained in the fit, which is therefore mostly independent of external inputs for the branching fractions. The residual dependence of the PRD model shapes on the relative branching fractions of the contributing decays is considered as a source of systematic uncertainty. The resulting fit, shown in Figure 2.20, yields 334 351 $B^+ \to J/\psi\, K^+$ decays with a statistical uncertainty of 0.3%. The ratio of yields of $B^+ \to J/\psi\, \pi^+$ and $B^+ \to J/\psi\, K^+$ is $(3.71 \pm 0.09)\%$ (where the uncertainty reported is statistical only), in agreement with the expectation from the world average [171] of $(3.84 \pm 0.16)\%$.

Some systematic uncertainties are included by design in the fit. For example, the effect of the limited MC sample size is included by performing a simultaneous fit to data and MC samples. Scale factors determined in the fit to data account for the differences in mass scale and resolution between data and simulation. Additional systematic uncertainties are evaluated by varying the default fit model described above. They take into account the kinematic differences between the data and the MC samples used in the fit, differences in efficiency between B^+ and B^- decays and uncertainties in the relative fractions and shapes of PRD and in the shape of the various fit components. The stability of this large sample fit is verified by repeating the fit with different initial parameter values. In each case, the change relative to the default fit is recorded, symmetrized and used as an estimate of the systematic uncertainty. The main contributions to the systematic uncertainty come from the functional models of the background components, the composition of the PRD and the signal charge asymmetry. The total systematic uncertainty in the B^+ yield amounts to 4.8%.

2.9 Evaluation of the $B^+ \to J/\psi\, K^+$ to $B^0_{(s)} \to \mu^+\mu^-$ Efficiency Ratio

The ratio of efficiencies $R_\varepsilon = \varepsilon(B^+ \to J/\psi\, K^+)/\varepsilon(B^0_{(s)} \to \mu^+\mu^-)$ enters the $\mathcal{D}_{\rm ref}$ term defined in Section 2.1: $\mathcal{D}_{\rm ref} = N_{J/\psi K^+}/R_\varepsilon$. Both channels are measured in the fiducial acceptance for the B meson, defined as $p_{\rm T}^B > 8.0$ GeV and $|\eta_B| < 2.5$. Correspondingly, $\varepsilon(B^+ \to J/\psi\, K^+)$ and $\varepsilon(B^0_{(s)} \to \mu^+\mu^-)$ are measured within the B meson fiducial acceptance and include additional final state particles acceptance as well as trigger, reconstruction and selection efficiencies. The final state particles acceptance is defined by the selection placed on the particles in the final state: $|\eta_\mu| < 2.5$ and $p_{\rm T}^\mu > 6.0$ (4.0) GeV for the leading (trailing) muon $p_{\rm T}$, $p_{\rm T}^K > 1.0$ GeV and $|\eta_K| < 2.5$ for kaons. The *signal reference* BDT selection, defined as BDT > 0.2455, has an efficiency of about 54% (51%) in the signal (reference) channel. The overall efficiency ratio R_ε is 0.1176 ± 0.0009 (stat.) $\pm\, 0.0047$ (syst.), with uncertainties determined as described below.

The ratio R_ε is computed using the mean lifetime of the B_s^0 [6, 171] in the MC generator. The same efficiency ratios apply to the $B_s^0 \to \mu^+\mu^-$ and $B^0 \to \mu^+\mu^-$ decays, within the MC statistical uncertainty of 0.8%. The statistical uncertainties in the efficiency ratios come from the finite number of events available for the simulated samples. The systematic uncertainty affecting R_ε comes from five sources.

The first contribution is due to the uncertainties in the data-driven weights introduced in Section 2.2, and amounts to 0.8%. This term is assessed by creating alternative datasets using correction factors that are randomly sampled in accord with their nominal values and uncertainties. The root mean square (RMS) value of the distribution of R_ε obtained from these datasets is taken as the systematic uncertainty.

A second contribution of 1.0% is related to the muon trigger and reconstruction efficiencies. The effect of the uncertainties in the data-driven efficiencies is evaluated using random sampling, as above.

A 3.2% systematic uncertainty contribution arises from the differences between data and simulation observed in the modeling of the discriminating variables used in the BDT classifier (Table 2.2). For each of the 15 variables, the MC samples for $B^0_{(s)} \to \mu^+\mu^-$ and $B^+ \to J/\psi\, K^+$ are reweighted with the ratio of the $B^+ \to J/\psi\, K^+$ event distributions in sideband-subtracted data and the MC simulation. The isolation variable $I_{0.7}$ is computed using charged-particle tracks only, and differences between the B^+ and B_s^0 are expected and were observed in previous studies [26]. Hence for this variable the reweighting procedure for the $B_s^0 \to \mu^+\mu^-$ MC sample is based on $B_s^0 \to J/\psi\, \phi$ data. For all discriminating variables except $I_{0.7}$, the value of the efficiency ratio is modified by less than 2% by the reweighting procedure and each variation is taken as an independent contribution to the systematic uncertainty in the efficiency ratio. For $I_{0.7}$ the reweighting procedure changes the efficiency ratio by about 6%. Because of the significant mis-modeling, the MC samples obtained after reweighting on the distribution of $I_{0.7}$ are taken as a reference, thus correcting the central value of the efficiency ratio. The 1% uncertainty in the $I_{0.7}$ correction is added to the sum in quadrature of the uncertainties assigned to the other discriminating variables. The total uncertainty in the modeling of the discriminating variables is the dominant contribution to the systematic uncertainty in R_ε.

A fourth source of systematic uncertainty arises from differences between the $B_s^0 \to \mu^+\mu^-$ and the $B^+ \to J/\psi\, K^+$ channels related to the reconstruction efficiency of the kaon track and of the B^+ decay vertex. These uncertainties are mainly due to inaccuracy in the modeling of passive material in the ID. The corresponding systematic uncertainty is estimated by varying the detector model in simulations, which results in changes between 0.4% and 1.5% depending on the η range considered [35].

The largest value is used in the full η range.

Finally, the uncertainty associated with reweighting the simulated events as a function of the pileup multiplicity distribution contributes 0.6%.

Table 2.8 summarizes these systematic uncertainties.

Source	Contribution [%]
Statistical	0.8
Kinematic reweighting (DDW)	0.8
Muon trigger and reconstruction	1.0
BDT input variables	3.2
Kaon tracking efficiency	1.5
Pileup reweighting	0.6

Table 2.8: Summary of the uncertainties in R_ε. This table was originally published in [29].

The efficiency ratio enters in Equation 2.1 with the $\mathcal{D}_{\rm ref}$ term defined in Section 2.1, multiplied by the number of observed $B^\pm$ candidates. The total uncertainty in $\mathcal{D}_{\rm ref}$ is $\pm 6.3\%$.

A correction to the efficiency ratio for $B_s^0 \to \mu^+\mu^-$ is needed because of the width difference $\Delta\Gamma_s$ between the B_s^0 eigenstates. According to the SM, the decay $B_s^0 \to \mu^+\mu^-$ proceeds mainly through the heavy state $B_{s,\rm H}$ [52, 70], which has width $\Gamma_{s,\rm H} = \Gamma_s - \Delta\Gamma_s/2$, which is 6.6% smaller than the average Γ_s [171]. The variation in the value of the $B_s^0 \to \mu^+\mu^-$ mean lifetime was tested with simulation and found to change the B_s^0 efficiency, and consequently the B_s^0 to B^+ efficiency ratio, by +3.3%. This correction is applied to the central value of $\mathcal{D}_{\rm ref}$ used in Section 2.11 for the determination of $\mathcal{B}(B_s^0 \to \mu^+\mu^-)$.[8] Due to the small value of $\Delta\Gamma_d$, no correction

[8]The decay time distribution of $B_s^0 \to \mu^+\mu^-$ is predicted to be different from the one of $B_{s,\rm H}$ in scenarios of new physics, with the effect related to the observable $\mathcal{A}_{\Delta\Gamma}^{\mu\mu}$ [51, 70]. The maximum possible deviation from the SM prediction of $\mathcal{A}_{\Delta\Gamma}^{\mu\mu} = +1$ is for $\mathcal{A}_{\Delta\Gamma}^{\mu\mu} = -1$, for which the decay

needs to be applied to the $B^0 \to \mu^+\mu^-$ decay.

2.10 Extraction of the Signal Yield

The dimuon candidates passing the preliminary selection and the selections against hadron misidentification and continuum background are classified according to four intervals (with boundaries at 0.1439, 0.2455, 0.3312, 0.4163 and 1) in the BDT output. Repeating the Run 1 analysis approach, each interval is chosen to give an equal efficiency of 18% for signal MC events, and they are ordered according to increasing signal-to-background ratio.

An unbinned extended maximum-likelihood fit is performed on the dimuon invariant mass distribution simultaneously across the four BDT intervals, each including models for the respective signal and background contributions. The first two bins (covering the lowest BDT values considered) contribute mostly to background modeling: it has been verified with MC pseudo-experiments that they have negligible impact on the signal extraction. MC pseudo-experiments are simplified MC simulations generated based on a probability density function that describes an observable in the analysis. These "toy" MCs are optimized for low computation time and allow for the generation of many simulated datasets each with different parameters that can be used to study the collision dataset.

The result of the fit is parameterized with the total yield of $B_s^0 \to \mu^+\mu^-$ and $B^0 \to \mu^+\mu^-$ events in the three highest intervals of BDT output. Section 2.10.1 describes the signal and background fit models. The parameters describing the background are allowed to vary freely and are determined by the fit. The normalizations

time distribution of $B_s^0 \to \mu^+\mu^-$ corresponds to the distribution of the $B_{s,\mathrm{L}}$ eigenstate. In the comparison with new-physics predictions, the value of $\mathcal{B}(B_s^0 \to \mu^+\mu^-)$ obtained from this analysis should be corrected by +3.6% or +7.8% respectively for $\mathcal{A}_{\Delta\Gamma}^{\mu\mu} = 0$ and -1.

of the individual fit components, including the signals, are completely unconstrained and allowed to take negative values. The ratios of the signal yields in different BDT bins are constrained to equal the ratios of the signal efficiencies in those same bins. The systematic uncertainties due to variations in the relative signal and background efficiencies between BDT intervals, to the signal parameterization and to the background model are discussed in Sections 2.10.2 and 2.10.3. Each is modeled in the likelihood as a multiplicative Gaussian distribution whose width is equal to the corresponding systematic uncertainty.

2.10.1 Signal and Background Model

The signal and background models are derived from simulations and from data collected in the mass sidebands of the search region.

The invariant mass distribution of the $B^0_{(s)} \to \mu^+\mu^-$ signal is described with two double-Gaussian distributions, centered respectively at the B^0 or B_s^0 mass. The shape parameters are extracted from simulation, where they are found to be uncorrelated with the BDT output. Systematic uncertainties on the mass scale and resolutions are considered separately. Figure 2.21 shows the invariant mass distributions for the B^0 and B_s^0, obtained from MC events and normalized to the SM expectations.

The background in the fit from which the signal will be derived is composed of the types of events described in Section 2.4: (a) the continuum background; (b) the background from partially reconstructed $b \to \mu^+\mu^- X$ events, which is present mainly in the low mass sideband; and (c) the peaking background.

The non-peaking contributions have a common mass shape model, with parameters constrained across the BDT bins in the fit as described below, and independent yields across BDT bins and components. Systematic uncertainties arising from model assumptions will be discussed in Section 2.10.3, including effects due to the presence

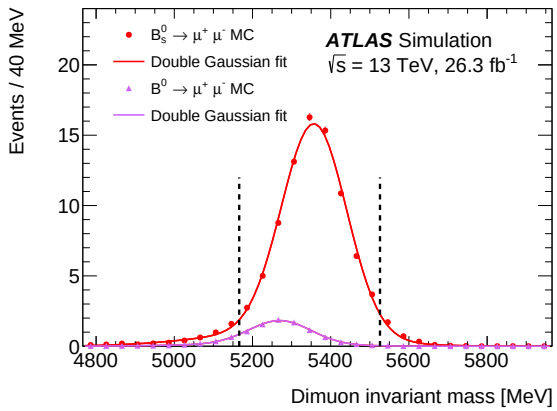


Figure 2.21: Dimuon invariant mass distribution for the B_s^0 and B^0 signals from simulation. The results of the double-Gaussian fits are overlaid. The two distributions are normalized to the SM prediction for the expected yield with an integrated luminosity of 26.3 fb^{-1}. This figure was originally published in [29].

of $B_c^+ \to J/\psi\mu^+\nu$ and semileptonic $B_{(s)}^0/\Lambda_b^0 \to h\mu\nu$ decays.

Both in simulation and sideband data, the continuum background has a small linear dependence on the dimuon invariant mass. In the simulation, the slope parameter has a roughly linear dependence versus BDT interval; the mass sidebands in data confirm this trend, albeit with large statistical uncertainty. This dependence is included in the fit model. The small systematic uncertainties due to deviations from this assumption are discussed below in Section 2.10.3.

The $b \to \mu^+\mu^- X$ background has a dimuon invariant mass distribution that falls monotonically with increasing dimuon mass. The mass dependence is derived from data in the low mass sideband, and described with an exponential function with the same shape in each BDT interval. The value of the shape parameter is extracted from the fit to data.

The invariant mass distribution of the peaking background is very similar to the B^0 signal, as shown in Figure 2.7(b). The description of this component is obtained

from MC simulation, which indicates that the shape and normalization are the same for all BDT bins. In the fit, this contribution is included with fixed mass shape and with a normalization of 2.9±2.0 events, as discussed in Section 2.5. This contribution is equally distributed among the three highest intervals of the BDT output.

The fitting procedure is tested with MC pseudo-experiments, as discussed in Section 2.10.3.

2.10.2 Relative Signal Efficiency Between BDT Bins

Section 2.9 explains how systematic uncertainties affect the overall selection efficiency for signal candidates. The separation of the candidates according to BDT bins introduces an additional dependence on the relative efficiencies in each BDT bin, and systematic uncertainties in these relative efficiencies must be accounted for. Two different procedures are explored. First, the distribution of the BDT output is compared between MC simulation and background-subtracted data for the reference and control channels. The differences observed in the ratio of data to simulation are described with a linear dependence on the BDT output. The linear dependencies observed for $B^+ \to J/\psi\, K^+$ and $B_s^0 \to J/\psi\, \phi$ are in turn used to reweight the BDT-output distribution in the $B_{(s)}^0 \to \mu^+\mu^-$ MC sample. The maximum corresponding absolute variations in the efficiencies are equal to $+1.7\%$ and -2.3% respectively in the second and fourth BDT intervals, with the third interval basically unaffected. A second assessment of the systematic uncertainties in the relative efficiency of the BDT intervals is obtained with a procedure similar to the one used for the event selection (Section 2.9). For each discriminating variable, the MC sample is reweighted according to the difference between simulation and data observed in the reference channels. The variation in the efficiency of each BDT interval is taken as the contribution to the systematic uncertainty due to mis-modeling of that variable. The sum in quadrature of the variations due to all discriminating variables is found to

be similar in the $B^+ \to J/\psi\, K^+$ and $B_s^0 \to J/\psi\, \phi$ channels. Absolute variations of $\pm 1.0\%$, $\pm 2.4\%$ and $\pm 4.4\%$ are found in the second, third and fourth BDT intervals respectively. The first of these procedures is used as a baseline for inclusion of Gaussian terms in the signal extraction likelihood to account for the uncertainty in the relative signal efficiency in the three most sensitive BDT bins. Care is taken in constraining the sum of the efficiencies of the three intervals sensitive to the signal, since that absolute efficiency and the corresponding uncertainty are parameterized with the R_ε term.

Figure 2.22 shows the distribution of the BDT output from data and simulation for the reference channels, after reweighting the MC sample. The MC distribution for $B_{(s)}^0 \to \mu^+\mu^-$ events is also shown, illustrating how the linear deviation obtained from the reference channels affects the simulated signal BDT output. When studying these effects, the linear fits to the ratios in Figures 2.22(a) and 2.22(b) are performed in the range corresponding to the three BDT bins with the highest signal-to-background ratio, since the remaining bin is insensitive to the signal contribution.

2.10.3 Systematic Uncertainties in the Fit

Studies based on MC pseudo-experiments are used to assess the sensitivity of the fit to the input assumptions. Variations in the description of signal and background components are used in the generation of these samples. The corresponding changes in the average numbers, N_s and N_d, of B_s^0 and B^0 events determined by the fit, run in the nominal configuration, are taken as systematic uncertainties. The size of the variations used in the generation of the MC pseudo-experiments is determined in some cases by known characteristics of the ATLAS detector (reconstructed momentum scale and momentum resolution), in others using MC evaluation (background due to semileptonic $B_{(s)}^0/\Lambda_b^0 \to h\mu\nu$ decays and to $B_c^+ \to J/\psi\mu^+\nu$), and in others from uncertainties determined from data in the sidebands or from simulation (shapes

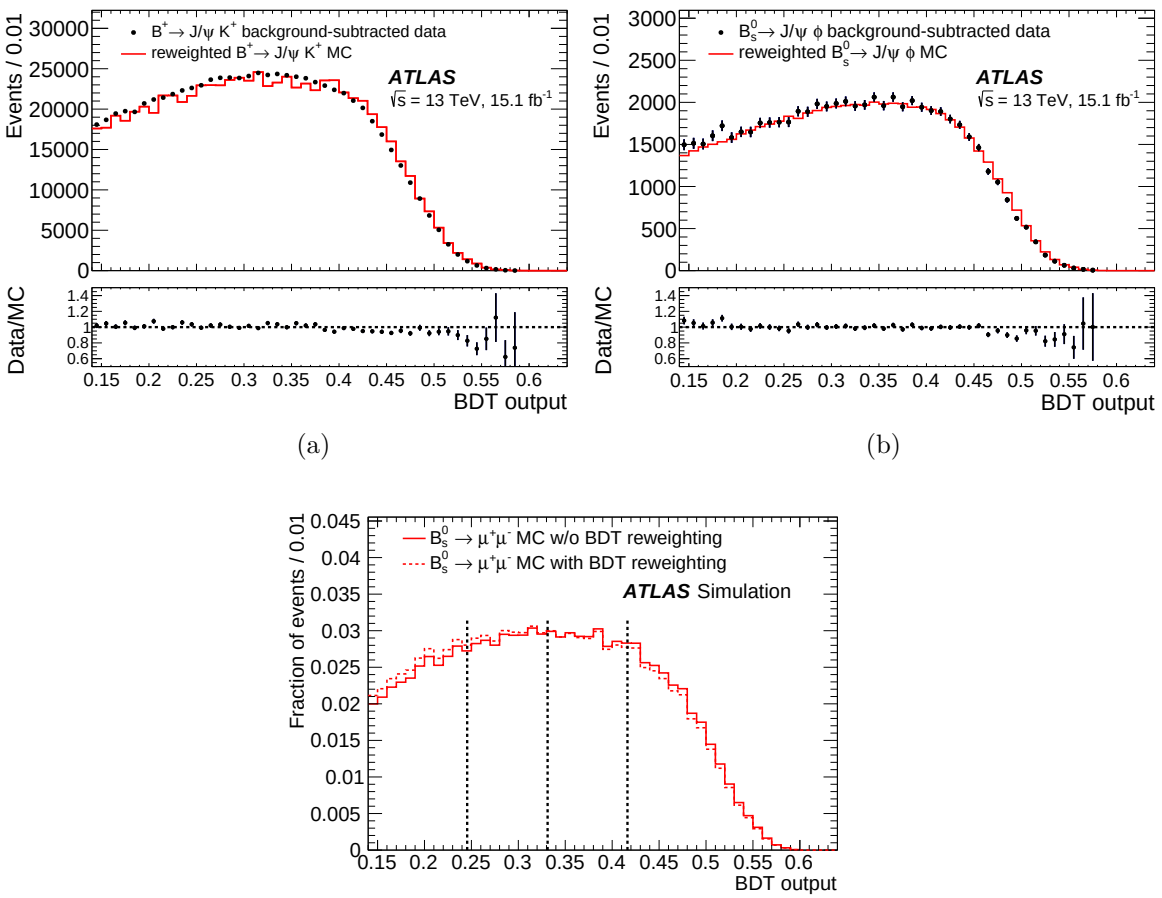


Figure 2.22: BDT value distributions in data and MC simulation for (a) $B^+ \to J/\psi\, K^+$, (b) $B_s^0 \to J/\psi\, \phi$. The MC samples are normalized to the number of data events passing the signal reference BDT selection (Section 2.6). Figure (c) illustrates the BDT output for the $B_s^0 \to \mu^+\mu^-$ signal, with the dashed histogram illustrating the effect of the linear reweighting on the BDT output discussed in the text. The vertical dashed lines correspond to the boundaries of the BDT intervals used in the $B_{(s)}^0 \to \mu^+\mu^-$ signal fit. These figures were originally published in [29].

of the background components and their variation across the BDT intervals).

The MC pseudo-experiments were generated with the normalization of the continuum and $b \to \mu^+\mu^- X$ components obtained from the fit to the data in the sidebands

of the invariant mass distribution, and the peaking background from the expectation discussed in Section 2.5. The signal was generated with different configurations, roughly covering the range between zero and twice the expected SM yield.

For all variations of the assumptions and all configurations of the signal amplitudes the distributions of the differences between fit results and generated values are used to evaluate systematic uncertainties. In addition, distributions obtained from MC pseudo-experiments generated and fitted according to the nominal fit model are used to study systematic biases deriving from the fit procedure. For both signal yields, the bias is smaller than 15% of the fit error, for true values of the $B_s^0 \to \mu^+\mu^-$ branching fraction above 5×10^{-10}.

The shifts in N_s or N_d are combined by considering separately the sums in quadrature of the positive and negative shifts and taking the larger as the symmetric systematic uncertainty. The total systematic uncertainty is found to increase with the assumed size of the signal, with a dependence $\sigma_{\rm syst}^{N_s} = 3 + 0.05N_s$ and $\sigma_{\rm syst}^{N_d} = 2.9 + 0.05N_s + 0.05N_d$. Most of the shifts observed have opposite signs for N_s and N_d, resulting in a combined correlation coefficient in the systematic uncertainties of $\rho_{\rm syst} = -0.83$.

The systematic uncertainties discussed in this section are included in the fit to the $\mu^+\mu^-$ candidates in data. The fit for the yield of B_s^0 and B^0 events is modified by including in the likelihood two smearing parameters for N_s and N_d that are constrained by a two-dimensional Gaussian distribution parameterized by the values of $\sigma_{\rm syst}^{N_s}$, $\sigma_{\rm syst}^{N_d}$ and $\rho_{\rm syst}$.

2.10.4 Results of the Signal Yield Extraction

The numbers of background events contained in the signal region (5166–5526 MeV) are computed from the interpolation of the data observed in the sidebands. This

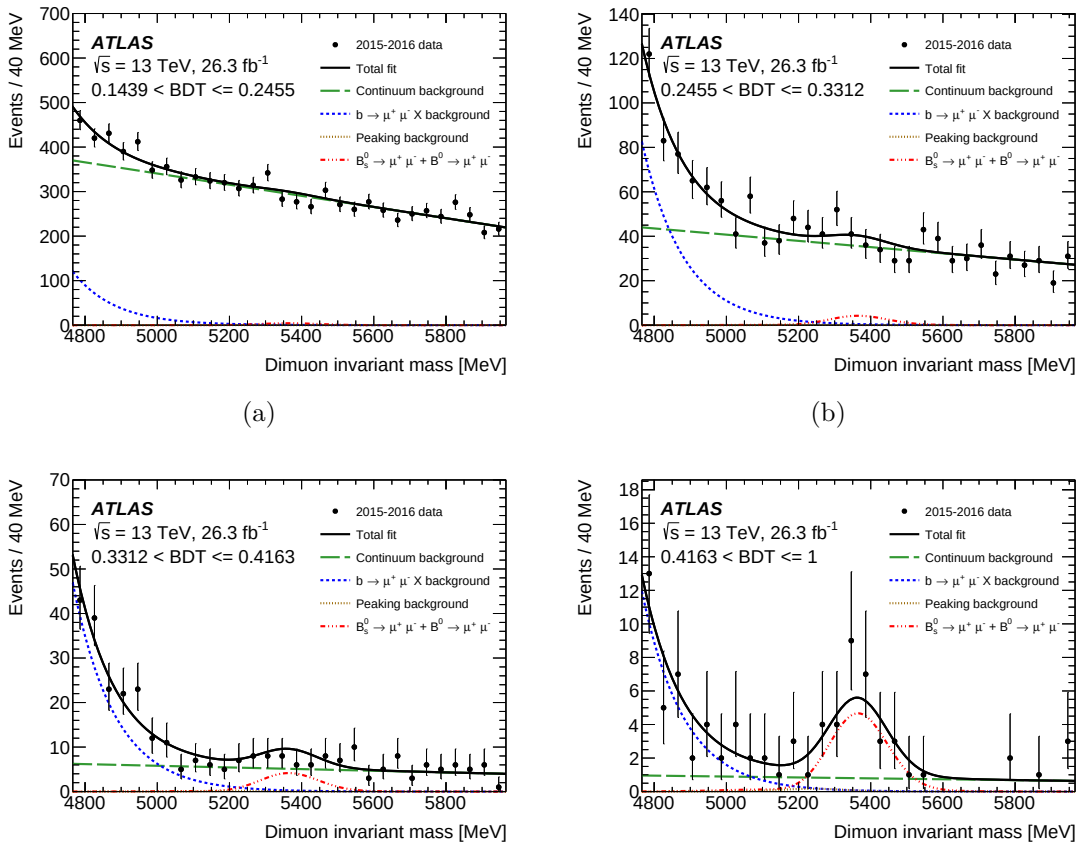


Figure 2.23: Dimuon invariant mass distributions in the unblinded data, in the four intervals of BDT output. Superimposed is the result of the maximum-likelihood fit. The total fit is shown as a continuous line, with the dashed lines corresponding to the observed signal component, the $b \to \mu^+\mu^- X$ background, and the continuum background. The signal components are grouped in one single curve, including both the $B_s^0 \to \mu^+\mu^-$ and the (negative) $B^0 \to \mu^+\mu^-$ component. The curve representing the peaking $B_{(s)}^0 \to hh'$ background lies very close to the horizontal axis in all BDT bins. These figures were originally published in [29].

procedure yields 2685 ± 37, 330 ± 14, 51 ± 6 and 7.9 ± 2.6 events respectively in the four intervals of BDT output. For comparison, the total expected numbers of signal events according to the SM prediction are 91 and 10 for N_s and N_d respectively,

equally distributed among the three intervals with the highest signal-to-background ratio.

In those three BDT intervals, in the unblinded signal region, a total of 1951 events in the full mass range of 4766–5966 MeV are used in the likelihood fit to signal and background. Without applying any bounds on the values of the fitted parameters, the values determined by the fit are $N_s = 80 \pm 22$ and $N_d = -12 \pm 20$, where the uncertainties correspond to likelihood variations satisfying $-2\,\Delta\ln(\mathcal{L}) = 1$. The likelihood includes the systematic uncertainties discussed above, but statistical uncertainties largely dominate. The result is consistent with the expectation from simulation. The uncertainties in the result of the fit are discussed in Section 2.11, where the measured values of the branching fractions are presented.

Figure 2.23 shows the dimuon invariant mass distributions in the four BDT intervals, together with the projections of the likelihood. A modified Kolmogorov–Smirnov (KS) test [113] is used to estimate the fit quality: the p-value is estimated by comparing the maximum of the KS distance across the four histograms of Figure 2.23 with the distribution of the same quantity from pseudo-experiments generated with the shape resulting from the fit to data. This procedure yields a compatibility probability of 84%.

2.11 Branching Fraction Extraction

The branching fractions for the decays $B_s^0 \to \mu^+\mu^-$ and $B^0 \to \mu^+\mu^-$ are extracted from data using a maximum-likelihood fit. The likelihood is obtained from the one used for N_s and N_d by replacing the fit parameters with the corresponding branching fractions divided by normalization terms in Equation 2.1, and including Gaussian multiplicative factors for the normalization uncertainties. All results are obtained by profiling the fit likelihood with respect to all parameters involved other than the

branching fraction(s) of interest.

The normalization terms include external inputs for the B^+ branching fraction and the relative hadronization probability. The branching fraction is obtained from world averages [171] as the product of $\mathcal{B}(B^+ \to J/\psi\, K^+) = (1.010 \pm 0.029) \times 10^{-3}$ and $\mathcal{B}(J/\psi \to \mu^+\mu^-) = (5.961 \pm 0.033)\%$. The relative hadronization probability is equal to one for the B^0, while for the B_s^0 it is taken from the latest available HFLAV average [6] $f_s/f_d = 0.256 \pm 0.013$, which assumes $f_u/f_d = 1$.

The efficiency-weighted and luminosity-weighted number of events for the reference channel enters in Equation 2.1 with the denominator $\mathcal{D}_{\rm ref}$. The values $\mathcal{D}_{\rm ref} = (5.69 \pm 0.36) \times 10^6$ for the B_s^0 and $(5.84 \pm 0.37) \times 10^6$ for the B^0 are obtained from the results of Sections 2.8 and 2.9, and include the correction to the $B_s^0 \to \mu^+\mu^-$ efficiency due to the lifetime difference between the $B_{s,\rm H}$ and the B_s^0. The combination of the B^+ branching fraction, hadronization probabilities and $\mathcal{D}_{\rm ref}$, i.e. the single-event sensitivity, is equal to $(4.02 \pm 0.35) \times 10^{-11}$ for $B_s^0 \to \mu^+\mu^-$ and $(1.059 \pm 0.074) \times 10^{-11}$ for $B^0 \to \mu^+\mu^-$.

The values of the branching fractions that maximize the profile likelihood are $\mathcal{B}(B_s^0 \to \mu^+\mu^-) = (3.2 \pm 0.9) \times 10^{-9}$ and $\mathcal{B}(B^0 \to \mu^+\mu^-) = (-1.3 \pm 2.1) \times 10^{-10}$, where the uncertainties, statistical and systematic combined, are estimated using a Gaussian approximation in the neighborhood of the likelihood function maximum. Figure 2.24(a) shows likelihood contours for the simultaneous fit to $\mathcal{B}(B_s^0 \to \mu^+\mu^-)$ and $\mathcal{B}(B^0 \to \mu^+\mu^-)$, for values of $-2\Delta \ln(\mathcal{L})$ equal to 2.3, 6.2 and 11.8, relative to the maximum of the likelihood.

Table 2.9 gives a breakdown of the estimated contributions of systematic and statistical uncertainties. The results are dominated by statistical uncertainties, with the most prominent source of systematic uncertainty coming from fit uncertainties, where the largest contributors are the mass scale and $b \to \mu^+\mu^- X$ background

Source	B_s^0 [%]	B^0 [%]
f_s/f_d	5.1	-
B^+ yield	4.8	4.8
R_ε	4.1	4.1
$\mathcal{B}(B^+ \to J/\psi\, K^+) \times \mathcal{B}(J/\psi \to \mu^+\mu^-)$	2.9	2.9
Fit systematic uncertainties	8.7	65
Stat. uncertainty (from likelihood est.)	27	150

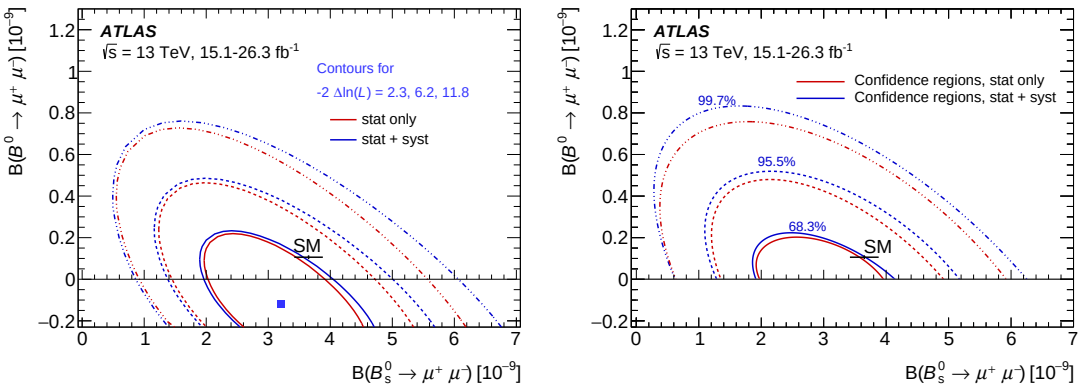
Table 2.9: Breakdown of the expected systematic uncertainties in $\mathcal{B}(B^0_{(s)} \to \mu^+\mu^-)$. The measurements are dominated by statistical uncertainty, followed by the systematic uncertainty from the fit. The latter is dominated by contributions from the mass scale uncertainty and the parameterization of the $b \to \mu^+\mu^- X$ background. The statistical uncertainties reported here are obtained from the maximization of the fit likelihood and are meant only as a reference for the relative scale uncertainties. This table was originally published in [29].

parameterization.

In the statistical regime of the analysis, the likelihood contours of Figure 2.24 (a) cannot be immediately translated into contours with the conventional coverage of one, two and three Gaussian standard deviations. Moreover, the contours extend into regions of negative branching fractions, which are unphysical. In order to address these points, a Neyman construction [148] is employed to obtain the 68.3%, 95.5% and 99.7% confidence intervals in the $\mathcal{B}(B_s^0 \to \mu^+\mu^-)$–$\mathcal{B}(B^0 \to \mu^+\mu^-)$ plane. This construction yields the contours shown in Figure 2.24(b). The same construction is used to determine the 68.3% confidence interval for $\mathcal{B}(B_s^0 \to \mu^+\mu^-)$ with MC pseudo-experiments, and results in

$$\mathcal{B}(B_s^0 \to \mu^+\mu^-) = \left(3.21^{+0.96+0.49}_{-0.91-0.30}\right) \times 10^{-9} = \left(3.2^{+1.1}_{-1.0}\right) \times 10^{-9}\,.$$

Statistical and systematic uncertainties (shown separately in the first expression, and combined in the last) are separated by repeating the likelihood fit after setting all systematic uncertainties to zero. The fitted branching fractions (obtained from the



(a) (b)

Figure 2.24: (a) Likelihood contours for the simultaneous fit to $\mathcal{B}(B_s^0 \to \mu^+\mu^-)$ and $\mathcal{B}(B^0 \to \mu^+\mu^-)$, for values of $-2\Delta\ln(\mathcal{L})$ equal to 2.3, 6.2 and 11.8. The SM prediction with uncertainties is indicated. (b) Neyman contours in the $\mathcal{B}(B_s^0 \to \mu^+\mu^-)$–$\mathcal{B}(B^0 \to \mu^+\mu^-)$ plane for 68.3%, 95.5% and 99.7% coverage. At each $-2\Delta\ln(\mathcal{L})$ or coverage value, the inner contours are statistical uncertainty only, while the outer ones include statistical and systematic uncertainties. The construction of these contours makes use of both the dimuon (26.3 fb^{-1}) and the reference channel (15.1 fb^{-1}) datasets. These figures were originally published in [29].

unconstrained likelihood maximum) are in all cases inputs to the Neyman construction, which, by design, results in physically allowed values for the resulting branching fractions.

The upper limit at 95% CL on $\mathcal{B}(B^0 \to \mu^+\mu^-)$, determined with the same Neyman procedure, is

$$\mathcal{B}(B^0 \to \mu^+\mu^-) < 4.3 \times 10^{-10}\,.$$

Using the predicted SM branching fractions from Section 2.1, the analysis is expected to yield on average a measurement of $\left(3.6^{+1.1}_{-1.0}\right) \times 10^{-9}$ for $\mathcal{B}(B_s^0 \to \mu^+\mu^-)$ and an upper limit at 95% CL of 7.1×10^{-10} for $\mathcal{B}(B^0 \to \mu^+\mu^-)$.

2.12 Combination with the Run 1 Result

The likelihood function from the current result is combined with the likelihood function from the Run 1 result [28]. The only common parameters in the combination are the fitted $\mathcal{B}(B^0_{(s)} \to \mu^+\mu^-)$ and the combination of external inputs $\mathcal{F}_{\text{ext}} = \mathcal{B}(B^+ \to J/\psi\, K^+) \times \mathcal{B}(J/\psi \to \mu^+\mu^-) \times (f_u/f_s) = (2.35 \pm 0.14) \times 10^{-4}$. Except for $\mathcal{F}_{\text{ext}}$, all nuisance parameters are treated as uncorrelated between the two likelihoods, with both likelihoods including their individual parameterizations of systematic uncertainty effects. A negligible change in the results, corresponding to shifts in central values and uncertainties between 1% and 4%, is found when all sources of systematic uncertainty are assumed to be fully correlated.

The maximum of the combined likelihood corresponds to

$$\mathcal{B}(B^0_s \to \mu^+\mu^-) = (2.8 \pm 0.7) \times 10^{-9}\,,$$
$$\mathcal{B}(B^0 \to \mu^+\mu^-) = (-1.9 \pm 1.6) \times 10^{-10}\,.$$

Figure 2.25 shows the likelihood contours for the combined Run 1 and Run 2 result for $\mathcal{B}(B^0_s \to \mu^+\mu^-)$ and $\mathcal{B}(B^0 \to \mu^+\mu^-)$, for values of $-2\Delta\ln(\mathcal{L})$ equal to 2.3, 6.2 and 11.8, relative to the maximum of the likelihood. The contours for the result from 2015–2016 Run 2 data are overlaid for comparison.

When applying the one-dimensional Neyman construction described in Section 2.11 to this combined likelihood, whose maximum is unconstrained and allowed to access the unphysical (negative) region, the 68.3% confidence interval obtained for $\mathcal{B}(B^0_s \to \mu^+\mu^-)$ is

$$\mathcal{B}(B^0_s \to \mu^+\mu^-) = \left(2.8^{+0.8}_{-0.7}\right) \times 10^{-9}\,.$$

The upper limit at 95% CL on $\mathcal{B}(B^0 \to \mu^+\mu^-)$ is determined with the same Neyman

procedure, yielding

$$\mathcal{B}(B^0 \to \mu^+\mu^-) < 2.1 \times 10^{-10}\,.$$

Using the predicted SM branching fractions from Section 2.1, the analysis is expected to yield on average a measurement of $\left(3.6^{+0.9}_{-0.8}\right) \times 10^{-9}$ for $\mathcal{B}(B_s^0 \to \mu^+\mu^-)$ and an upper limit of 5.6×10^{-10} for $\mathcal{B}(B^0 \to \mu^+\mu^-)$.

The Run 1 and Run 2 results are found to be 1.2 standard deviations apart. Using both runs, the combined significance of the $B_s^0 \to \mu^+\mu^-$ signal is estimated to be 4.6 standard deviations, and the combined branching fraction measurements differ by 2.4 standard deviations from the SM values in the $\mathcal{B}(B^0 \to \mu^+\mu^-)$–$\mathcal{B}(B_s^0 \to \mu^+\mu^-)$ plane. These significances are assessed purely from the evaluation of likelihood ratios.

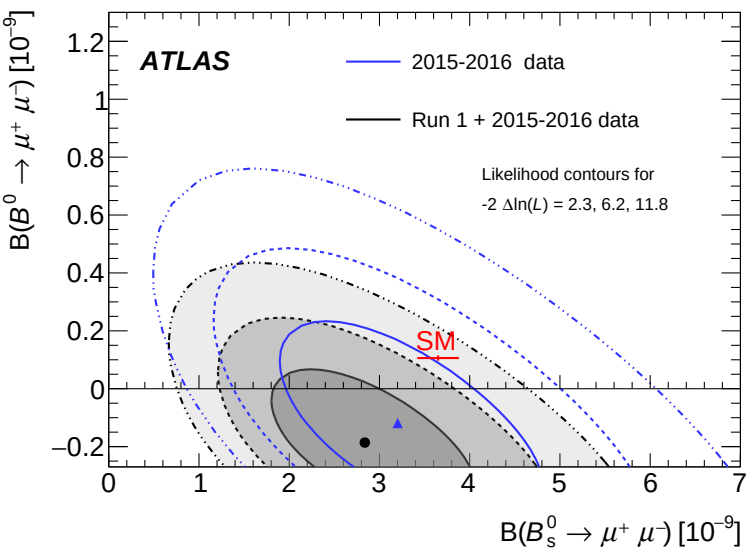


Figure 2.25: Likelihood contours for the combination of the Run 1 and 2015–2016 Run 2 results (shaded areas). The contours are obtained from the combined likelihoods of the two analyses, for values of $-2\Delta\ln(\mathcal{L})$ equal to 2.3, 6.2 and 11.8. The empty contours represent the result from 2015–2016 Run 2 data alone. The SM prediction with uncertainties is indicated. This figure was originally published in [29].

2.13 Conclusions for the 2015-2016 Dataset Combined with Run 1 Results

A study of the rare decays of B_s^0 and B^0 mesons into oppositely charged muon pairs is presented, based on 36.2 fb^{-1} of 13 TeV LHC proton–proton collision data collected by the ATLAS experiment in 2015 and 2016.

For the B_s^0 the branching fraction is determined to be $\mathcal{B}(B_s^0 \to \mu^+\mu^-) = \left(3.2^{+1.1}_{-1.0}\right) \times 10^{-9}$, where the uncertainty includes both the statistical and systematic contributions. The result is consistent with the analysis expectation of $\left(3.6^{+1.1}_{-1.0}\right) \times 10^{-9}$ in the SM hypothesis. For the B^0 an upper limit $\mathcal{B}(B^0 \to \mu^+\mu^-) < 4.3 \times 10^{-10}$ is placed at the 95% confidence level, with an expected upper bound of 7.1×10^{-10} in the SM hypothesis. The limit is compatible with the SM prediction.

The result presented here is combined with the ATLAS result from the full Run 1 dataset to obtain $\mathcal{B}(B_s^0 \to \mu^+\mu^-) = \left(2.8^{+0.8}_{-0.7}\right) \times 10^{-9}$ and $\mathcal{B}(B^0 \to \mu^+\mu^-) < 2.1 \times 10^{-10}$. All the results presented are compatible with the branching fractions predicted by the SM as well as with currently available experimental results.

2.14 Combination of ATLAS, CMS and LHCb Results

The ATLAS analysis of the branching fractions $B_s^0 \to \mu^+\mu^-$ and $B^0 \to \mu^+\mu^-$, described in the previous sections of this chapter, is combined with the latest experimental measurements of these branching fractions performed by other experiments at the LHC. The combination provides a benchmark in the context of an historically long sought after measurement. The analyses and data sets from the ATLAS [29], CMS [61], and LHCb [122] experiments are combined to provide the most precise results to date. Full details of the combination of the LHC data from 2011-2016 can

be found in [38], and a summary is provided here.

The analyses of all three experiments are performed using very similar techniques. Each uses data triggered mostly by muons, and two well-identified oppositely charged muons are combined to form a vertex displaced from a primary proton-proton interaction. The resulting $B^0_{(s)} \to \mu^+\mu^-$ candidates are further selected with additional criteria based on kinematics and geometry, as well as isolation. In each analysis, multivariate discriminators are trained to distinguish signal from the combinatorial background based on a variety of observables that are not correlated with the dimuon mass. The signal yields are extracted from a simultaneous fit to the dimuon mass distributions in bins of the output of the multivariate discriminator. In addition to the residual combinatorial component, the fit accounts for expected backgrounds where hadrons have been misidentified as muons in the cases of both hadronic two-body decays and semileptonic decays.

In each analysis the branching ratios are normalized with a reference channel, see Equation 2.1. ATLAS, CMS and LHCb use $B^+ \to J/\psi\, K^+$ as a reference channel; LHCb uses $B^0 \to K^+\pi^-$ as an additional reference channel. The systematic uncertainties from each experiment are expected to be uncorrelated with the exception of the ratio of the hadronization fractions f_d/f_s in the $B^0_s \to \mu^+\mu^-$ branching fraction. It is assumed that the fragmentation fractions of B^0 and B^+ mesons are equal due to isospin symmetry [171]. The ratio f_d/f_s is the largest systematic uncertainty in the $B^0_s \to \mu^+\mu^-$ branching fraction [38].

Full details of the signal extractions in the three analyses can be found in [29, 61, 122]; the central values of the extracted branching fractions in each experiment, used for input in the combination, are provided here. For ATLAS, the extracted

branchings are, as stated previously:

$$\mathcal{B}(B_s^0 \to \mu^+\mu^-) = \left(2.8^{+0.8}_{-0.7}\right) \times 10^{-9}$$
$$\mathcal{B}(B^0 \to \mu^+\mu^-) = (-1.9 \pm 1.6) \times 10^{-10}\,.$$

The significance for the $B_s^0 \to \mu^+\mu^-$ signal is 4.6 standard deviations (σ). A 95% CL upper limit for the $B^0 \to \mu^+\mu^-$ decay is $\mathcal{B}(B^0 \to \mu^+\mu^-) < 2.1 \times 10^{-10}$. For CMS, the extracted branchings are:

$$\mathcal{B}(B_s^0 \to \mu^+\mu^-) = \left[2.9^{+0.7}_{-0.6}(\text{exp.}) \pm 0.2(\text{frag.})\right] \times 10^{-9}$$
$$\mathcal{B}(B^0 \to \mu^+\mu^-) = \left(0.8^{+1.4}_{-1.3}\right) \times 10^{-10}\,.$$

The values of the significance of the signals of the $B_s^0 \to \mu^+\mu^-$ and $B^0 \to \mu^+\mu^-$ branching fractions are 5.6σ and 1.0σ, respectively. A 95% CL upper limit for the $B^0 \to \mu^+\mu^-$ decay is $\mathcal{B}(B^0 \to \mu^+\mu^-) < 3.6 \times 10^{-10}$. For LHCb, the extracted branchings are:

$$\mathcal{B}(B_s^0 \to \mu^+\mu^-) = \left(3.0 \pm 0.6^{+0.6}_{-0.3}\right) \times 10^{-9}$$
$$\mathcal{B}(B^0 \to \mu^+\mu^-) = \left(1.5^{+1.2+0.2}_{-1.0-0.1}\right) \times 10^{-10}\,.$$

The first uncertainty is statistical and the second systematic, with signal significances of 7.8 σ and 1.6 σ. A 95% CL upper limit for the $B^0 \to \mu^+\mu^-$ decay is $\mathcal{B}(B^0 \to \mu^+\mu^-) < 3.4 \times 10^{-10}$.

The combination of the three experimental results is performed using binned two-dimensional profile likelihoods obtained by each experiment from their fit to the dimuon invariant mass distribution. The three likelihoods are profiled separately with respect to the nuisance parameters, since systematic uncertainties of each experiment are expected to be uncorrelated. The only exception is the ratio of the fragmentation fractions f_d/f_s, a common nuisance parameter, which represents the only relevant source of correlation among the three experiments. The LHCb experiment result utilizes the fragmentation fraction measured by LHCb for $\sqrt{s} = 7$ TeV [123], $0.259 \pm$

0.015, and applies a scale factor for 1.068 ± 0.046 for $\sqrt{s} = 13$ TeV data. CMS use the LHC average [171] (including measurements from ATLAS [11] and LHCb [123]), 0.252 ± 0.012 (exp) $\pm$ 0.015 (CMS). The experimental uncertainty (exp) is taken from [171]. The second uncertainty is determined in the CMS analysis [61], obtained through comparisons of the fragmentation fraction in [123] and the average p_{T} of the $B_s^0 \to \mu^+\mu^-$ candidates in [61] with those results from LHCb for $\sqrt{s} = 13$ TeV in [119] and [120]. As discussed previously, ATLAS uses the HFLAV world average value of measurements made at LEP, the Tevatron and at the LHC [6], 0.256 ± 0.013. For the combination, the f_d/f_s factor is profiled separately in each likelihood, retaining its uncertainty in only one of the three experiments, LHCb. The effect of the correlation of f_d/f_s is tested by comparing results of the combination obtained with and without the f_d/f_s uncertainty in the ATLAS and CMS results. The effect is found to be negligible compared to statistical uncertainties.

An analytical function is fit to the measured binned likelihood for each experiment. Good agreement is observed between the fit and the likelihoods. The binned log-likelihoods from each experiment are then summed and fit using a two-dimensional variable-width Gaussian. The central values and uncertainties, determined from the fit, are:

$$\mathcal{B}(B_s^0 \to \mu^+\mu^-) = \left(2.69^{+0.37}_{-0.35}\right) \times 10^{-9}$$
$$\mathcal{B}(B^0 \to \mu^+\mu^-) = (0.6 \pm 0.7) \times 10^{-10}\,.$$

The two-dimensional likelihood contours for the branching ratios of $B_s^0 \to \mu^+\mu^-$ and $B^0 \to \mu^+\mu^-$ decays of the three experiments are shown together with their combination in Figure 2.26 (upper). The red dashed line in the figure represents the ATLAS experiment, the green dot-dashed line the CMS experiment, the blue long-dashed line the LHCb experiment and the continuous line their combination. For each experiment and for the combination, likelihood contours correspond to the values of $-2\Delta\ln\mathcal{L} = 2.3$, 6.2, and 11.8. The combination of the three experiments is

shown in Figure 2.26 (lower) with contours of different shades. Likelihood contours correspond to the values of $-2\Delta\ln\mathcal{L} = 2.3$, 6.2, 11.8, 19.3, and 30.2, represented in order from darkest to lightest. In both plots, the red point shows the SM predictions with their uncertainties.

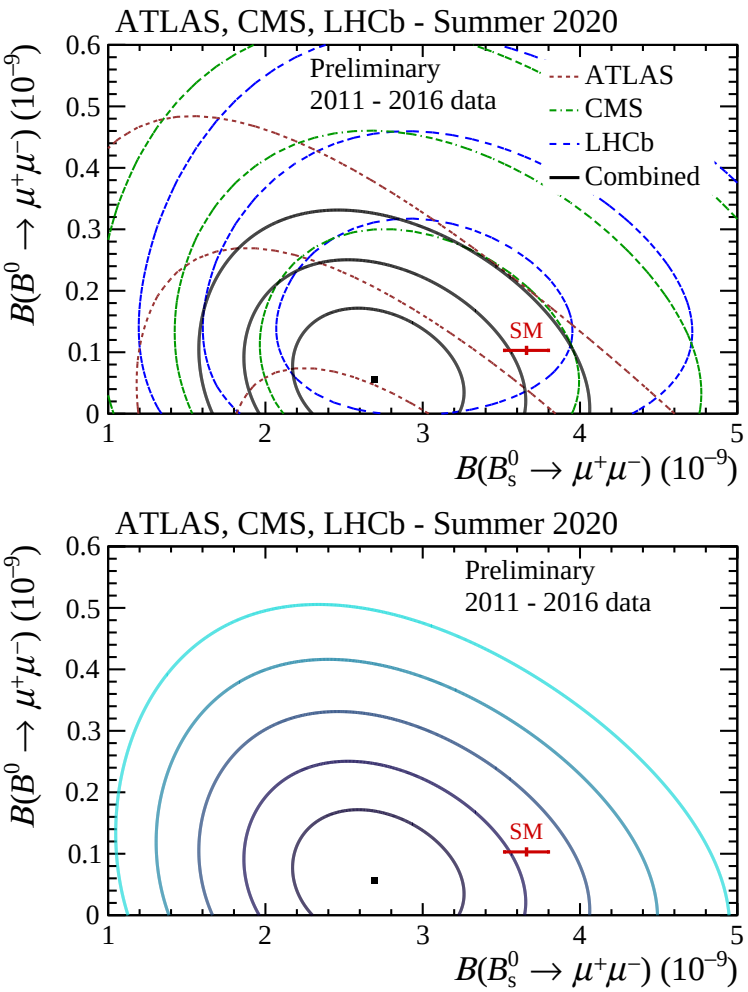


Figure 2.26: (Upper) The two-dimensional likelihood contours of the branching ratio results for the $B_s^0 \to \mu^+\mu^-$ and $B^0 \to \mu^+\mu^-$ decays for the three experiments and their combination. (Lower) The two-dimensional likelihood contours for the branching ratios of the combined results. Both plots are compared to the current SM prediction, shown with the red cross. The published results from ATLAS, CMS and LHCb experiments are detailed in References [29, 61, 122]. These figures were originally published in [38].

The negative log-likelihoods, $-2\Delta\ln\mathcal{L}$, for $\mathcal{B}(B_s^0 \to \mu^+\mu^-)$ and $\mathcal{B}(B^0 \to \mu^+\mu^-)$, are shown in the left and right plots, respectively, in Figure 2.27. In the left plot, the dark (light) green dashed lines represent the 1σ (2σ) interval. In the right plot, the dark (light) blue dashed lines represent the 90% (95%) CL. The red solid band shows the SM prediction with its uncertainty in both plots of Figure 2.27.

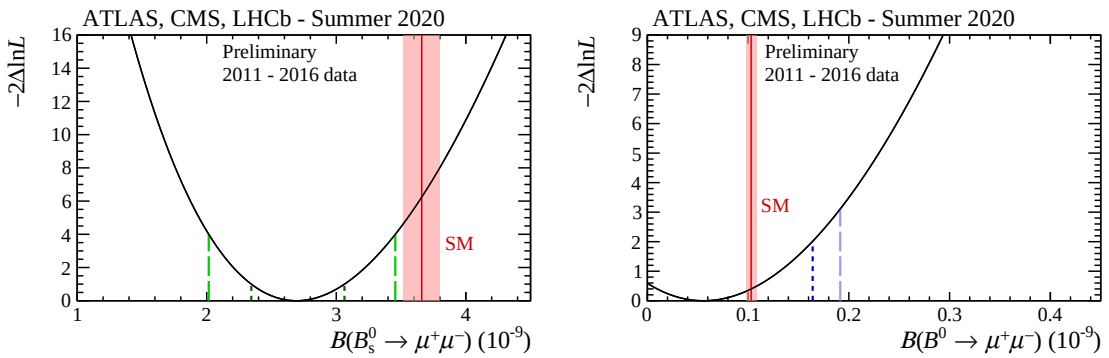


Figure 2.27: The negative log-likelihood fit values of the LHC experiments combination results for (left) $\mathcal{B}(B_s^0 \to \mu^+\mu^-)$ and (right) $\mathcal{B}(B^0 \to \mu^+\mu^-)$ compared to the SM and its uncertainty (red line and band, respectively). The published results from ATLAS, CMS and LHCb experiments are detailed in References [29, 61, 122]. These figures were originally published in [38].

The negative log-likelihood, $-2\Delta\ln\mathcal{L}$, for the ratio of the $B^0 \to \mu^+\mu^-$ and $B_s^0 \to \mu^+\mu^-$ branching fractions, $\mathcal{R}$, is shown in Figure 2.28. The light (dark) blue dashed line represents the 90% (95%) CL and the red solid band shows the SM prediction with its uncertainty.

The final results of the combination are determined as follows. The extracted branching fraction of $B_s^0 \to \mu^+\mu^-$ from the combination of all three experiments is:

$$\mathcal{B}(B_s^0 \to \mu^+\mu^-) = \left(2.69^{+0.37}_{-0.35}\right) \times 10^{-9}\,.$$

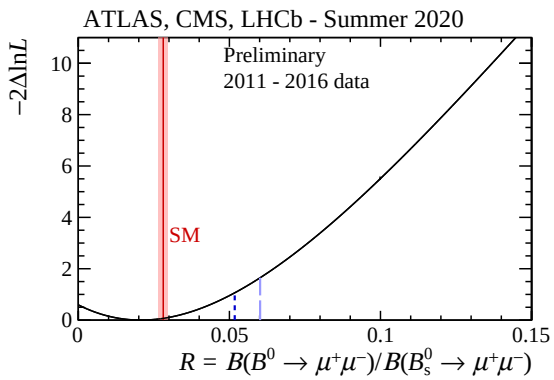


Figure 2.28: The negative log-likelihood, $-2\Delta\ln\mathcal{L}$, for the ratio of the $B^0 \to \mu^+\mu^-$ and $B_s^0 \to \mu^+\mu^-$ branching fractions of the LHC experiments combination results. The results are compared to the SM and its uncertainty (red line and band, respectively) The published results from ATLAS, CMS and LHCb experiments are detailed in References [29, 61, 122]. This figure was originally published in [38].

The upper limits on the $B^0 \to \mu^+\mu^-$ branching fractions are:

$$\mathcal{B}(B^0 \to \mu^+\mu^-) < 1.6 \times 10^{-10} \text{ at } 90\% \text{ CL, and}$$
$$\mathcal{B}(B^0 \to \mu^+\mu^-) < 1.9 \times 10^{-10} \text{ at } 95\% \text{ CL.}$$

The ratio of the $B^0 \to \mu^+\mu^-$ and $B_s^0 \to \mu^+\mu^-$ branching fractions is: $\mathcal{R} < 0.052$ (0.060) at 90% (95%) confidence level. The results are compatible with the SM predictions within 2.1 standard deviations in the two-dimensional plane of the branching fractions, when the theoretical uncertainties are included.

2.15 Modified Procedure and Analysis of the Full Run 2 Statistics

In addition to the completion of the analysis of the 2015 and 2016 ATLAS data, development of the analysis procedures for the full Run 2 data has been undertaken.

This section describes the steps made towards improving the analysis techniques in the consideration of all available data.

2.15.1 Motivation for Improvement of Analysis Techniques

The motivation for improving the analysis of the full Run 2 statistics stems from loss in performance of the BDT in the analysis of the 2015-2016 data compared to that of the Run 1 data. A comparison of the Run 1 BDT applied to Run 1 data to the 2015-2016 BDT applied to 2015-2016 data was shown in Figure 2.13. The majority of the Run 1 curve shows better background rejection (1 - efficiency) in the signal efficiency region of interest (from 0 to 54%).

Upon looking further into the 2015-2016 data, it becomes apparent that a select set of variables is responsible for the performance degradation. To illustrate this, the computation of the separation power between the signal and background distributions for each BDT variable is investigated. The separation power is a measure of the amount of overlap of the signal and background distributions of a variable.

As noted previously, the separation power is greater when the distributions have less overlap. Separation power is defined in Equation 2.2.

Comparison of the signal-to-background separation power for the analysis variables in the Run 1 and the 2015-2016 analysis is shown in Figure 2.29. It can be seen that most variables have better separation power in the 2015-2016 analysis. This improvement is due primarily to the commissioning of the IBL for Run 2 data taking. Two variables with significant separation power had better separation power in the Run 1 than in the 2015-2016 analysis: B_{iso} and the distance of closest approach of a track to the primary vertex of the B meson decay ($\text{DOCA}_{\text{xtrk}}$). These two variables fit into category (c) in Table 2.2 - associated with the isolation of the B candidate. Isolation of the B candidate is expected to be closely related to pileup.

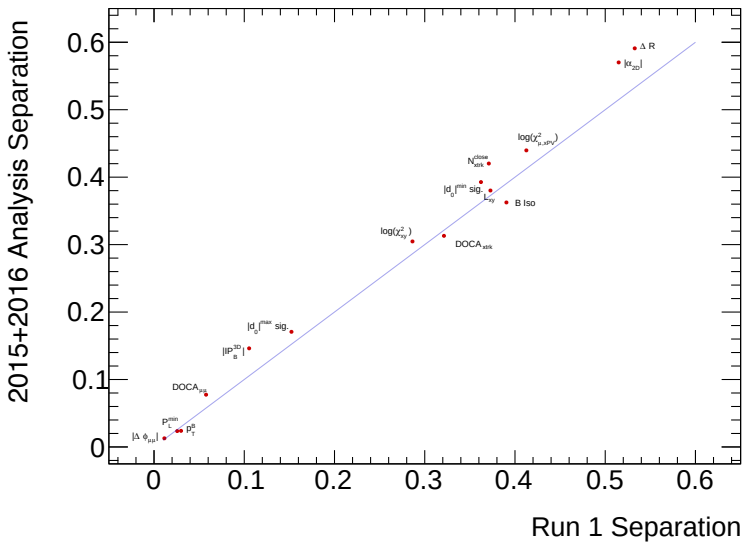


Figure 2.29: Comparison of the signal to background separation power (defined in Equation 2.2) for the analysis variables in the Run 1 and Run 2 data. Use of the term separation in the axis label implies separation power. Two variables had better separation power in the Run 1, B isolation and Distance of closest approach for a track to the primary vertex of the B meson decay.

Pileup is a measure of the number of proton interactions per LHC beam crossing. It is expected that the pileup is higher in Run 2 because the LHC was able to achieve higher luminosity levels by increasing the number of interactions per bunch crossing. While pileup could be considered a leading hypothesis for the degradation in these variables, it appears more likely that the lower separation power is due to stricter transverse momentum (p_{T}) selections on reconstructed tracks in an event. To mitigate data storage limitations, the selection based on transverse momentum of tracks in an event was changed between Run 1 and Run 2. In Run 1 the track selection criterion was $p_{\mathrm{T}} > 400$ MeV and in Run 2 this was increased to $p_{\mathrm{T}} > 500$ MeV. This cut is likely the primary cause of the degradation seen in $\mathrm{DOCA}_{\mathrm{xtrk}}$.

2.15.2 Improvements to the Reconstruction Procedures of B Meson Isolation Variables

Tunings and optimizations of the reconstruction procedures for the isolation variables B_{iso}, $N_{\text{xtrk}}^{\text{close}}$, and $\text{DOCA}_{\text{xtrk}}$ have been investigated and are presented here. The definitions of these variables are provided in Table 2.2 and are elaborated here.

The B meson isolation variable (B_{iso}) is computed as

$$B_{\text{iso}} = \frac{|p_{\text{T}}^{B}|}{|p_{\text{T}}^{B}| + \sum |p_{\text{T}}^{add}|} \tag{2.3}$$

where p_{T}^{B} is the transverse momentum of the B meson and p_{T}^{add} is the transverse momentum of the other tracks (excluding the signal muon tracks) in the event. Only tracks that are matched to the B primary vertex and tracks that meet the condition ΔR (between the track vector and the B meson vector) < 0.7 are considered in the computation of B_{iso}.

The variable $\text{DOCA}_{\text{xtrk}}$ is the closest distance from a track in the event to the B decay vertex. The variable $N_{\text{xtrk}}^{\text{close}}$ is determined by counting the number of tracks that are near the decay vertex of the B meson. The proximity of the tracks to a vertex is determined using the χ^2 function defined as:

$$\ln(\chi^2) = \ln((d_0/\sigma_{d_0})^2 + (z_0/\sigma_{z_0})^2), \tag{2.4}$$

where d_0 and z_0 are the transverse and longitudinal components of the impact parameter, respectively. The impact parameter is defined as the distance at the point of closest approach of a track to a spatial coordinate, in this case to a vertex. The σ_{d_0} and σ_{z_0} are the transverse and longitudinal impact parameter resolutions, respectively. The computations of both $\text{DOCA}_{\text{xtrk}}$ and $N_{\text{xtrk}}^{\text{close}}$ only consider the tracks that are matched to the B candidate primary vertex and exclude the tracks of B meson decay products. In the 2015-2016 analysis tracks considered in the $\text{DOCA}_{\text{xtrk}}$ computation required a proximity to the B candidate decay vertex with a requirement

of $\ln(\chi^2_{DV}) < 7$ and those considered for the $N^{\text{close}}_{\text{xtrk}}$ computation were selected such that $\ln(\chi^2_{DV}) < 1$.

Computation time and data storage constraints restrict the amount of data that can be used to refine the reconstruction procedures of these variables. There are many tracks in every event and the properties of each track must be considered (computationally) when assigning a value to an isolation variable in an event. Typically, during data processing only the muon tracks that originate from the B decay vertex are stored after the computations of the analysis variables. This allows for manageable file sizes while the subsequent analysis procedures are defined. However, to analyze changes in the isolation variable reconstruction procedures a small sample of the full Run 2 data is produced. In this sample, all reconstructed tracks kept in order to study various constructions of the isolation variables.

Robustness against pileup is of high importance while analyzing Run 2 data and will grow in importance for future analyses of Run 3 data and HL-LHC data. The isolation variables provide information to the BDT about the pileup conditions and so particular care is taken to understand how these variables are affected by pileup. A measure of the pileup is the mean number of proton-proton interactions per proton bunch crossing, μ, corresponding to the mean of the Poisson distribution of the number of interactions per crossing calculated for each bunch. It is calculated from the instantaneous per bunch luminosity as $\mu = L_{\text{bunch}} \times \sigma_{\text{inel}}/fr$ where L_{bunch} is the per bunch instantaneous luminosity, σ_{inel} is the inelastic cross section which is taken to be 80 mb for 13 TeV collisions, and fr is the LHC revolution frequency. The μ values for 2015-2018 data-taking periods are shown in Figure 2.30 [10]. The luminosity shown is based on van der Meer beam-separation scans [175].

Three sets of data are chosen for studying the reconstruction of the isolation variables. One run in each of three years of Run 2 is selected: run number 302393 (2016), run number 339849 (2017), and run number 358096 (2018). The run in 2017

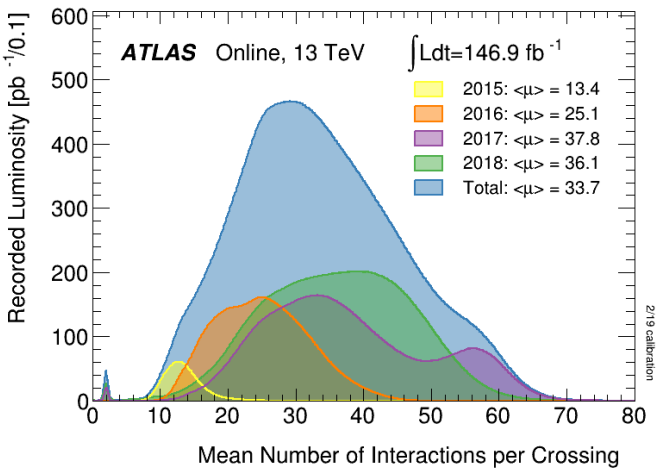


Figure 2.30: Mean number of proton-proton interactions per bunch crossing, μ, in the Run 2 data [10].

is selected because it has a relatively high $\langle\mu\rangle$ value of 48; the $\langle\mu\rangle$ of all runs in 2017 is 37.8. The run in 2018 is selected because it has a low $\langle\mu\rangle$ value, 23.3; the average of all runs of 2018 is 36.1. These values can be compared to the $\langle\mu\rangle$ value in Run 1: $\langle\mu\rangle = 18.5$, and the 2015-2016 mean value, $\langle\mu\rangle = 23.7$. The run from 2016 is selected as a representative run from the 2015-2016 dataset and is used for cross-checking any findings in the two runs from 2017 and 2018 which have not previously been analyzed. Each dataset is blinded in the $B_s^0 \to \mu^+\mu^-$ signal region and are used to study the background. Three simulated signal samples are also produced, corresponding to the data taking conditions in each of the three selected runs.

In addition to μ, the number of reconstructed primary vertices for every $B_{(s)}^0 \to \mu^+\mu^-$ candidate, is a reflection of the pileup conditions in a dataset. The distributions of the number of primary vertices in three selected datasets are shown in Figure 2.31. These distributions are compared to those of the full Run 1 dataset and full 2015-2016 dataset.

Three simulated datasets from three Monte Carlo productions are produced:

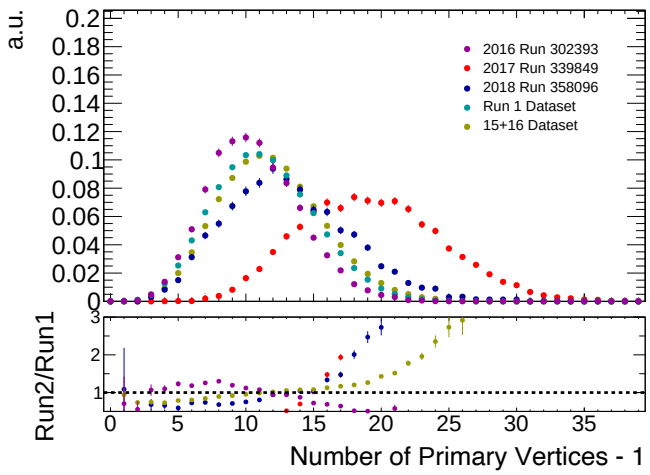


Figure 2.31: Number of primary vertices of single data runs: run 302393 (2016), run 339849 (2017), and run 358096 (2018). The distributions are compared to the number of primary vertices in the full 2015-2016 dataset, the LHC Run 1 dataset, and the simulated datasets MC16a, MC16d and MC16e. The number of primary vertices − 1 is plotted here to match the Run 1 computation choice.

MC16a, MC16d, and MC16e. The μ distributions of MC16a, MC16d, and MC16e are weighted to match pileup distributions of the selected runs in 2016, 2017 and 2018, respectively. This procedure involves applying event by event weights based on the difference between the μ distributions in data and MC. The studies performed on the individual runs in 2016, 2017 and 2018 are performed in parallel with those of the MC16a, MC16d and MC16e samples.

The selection criteria of the tracks that are considered during the computation of B_{iso}, $N_{\text{xtrk}}^{\text{close}}$, and $\text{DOCA}_{\text{xtrk}}$ are the focus of this study. Optimal performance, as measured with receiver operating characteristic (ROC) curves, is obtained in these three variables after tuning of the selection criteria of the tracks. The ROC is plotted as background rejection versus signal efficiency for a given variable. The aim of the studies is to increase both background rejection and signal efficiency - this is called the reach of the ROC curve. ROC acceptance curves (background efficiency versus signal efficiency) are also used to assess performance of the variables. The reconstruction

studies have been performed on each of the three datasets and for finer selections on pileup to investigate the impact of a higher number of collisions per beam crossing in the Run 2 data.

Investigations of the number of hits in the Pixel and SCT detector subsystems are performed. These selections help to reduce fake track reconstructions. Fake tracks are tracks that do not correspond to a particle but are reconstructed in the Inner Detector due to combinatorial effects while fitting hits together to form tracks. Figure 2.32 shows the number of hits for several options of ID hit requirements in the IBL, the Pixel Detector and the SCT Detector. Two sets of requirements are labeled *Loose* and *Tight*. These names are not the same as the *loose* and *tight* muon requirements discussed in Sections 2.3 and 2.5, which are applied after variable reconstruction procedures. The definitions are as follows:

Loose: Total number of hits in the Pixel and SCT detectors ≥ 7, number of hits assigned to multiple tracks in the Pixel Detector plus the number of hits assigned to multiple tracks in the SCT Detector divided by two ≤ 1, number of holes (missed hits) in the Pixel and SCT detectors ≤ 2, and number of holes (missed hits) in the Pixel Detector ≤ 1.

Tight: Total number of hits in the Pixel and SCT detectors ≥ 7 (if $|\eta| \leq 1.65$) or ≥ 11 (if $|\eta| > 1.65$), number of hits on the IBL and B-Layer > 0, number of holes (missed hits) in the Pixel Detector $= 0$.

All reconstructed tracks fulfill the *Loose* selection criteria by definition. The *Tight* selection criteria are primarily used for reconstructing physics objects and suppressing fake tracks.

In addition, the selections used in the Run 1 analysis are investigated. These are: the number of hits in the Pixel Detector ≥ 1 and in the SCT Detector ≥ 2 in addition to the *Loose* requirements. The requirements in Run 1 do not include the IBL layer in the Pixel Detector, as this run took place before IBL was installed. This

investigation focuses on an observed difference between the performance of isolation variables between Run 1 and Run 2, so the Run 1 hit requirements including and excluding IBL are also shown in Figure 2.32. In the 2015-2016 analysis, the Run 1 hit requirements including IBL as part of the Pixel Detector were used. Figure 2.32 shows the hit distribution for the 2017 run. Similar studies are performed on the 2016 and 2018 runs and the simulated data samples MC16a, MC16d, and MC16e.

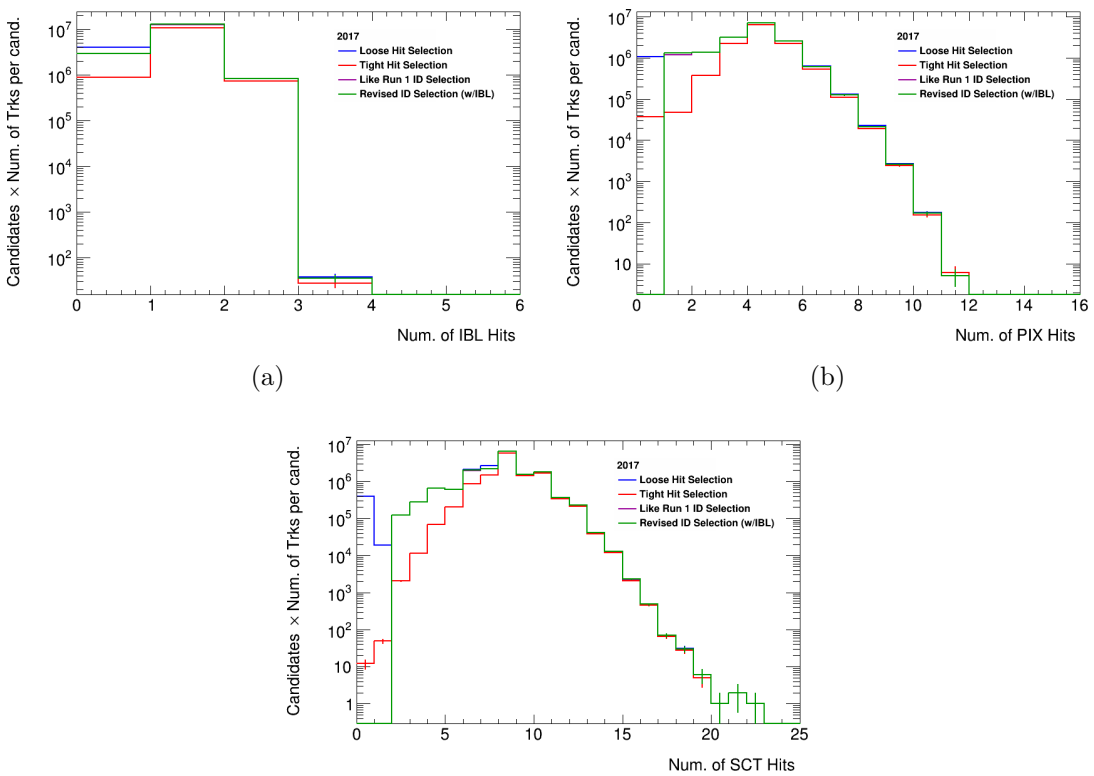


Figure 2.32: The number of hits in the Inner Detector systems in 2017 run 339849 under different hit selection criteria. The hit distributions for (a) the IBL, (b) the Pixel Detector, and (c) the SCT Detector are investigated separately.

There is no major difference between the Run 1 and the revised Run 1 (including IBL hits in the Pixel hit count) hit distributions, as is observed in Figure 2.32.

The increased requirements of hits in both Pixel and SCT over the *Loose* selection criteria will help reduce fakes and keep the efficiency of track collection high. The *Tight* selection criteria removes too much information and the improvements in track identification are not needed for the isolation study. The revised Run 1 hit selections, as were implemented in the 2015-2016 analysis, serve as a compromise between the *Loose* and *Tight* hit selections and maintain consistency with the Run 1 analysis. For these reasons the hit selections used in the 2015-2016 analysis are kept for the remainder of the studies.

In the Run 1 analysis tracks in a candidate event with $p_{\mathrm{T}} > 400$ MeV are stored for further analysis. In the 2015-2016 analysis tracks with $p_{\mathrm{T}} > 500$ MeV are stored. In both the Run 1 and the 2015-2016 analyses tracks that are associated with the primary vertex of a candidate event are used and an additional selection of $\ln(\chi^2) < 5$ (where χ^2 is defined as in Equation 2.4) is applied. In Run 1, tracks not associated with any primary vertex are also included prior to the $\ln(\chi^2)$ selection. The final selection on the tracks in the Run 1 and the 2015-2016 analyses is a restriction of $\Delta R < 0.7$ between the track momentum vector and the B meson momentum vector. The conditions in Run 2 are different from Run 1, as discussed above; the performance of the three isolation variables after altering these restrictions is investigated, using ROC curves between data sidebands (background) and MC (signal) as a measure of the performance.

Studies to find the most pertinent selections for matching a track to a primary vertex are performed. Several sets of restrictions for matching a track and a primary vertex in the event are investigated, implementing restrictions on the impact parameters d_0 and z_0 and their corresponding resolutions σ_{d_0} and σ_{z_0}. These Track to Vertex Association (TVA) sets of restrictions are defined as:

Loose TVA: Track was used in the primary vertex fit; if the track was not used in any vertex fit then $|\Delta z_0 \sin(\theta)| < 3$ mm.

Nominal TVA: $|d_0| < 2$ mm and $|\Delta z_0 \sin(\theta)| < 3$ mm.

Tight TVA: $|d_0| < 0.5$ mm and $|\Delta z_0 \sin(\theta)| < 0.5$ mm.

Custom TVA: The value $\ln(\chi^2) = \ln((d_0/\sigma_{d_0})^2 + (z_0/\sigma_{z_0})^2)$ is computed between the track and every primary vertex in the event. The primary vertex corresponding to the minimum $\ln(\chi^2)$ is selected as the vertex associated with the track.

The *Loose TVA*, *Nominal TVA*, and *Tight TVA* working points were previously developed [37] and the *Custom TVA* was created specifically for the $B^0_{(s)} \to \mu^+\mu^-$ analysis. These selection criteria are investigated in combination with other selection criteria including different restrictions on $\ln(\chi^2)$ and a wider isolation cone around the B flight direction, ΔR. The most promising constructions have been narrowed down and are presented in the following text. The most promising constructions are compared with the corresponding construction used in the analysis of the 2015-2016 data. Comparisons are also made with the corresponding selections from Run 1 as implemented in the Run 1 dataset to show how much BDT performance may be recovered and in some cases surpassed.

Promising constructions for B_{iso}

Investigations of different combinations of possible selection criteria are performed for the three isolation variables. The best-performing sets of track selection criteria are narrowed down to the following for B_{iso}:

Loose TVA: Tracks with $p_{\text{T}} > 500$ MeV that meet *Loose TVA* selection criteria and $\Delta R < 1.0$.

Custom TVA: Tracks with $p_{\text{T}} > 500$ MeV that meet the *Custom TVA* selection criteria and $\Delta R < 1.0$.

As in Run 1: Select all tracks with $p_{\text{T}} > 500$ MeV, require $\ln(\chi^2) \leq 5$ for the track to primary vertex association and $\Delta R < 0.7$.

For comparison to previous reconstruction criteria, the following definitions are also

implemented:

As in 2015-2016: Select all tracks with $p_{\mathrm{T}} > 500$ MeV associated with the primary vertex, require $\ln(\chi^2) \leq 5$ for the track to primary vertex association, exclude tracks that were not used in that primary vertex fit, and $\Delta R < 0.7$.

Run 1 Data (applied to the full Run 1 dataset): Select all tracks with $p_{\mathrm{T}} > 500$ MeV, require $\ln(\chi^2) \leq 5$ for the track to primary vertex association and $\Delta R < 0.7$. (Note that these requirements are identical to the **As in Run 1** requirements for B_{iso})

For all constructions, signal tracks are excluded from the computations.

The B_{iso} distributions are compared for each of the five selections in Figure 2.33 in both the 2017 run 339849 sideband data and the corresponding MC16d dataset. The candidates are more isolated when the distribution is closer to one and less isolated further away from one. The distributions alone do not indicate better signal discrimination power, because both pileup information (less isolation) and isolated candidates may be useful for the BDT training. The B_{iso} ROC performance using the 2017 run 339849 sideband data for the background sample and the corresponding MC16d dataset for the signal sample is shown in Figure 2.34 (left). A magnified conversion of the ROC distributions to background acceptance ROCs is shown in Figure 2.34 (right). Fewer background candidates while maintaining high signal efficiency is the performance indicator. As seen in Figure 2.34 (right), the **As in Run 1**, **Custom TVA**, and **Loose TVA** selection criteria reveal better background rejection and improved signal efficiency when compared to the **As in 2015-2016** and **Run 1** selections. These ROC comparisons indicate that any one of these three selection criteria will provide improved BDT performance when used as a replacement for the **As in 2015-2016** B_{iso} input variable in the Run 2 datasets. In the full ROC curves for all scenarios, Figure 2.34 (left), the same trends are seen for the full range of the ROC. The **Custom TVA** construction crosses the **As in 2015-2016** construction and remains comparable within errors, but when the BDT output cuts are implemented

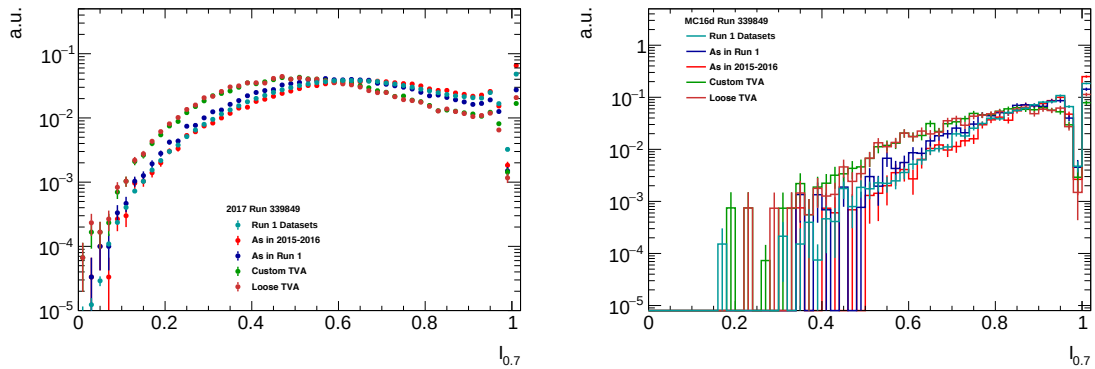


Figure 2.33: B_{iso} variable distributions for five track selection criteria described in the text for (left) the 2017 run 339849 sideband data and (right) the corresponding MC16d dataset.

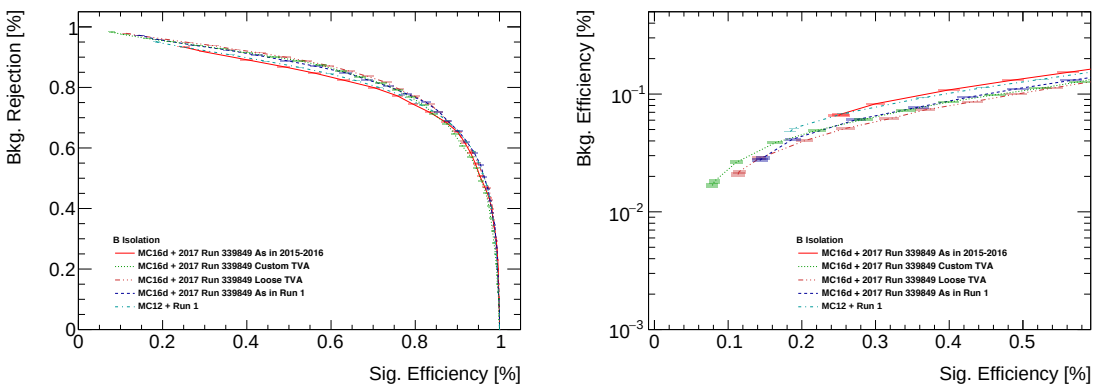


Figure 2.34: (Left) the B_{iso} ROC performance and (right) ROC acceptance curves using the 2017 run 339849 sideband data for the background sample and the corresponding MC16d dataset for the signal sample.

in the final analysis this region of the curve will have little influence because the signal extraction is performed only for the candidates fulfilling the high background rejection criteria, defined by the BDT output. Similar performance curves for the 2016 and MC16a datasets and the 2018 and MC16e datasets are also investigated with comparable results.

Further investigation of the pileup dependence of the B_{iso} selection criteria is

performed. The pileup bins are defined by equally spaced regions of the variable $\langle\mu\rangle$, defined as:

$12. \leq \langle\mu\rangle \leq 22.$

$23. \leq \langle\mu\rangle \leq 33.$

$34. \leq \langle\mu\rangle \leq 44.$

$45. \leq \langle\mu\rangle \leq 55.$

The lowest region is investigated with the 2018 and MC16e datasets and the other three are investigated with 2017 and MC16d.

The ROC acceptance plots of the B Isolation variable, separated into four pileup bins, are shown in Figure 2.35. The **Custom TVA** and **Loose TVA** constructions perform better than the other constructions. Lower background efficiency across the curve will allow the BDT to better reject the background. There is a clear pileup dependence for the **As in Run 1**. There is no apparent pileup dependence of the variables when constructed using **Custom TVA** and **Loose TVA** constructions. These results indicate that the **Custom TVA**, **Loose TVA**, and **As in Run 1** are still superior constructions when compared to the **As in 2015-2016** variable and that further recovery of the **Run 1** construction can be obtained with these variables.

Promising constructions for $\mathbf{DOCA_{xtrk}}$

Several sets of track selection criteria for $\mathrm{DOCA_{xtrk}}$ are identified as the most promising for the $\mathrm{DOCA_{xtrk}}$ variable construction when compared to other *TVA* and $\ln(\chi^2)$ track selections. The promising selections are:

Loose TVA: Tracks with $p_\mathrm{T} > 500$ MeV that meet the *Loose TVA* selection criteria and $\ln(\chi^2) \leq 7$ for the secondary vertex.

Custom TVA: Tracks with $p_\mathrm{T} > 500$ MeV that meet the *Custom TVA* selection criteria and $\ln(\chi^2) \leq 7$ for the secondary vertex.

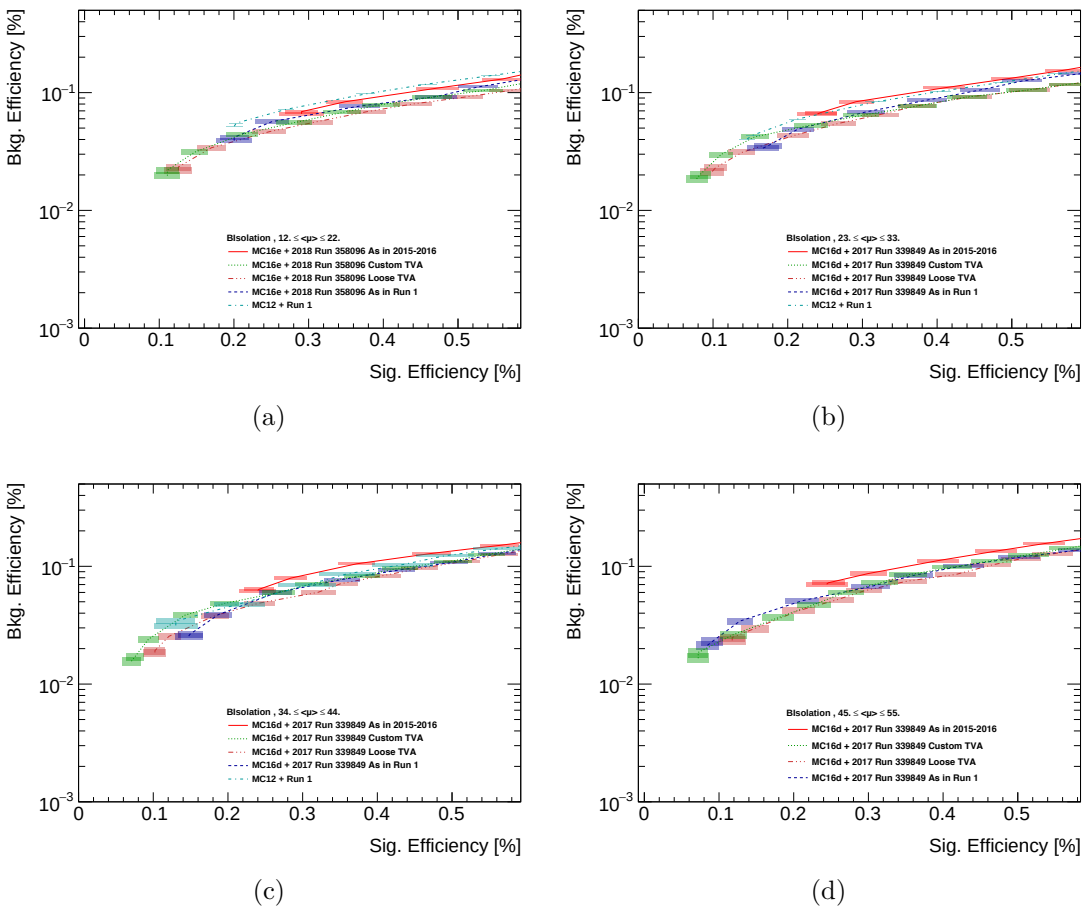


Figure 2.35: Pileup binned comparisons of the B_{iso} variable constructions described in the text. Each comparison is made for a selected range of $\langle\mu\rangle$ values; the comparisons, (a), (b), (c) and (d), are ordered in increasing pileup. The pileup selections are described in the text.

The following track selections are maintained for demonstrating the improvements seen in the **Loose TVA** and **Custom TVA** track selection criteria:

As in 2015-2016: Select tracks with $p_{\text{T}} > 500$ MeV associated with the primary vertex and require $\ln(\chi^2) \leq 7$ for the secondary vertex.

Run 1 Data (applied to the full Run 1 dataset): Select tracks with $p_{\text{T}} > 400$ MeV associated with the primary vertex and tracks with $p_{\text{T}} > 400$ MeV not associated with any primary vertex, and require $\ln(\chi^2) \leq 7$ for the secondary

vertex.
For all constructions, signal tracks are excluded from the computations.

The $\mathrm{DOCA}_{\mathrm{xtrk}}$ variable distributions comparing the different constructions for the 2017 run 339849 sideband data and the corresponding MC16d dataset are shown in Figure 2.36. Each variable distribution reflects a requirement that if $\mathrm{DOCA}_{\mathrm{xtrk}}$ is greater that three, than $\mathrm{DOCA}_{\mathrm{xtrk}}$ is set equal to three. This condition was put in place because some vertices do not record a value for $\mathrm{DOCA}_{\mathrm{xtrk}}$, which may indicate that the vertex is very well isolated. This information may be useful for the BDT when discriminating signal from background. This requirement was not implemented in the analyses of the Run 1 and 2015-2016 datasets, but is required in the comparisons shown in Figure 2.36. Again the variable distributions alone cannot be used for determining the best variable constructions. The ROCs and acceptance curves for the $\mathrm{DOCA}_{\mathrm{xtrk}}$ variables are shown in Figure 2.37.

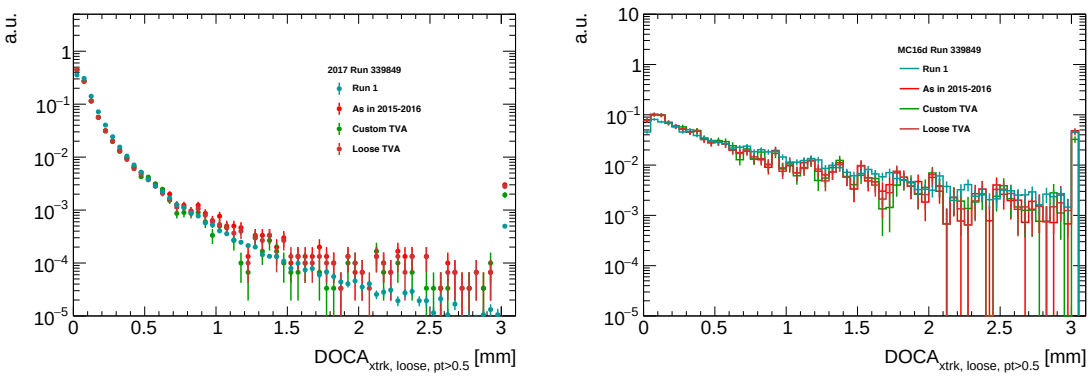


Figure 2.36: $\mathrm{DOCA}_{\mathrm{xtrk}}$ variable distributions for four track selection criteria described in the text for (left) the 2017 run 339849 sideband data and (right) the corresponding MC16d dataset.

In these ROC comparisons the **Run 1** constructions (applied to Run 1 data) show the best signal efficiency and background rejection. The increase in the track p_{T} cut from 400 MeV to 500 MeV lead to this effect and cannot be recovered. The improved

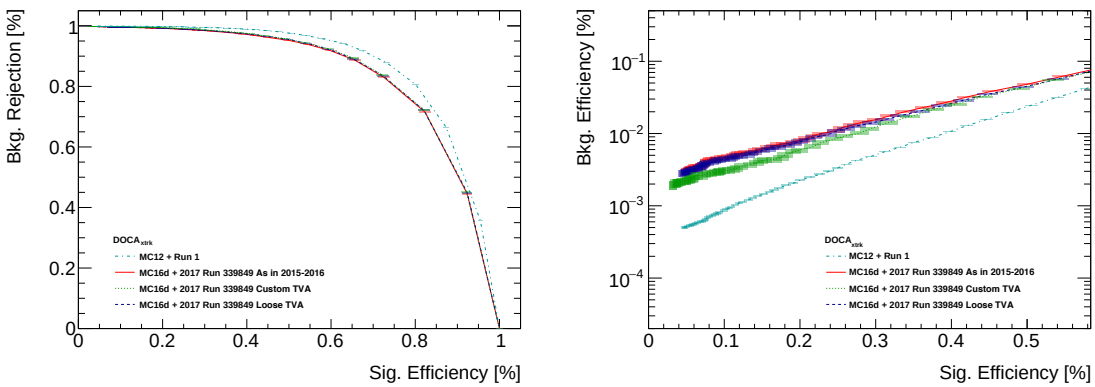


Figure 2.37: (Left) The $\mathrm{DOCA}_{\mathrm{xtrk}}$ ROC performance and (right) ROC acceptance curves using the 2017 run 339849 sideband data for the background sample and the corresponding MC16d dataset for the signal sample.

selection criteria implemented in **Custom TVA** and **Loose TVA** do recover some of the background rejection observed in **As in 2015-2016**. **Custom TVA** is the preferred construction in this case, given the constraints imposed by the pileup conditions in Run 2. Similar performance curves for the 2016 and MC16a datasets and the 2018 and MC16e datasets also show comparable results.

To check the pileup dependence of the $\mathrm{DOCA}_{\mathrm{xtrk}}$ constructions, the ROC acceptance curves are compared in the four pileup bins defined above. These comparisons are shown in Figure 2.38. As the pileup restrictions increase, the statistics in the Run 1 dataset decrease and are reflected in the larger errors. The **Run 1** construction does not have sufficient statistics in the highest pileup bin and so is excluded from Figure 2.38 (d). In all pileup bins **Custom TVA** is the best-performing variable construction, although higher statistics are needed for confirmation of this observation.

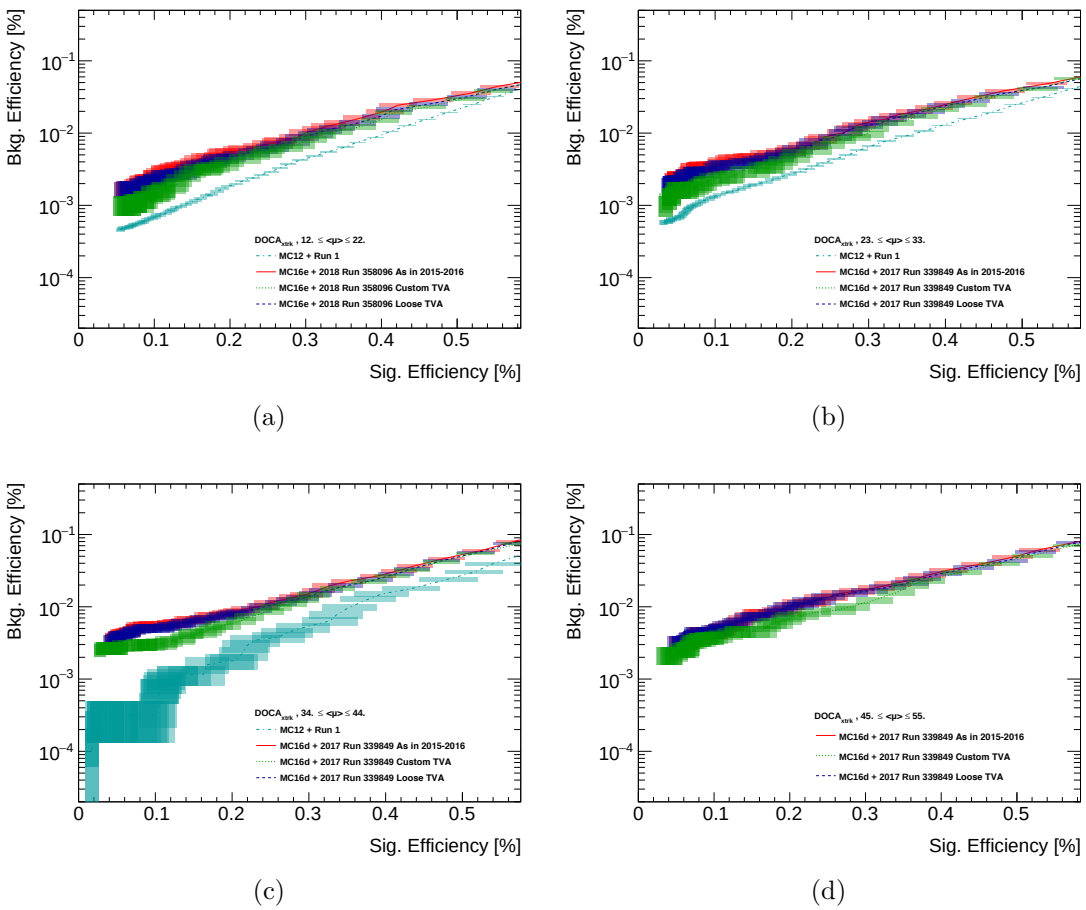


Figure 2.38: Pileup binned comparisons of the $\mathrm{DOCA}_{\mathrm{xtrk}}$ variable constructions described in the text. Each comparison is made for a selected range of $\langle\mu\rangle$ values; the comparisons, (a), (b), (c) and (d), are ordered in increasing pileup. The pileup selections are described in the text.

Promising constructions for $N_{\mathrm{xtrk}}^{\mathrm{close}}$

Several sets of track selection criteria for $N_{\mathrm{xtrk}}^{\mathrm{close}}$ are identified as the most promising for the $N_{\mathrm{xtrk}}^{\mathrm{close}}$ variable construction when compared to other *TVA* and $\ln(\chi^2)$ track selections. The promising selections are:

Loose TVA: Tracks with $p_{\mathrm{T}} > 500$ MeV that meet the *Loose TVA* selection criteria and $\ln(\chi^2) \leq 2$ for the secondary vertex.

Custom TVA: Tracks with $p_{\mathrm{T}} > 500$ MeV that meet the *Custom TVA* selection criteria and $\ln(\chi^2) \leq 2$ for the secondary vertex.

Once again, for purposes of direct comparison of the improvements obtained with **Loose TVA** and **Custom TVA** the following track selections are also included in comparisons:

As in 2015-2016: Select tracks with $p_{\mathrm{T}} > 500$ MeV associated with the primary vertex and $\ln(\chi^2) \leq 1$ for the secondary vertex.

Run 1 Data (applied to the full Run 1 dataset): Select tracks with $p_{\mathrm{T}} > 400$ MeV associated with the primary vertex and tracks with $p_{\mathrm{T}} > 400$ MeV not associated with any primary vertex, require $\ln(\chi^2) \leq 1$ for the secondary vertex.

For all constructions, signal tracks are excluded from the computations.

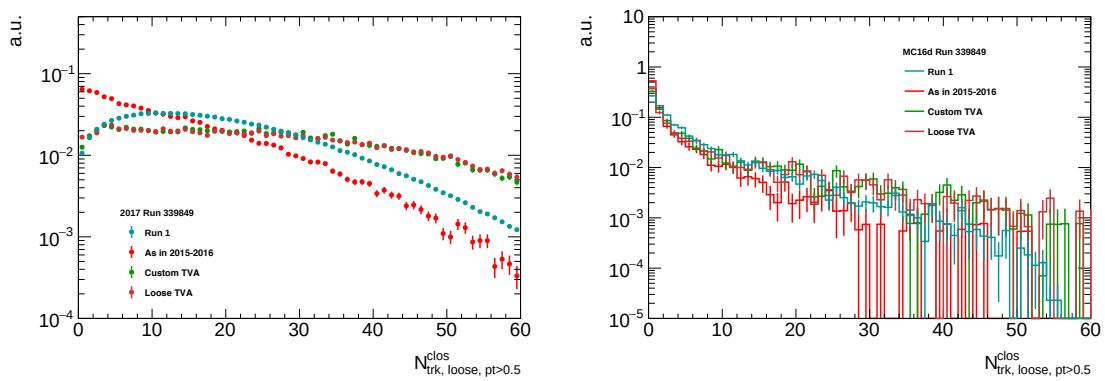


Figure 2.39: $N_{\mathrm{xtrk}}^{\mathrm{close}}$ variable distributions for four track selection criteria described in the text for (left) the 2017 run 339849 sideband data and (right) the corresponding MC16d dataset.

The $N_{\mathrm{xtrk}}^{\mathrm{close}}$ variable distributions are shown in Figure 2.39 for the 2017 run 339849 sideband data and the corresponding MC16d dataset. The improved selections, **Loose TVA** and **Custom TVA**, have the effect of making the background sample less isolated - as seen in Figure 2.39 (left), where the number of candidates with a low number of tracks is decreased. This effect is also seen in the signal sample, but to a lesser degree. The improved performance of these constructions is evident in

the ROCs and acceptance curves for the $N_{\text{xtrk}}^{\text{close}}$ variables, shown in Figure 2.40. The

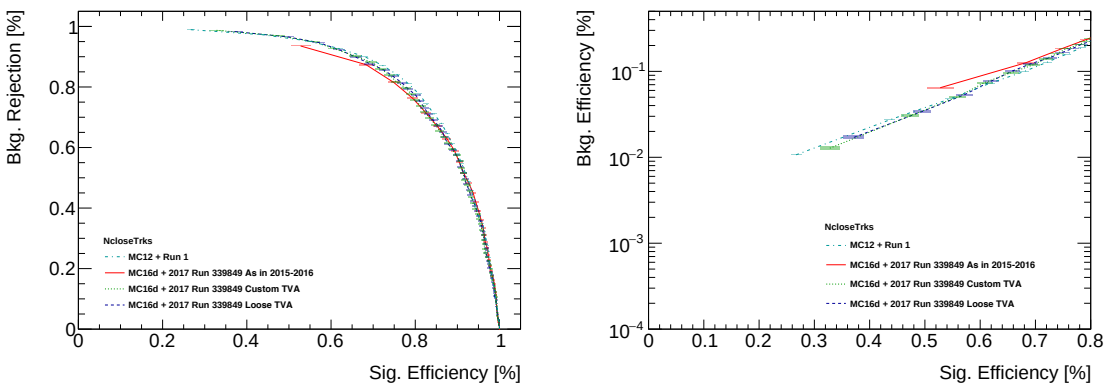


Figure 2.40: (Left) The $N_{\text{xtrk}}^{\text{close}}$ ROC performance and (right) ROC acceptance curves using the 2017 run 339849 sideband data for the background sample and the corresponding MC16d dataset for the signal sample.

background rejection of the **Run 1** variable is completely recovered and the signal efficiency (the reach of the curve) is almost recovered. With more statistics, it may be determined that the reach of the **Run 1** construction is fully recovered. Similar performance curves for the 2016 and MC16a datasets and the 2018 and MC16e datasets show comparable results.

A study of the $N_{\text{xtrk}}^{\text{close}}$ variable separated into pileup bins is performed, similar to the studies of the other two isolation variables previously discussed. The ROC acceptance curves in the four pileup bins discussed above are shown in Figure 2.41. The improvements seen before pileup binning persist and no clear dependence on the pileup is observed. Once again the **Custom TVA** construction is slightly preferable to **Loose TVA**, but a final selection will need to be made on a larger sample.

The most promising variable constructions for the three isolation variables B_{iso}, $\text{DOCA}_{\text{xtrk}}$, and $N_{\text{xtrk}}^{\text{close}}$ have been presented and show encouraging results for recovering the Run 1 analysis BDT performance. To select the optimal variable constructions from the sets described here, it is determined that more statistics are needed

to make final decisions. The 2015-2016 datasets are re-processed with these isolation variables included. With these higher statistics, new implementations of the BDT can be trained replacing the previous isolation input variables with these new variable constructions. A measure of BDT performance is the best tool for making the variable selections for the full Run 2 dataset.

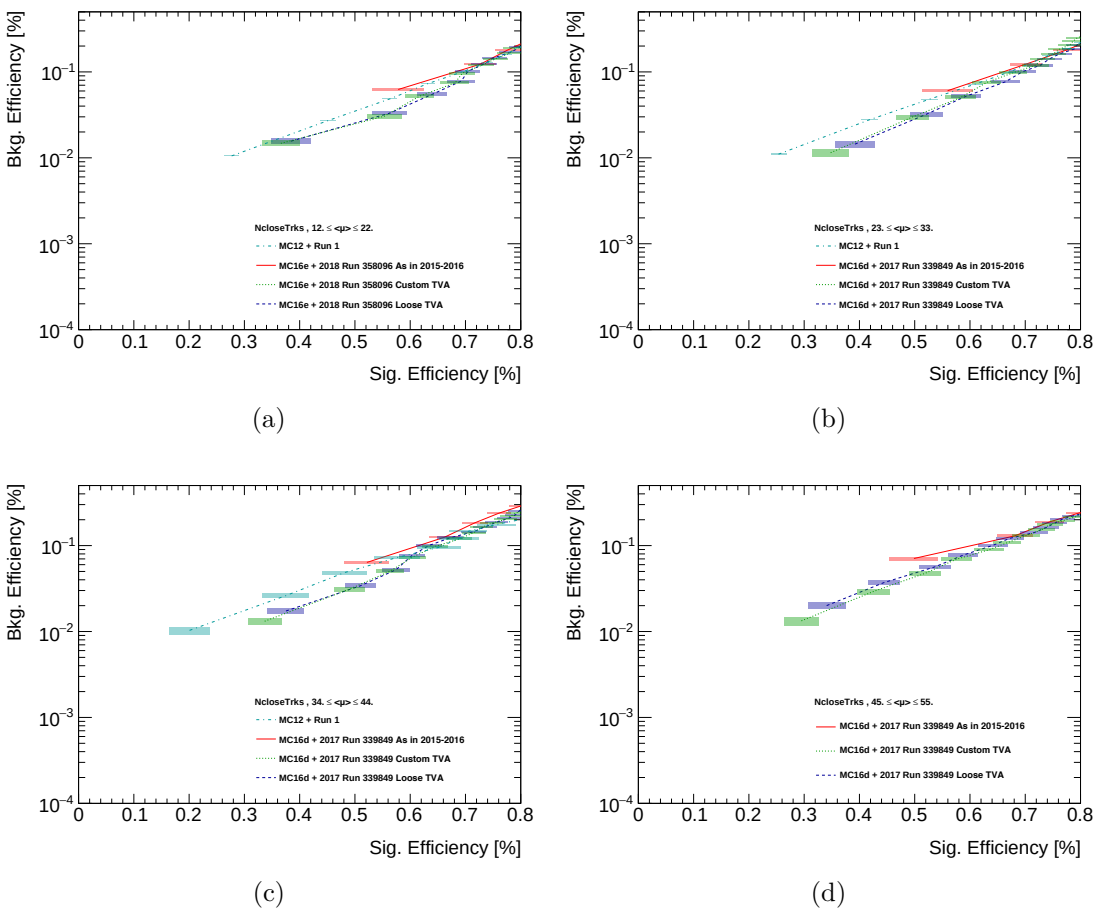


Figure 2.41: Pileup binned comparisons of the $N_{\text{xtrk}}^{\text{close}}$ variable constructions described in the text. Each comparison is made for a selected range of $\langle\mu\rangle$ values; the comparisons, (a), (b), (c) and (d), are ordered in increasing pileup. The pileup selections are described in the text.

2.15.3 Assessment of the Isolation Variables in the Re-processed 2015-2016 Dataset

The 2015-2016 data are re-processed and used for making final selections of the isolation variable constructions prior to processing the 2017-2018 Run 2 data. The re-processed data, henceforth referred to as the new nTuples, are first compared to the original 2015-2016 analysis dataset. Each analysis variable is investigated and no major discrepancies are found in the variable distributions between the two nTuples. The fitting tools used for assigning muon tracks ("muon smearing and calibration") were updated between the first data processing and the processing of the new nTuples. These new calibrations lead to a slight increase in the yield (number of candidate events per fb^{-1}) as is seen in Figure 2.42, after the nominal analysis cuts were applied (discussed in Table 2.1). A comparison between the sideband data in the new and old nTuples for each ATLAS data-taking period in 2015 and 2016 is shown in the figure. The total luminosity accumulated in the 2015-2016 analysis is 26.2 fb^{-1}, and the progression of data collection per data-taking period is also shown in Figure 2.42. As can be seen in the lower panel of the figure, the increase in yield per data-taking period is less than 2.5% in the central value and less than about 5% within error.

A dataset validation campaign for the new nTuples is completed where each BDT variable distribution is investigated along with several variables relevant to the analysis. This validation is performed by comparing all analysis variable distributions of the new nTuples to those in the old nTuples. This validation step only concerns similar reconstruction definitions and is required to ensure that subsequent comparisons with the new variable constructions accurately reflect changes in the reconstruction procedures. Several comparisons are selected from the new nTuples validation study: B_{iso}, the number of tracks in the B_{iso} cone (ΔR), $\text{DOCA}_{\text{xtrk}}$, and $N_{\text{xtrk}}^{\text{close}}$; the compar-

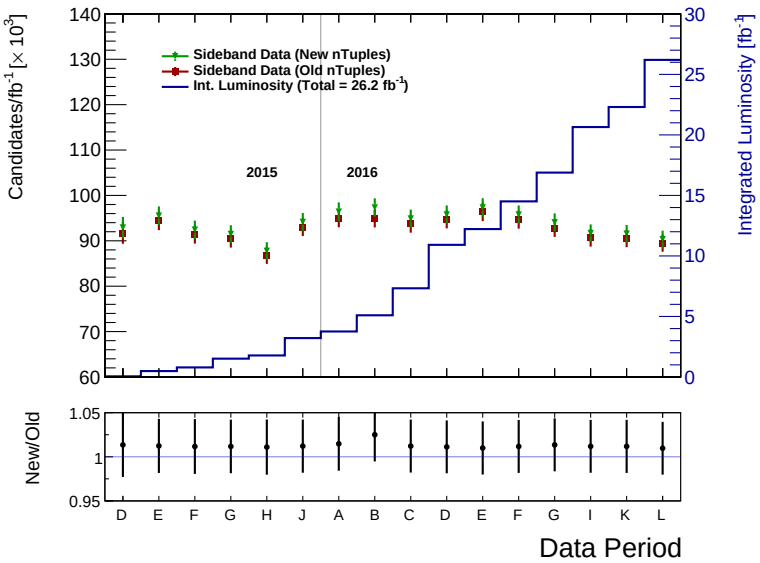


Figure 2.42: The sideband yield (of candidates) per data-taking period in the 2015 and 2016 data-taking years. The luminosity is overlaid and is reported with the axis on the right.

ison distributions are shown in Figure 2.43. The new and old nTuple distributions are overlapping in each case for the full range of the distribution. The differences are less than 1% in any given bin, as can be seen in the ratio of the new to old distributions in the bottom panel of Figure 2.43. Some differences may be expected due to the change in yield and the expected resulting statistical fluctuations.

As no major differences between the new and old nTuples (for the old variable constructions) have been found, the new isolation variable constructions can now be compared to the previous constructions: **As in 2015-2016** in the new nTuples and **Run 1** in the Run 1 datasets. These include variable distribution and ROC comparisons as well as a comparison of the signal and background separation power values. These two studies are performed because they are good indicators of how the variables will perform in the BDT, but final construction selection is subsequently made using comparisons of newly trained BDTs.

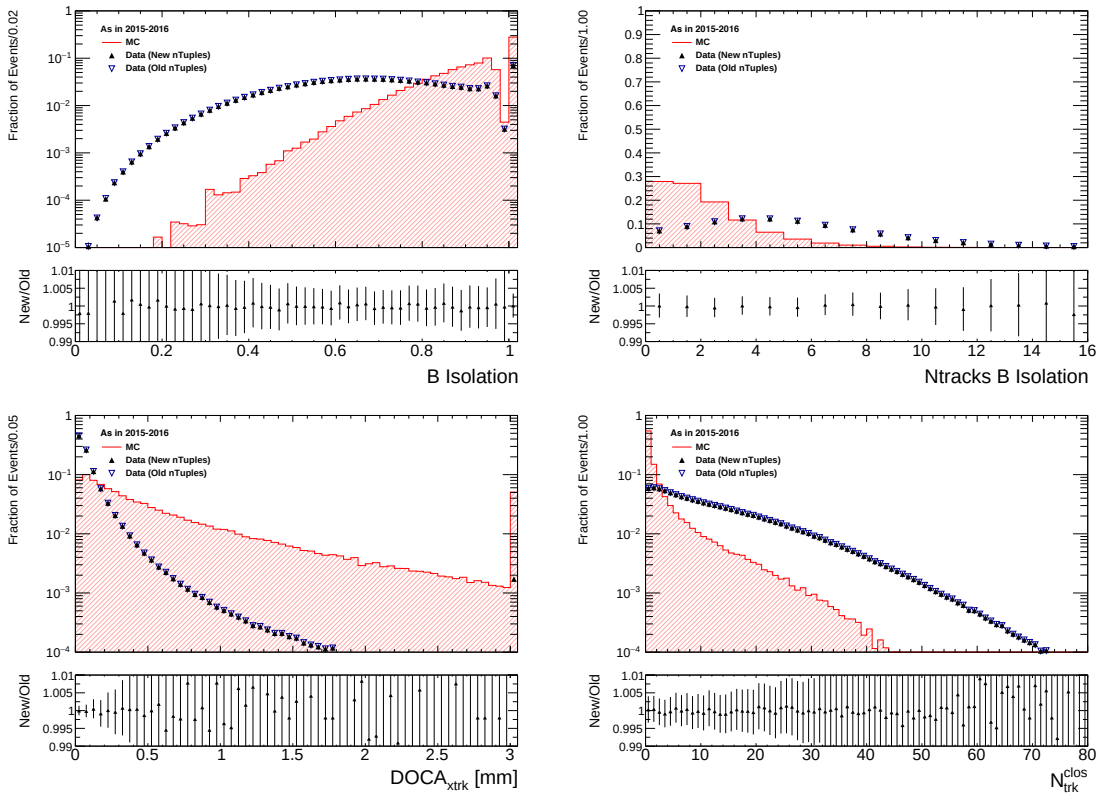


Figure 2.43: Subset of the variable distribution visualizations from the validation study of the re-processed 2015-2016 sideband dataset (new nTuples) compared to the original 2015-2016 sideband dataset (old nTuples). The ratio of distributions in the new and old nTuples is shown in the bottom panels. The ratio axis is magnified to reveal that the new and old nTuples are identical within error. The Monte Carlo distributions are also shown in the main panels as a subsidiary comparison, demonstrating the difference between signal and background.

The ROC curves and ROC acceptance plots for the B_{iso} variable constructions are shown in Figure 2.44. These figures are analogous to the ROCs shown in the previous section - but now include much higher statistics, and therefore are a stronger indicator of expected BDT performance. Here it is seen that the **Custom TVA** construction has the largest reach of all constructions and **Loose TVA** shows a slight improvement over **Custom TVA** in terms of background rejection. Both **Loose TVA** and **Custom TVA** appear to outperform **As in Run 1** as well as the **Run 1** and **As**

in 2015-2016 constructions. The BDT will take many input variables alongside B_{iso}, so it is possible that the BDT will prefer any of the three new constructions as they may provide additional information when combined with the $\text{DOCA}_{\text{xtrk}}$ and $N_{\text{xtrk}}^{\text{close}}$ variables.

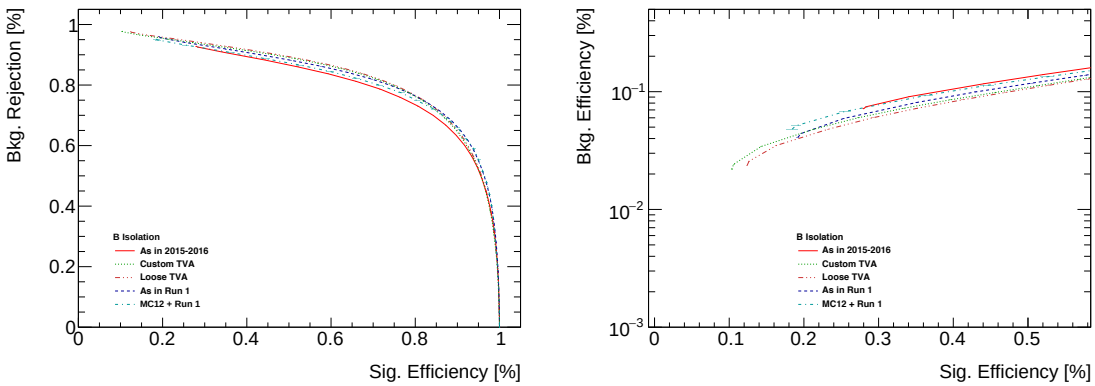


Figure 2.44: (Left) The full ROC curve and (right) the magnified ROC acceptance for the **Custom TVA**, **Loose TVA**, **As in Run 1**, **As in 2015-2016**, and **Run 1** B_{iso} variable constructions.

Similar comparisons for the corresponding muon isolation variables are investigated. The muon isolation variables contain information similar to that of B_{iso}, but it is possible that the BDT has a preference for the individual muon isolation over B_{iso}. The positively (negatively) charged muon isolation variable in a candidate event is computed analogously to B_{iso} (Equation 2.3): replacing p_{T}^{B} with $p_{\text{T}}^{\mu^+}$ ($p_{\text{T}}^{\mu^-}$). The construction criteria described for B_{iso} in the previous section apply also to the muon isolation variables. The new constructions are used for ROC acceptance comparisons for the positive and negative muon isolation variables in Figure 2.45. As is the case for B_{iso}, **Loose TVA** and **Custom TVA** outperform the other constructions. The difference between the **Loose TVA** and the **As in 2015-2016** may be larger for each muon isolation variable separately, but as the BDT should take both muon isolation variables as input in place of B_{iso} it is not immediately clear how the performance will be impacted.

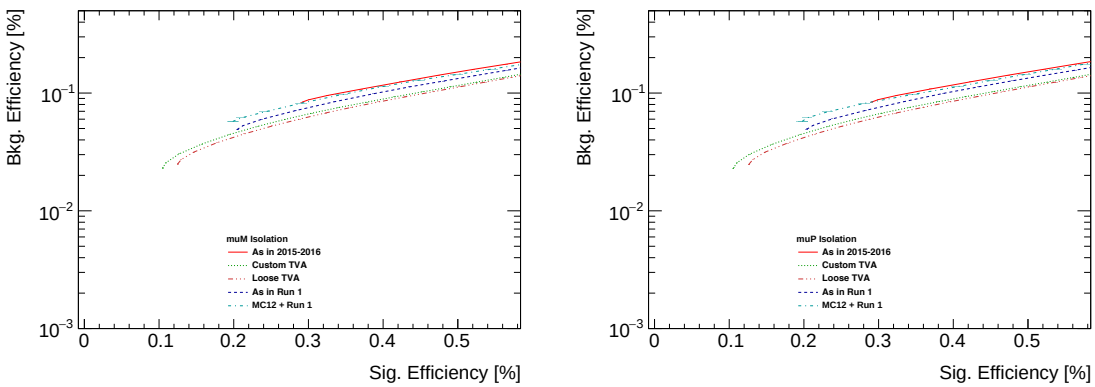


Figure 2.45: The magnified ROC acceptance curves for the **Custom TVA**, **Loose TVA**, **As in Run 1**, **As in 2015-2016**, and **Run 1** (left) negative muon and (right) positive muon isolation variable constructions.

The $\text{DOCA}_{\text{xtrk}}$ ROC curve and magnified ROC acceptance comparisons are shown in Figure 2.46. As was the case in the previous study of the $\text{DOCA}_{\text{xtrk}}$ variables, the **Run 1** construction in the Run 1 dataset still outperforms the new constructions in the new nTuples. As mentioned before, this is likely due to the change in the initial p_{T} cut on the tracks included in the computation (an irreversible change in the construction between Run 1 and Run 2).

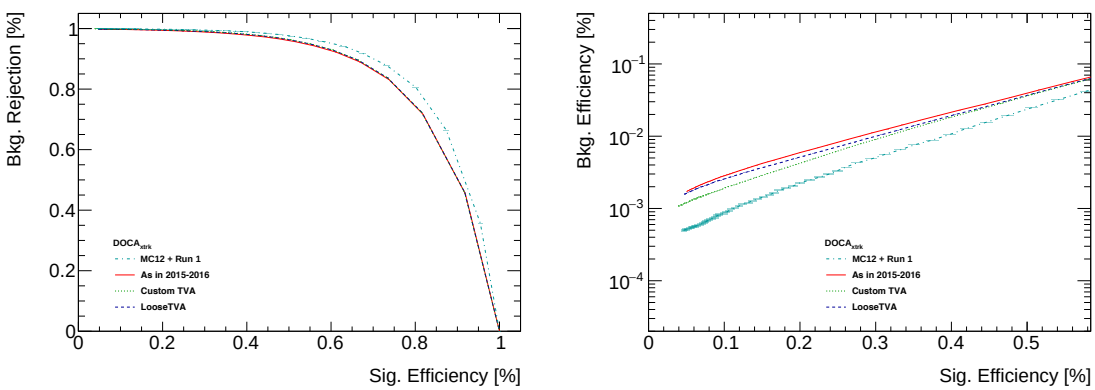


Figure 2.46: (Left) The full ROC curve and (right) the magnified ROC acceptance for the **Custom TVA**, **Loose TVA**, **As in 2015-2016**, and **Run 1** $\text{DOCA}_{\text{xtrk}}$ constructions.

The $N_{\text{xtrk}}^{\text{close}}$ ROC curve and magnified ROC acceptance comparisons are shown in Figure 2.47. With higher statistics it is still evident that the **Run 1** construction has a larger reach than the **Custom TVA** and **Loose TVA**, although the new constructions appear to have superior background rejection power. Both **Custom TVA** and **Loose TVA** seem to far outperform the **As in 2015-2016** construction.

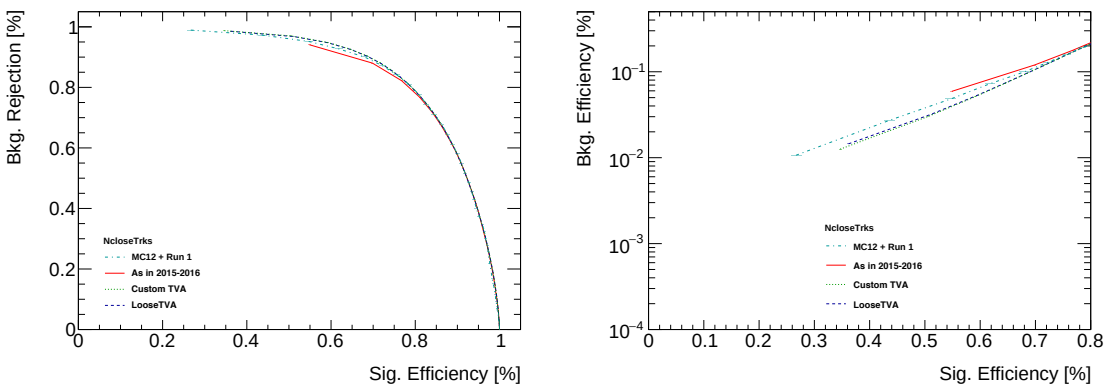


Figure 2.47: (Left) The full ROC curve and (right) the magnified ROC acceptance for the **Custom TVA**, **Loose TVA**, **As in 2015-2016**, and **Run 1** $N_{\text{xtrk}}^{\text{close}}$ variable constructions.

The separation power (as defined in Equation 2.2) of the BDT variables in the re-processed 2015-2016 dataset is computed and compared to the previous dataset separation powers. In Figure 2.48, the separation power of each analysis variable in the new nTuples is compared to the separation power of the 2015-2016 analysis variables. As expected, most variables have nearly identical separation power - the exception being the newly reconstructed isolation variables which are compared here with the previous construction definitions. There are significant increases observed in B_{iso} and $N_{\text{xtrk}}^{\text{close}}$ and a modest increase observed in $\text{DOCA}_{\text{xtrk}}$.

Figure 2.49 shows the comparison of the separation power in the new nTuples compared to the Run 1 datasets. Inclusion of the IBL layer in Run 2 is responsible for the increase in separation power seen in many of the analysis variables when

compared to Run 1. The definitions of the isolation variables in the 2015-2016 analysis resulted in degradation of the separation power of these variables. With the improved definitions of these variables the separation power is not only recovered but surpassed when compared to the Run 1 separation power. Improved separation power is observed in each of the three isolation variables. The significant increase observed in the $\mathrm{DOCA}_{\mathrm{xtrk}}$ variable is due to inclusion of $\mathrm{DOCA}_{\mathrm{xtrk}}$ values greater than three. Equivalent to the discussion on this change presented earlier in this chapter, some primary vertices do not register any nearby tracks (because they are highly isolated) and no $\mathrm{DOCA}_{\mathrm{xtrk}}$ value is recorded. In these instances the $\mathrm{DOCA}_{\mathrm{xtrk}}$ value is set equal to three (along with any $\mathrm{DOCA}_{\mathrm{xtrk}}$ value computed to be greater than three).

Having now investigated the individual variable ROC performances of the various isolation variables it is apparent that any combination of the new variable constructions for B_{iso}, $\mathrm{DOCA}_{\mathrm{xtrk}}$, and $N_{\mathrm{xtrk}}^{\mathrm{close}}$ will lead to better BDT performance than was observed in the 2015-2016 analysis. With the improvements seen in the B_{iso} con-

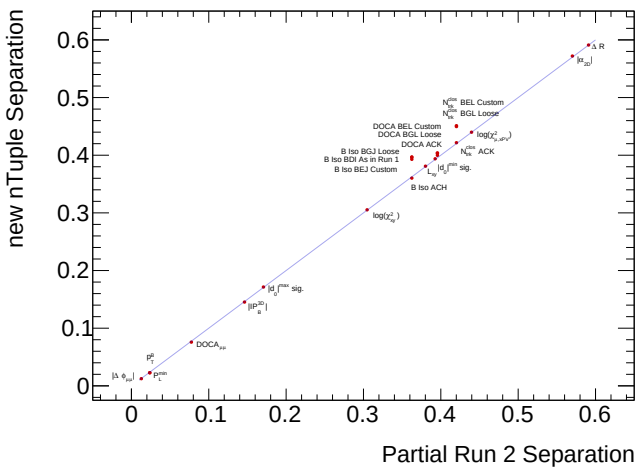


Figure 2.48: The separation power of the analysis variables in the new Run 2 datasets is compared to the separation power in the old Run 2 datasets. Use of the term separation in the axis label implies separation power.

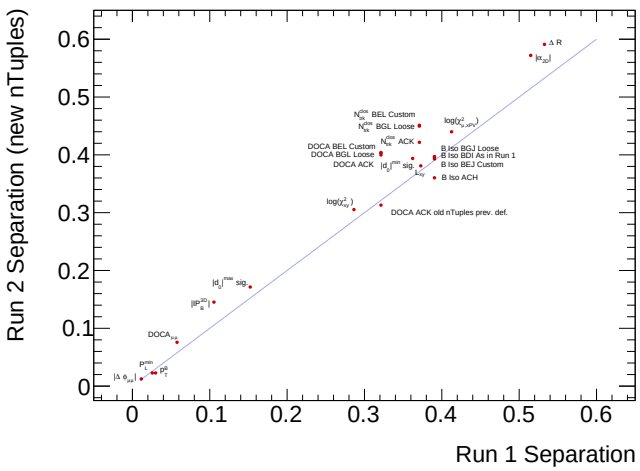


Figure 2.49: The separation power of the analysis variables in the new Run 2 datasets is compared to the separation power in the Run 1 datasets. Use of the term separation in the axis label implies separation power.

struction, comparable performance with the Run 1 BDT (applied to Run 1 data) may also be observed. Similar behaviors for B_{iso} and the individual muon (positive and negative) isolation variables have been observed, and a replacement of B_{iso} with the muon variables will likely produce similar results during BDT training.

2.15.4 Improvements in BDT Performance

A search for the optimal input variables to the BDT is performed, by investigating the impact on the BDT performance of the new variable constructions described in the previous section. The same training, testing and evaluation procedures described previously for the analysis of the 2015-2016 dataset are implemented. Several variations of the BDT procedures are performed using different input variables. Nominally, the variables described in Table 2.2 are used for input. The three variables in category (c) of the table (B_{iso}, $\text{DOCA}_{\text{xtrk}}$, $N_{\text{xtrk}}^{\text{close}}$) are exchanged with the candidate variable constructions.

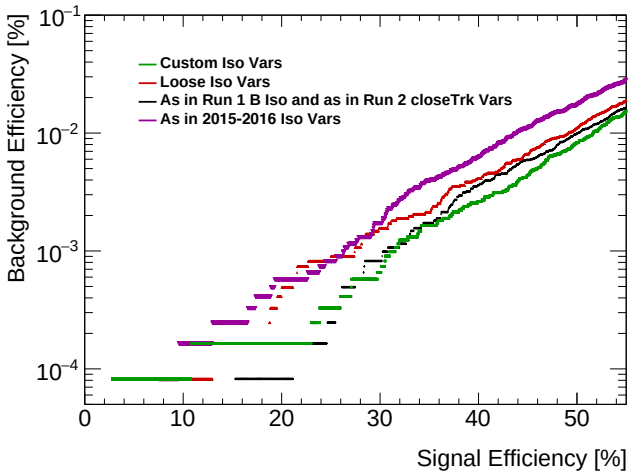


Figure 2.50: ROC comparison of four BDTs, each trained with 15 input variables: 12 nominal analysis variables and a unique set of three isolation variables. The BDTs compared here are selected based on the consistency in the definitions of the three isolation variables.

A comparison of the ROC performance of four BDTs in the evaluation dataset is shown in Figure 2.50. Each BDT in this figure is trained with a different set of isolation variables - selected based on the consistency in the definitions of the three variables. One BDT is trained using the 12 nominal input variables in categories (a), (b) and (d) in Table 2.2 and the three **Custom TVA** isolation variables, a second with the 12 nominal input variables and the three **Loose TVA** isolation variables, and a third with the 12 nominal input variables and **As in Run 1** B_{iso} and the **As in 2015-2016** close track variables ($N_{\text{xtrk}}^{\text{close}}$ and $\text{DOCA}_{\text{xtrk}}$). For a comparison to the previous definitions a BDT is trained with **As in 2015-2016** isolation variables. Figure 2.50 shows that using the **Custom TVA** constructions leads to the best performance for a majority of the acceptance curve. Clear improvement is obtained over the BDT trained with the **As in 2015-2016** constructions. As the curves approach lower signal efficiency, lower statistics in the background sample are available for the construction of the ROC plot. This leads to the apparent stepped behavior. In the larger statistical section of the curve, there is clear preference for the **Custom TVA** BDT. For this

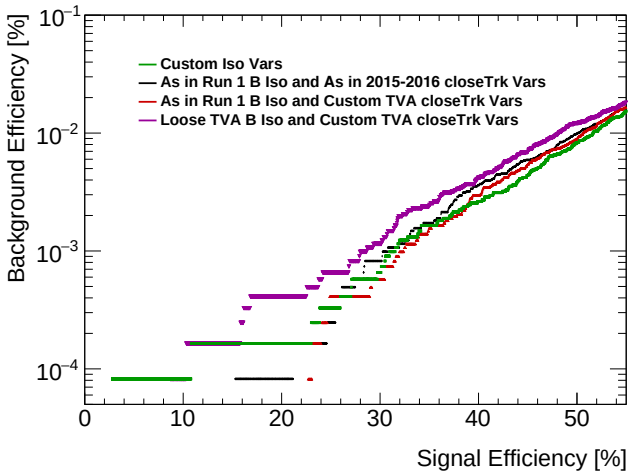


Figure 2.51: ROC comparison of four BDTs, each trained with 15 input variables: 12 nominal analysis variables and a unique set of three isolation variables. Two of the BDTs compared here are selected based on the highest separation power of the three variables, the other two are the best performing BDTs selected based on the consistency in the definitions of the three isolation variables.

reason, the **Custom TVA** constructions are selected as the most suitable isolation constructions.

A cross-check to compare the **Custom TVA** BDT to BDTs trained with non-matching variable constructions (i.e. not all of B_{iso}, $\text{DOCA}_{\text{xtrk}}$, and $N_{\text{xtrk}}^{\text{close}}$ trained with the **Custom TVA** selection criteria or **Loose TVA**) is performed. The combination of the isolation variable definitions with the largest separation power (see Figure 2.49) is used in a BDT. These are **Custom TVA** for the close track variables and **Loose TVA** for B_{iso}. The comparison of the ROC acceptance curves is shown in Figure 2.51. Also shown in the figure is a BDT trained with **Custom TVA** for the close track variables and **As in Run 1** construction for B_{iso}. The second best-performing BDT from the Figures 2.50, **As in Run 1** B_{iso} and **As in Run 2015-2016** close track variables, is included in the comparison for additional context. In the higher statistics section of the ROC acceptance plot, the **Custom TVA** definitions lead to the best-performing BDT. In the center of the plot there is significant over-

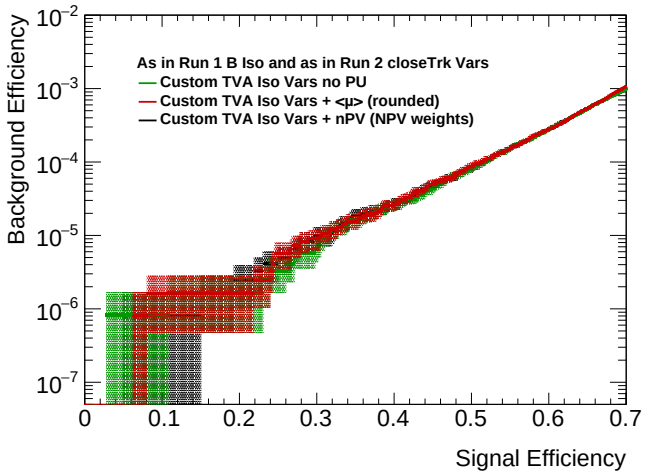


Figure 2.52: ROC acceptance curves for BDTs trained with and without pileup used as an input variable. The BDTs are trained with **Custom TVA** isolation variables and the 12 other nominal input variables. One includes $\langle\mu\rangle$ as an additional input variable and one includes nPV.

lap with the BDT trained with **Custom TVA** close track variables and **As in Run 1** construction for B_{iso}. The lowest signal efficiency section of the plot is, once again, not used for performance analysis due to low statistics. For these reasons, the BDT trained with the three **Custom TVA** isolation variable constructions is selected as the best-performing BDT.

Investigations seeking further improvements to the BDT by including a pileup variable as a BDT input are undertaken. A BDT trained with **Custom TVA** isolation variables and 12 other nominal input variables is compared to two BDTs trained with identical inputs and one additional input variable. In one case the additional input is $\langle\mu\rangle$ (the mean number of proton-proton interactions) and in the other it is nPV (the number of reconstructed primary vertices in the candidate event). The comparison of the ROC performances of the BDT output variables is shown in Figure 2.52. The ROC error bands are included [129]. As is evident from the significant overlap of the ROCs over the entire range of interest, the pileup does not impact the ROC

performance.

Further investigation of the impact of including a pileup variable as an input to the BDT training is performed. The hypothesis is that by including a pileup variable in the training, the BDT will be more robust against the pileup. The studies focus on the effects of BDT selections on the isolation variable B_{iso}. The study uses the variable efficiencies after the BDT selections for the pileup variable μ. Variable efficiency is computed by imposing a restriction on a given variable with the BDT output at 54% signal efficiency, 36% signal efficiency or 18% signal efficiency and dividing the resulting variable histogram by the histogram without any restrictions. The BDT restrictions for this study are inclusive (everything greater than the respective BDT value is included in the efficiency calculation).

The impacts of the BDT selections on the efficiencies are compared in each plot in Figure 2.53 for two independently trained BDTs. One BDT is trained including μ as an input during training and the other does not include any pileup variable. Both BDTs are trained with the nominal 15 discriminating variables including the three **Custom TVA** isolation variable constructions.

Figure 2.53 indicates that including a pileup variable in the training does have an impact on the pileup, an effect that begins around $\langle\mu\rangle = 25$. To investigate further, the efficiencies of B_{iso} for the selections with the two BDTs are compared, with and without a selection on $\langle\mu\rangle > 25$. Figure 2.54 (left) shows the comparison of the B_{iso} efficiencies for the 18% signal efficiency BDT selections. In Figure 2.54 (right), the selection of $\langle\mu\rangle > 25$ shows that the BDT trained with the pileup variable is less impacted by a change in pileup than the BDT trained without a pileup variable. This study may prove important for future analyses at the HL-LHC where the pileup is expected to be much higher. The effect is small enough during Run 2 that the pileup variables will not be used in the BDT training.

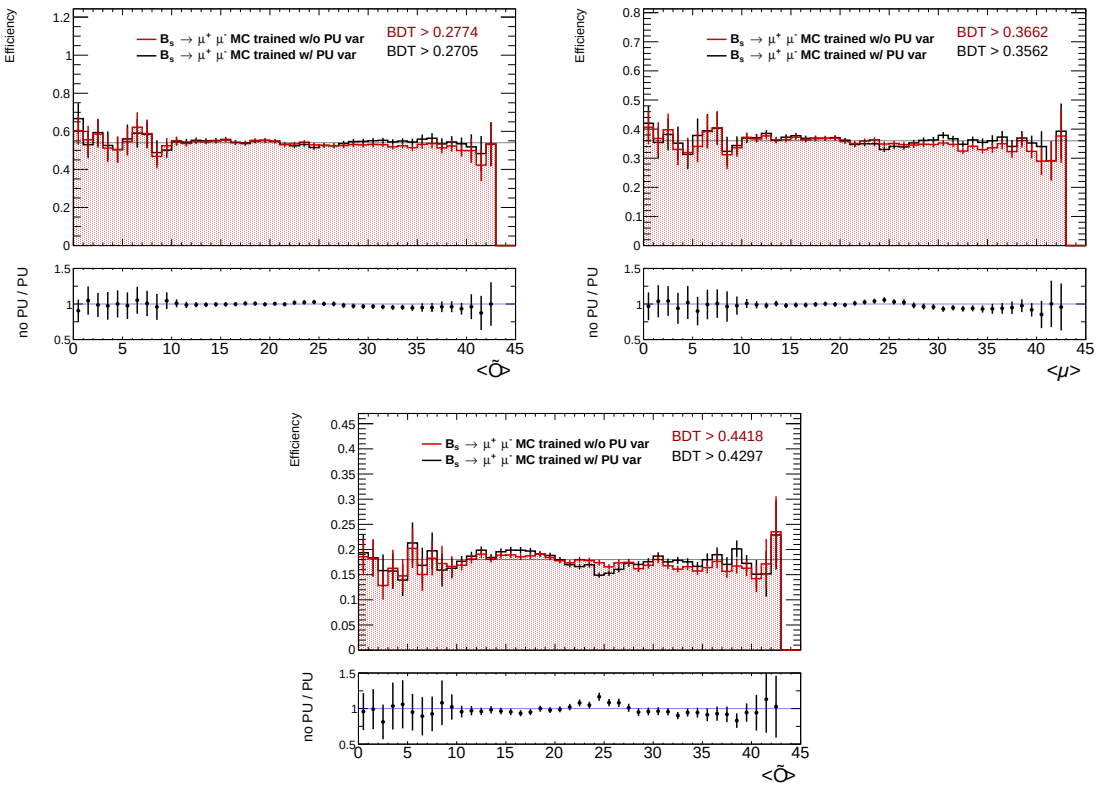


Figure 2.53: Efficiencies for the pileup variable μ for three BDT selections: (top left) 54% signal efficiency, (top right) 36% signal efficiency or (bottom) 18% signal efficiency in the signal MC sample. A horizontal line indicates 54%, 36% and 18% signal efficiency in each plot, respectively.

Preliminary results with the fitting procedures indicate that the improved BDT training will lead to major improvements in the yield extraction. In the 2015+2016 data, using the original BDT, the yields are:

$$N_{\mathrm{s}} = 81 \pm 21$$

$$N_{\mathrm{d}} = -11 \pm 19.$$

Implementing the improved BDT, the preliminary expected results with the same

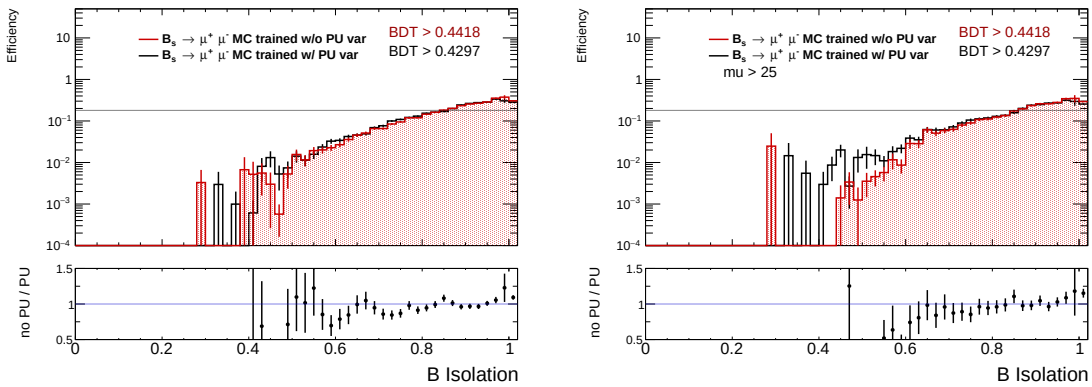


Figure 2.54: Efficiencies for B_{iso} with BDT selection at 18% signal efficiency. The efficiencies are computed (left) before and (right) after a selection of $\langle\mu\rangle > 25$ is applied. Horizontal lines in the upper plots indicate 18% signal efficiency.

dataset are:

$$N_{\text{s}} = 75 \pm 18$$

$$N_{\text{d}} = -9 \pm 16.$$

Due to the improved combinatoric background suppression, the uncertainty in the yields is lower. This improvement in the statistical uncertainty is roughly equivalent to a 36% increase in signal events.

Chapter 3

Analysis of Leakage Current in ATLAS Pixel Detector

3.1 Introduction to the Pixel Detector Leakage Current Analysis

The radiation fields in which the ATLAS Pixel Detector [1] has been immersed in LHC Run 2 have been unprecedented for a full scale particle physics detector. In order to continue to collect of high quality data for analyses such as the $B^0_{(s)} \to \mu^+\mu^-$ analysis, the impact of these radiation fields needs to be understood. The $B^0_{(s)} \to \mu^+\mu^-$ analysis will greatly benefit from the collection of even more data, and this is anticipated in the coming decade. The radiation fields expected during Run 3 of the Large Hadron Collider (LHC) and on into the High Luminosity-LHC (HL-LHC) era will reach even higher levels than those yet observed [32]. Measurement of the radiation damage is needed to ensure the safe operation of the detectors needed for producing results like the ones achieved in the previous chapter; measurement of

the leakage current in the silicon sensors provides access to this. Leakage current, or reverse current, is the current through the junction, due to thermally generated minority carriers (generation current), when reverse bias is applied [64]. Electrons and holes drift in the reverse biased depletion zone under the influence of the electric field giving rise to the leakage current. There can also be a diffusion component coming from charge generated in the neutral silicon and diffusing into the space charge (depletion) region but this current is minimized in the fabrication processing by taking special care to keep the crystal clean. Under normal operating conditions, a silicon particle detector is fully depleted and the measured leakage current is the generation current. Measurements of leakage current during the present era can be used to optimize the operating conditions in the future. Leakage current in ATLAS Pixel Detector silicon modules from February 2011 of LHC Run 1 through the end of LHC Run 2 in November 2018 is measured and compared to predictions made with the Hamburg Model [128, 144, 145] and fluence simulations created with the FLUKA framework [41]. A description of the leakage current sector of the Hamburg Model is provided presently, and a description of the depletion voltage sector of the model is presented in Section 5.4.

A linear relationship between particle fluence and leakage current applies to silicon sensors. The effective fluence, Φ_{eq}, is the number of 1 MeV neutrons applied to a sensor of surface area 1 cm^2 that cause damage equivalent to that of all particles that went through the sensor. The linear relationship between fluence and ΔI, the difference in leakage current at fluence Φ_{eq} relative to the value before irradiation, is given as

$$\Delta I = \alpha \cdot \Phi_{\text{eq}} \cdot V \tag{3.1}$$

where V is the depleted volume of the silicon sensor and α is the current-related damage coefficient [128]. The leakage current data and predictions are normalized to the same temperature for direct comparison (the normalization is discussed in

Section 3.3). The normalization is made using the known leakage current dependence on temperature and the effective silicon band gap energy, E_{eff} [56]. The goal of this measurement is to use the leakage current data to measure sensor damage resulting from unprecedented radiation fluence and project the lifetime of the Pixel Detector.

The magnitude of the reverse bias voltage applied to sensors in the Pixel Detector is set based on simulation results and sensor voltage scans; the bias voltage is expected to produce full depletion of the sensors. The modules selected for this analysis sample the full range of r, ϕ, and z of the Pixel Detector. The positions of the selected modules can be seen in Figures 3.1 and 3.2. Some data are not accessible due to power outages and other cases of system unavailability.

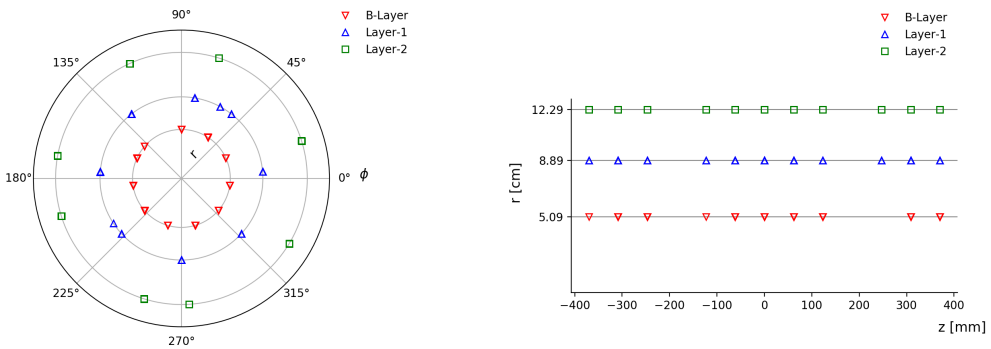


Figure 3.1: The positions of monitored modules in ϕ and r on the barrel layers. Between 4 and 10 modules are monitored at each location indicated in the figures.

Detailed simulations of particle production (Pythia8) [166] and particle transport (FLUKA) [42, 81], together with damage factors [177], are used to predict the accumulated fluence. An alternative transport model (provided in Geant4) [4] using the detailed geometry of the ATLAS detector is also investigated. The fluence is measured by performing a fit to the leakage current data: the Hamburg Model is used to predict the leakage current evolution with luminosity up to an overall scale factor that is fit to the leakage current data.

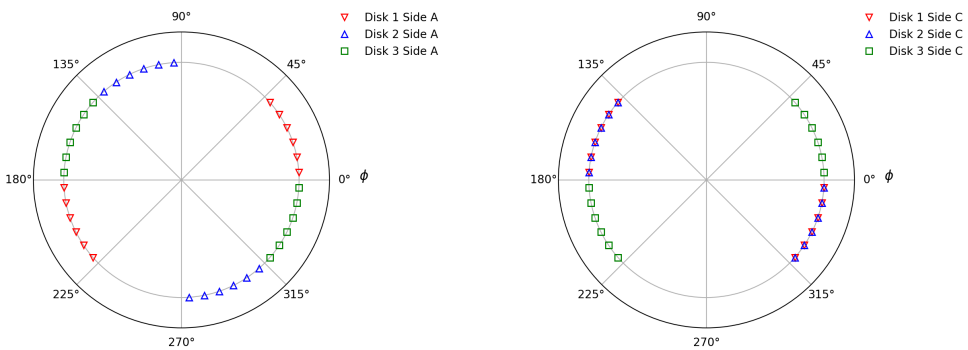


Figure 3.2: The positions of monitored modules in ϕ on the disks side A (left) and side C (right). The modules on each disk are centered at a radial distance: 119.2 mm.

A description of the subsystems used to measure the leakage current in the silicon sensors is in Section 3.2. Details of how the measurement was performed are in Section 3.3. Details of the method used to calculate the luminosity for this study are discussed in Section 3.4. The Hamburg Model leakage current predictions and FLUKA simulation fluences are described in Section 3.5. Contributions to the uncertainty on the measurements of leakage current are discussed in Section 3.6, and the results of the study are presented in Section 3.7. A brief discussion on the sensitivity to the choice of E_{eff} is presented in Section 3.8. Section 3.10 presents a comparison of the predicted and measured fluences. A lifetime projection of the B-Layer is in Section 3.11.

3.2 Measurement Subsystems

Leakage current data are collected using two independent subsystems, the per-module high voltage patch panel subsystem (HVPP4) and the multi-module power supply subsystem used to confirm and augment the HVPP4 measurement. The HVPP4 serves as a fan-out point for the bias voltages delivered to the Pixel mod-

ules from the Iseg high voltage power supplies [107] and monitors leakage current at the Pixel module granularity level by a Current Monitoring Board system. Further details on the HVPP4 system can be found in Reference [8].

During Run 1, each power supply channel was used to power and read out 6 or 7 modules in parallel. During the long shutdown of the LHC between 2013 and 2015, more power supply units were installed for use in the Pixel Detector. During LHC Run 2, each power supply channel supplied one or two modules. The sum of the leakage current values is measured for the modules supplied by a common power supply unit. The precision of measurements of the leakage current read with the power supply units is improved during LHC Run 2. The raw leakage current data measured by both the HVPP4 system and the power supplies are stored in the COOL database [174].

3.3 Details of the Measurement

The leakage current data are collected from the COOL database and quality cuts are applied. Leakage current data are excluded for modules during periods when their bias voltage was not applied. The few non-working modules with bias voltage not applied are excluded from the study. Data collected within one minute of high voltage turn-on are also excluded. Analysis of the leakage current data is restricted to times when the LHC has declared the proton beams to be stable. Luminosity recorded outside of these periods is included in this study, see Section 3.4.

Leakage current depends on the temperature of the sensor [145, 170]. The following equation converts the leakage current of a sensor measured at temperature T to that at a reference temperature T_{R}:

$$I(T_{\mathrm{R}}) = I(T) \times R(T), \tag{3.2}$$

where

$$R(T) = (T_{\mathrm{R}}/T)^2 \cdot \exp\left[-\frac{E_{\mathrm{eff}}}{2k_{\mathrm{B}}}(1/T_{\mathrm{R}} - 1/T)\right]. \tag{3.3}$$

E_{eff} is the effective silicon band gap energy after irradiation, also called activation energy, and k_{B} is the Boltzmann constant. T and T_R must be expressed in Kelvin. The value of 1.21 eV has been used for E_{eff} following a study on how this value changes under different radiation conditions [56]. This can be compared to the nominal silicon band gap energy of 1.12 eV before irradiation. It is worth noting that the temperature normalization is dependent on the choice of E_{eff}. A nominal reference temperature $T_{\mathrm{R}} = 0$ °C has been used throughout this study. The temperature of the sensors is held at about -12 °C during operation and 18 °C during times when the detector is turned off.

The temperature of each monitored module is read from the DCS database. Equation 3.2 is applied to the leakage current data on a per module basis.

Luminosity data are collected for every luminosity block, corresponding to approximately one minute of data collection. Luminosity is proportional to fluence and is thus chosen for comparison with the leakage current. The temperature-corrected leakage current is sampled once per luminosity block.

Leakage currents are measured for each module individually using the HVPP4 subsystem in LHC Run 1 and Run 2 and for pairs of modules using the power supply subsystem in LHC Run 2. These measurements are subsequently averaged for each barrel layer and each disk. Averaged binned measurements are also examined for ϕ and z dependence for a more refined investigation of the spatial dependence of the radiation damage.

3.4 Details of Luminosity Accumulation

The luminosity is determined by a set of dedicated bunch-by-bunch luminosity detectors [15] that are calibrated using the van der Meer method [175]. The absolute luminosity used in this study accounts for luminosities accumulated during times when the ATLAS detector is not operating, because all particle fluence received by the silicon sensors will impact the leakage current. Luminosities outside of the LHC stable beams, ATLAS ready, and ATLAS physics declarations are included. The values used for this study surpass the quantities reported as official ATLAS luminosity usable for physics [9]. The total delivered luminosity in Run 2 used throughout this analysis is shown in Figure 3.3.

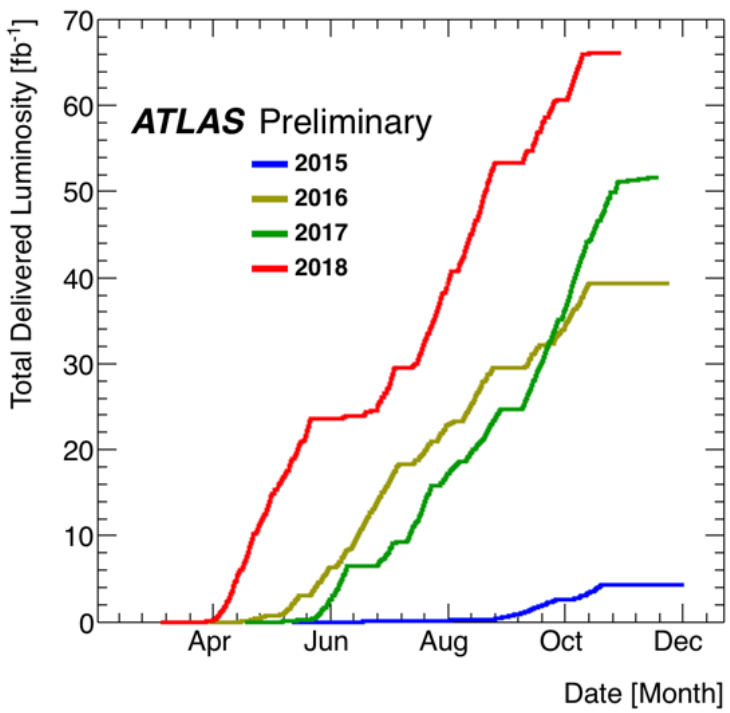


Figure 3.3: Luminosity accumulated by ATLAS during LHC Run 2.

3.5 Hamburg Model Predictions

The complex radiation fields in the ATLAS detector are simulated using the particle transport code FLUKA [42, 81]. The Inner Detector and Calorimeter are modeled with high accuracy in the ATLAS FLUKA simulation framework [41]. This is important for modeling high energy hadron cascades in the material that lead to increased particle fluences in the Inner Detector, especially neutrons. Inelastic proton-proton interactions generated by Pythia8 [166] using the MSTW2008LO parton distribution functions [138] and the A2 tune [31] are used for input to the FLUKA simulation. All of the products of the proton-proton interactions are simulated with FLUKA. The particle and energy spectra are folded with silicon damage factors to compute the 1 MeV neutron equivalent damage from the RD50 database [87, 106, 114, 169]. The tabulated weights cover neutrons, protons, charged pions and electrons. For charged kaons the pion weights are used, while for anti-neutrons, anti-protons, baryons and ions the proton weights are used and positrons are treated like electrons.

The dominant radiation damage type is assumed to be displacement defects in the bulk of the Pixel sensor, initiated by hadronic species and caused by non-ionizing energy loss (NIEL). A compilation of damage factors due to NIEL can be found in [177]. Surface ionization is neglected in this treatment. Charged pions originating directly from the proton-proton collisions are the largest contributor to the bulk damage for the radii covered by the Pixel Detector. Albedo neutrons originating in the outer ATLAS detectors also contribute. The resulting displacement defects increase the reverse leakage current, degrade the charge collection efficiency, and change the effective doping concentration which directly determines the depletion voltage. Predictions of the 1 MeV neutron-equivalent (n_{eq}) fluences per cm^2 (Φ_{eq}) per fb^{-1} in the ATLAS FLUKA Inner Detector geometry are shown in Figure 3.4.

The values collected in Table 3.1 represent the highest fluence simulated by

FLUKA for each layer and disk. The barrel layer values correspond to the points with z-projection closest to the interaction point (closest to $z = 0$). The z-dependence of the fluence, which depends on the distance from the interaction point, is also accounted for in the simulation (see Figures 3.4 and 3.28 below). The fluence of charged particles produced at the primary collision goes as $1/r^2$. The fluence of neutrons depends on the detector geometry as these are primarily due to backscattering from the calorimeter. The simulation is used for conversion between luminosity and fluence.

The fluence Φ_{eq} accumulated by the ATLAS Pixel Detector, and measured in units of cm^{-2}, is expected to be proportional to integrated luminosity $\int \mathcal{L} dt$, measured in fb^{-1}. By the end of the proton-proton collision runs in 2018, the B-Layer was predicted, by PYTHIA8 + FLUKA, to have received an integrated fluence of $\Phi_{\text{eq}} = 5.27 \times 10^{14}\ n_{\text{eq}}\ /\text{cm}^2$. The B-Layer was designed to receive a total integrated fluence of about $1 \times 10^{15}\ n_{\text{eq}}\ /\text{cm}^2$ over the span of its lifetime [33]. The evolution of fluence accumulation over the lifetime of the detectors is shown in Figure 3.5.

The FLUKA simulated fluence is used as an input to the Hamburg Model [145] to predict the change in leakage current, ΔI_{leak}, after irradiation:

$$\Delta I = (\Phi_{\text{eq}}/L_{\text{int}}) \times V \cdot \sum_{i=1}^{n} L_{\text{int},i} \cdot \left[\alpha_{\text{I}} \exp\left(-\sum_{j=i}^{n} \frac{t_j}{\tau(T_j)} \right) + \alpha_0^* - \beta \log\left(\sum_{j=i}^{n} \frac{\Theta(T_j) \cdot t_j}{t_0} \right) \right]. \tag{3.4}$$

Here, $L_{\text{int},i}$ is the integrated luminosity, t_i is the time, and T_i is the temperature in period i. The first sum is over all time periods and the two sums inside the exponential and logarithmic functions are over the time between the irradiation in time period i and the time of the measurement. The other symbols in Equation (3.4) are $t_0 = 1$ min, $V =$ depleted volume[1] (in cm^3), $\alpha_{\text{I}} = (1.23 \pm 0.06) \times 10^{-17}$ A/cm, τ

[1]The fully depleted volume of the sensor module is $V = 0.25\ \text{cm}^3$.

C.O.M. Energy	*B*-Layer	Layer-1	Layer-2	Disk-1	Disk-2	Disk-3
7 TeV	20.53	8.69	5.39	5.52	5.25	5.13
8 TeV	21.73	9.11	5.67	5.63	5.29	5.14
13 TeV	28.94	12.41	7.87	8.25	7.99	7.91

Table 3.1: Fluence values simulated using the ATLAS FLUKA simulation package for three center-of-mass (C.O.M.) energies. The units of the values in the table are 10^{11} n_{eq} /cm^2 per fb^{-1}.

follows an Arrhenius equation $\tau^{-1} = (1.2^{+5.3}_{-1.0}) \times 10^{13}$ s$^{-1} \times e^{(-1.11 \pm 0.05)/k_{\text{B}}T}$ (where the units of $k_{\text{B}}T$ are eV), $\alpha_0^* = 7.07 \cdot 10^{-17}$ A/cm, and $\beta = (3.29 \pm 0.18) \times 10^{-18}$ A/cm. A small temperature dependence has been observed in the value of β [145]; for this analysis, the value at 21 °C is used - its lowest known value and the one closest to the operational temperature of the sensors in the detector. Equation 3.4 represents the Hamburg Model as presented in [145]; under different conditions different terms will dominate. The temperature scaling function $\Theta(T)$ is defined by

$$\Theta(T) = \exp\left[-\frac{E_{\text{I}}^*}{k_{\text{B}}}\left(\frac{1}{T} - \frac{1}{T_{\text{R}}}\right)\right], \tag{3.5}$$

where ($E_{\text{I}}^* = 1.30 \pm 0.14$) eV, k_{B} is the Boltzmann constant, and $T_{\text{R}} = 21$ °C. Once the simulation is complete, a temperature correction to the full simulation is made so that it may be compared to the leakage current data. The simulation is corrected from its initial temperature of 21 °C to 0 °C.

The implementation of the Hamburg Model can be found in Reference [13]; the treatment in this analysis is identical to the treatment in the ATLAS Radiation Modeling paper [20].

The luminosity-to-fluence conversion factor, $\Phi_{\text{eq}}/L_{\text{int}}$, in Equation 3.4 requires a scale factor to match the leakage current data. The scale factor is determined from the constant fit to the ratio of the leakage current data and the Hamburg Model

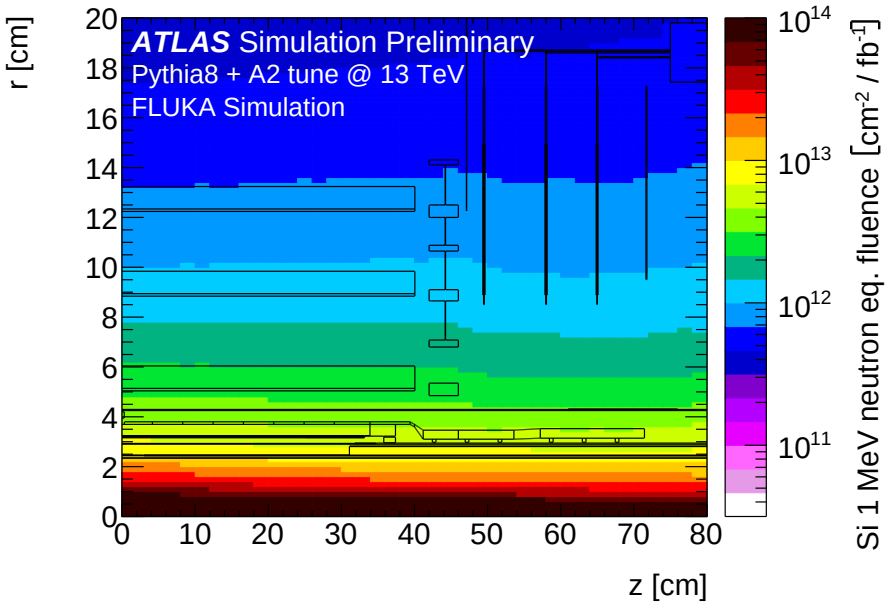


Figure 3.4: Simulated n_{eq} fluence shown as a function of the radial and longitudinal distance from the geometric center of the detector for a one-quarter slice through the ATLAS FLUKA geometry. This figure was originally published in [18].

prediction. Hamburg Model predictions are made in four bins along the z-axis for each barrel layer (a total of 12 predictions) and for each disk. Each prediction (12 for the barrel layers and 6 for the disks) is fit to the data with a scale factor. For each barrel layer, the average of the scaled predictions associated with the four bins along the z axis is compared to the average leakage current data in the same four bins.

3.6 Precision and Systematic Uncertainties

This section provides the elements that contribute to the uncertainty of the measurement of the leakage current, the Hamburg Model predictions, and the measurement of the fluence. The final uncertainty is calculated by adding all contributing

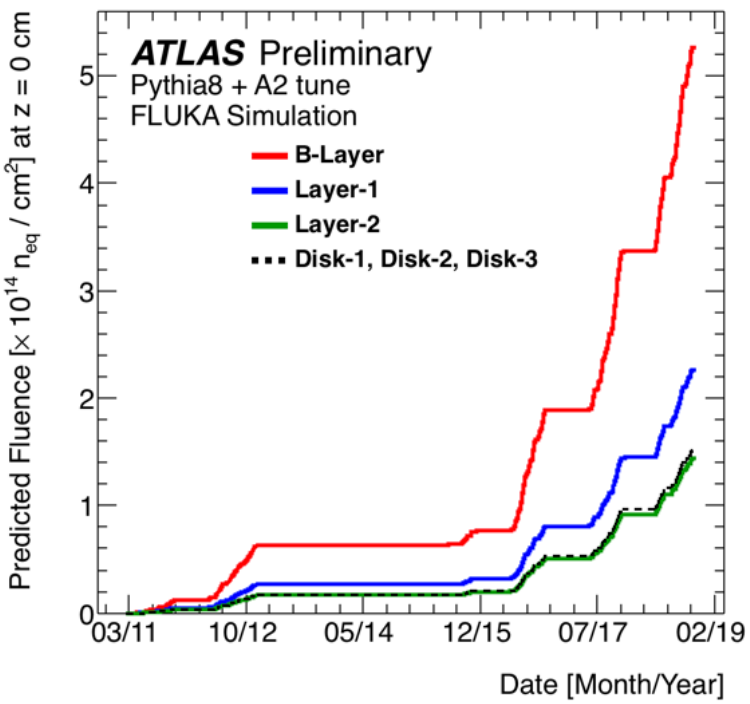


Figure 3.5: Applied fluence for the *B*-Layer, Layer-1, Layer-2, and the Disks, calculated by the FLUKA factors shown in Figure 3.4 and summarized in Table 3.1. PYTHIA8 is used for particle production, MSTW2008LO parton distribution functions [138] and the A2 tune [31] are used for input to the FLUKA simulation.

elements in quadrature. The precision on current measurements made with the HVPP4 current monitoring circuit contributes 12% uncertainty. The precision on current measurements made with the power supply units contributes 4% to the total measurement uncertainty [107]. The current measurements are made approximately once per minute and that interval contributes 0.5% uncertainty; this uncertainty is calculated by investigating the deviations in the data over ten minute intervals - a time interval over which the leakage current is not expected to change. The precision of the temperature measurements contributes 2.9% uncertainty; the temperature is also not expected to fluctuate over short time intervals and is thus calculated in the same way as the current uncertainty. Uncertainties due to possible difference

between the temperature of the point on the module at which the temperature is measured, and the point on the silicon sensor to which the temperature is attributed are found to be 10% through changes to the modeled leakage current when a difference in temperature of 1 °C is applied through Equation 3.2. The total uncertainty on the leakage current data collected with HVPP4 is determined by adding in quadrature the HVPP4 current monitoring circuit measurement uncertainty, the current measurement uncertainty, and each of the two temperature uncertainties; the HVPP4 data uncertainty is found to be 15.9%. The total uncertainty on the leakage current data collected with the dual-module power supply units is determined by adding in quadrature the power supply precision uncertainty, the current measurement uncertainty, and each of the two temperature uncertainties; the power supply data uncertainty is found to be 11.2%. The measurement uncertainties are shown in Table 3.2.

The uncertainty on the predicted leakage current is determined from the uncertainties on the inputs to the model. These are summarized in Table 3.3. The uncertainty on the scale factor fit is obtained from the constant fit to the ratio of the Hamburg Model prediction to the data. The scale factor fit is determined using the statistical uncertainties of Table 3.2.

The fluence predicted from the leakage current data and the Hamburg Model is investigated in Section 3.10. The statistical uncertainty on the fluence predictions made by Pythia8 + FLUKA is 1.0%. There are sources of uncertainty introduced to both the Hamburg Model and the predicted fluence through the silicon hardness factors [177] which are not taken into account in this analysis. The hardness factors [87, 106, 114, 169] used here are from the RD50 database, but all of these values are without uncertainty and many are based only on simulation. The uncertainty on the fluence extracted from the leakage current data and the Hamburg Model is summarized in Table 3.4.

The uncertainty on the luminosity does not contribute to uncertainty on the leakage current data but is included in the fluence measurement. The uncertainty in the combined 2015-2018 integrated luminosity is 2.5%. It is derived, following a method similar to that detailed in Reference [15], from calibrations of the luminosity scale using x-y beam-separation scans performed in August 2015, May 2016, and July 2017. These scans are equivalent to the van der Meer scans mentioned in Section 3.4.

	Hardware	Current Precision	Temperature Precision - Data	Temperature Offset - Data	Total
HVPP4	12.0%	0.5%	2.9%	10.0%	15.9%
Power Supply	4.0%	0.5%	2.9%	10.0%	11.2%

Table 3.2: Summary of the contributing and total measurement uncertainties. The current precision and temperature precision are the statistical uncertainties. The hardware and temperature offset uncertainties are the systematic uncertainties.

	Scale Factor Fit	Temperature Precision - Model	Temperature Offset - Model	Total
Scaled Hamburg Model	1.6%	2.9%	10.0%	10.5%

Table 3.3: Summary of the contributing and total uncertainties for the Hamburg Model. The temperature offset uncertainty does not apply during periods when the power and cooling of the detector are off. The scale factor fit is determined using the statistical uncertainties of Table 3.2.

3.7 Leakage Current Results

Measurements of leakage current in all three barrel layers from February 2011 (early in LHC operation) to November 2018 are shown in Figure 3.6. The B-Layer (red

	SFF	Hardware	Temperature Precision (Combined)	Temperature Offset (Combined)	Lumi.	Total
Extracted Fluence	1.6%	4.0%	2.9%	10.0%	2.5%	11.5%

Table 3.4: Summary of the contributing and total uncertainties for the combined model and data fluence measurement. The abbreviation SFF refers to the scale factor fit uncertainty and Lumi. refers to the luminosity uncertainty. The temperature offset uncertainty does not apply during periods when the power and cooling of the detector are off. The scale factor fit is determined using the statistical uncertainties of Table 3.2. The fluence measurement uses data from the power supply subsystem.

points) shows the highest leakage current consistently. Layer-1 (blue points) and Layer-2 (green points) have progressively lower levels. Measurements on each layer are averaged over the representative sample of modules in z and ϕ as is shown in Figures 3.1 and 3.2. The measurements are consistent with expected higher levels of radiation for sensors closer to the interaction point. The Hamburg Model predictions have been scaled to match the measured leakage current with a luminosity-to-fluence scale factor applied for each layer. The scale factors are determined in four z-binned regions for each layer; these can be found in Table 3.5. The average of the scaled Hamburg Model predictions in each is used to compare to the average leakage current data. After the application of the scale factors, the Hamburg Model predictions fit well to the data throughout the full period of the measurement. The leakage current data are normalized to 0 °C; the average module temperature is shown in the top panel. Leakage current data are shown for periods of operation when the high voltage is applied across the silicon sensor; the average module bias voltage is shown in the middle panel of Figure 3.6. Some dates corresponding to extended periods when the LHC beams were off, resulting in annealing of the sensors, are displayed within the lower panel with gray vertical lines. The module temperatures are taken to be 18 °C

during these shutdown periods. During part of the shutdown (LS1) between LHC Run 1 and Run 2, from February 2013 to February 2014 (LS1 ended in April 2015), the Pixel Detector was removed from the ATLAS cavern and kept at 22 °C.

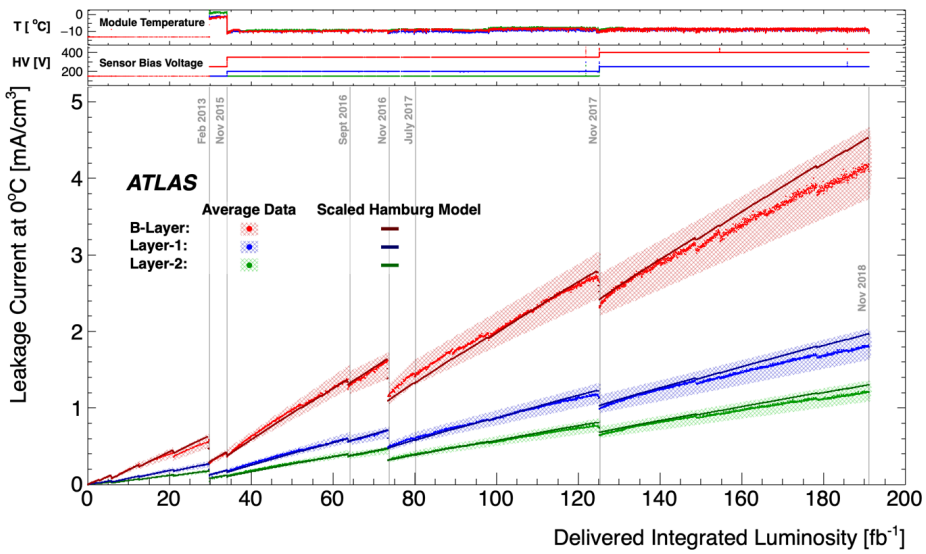


Figure 3.6: Average measured leakage current of a representative sample of modules in the ATLAS Pixel Detector barrel layers over the full period of operation. The scaled prediction from the Hamburg Model is also shown.

Measured ratios of the average leakage current for modules on the *B*-Layer relative to the average leakage current for modules on Layer-2, and of the average leakage current for modules on Layer-1 relative to the average leakage current of modules on Layer-2, are shown in Figure 3.7 for LHC Run 2. These ratios are, as predicted, constant as a function of integrated luminosity. Once again, some dates corresponding to extended periods when the LHC beams were off are displayed with gray vertical lines. Also shown in Figure 3.7 are the ratios of the unscaled Hamburg Model predictions for LHC Run 2. The vertical axis is proportional to the ratio of the applied fluences. The fluence of one layer relative to other layers is well predicted without the need for scale factors.

Region	z Bin	Scale Factor	Uncertainty
B-Layer	-38.0 cm $< z <$ -23.7 cm	1.31	0.02
	-13.3 cm $< z <$ 1.0 cm	1.47	0.02
	5.17 cm $< z <$ 13.3 cm	1.28	0.02
	29.9 cm $< z <$ 38.0 cm	1.15	0.02
Layer-1	-38.0 cm $< z <$ -23.7 cm	1.26	0.02
	-13.3 cm $< z <$ 1.0 cm	1.42	0.02
	-1.0 cm $< z <$ 13.3 cm	1.31	0.02
	23.7 cm $< z <$ 38.0 cm	1.25	0.02
Layer-2	-38.0 cm $< z <$ -23.7 cm	1.32	0.02
	-13.3 cm $< z <$ 1.0 cm	1.43	0.02
	-1.0 cm $< z <$ 13.3 cm	1.36	0.02
	23.7 cm $< z <$ 38.0 cm	1.25	0.02

Table 3.5: Barrel Layer scale factors. The bin limits are determined by the paired module powering scheme. Each bin is defined based on the center location of the modules that are included in the bin; one centimeter is added to or subtracted from the center location in defining the bin limits to include the center position of all modules in the bin.

The leakage current shows a dependence on the axial position, z, and this dependence is discussed in Section 3.7.1. The leakage current does not show dependence on ϕ, see Section 3.7.2. Leakage current magnitude is highest in modules closest to the interaction point.

3.7.1 Leakage Current versus Axial Position

The Hamburg Model prediction has been scaled to match the leakage current data in the bins of z that are monitored by the power supply system. Figure 3.8 shows the z-dependence of the leakage current data with single module precision as well as multiple module precision. The quality of the scaled Hamburg Model is confirmed

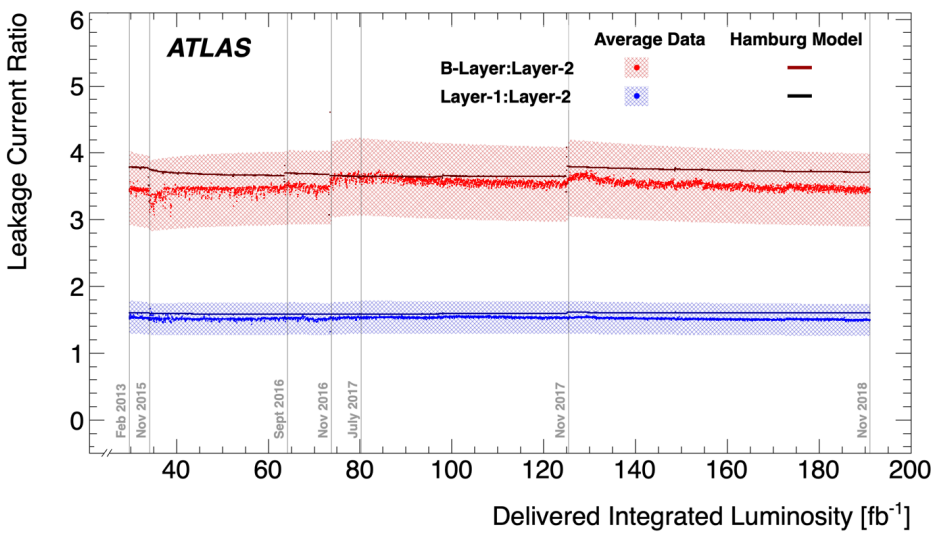


Figure 3.7: Ratios of the *B*-Layer and Layer-1 leakage current data to Layer-2 leakage current for the LHC Run 2 period of ATLAS operation.

with the two independent measurements. The uncertainty on the Hamburg Model prediction is 3.8%. Missing HVPP4 data are due to temporary power shutdowns.

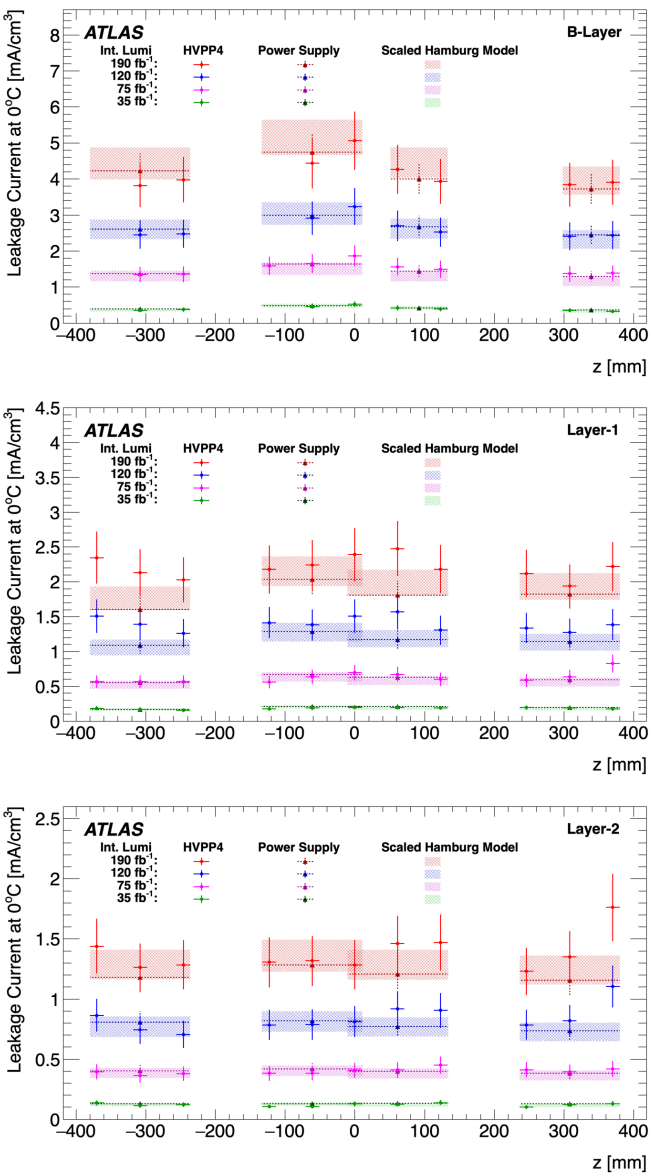


Figure 3.8: *B*-Layer, Layer-1, and Layer-2 leakage current data binned in z (the axis along the beam line) measured at four values of integrated luminosity using single module precision with the HVPP4 subsystem and multiple module precision with the module power supply subsystem. The scaled Hamburg Model prediction is also shown. Missing HVPP4 data are due to temporary power shutdowns. Twenty to twenty-two modules are included in each power supply bin for the *B*-Layer and twelve to sixteen modules are included in each power supply bin for Layer-1 and Layer-2.

3.7.2 Leakage Current versus Azimuthal Angle

The ϕ-dependence of the leakage current was also studied. There is no apparent dependence of the leakage current on the azimuthal angle. B-Layer leakage current data binned in ϕ are shown in Figure 3.9. The ratios of the various ϕ bins of the B-Layer with respect to the $225^\circ < \phi < 315^\circ$ bin are presented in Figure 3.10. Layer-1 leakage current data binned in ϕ are shown in Figure 3.11. The ratios of currents in the various ϕ bins of Layer-1 with respect to the $225^\circ < \phi < 315^\circ$ bin are presented in Figure 3.12. Layer-2 leakage current data binned in ϕ are shown in Figure 3.13. The ratios of currents in the various ϕ bins of Layer-2 with respect to the $225^\circ < \phi < 315^\circ$ bin are presented in Figure 3.14.

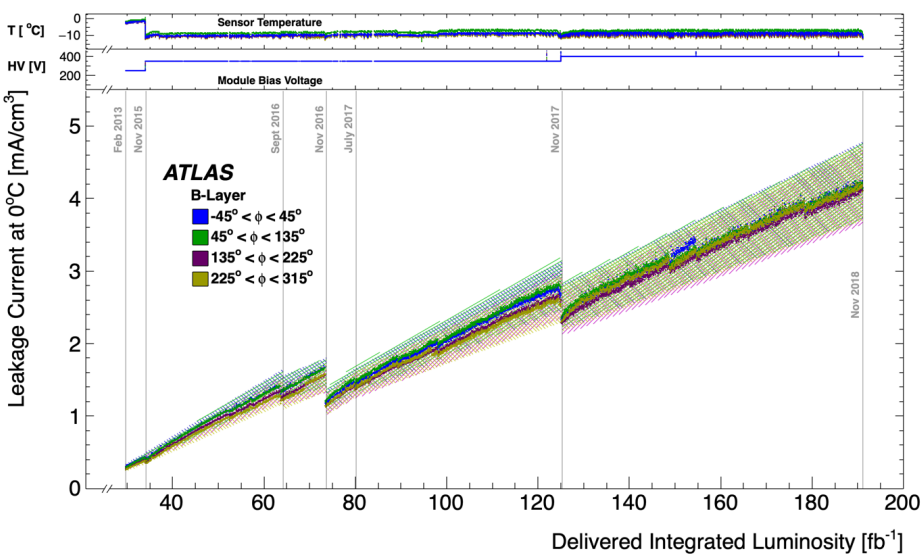


Figure 3.9: Average measured leakage current of a representative sample of modules on the B-Layer binned in ϕ for the LHC Run 2 period of operation.

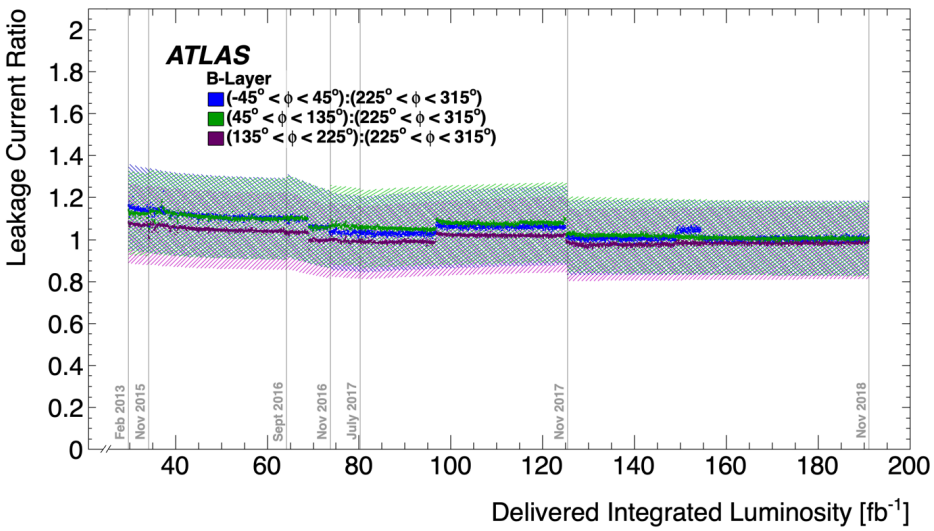


Figure 3.10: Ratios of the various ϕ binned leakage current data on the B-Layer with respect to the $225^\circ < \phi < 315^\circ$ bin for the LHC Run 2 period of operation.

3.7.3 Leakage Current on the Disks

The average measured leakage current of a representative sample of modules in the ATLAS Pixel Detector disks for the LHC Run 2 period of operation is shown in

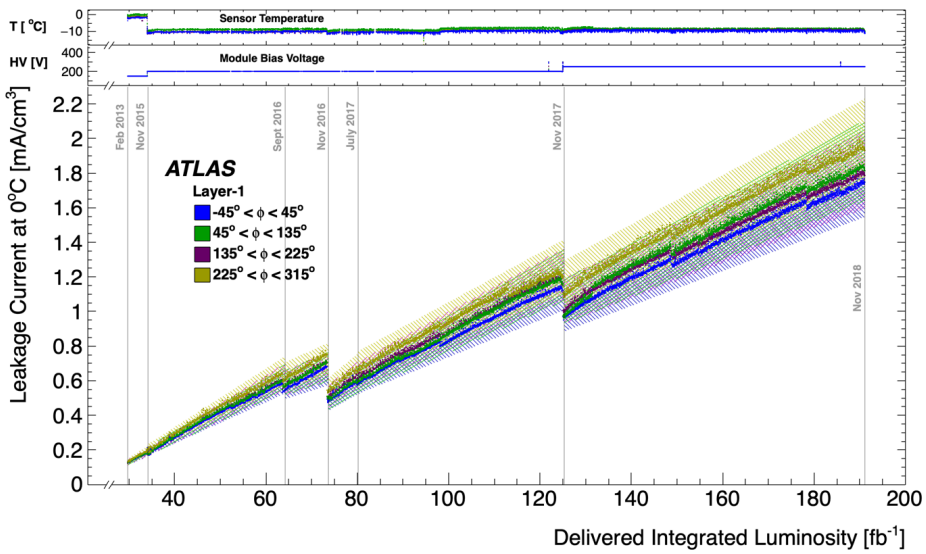


Figure 3.11: Average measured leakage current of a representative sample of modules on Layer-1 binned in ϕ for the LHC Run 2 period of operation.

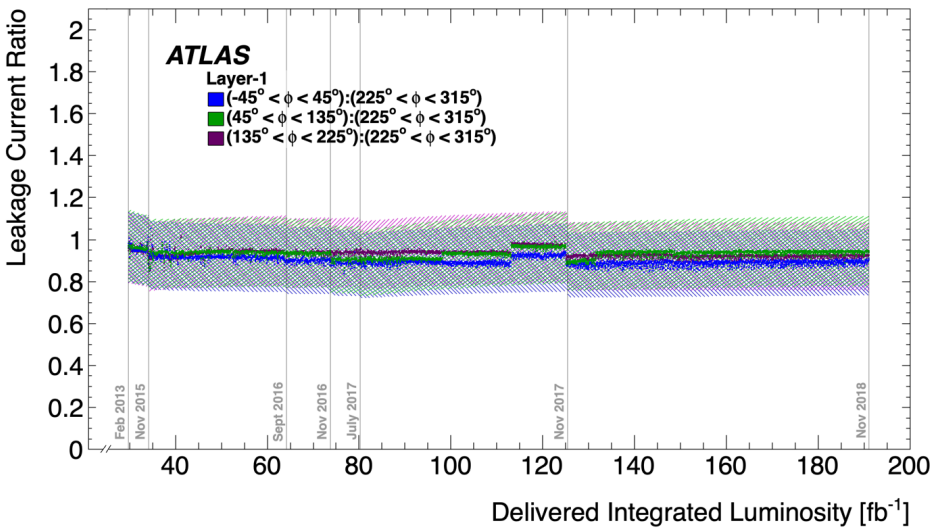


Figure 3.12: Ratios of the various ϕ binned leakage current data on Layer-1 with respect to the $225^\circ < \phi < 315^\circ$ bin for the LHC Run 2 period of operation.

Figures 3.15 and 3.17. Disk-1, Disk-2, and Disk-3 show comparable values of leakage

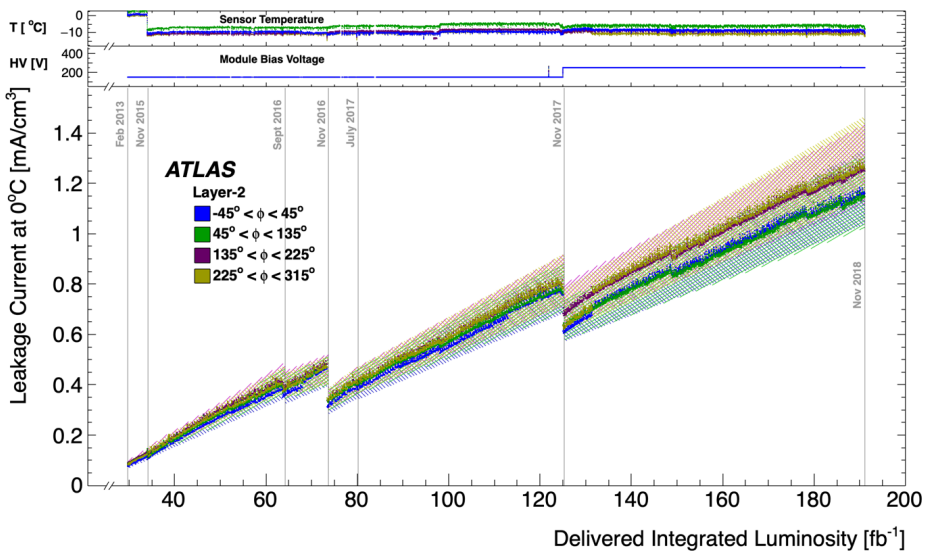


Figure 3.13: Average measured leakage current of a representative sample of modules on Layer-2 binned in ϕ for the LHC Run 2 period of operation.

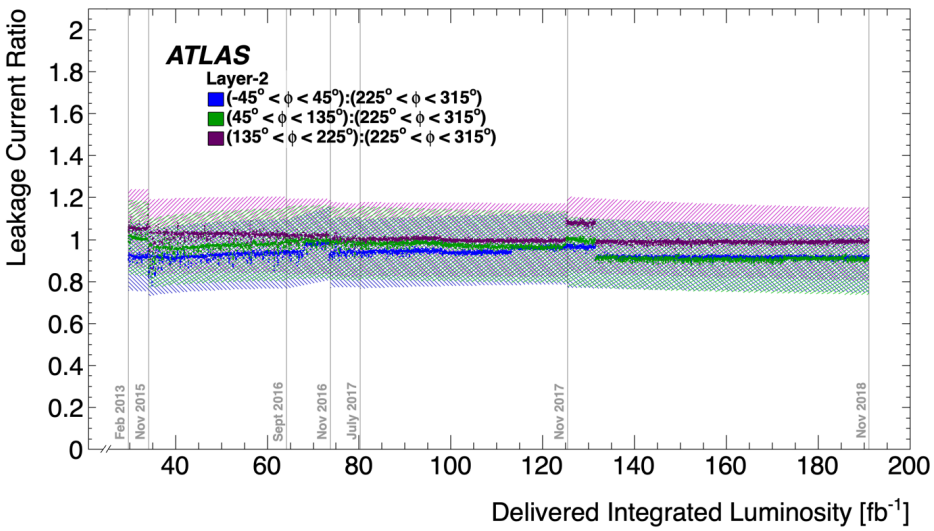


Figure 3.14: Ratios of the various ϕ binned leakage current data on Layer-2 with respect to the $225^\circ < \phi < 315^\circ$ bin for the LHC Run 2 period of operation.

current. In reporting the disk data, side A and side C of the Pixel Detector are shown separately. The Hamburg Model prediction has been scaled to match the measured leakage current independently for Disk-1, Disk-2, and Disk-3 (for both side A and side C). The scale factors used for each disk can be found in Table 3.6. As before, the average sensor temperature is shown in the top panel, the module bias voltage is

Region	Scale Factor	Uncertainty
Disk-1A	1.35	0.02
Disk-2A	1.33	0.02
Disk-3A	1.36	0.02
Disk-1C	1.36	0.02
Disk-2C	1.34	0.02
Disk-3C	1.41	0.02

Table 3.6: Disk scale factors.

shown in the middle panel, and some dates corresponding to extended periods when the LHC beam was off, resulting in annealing of the sensors, are displayed within the lower panel with gray vertical lines. Ratios of Disk-1A and Disk-2A leakage current data to Disk-3A leakage current data for the LHC Run 2 period of operation are shown in Figure 3.16, and similarly for side C in Figure 3.18. Also shown are the ratios of the Disk-1 and Disk-2 unscaled Hamburg Model predictions to the Disk-3 unscaled Hamburg Model prediction. All of the disks have been exposed to similar fluences; the leakage current ratios shown in Figures 3.16 and 3.18 remain close to one as a result.

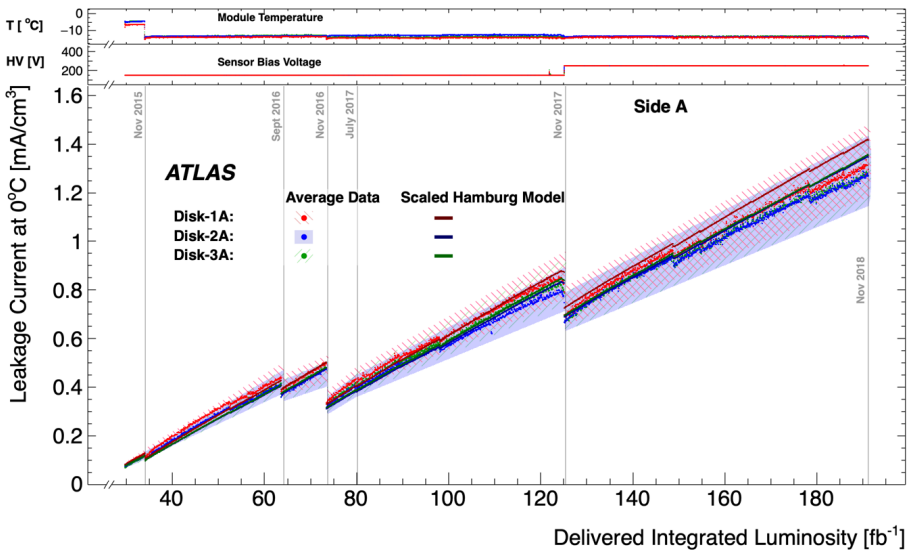


Figure 3.15: Average measured leakage current of a representative sample of modules in the ATLAS Pixel Detector disks on side A for the LHC Run 2 period of operation. The scaled Hamburg Model prediction is also shown.

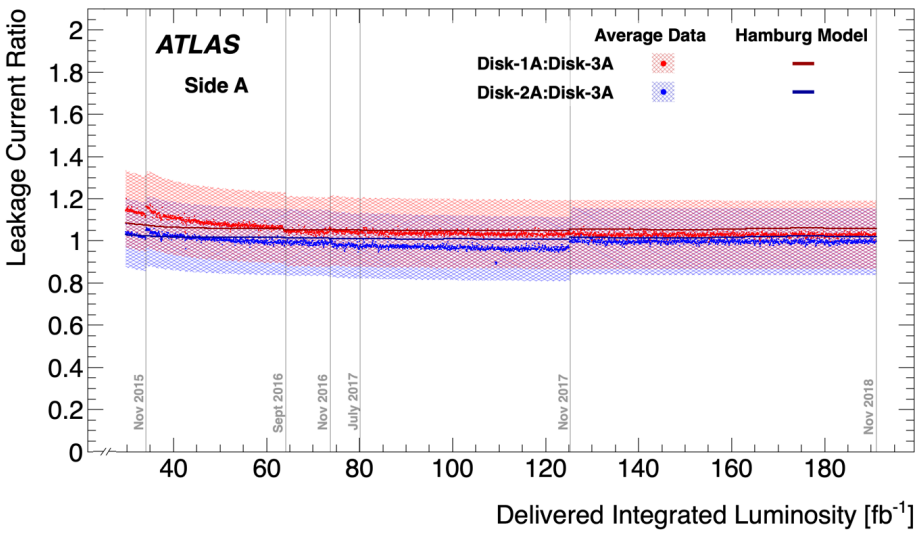


Figure 3.16: Ratios of Disk-1A and Disk-2A leakage current data to Disk-3A leakage current data for the LHC Run 2 period of operation. Also shown are the ratios of the Disk-1 and Disk-2 unscaled Hamburg Model predictions to the Disk-3 unscaled Hamburg Model prediction.

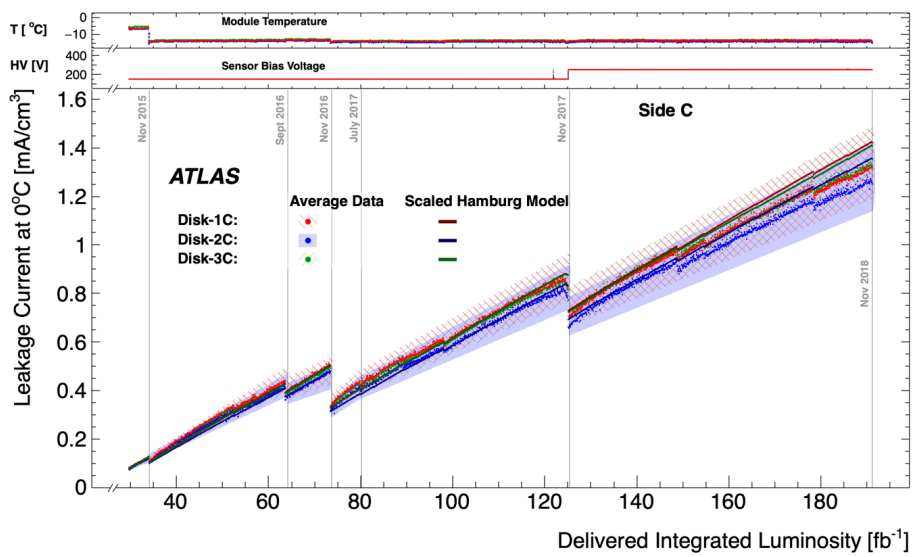


Figure 3.17: Average measured leakage current of a representative sample of modules in the ATLAS Pixel Detector disks on side C for the LHC Run 2 period of operation. The scaled Hamburg Model prediction is also shown.

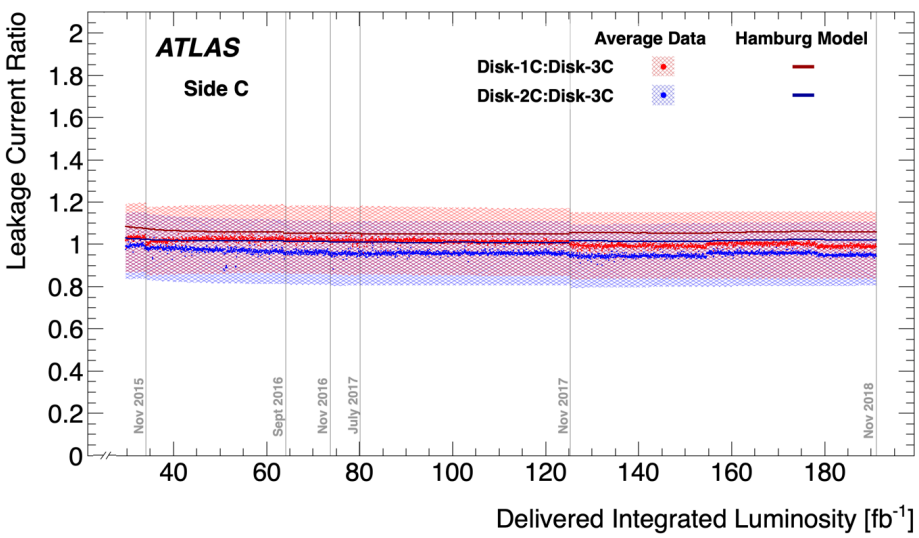


Figure 3.18: Ratios of Disk-1C and Disk-2C leakage current data to Disk-3C leakage current data for the LHC Run 2 period of operation. Also shown are the ratios of the Disk-1 and Disk-2 unscaled Hamburg Model predictions to the Disk-3 unscaled Hamburg Model prediction.

3.8 Sensitivity to the Effective Silicon Band Gap Energy Value

A study is performed to investigate the sensitivity of the predicted leakage current to the value used for effective silicon band gap, E_{eff}. The study uses currents recorded in modules located in the range $[-38.0 < z < -23.7]$ cm. Several predictions were generated, all normalized to 0 °C, each using a different value of E_{eff}. The leakage current data were also normalized to 0 °C and analyzed once with each unique value of E_{eff}. Note that the value of E_{eff} is also used in the temperature normalization step. The impact of using different values of E_{eff} can be seen in Figure 3.19. Empirical studies show that E_{eff} depends on received fluence [56], and selecting the nominal silicon band gap energy (E_{g} =1.12) for analyzing leakage current is not suitable. Figure 3.19 demonstrates that the value of E_{eff} impacts the analysis. If the value of E_{eff} deviates from 1.21, the scale factor needed to bring the Hamburg Model into agreement with the data will change.

Further empirical evidence with data from silicon sensors in the ATLAS Pixel Detector is used to determine the optimal value of E_{eff} in Section 3.9. The study presented in this section is superseded by the one in Section 3.9, which is performed on data collected with the ATLAS sensors and and does not rely on the model.

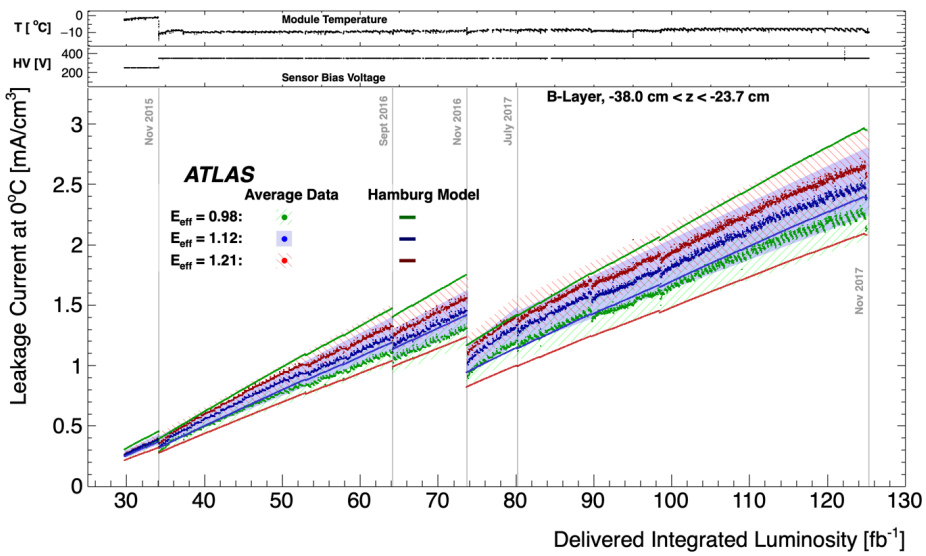


Figure 3.19: Several predictions of leakage current were generated, all normalized to 0 °C, each using a different value of E_{eff}. The leakage current data were also normalized to 0 °C and analyzed once with each unique value of E_{eff}. The value of E_{eff} is used in the temperature normalization step. Three pairs of leakage current data and predictions with the Hamburg Model, with three E_{eff} values used to analyze them are shown here. Leakage current are compared to a Hamburg Model prediction using 3 different values of E_{eff}.

3.9 Determination of the Optimal Value of Effective Band Gap Energy with Irradiated Silicon Sensors in the ATLAS Pixel Detector

Two dedicated measurements have been performed on the silicon sensors of the ATLAS Pixel Detector to study the proper value of E_{eff} to be used in Equation 3.2. The study is performed by measuring leakage current at various temperatures. Data were collected for sensors in the IBL in Feb. 2018, after the sensors had received a fluence of about 6×10^{14} $n_{\text{eq}}/\text{cm}^2$. Another set of data was collected in May 2019 on all layers of the Pixel Detector, after the full fluence through the end of LHC Run 2 had been delivered to the sensors. Every module in IBL is used to perform the study and a representative sample of modules on the B-Layer, Layer-1, Layer-2 and the Disks is used.

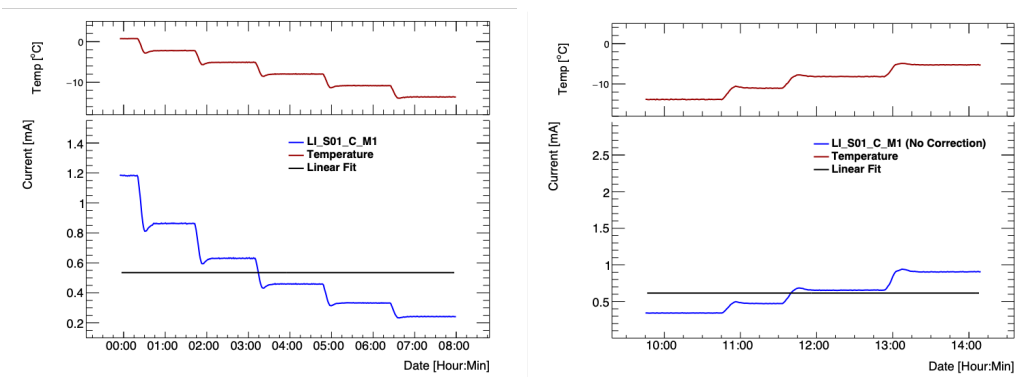


Figure 3.20: Leakage current data at various temperatures for a module in the IBL. Data were collected (left) in Feb. 2018 and (right) in May 2019. The temperature of each module is shown in the top panel.

The χ^2 of the linear fit is computed for each temperature-corrected leakage current in the E_{eff} range. The E_{eff} value corresponding to the minimum χ^2 is selected as the optimal E_{eff} for the module. The average E_{eff} in bins of z is computed and

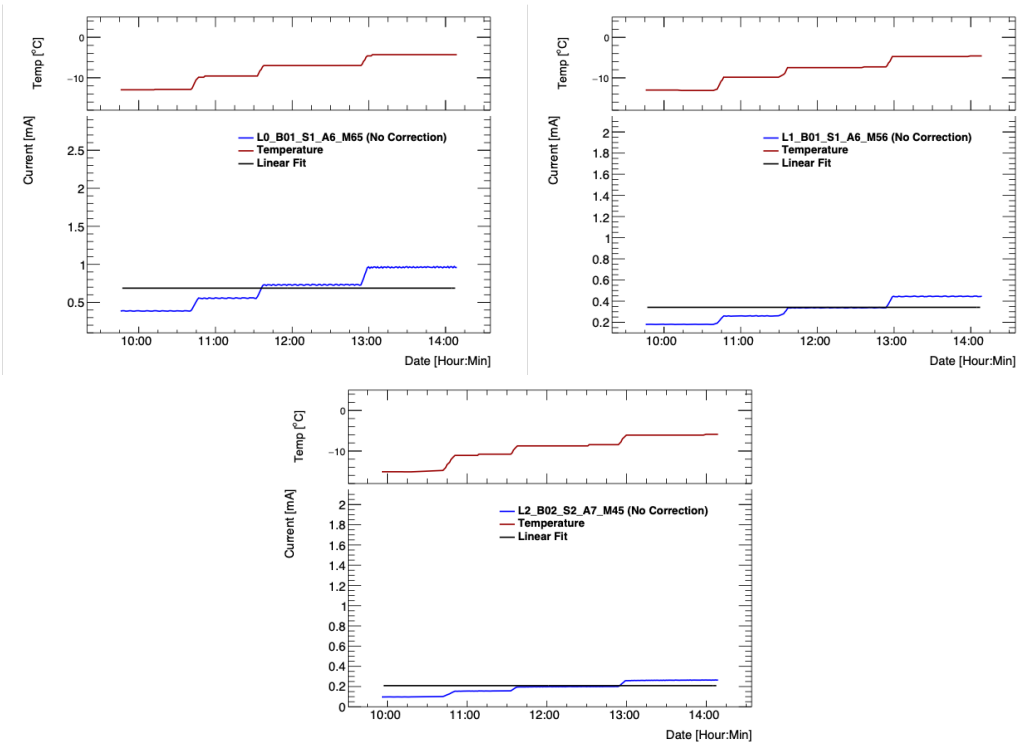


Figure 3.21: Leakage current data at various temperatures for the (top left) B-Layer, (top right) Layer-1, and (bottom) Layer-2. Data were collected in May 2019. The temperature of each module is shown in the top panel.

reported here.

A summary of the process of the investiagation is shown in Figure 3.25. The temperature of the Pixel Detector modules was set to several fixed values, and measured with the module temperature sensor. The leakage current data are examined (black line) and show a clear temperature dependence. The leakage current is corrected to a reference temperature $T_R = 0$ °C with several values of E_{eff}. The optimal value of E_{eff} in the temperature correction equation is the value that results in corrected leakage current data that best fit a line of zero slope. The best fit is determined using a minimum χ^2 figure of merit. The optimal E_{eff} is 1.26 eV for the module shown in Figure 3.25. The measurement corresponds to data of integrated luminosity 161 fb^{-1}

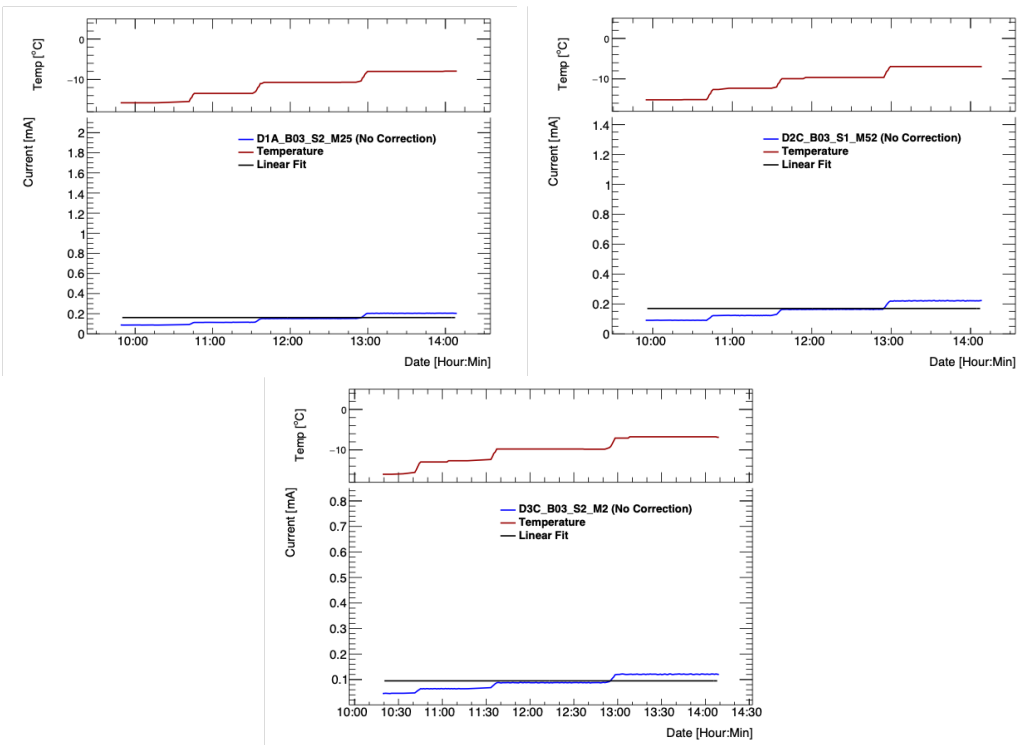


Figure 3.22: Leakage current data at various temperatures for the (top left) Disk-1, (top right) Disk-2, and (bottom) Disk-3. Data were collected in May 2019. The temperature of each module is shown in the top panel.

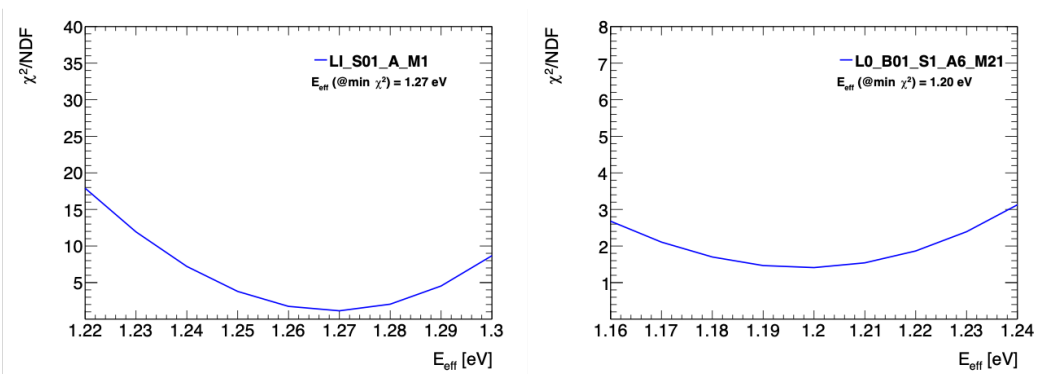


Figure 3.23: The χ^2 distribution is computed for a module (left) in the IBL and (right) for a module in the *B*-Layer.

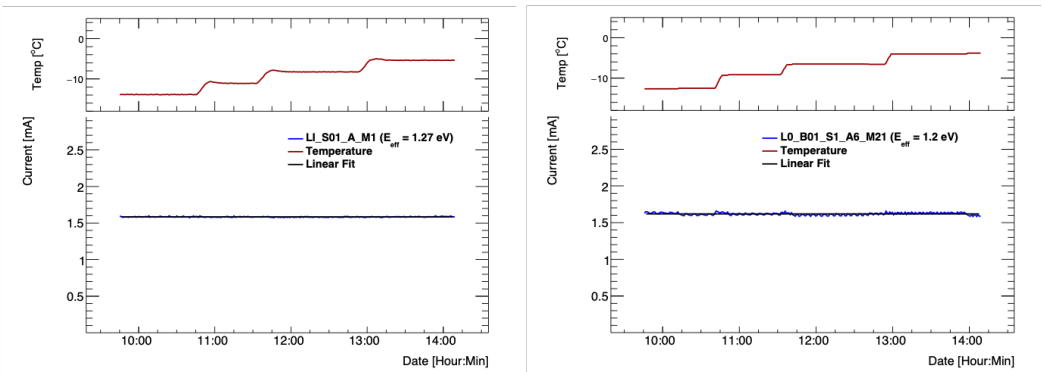


Figure 3.24: (left) Leakage current is analyzed for one module in the IBL and (right) one module in the B-Layer. The leakage current is corrected for temperature using the optimal E_{eff} value for the module. The optimal E_{eff} value for each module is shown in the legend of the figure. The temperature of each module is shown in the top panel.

delivered to the IBL. The absolute luminosity used in this study accounts for luminosities accumulated during times when the ATLAS detector is and is not operating, because all particle fluence received by the silicon sensors will impact the leakage current. Luminosity data recorded without the LHC stable beams, ATLAS ready, or ATLAS physics declarations are included.

The optimal E_{eff} value is determined for each module and then the average value is computed in bins of z (the direction along the beam line) for each layer and disk and shown in Figure 3.26. The Feb. 2018 (May 2019) measurements correspond to data of integrated luminosity 95 (161) fb^{-1} delivered to the IBL. The 2019 measurements correspond to data of integrated luminosity 191 fb^{-1} delivered to the B-Layer, Layer-1, Layer-2, and the Disks. The vertical error bars represent the impact on the optimal E_{eff} value of ± 2 °C uncertainty on the module temperature. Horizontal error bars represent z bin ranges. Each bin is defined based on the average position of the modules whose data are used.

The χ^2 figure of merit is determined for a range of E_{eff} values and variations of

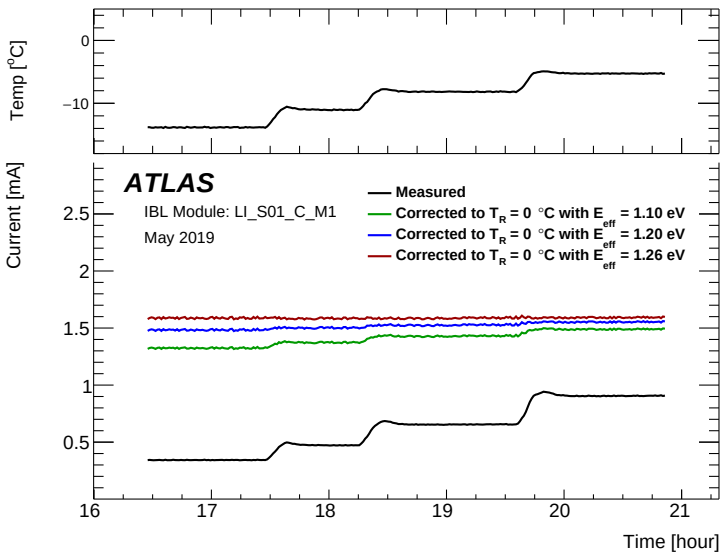


Figure 3.25: Summary of the optimal E_{eff} study process.

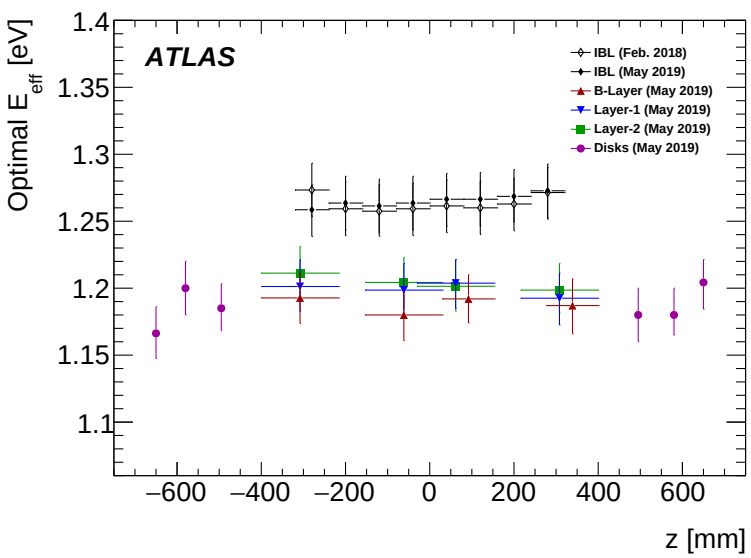


Figure 3.26: Average values of the optimal E_{eff} study for each layer and disk of the Pixel Detector, binned in z.

the module temperature data, for one module on the IBL (Figure 3.27). Steps of 0.01 eV, in the range 0.5 eV to 1.5 eV, for E_{eff} and steps of 0.1 °C, in the range -2.0 °C

to 2.0 °C, for the temperature variation are investigated independently. Here the definition of variation is the measured module temperature plus or minus a constant that corresponds to a systematic uncertainty in the temperature sensor reading.

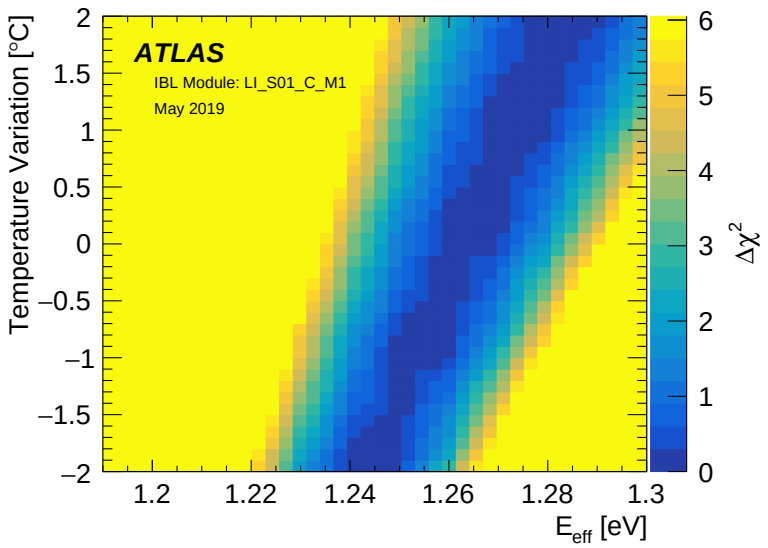


Figure 3.27: The χ^2 figure of merit in the E_{eff} and temperature offset phase space is investigated.

3.10 Comparisons of Measured and Predicted Fluence

Comparisons of fluence predictions by Pythia8 + FLUKA to the fluence determined from leakage current data combined with predictions by the Hamburg Model are shown in Figure 3.28 for the *B*-Layer, Layer-1, and Layer-2 and for the disks in Figure 3.29. Fluence predictions by Pythia8 + FLUKA are weighted averages of the fluence predicted at the three center-of-mass energies for the full period of the measurement. The statistical uncertainty on the fluence as predicted with Pythia8 + FLUKA is less than 1%. The combined statistical and systematic uncertainty on the fluence as determined from leakage current data and the Hamburg Model predic-

tions is 11.5%; this excludes systematics associated with hardness factors. Fluence predicted with PYTHIA8 + GEANT4 in Run 2 and PYTHIA8 + FLUKA in Run 1 is also shown in Figure 3.28. GEANT4 provides an alternative transport model. The horizontal bars on the fluence points determined from leakage current data combined with predictions by the Hamburg Model reflect the bin ranges.

Differences between the fluence predictions and the fluence determined from leakage current data combined with predictions by the Hamburg Model is an open area of research. Further empirical evidence of the value of E_{eff} is needed. Further studies of the particle hardness factors used as input to the fluence simulations are also critical for improving the comparisons. A comparison of the end of Run 2 leakage currents for all silicon sensors in the Inner Detector, as well as a comparison with PYTHIA8 + FLUKA and PYTHIA8 + GEANT4, is available in [27].

Example results from Reference [27] are shown here in Figures 3.30 and 3.31. The predicted values are symmetric in z by construction. Distances given in parentheses after the layer names correspond to the radius of the sensors with respect to the geometric center of ATLAS. For the IBL, the error bars are dominated by the residual dependence of the leakage current on the high voltage past full depletion; for the outer Pixel Detector, the uncertainty is dominated by a power supply uncertainty, an uncertainty on the temperature, and on the luminosity; for the SCT, the uncertainty is due to the sensor temperature, the luminosity, and the sensor thickness (for fluence) and the RMS spread across modules (leakage current). Uncertainties on the silicon damage factors (relevant for the simulation and the Hamburg Model) are not included.

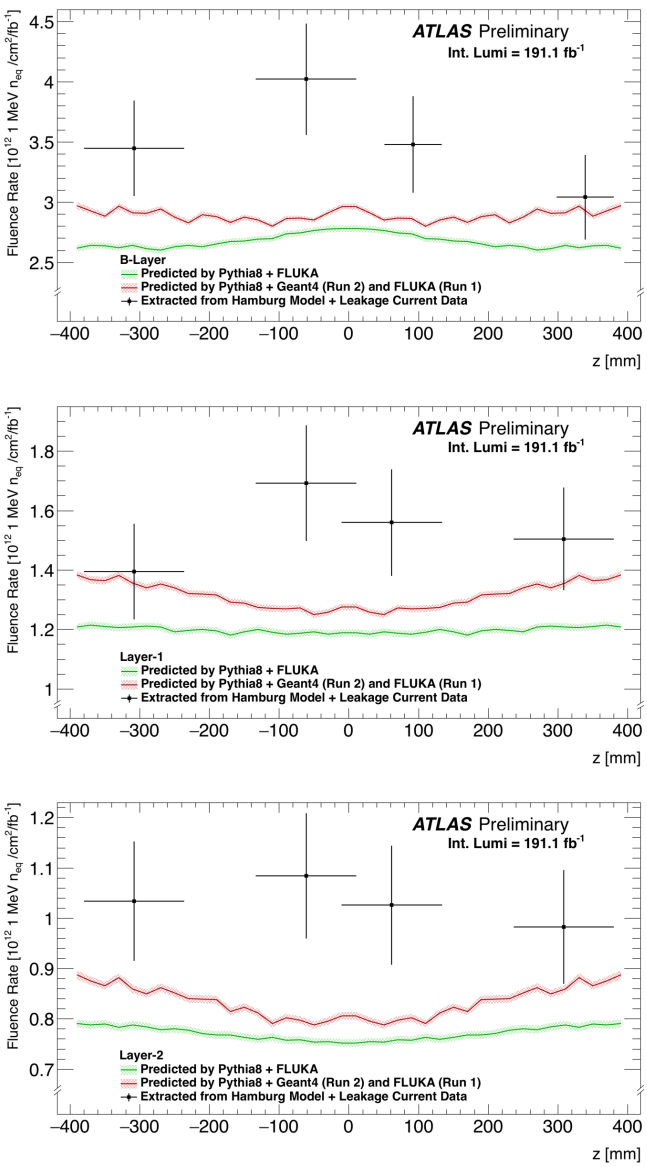


Figure 3.28: Comparisons of fluence predictions by PYTHIA8 + FLUKA for the full period of operation, the fluence predicted by PYTHIA8 + GEANT4 in Run 2 and PYTHIA8 + FLUKA in Run 1, and the fluence determined from leakage current data combined with predictions by the Hamburg Model, for the *B*-Layer, Layer-1, and Layer-2. The horizontal bars on the fluence points determined from leakage current data combined with predictions by the Hamburg Model reflect the bin ranges.

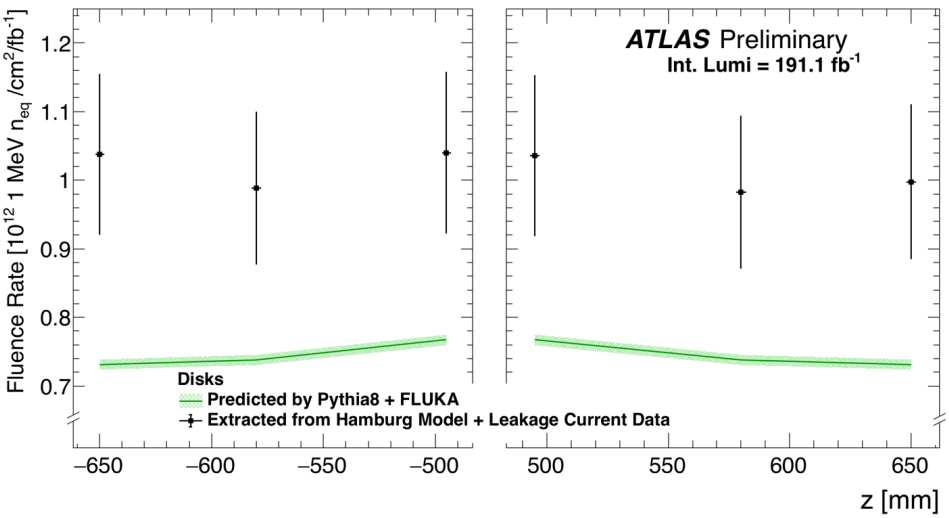


Figure 3.29: Comparison of fluence predictions by PYTHIA8 + FLUKA to the fluence determined from leakage current data combined with predictions by the Hamburg Model, for the disks.

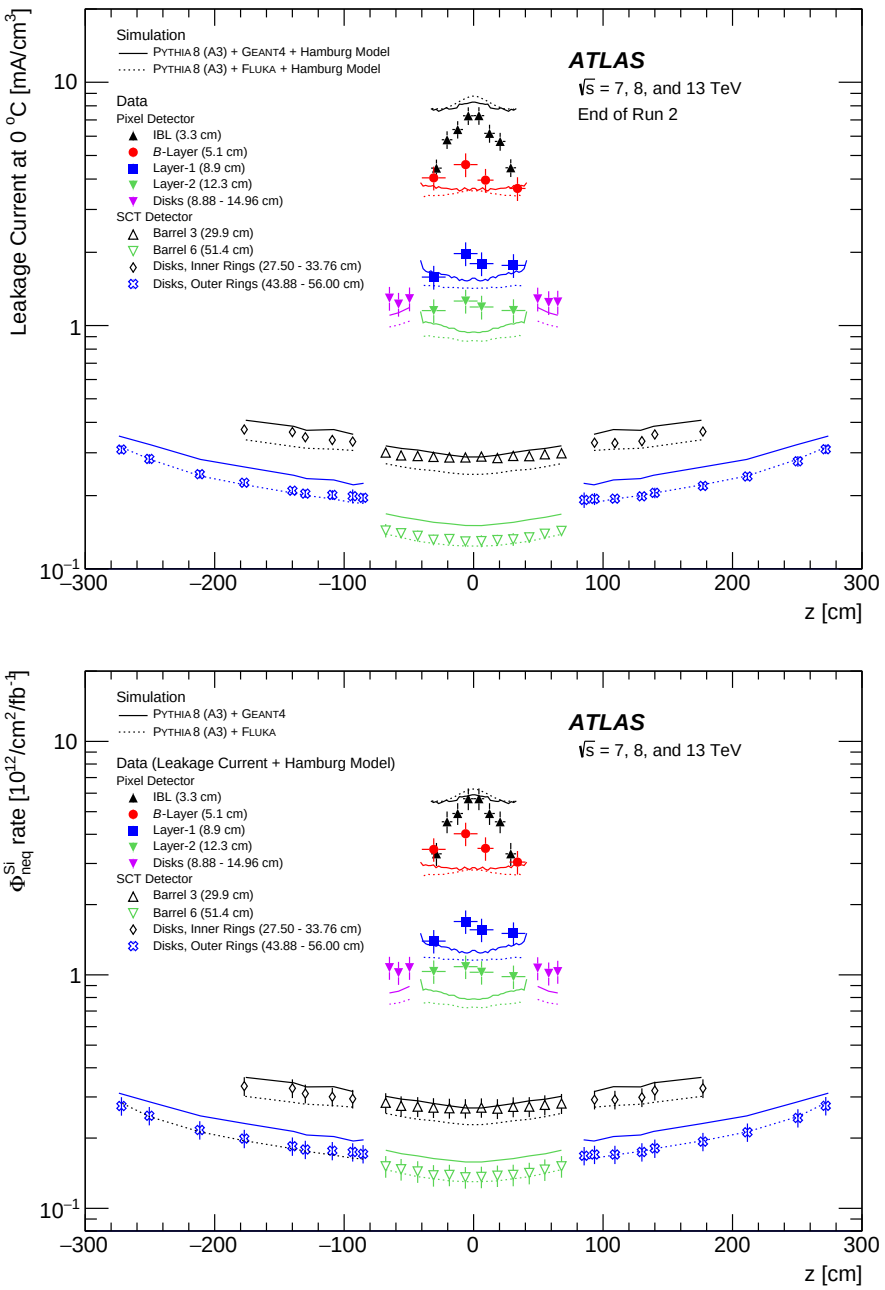


Figure 3.30: (Top) The leakage current at the end of Run 2 and (bottom) the fluence rate as a function of z for the entire silicon-based ATLAS inner detector. These figures were originally published in Reference [27].

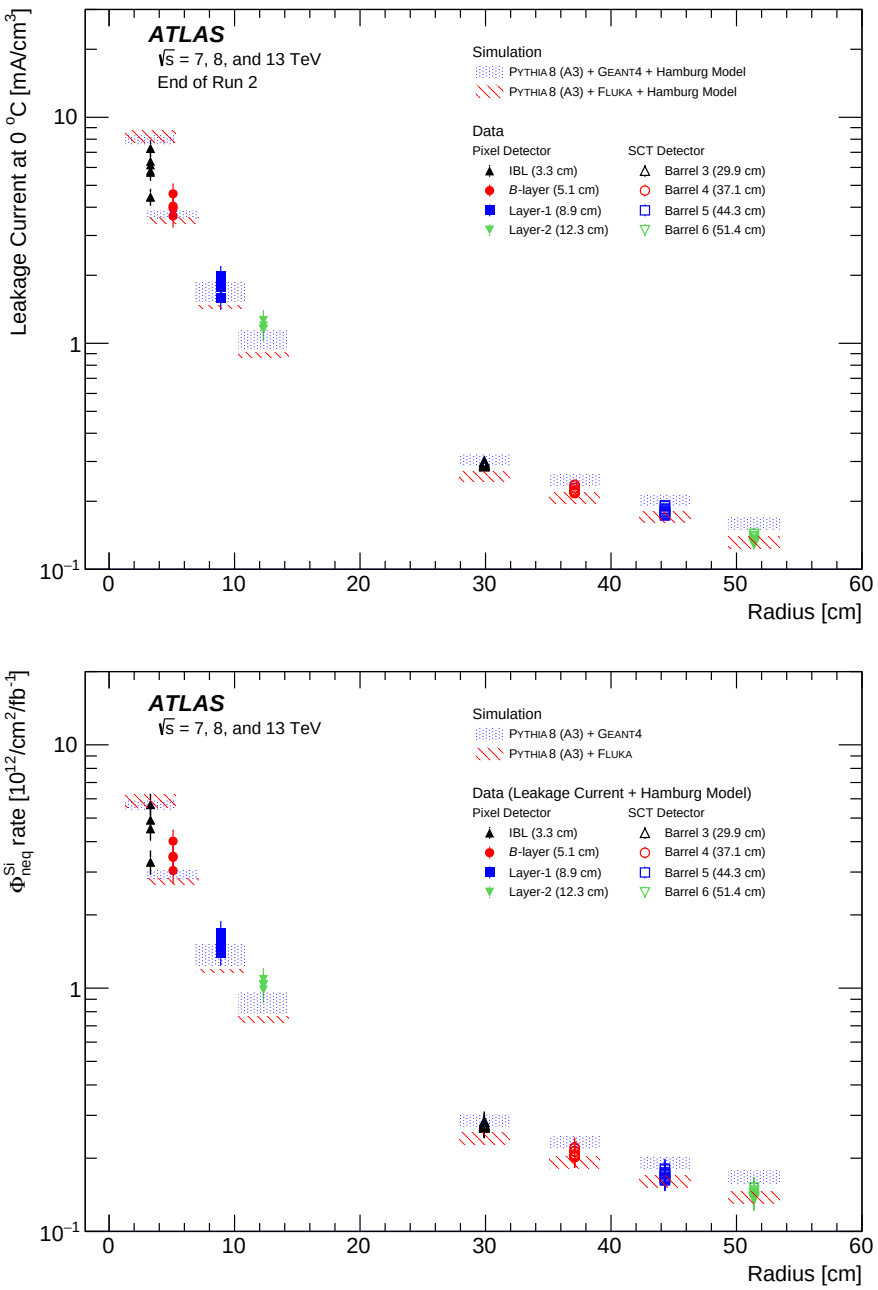


Figure 3.31: (Top) The leakage current at the end of Run 2 and (bottom) the fluence rate as a function of radius for the entire silicon-based ATLAS inner detector. The size of the horizontal bands on the simulation is chosen to aid the comparison with data - the actual radial uncertainty from the finite size of the sensors is comparable to the marker sizes. These figures were originally published in Reference [27].

3.11 Lifetime Projections

The existing data trends are used to extrapolate the leakage currents in the *B*-Layer through Run 3 of the LHC. The second long shutdown (LS2) of LHC activities and beam deliveries began in 2018 with the completion of data-taking in LHC Run 2 and it will end when the LHC begins operations and delivery of high energy proton beams in Run 3. Run 3 is expected to last three years. The extrapolation, see Figure 3.32, is made using a temperature scenario (Scenario 1) where, during periods when the detector is off, the temperature of the detector will be maintained at -5 °C. For comparison, two additional scenarios are also considered, where the temperature is maintained at -1 °C and at -9 °C during shutdown periods (Scenarios 2 and 3, respectively). There will be times during the shutdown when, to permit detector maintenance, the temperature cannot be maintained at the nominal level. In these situations, when the cooling is off, it is expected that the temperature of the detector will come to equilibrium with the temperature of the ATLAS pit (18 °C). The objective in LS2 is to keep these times to a minimum. Four weeks at 18 °C have been introduced into these scenarios for LS2. During LHC Run 3 the sensors are expected to be kept at -12 °C during operation and -5 °C during planned technical and machine development shutdowns. Again, two additional scenarios, with -1 °C and with -9 °C, are simulated for comparison. An additional four weeks where the detector is kept at the temperature of the ATLAS pit (18 °C) is introduced during these yearly shutdowns in LHC Run 3. The LHC is expected to deliver an additional integrated luminosity of 240 fb^{-1} during Run 3 at $\sqrt{s} = 14$ TeV. This integrated luminosity is converted to expected fluence using predictions made with Pythia8 + FLUKA. The Hamburg Model projections of leakage current through Run 3 are made with these parameters and scaled with the scale factors extracted from the Run 2 measurements and Hamburg Model predictions. These projections are based on the Run 1 and Run 2 temperatures for the *B*-Layer bin overlapping the interac-

tion point, $[-13.3 < z < 1.0]$ cm, where the leakage current level is highest. For comparison, Figure 3.32 includes the leakage current data from this bin.

The leakage current drop due to annealing during shutdown periods is larger when the sensors are held at higher temperatures; but in higher temperature scenarios the bias voltage level required for full depletion increases. A compromise must be met to obtain optimal functionality in Run 3. Scenario 2 is the planned temperature scenario for LS2 and Run 3. The projection shows that maintaining the temperature below 0 °C during shutdown periods produces a situation where the projected leakage current is relatively insensitive to the temperature.

Projections based on other sensor characteristics limitations, such as bias voltage requirements, can be used to estimate the lifetime of the sensors. The magnitude of the power supply and services limit on bias voltage is 600 V. Predicted bias voltages required for full depletion of the silicon sensors are not covered in this thesis. If the applied current exceeds approximately 2 mA per module, the power supplies and services will not be able to sustain power necessary to operate the modules. This is an investigation of the expected requirement on power supply current after fluences received in Run 3. The volume normalization applied to the previous measurements has been removed in Figure 3.32 in order to investigate the current supplied directly by the power supply system. For an exact comparison the temperature normalization of the projection is also scaled down to -12 °C, the approximately nominal operating temperature of the sensors. Including a safety factor on the projections, by multiplying the projected leakage current in Figure 3.32 by two, indicated that the detector will remain within the power supplies and services limitations for applied current.

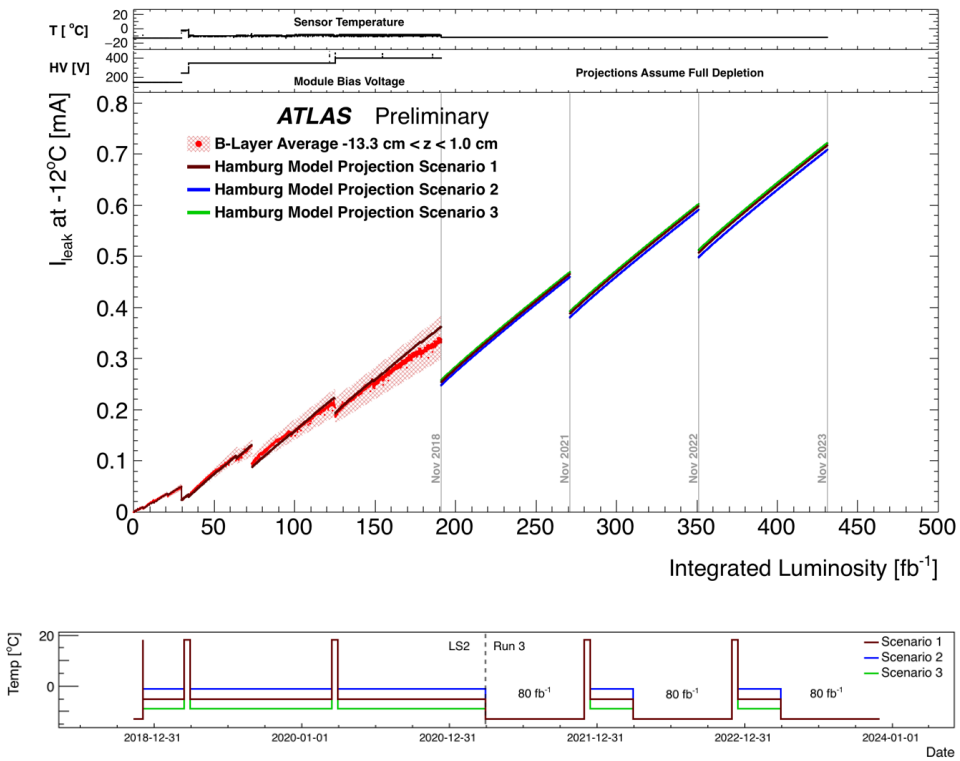


Figure 3.32: (a) The projection of leakage current levels through LHC Run 3. The simulation of Runs 1 and 2 use the temperature recorded in the *B*-Layer bin overlapping the interaction point, $(-13.3 < z < 1.0)$ cm. Leakage current data in this bin are also shown. The temperature normalization is applied using the operating temperature of the sensors (which is roughly -12 °C). The volume normalizations are removed so that the leakage current projections represent the leakage current per module. The power supply and services limitations on leakage current is 2 mA per module and in the projection scenarios shown here the leakage current will remain below this limit. (b) The projected temperature levels throughout the long shutdown and the LHC Run 3 operations for three scenarios are shown as a function of date.

3.12 Summary and Conclusions of the Leakage Current Analysis

Measurements of leakage current for the ATLAS Pixel Detector barrel layers *B*-Layer, Layer-1, and Layer-2 are presented and compared to predictions by the Hamburg Model. The first leakage current measurements of the disks are also presented. The leakage current levels of the disk sensors are higher than the levels on Layer-2. The Hamburg Model matches the data well over the full time period of the measurement after a scale factor is applied for each layer and disk. These Hamburg Model predictions are instructive for making lifetime predictions.

The difference between the fluence predicted by Pythia8 + FLUKA and the fluence extracted from the leakage current data and the Hamburg Model predictions provides input for corrections to the predicted fluence throughout the detector. The differences between the predictions and the data (summarized in Tables 3.5 and 3.6) range from 20% at the barrel ends to as much as 50% at $z = 0$. Direct comparison of the fluence determined by Pythia8 + FLUKA is shown in Figures 3.28 and 3.29.

The *B*-Layer sensors are projected to require well under 2 mA at the end of Run 3 (expected to begin in 2022 and end in 2025) implying that leakage current will not limit the operation of the Pixel Detector sensors throughout Run 3. The investigations of leakage current presented here, together with plans for continued monitoring, provide confidence that the Pixel Detector will continue to collect data with high efficiency through the end of LHC Run 3.

Chapter 4

Quality Assurance of the Next Generation ATLAS Detector

4.1 Inner Tracker (ITk) Overview

In order for the $B^0_{(s)} \rightarrow \mu^+\mu^-$ analysis to achieve higher precision results, more data will need to be collected. For this purpose, the HL-LHC is expected to begin operations within the decade - and during its lifetime, ATLAS will collect on the order of five times more data than it has during the operation for the LHC. To make this possible, the HL-LHC will produce higher instantaneous and integrated luminosities than any collider before it, and ATLAS will need to be upgraded to handle the higher data rates and fluences. The ATLAS Collaboration is resolved to construct the largest silicon detector ever built. The aim is to increase precision to mitigate the anticipated high pileup conditions. The two innermost layers are named Layer-0 and Layer-1, with increasing radii from the proton beam line, respectively. At this time Layer-0 is planned to operate just over 3 cm from the HL-LHC beam

line. The expected lifetime in terms of luminosity of these two inner layers is 2000 fb^{-1}. As a result, these layers will receive about 10 times higher fluences than any other fully operational silicon detector ever has. The impact of the fluence on the silicon sensor leakage current in the detector has been discussed in detail in the previous chapter, work that provides valuable input for the development of a new ATLAS Inner Tracker (ITk) detector. The constraints on radiation hardness and the speed of data throughput motivate strict quality assurance parameters of the ITk construction.

4.2 Contribution to Detector Construction

Research for the assembly process and quality assurance of the two innermost layers of the ITk silicon Pixel Detector is discussed here. The local support framework is made up of staves for the barrel layers and disks on either end of the barrel layers. A diagram of the layout is shown in Figure 4.1 along with an image of prototype stave. The staves and disks are made of carbon fiber laminate surrounding carbon fiber foam and a CO_2 cooling pipe. They are designed for optimal thermal conductivity and structural integrity. The staves will support silicon modules in a linear pattern and the disks will support modules in a circular pattern.

The fundamental unit of the ITk detector is the module. A module is made of a silicon sensor and its readout electronics. A schematic of the layout is shown in Figure 4.2. There are flexible printed circuit electronics on the top of the sensors that provide power for biasing and operating the sensor. The electronics are designed to be flexible so that they can be employed to transport power and data throughout the detector, including in unsupported and constricted spaces. The electronics on the front end of the silicon sensor are used for readout of each pixel sensor through a bump bond connection. To optimize coverage and resources, the module will be

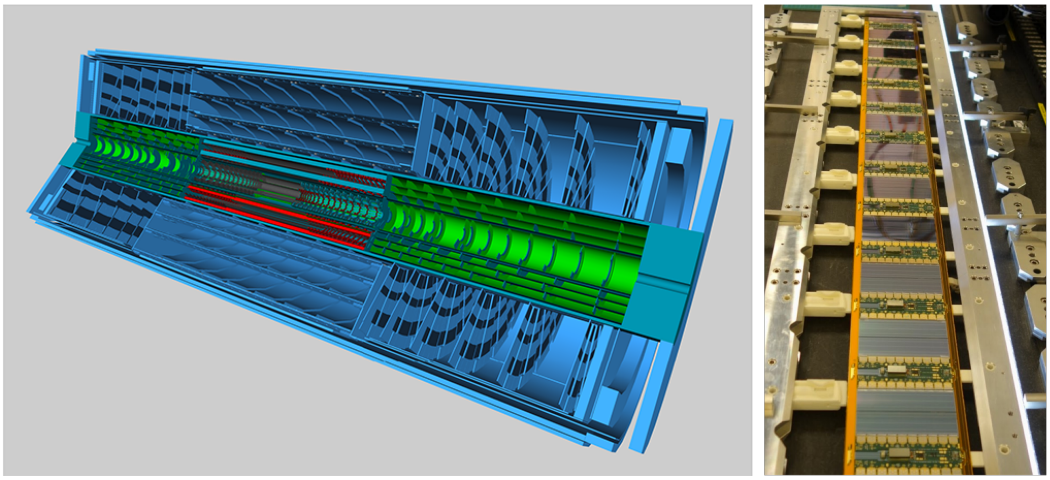


Figure 4.1: (Left) diagram of the ATLAS ITk layout [32] and (right) image of a stave prototype.

designed in two layouts. A single module design will use a silicon sensor with the dimensions 21 mm $\times$ 23 mm. A second geometry, called a quad module, will have a silicon sensor with a 2 $\times$ 2 matrix of front end ASICs.

The modules will be supported on the staves and disks. There will be 2 types of staves, one that supports single modules and one that supports quad modules. There will be three types of disks, (1) coupled disks which will support single modules on an inner ring and quad modules on an outer ring, (2) disks that will support single modules, and (3) disks that will support quad modules. Figure 1.11 shows a quarter profile of the ITk layout.

The modules will be attached to the local supports via a thermally conductive adhesive. Details on selection and application of this adhesive are described below.

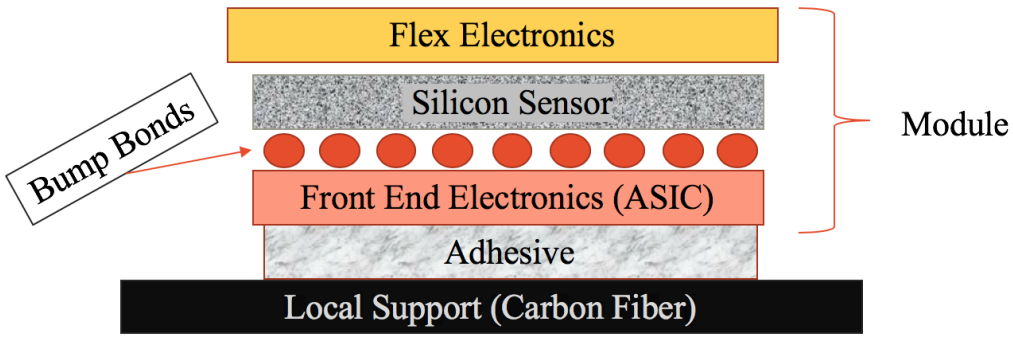


Figure 4.2: Schematic of the single module geometry layout (not to scale). The silicon sensor is operated throughout the front end electronics (ASIC) and power is supplied and data are transfered through the flexible electronics. The modules are attached to the local supports (staves and disks) with a thermally conductive and radiation hard adhesive. For optimal thermal performance, the thickness of the adhesive is required to be 100 micrometers.

4.3 Adhesive Introduction

The requirements of the adhesive choice are that it be highly thermally conductive, have low viscosity so that it can be applied as a thin layer, and be radiation hard.

SE4445 has superior thermal conductivity and lower viscosity than other candidate adhesives. Araldite 2011 has lower thermal conductivity and higher viscosity when compared to SE4445, but has been shown to be more resistant to radiation damage. A summary of the key properties of these two adhesives is shown in Table 4.1.

SE4445 is selected for further study and development of the module loading procedures. For insurance against structural degradation after intense irradiation, small deposits of Araldite 2011 are considered as a possible solution.

Characteristic	Dow Corning SE4445	Huntsman: Araldite 2011
Number of Components	2 (mix 1 to 1 by volume)	2 (mix 1 to 1 by volume)
Pot Life	5 hrs @25 °C	2 hrs @25 °C
Viscosity [centipoise]	14,000	45,000
Cure Time	45 min @125 °C	15(12) hrs @20(25) °C
Thermal Conductivity [Watt/meter-K]	1.34 @25 °C	0.22 @25 °C

Table 4.1: The key properties of SE4445 and Araldite 2011 as described in the manufacturers' data sheets.

4.4 Irradiations

Irradiations of SE4445 and Araldite 2011 have been undertaken. Proper characterization of the adhesives before and after irradiation is important for assurance that the detector will survive the harsh conditions in the HL-LHC. FLUKA simulation studies [32] have indicated that the maximum 1 MeV neutron equivalent fluence in the ITk Pixel Detectors will be 1.31×10^{16} and the maximum ionizing dose will be 9.9 MGy. These values include a multiplicative safety factor of 1.5.

The critical test of an adhesive is represented by a stress versus strain curve. This measurement is made using the machine shown in Figure 4.4, a Zwick/Roell Z050. An adhesive lap joint is held from two ends by the machine and pulled apart at increasing levels of stress. Figure 4.3 shows a diagram of a lap joint and the aluminum bars that are pulled by the machine. The machine is operated by a computer and the strain on the lap joint is measured until it reaches a failure mode. Apparent stress versus strain curves for Araldite 2011 irradiated to doses of 2 MGy, 5 MGy, and 7 MGy are shown in Figures 4.5, 4.6, and 4.7. Apparent stress versus strain curves for SE4445 samples irradiated to doses of 5 MGy, 7 MGy, and 10 MGy are shown in Figures 4.8, 4.9, and 4.10.

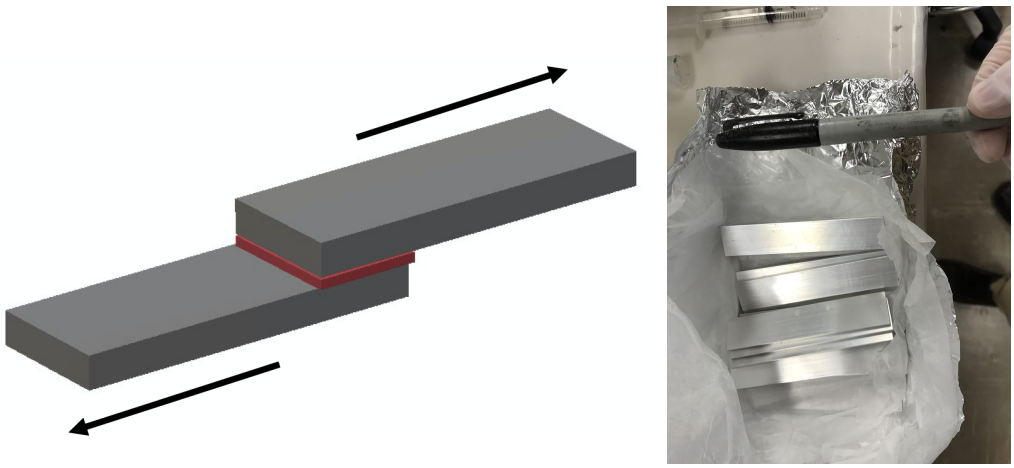


Figure 4.3: (Left) Diagram of a lap joint used for stress versus strain measurements. Adhesive is shown in red and the two surfaces shown in grey are pulled in the direction of the arrows. (Right) Aluminum bars that could be used for this purpose are cut to identical lengths and sanded down where the adhesive may be applied.

The results indicate that both Araldite 2011 and SE4445 perform well under the tensile strength test after gamma irradiation to high doses. Further campaigns for both gamma and hadron irradiations are planned and should be studied to qualify the adhesives.

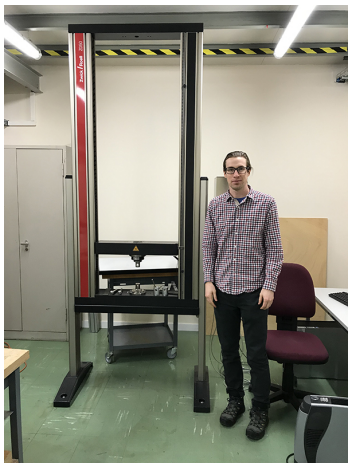


Figure 4.4: Zwick/Roell Z050 machine used for measuring stress versus strain of irradiated samples at CERN.

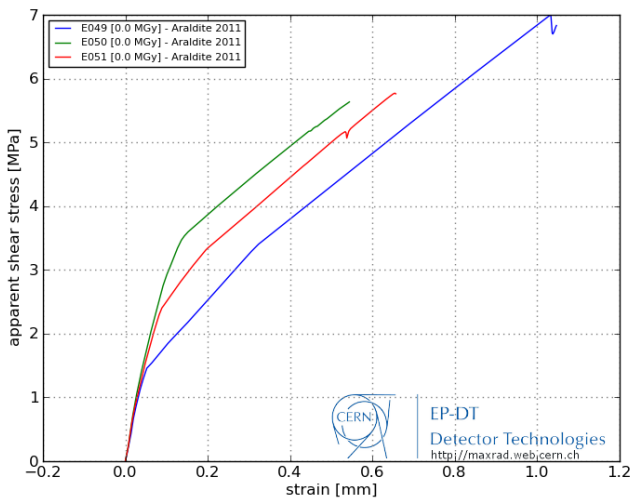


Figure 4.5: Apparent stress versus strain of unnirradiated Araldite 2011 samples [77].

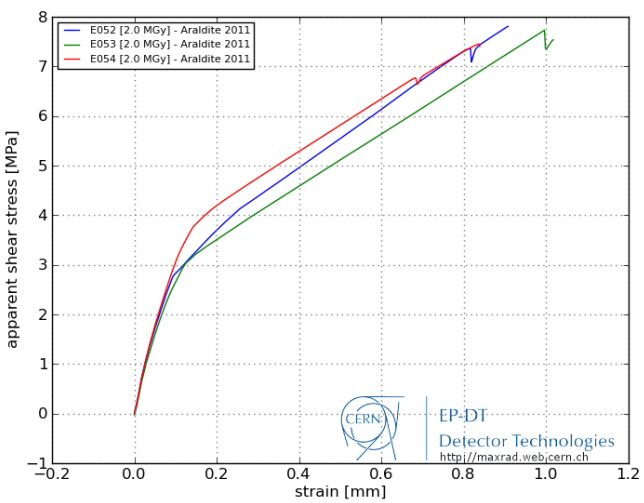


Figure 4.6: Apparent stress versus strain of Araldite 2011 samples irradiated with a dose of 2 MGy [77].

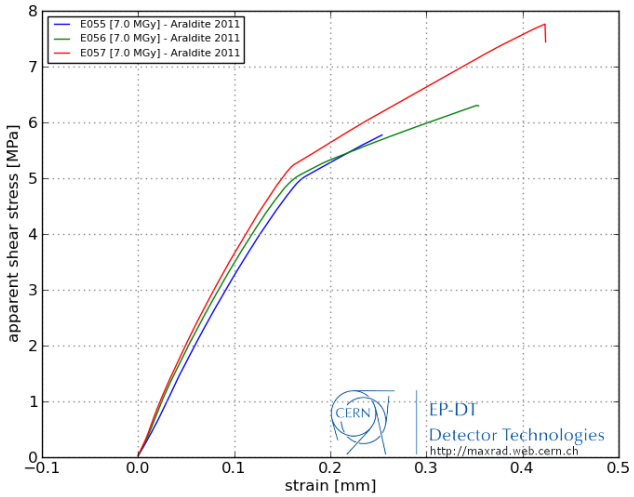


Figure 4.7: Apparent stress versus strain of Araldite 2011 samples irradiated with a dose of 7 MGy [77].

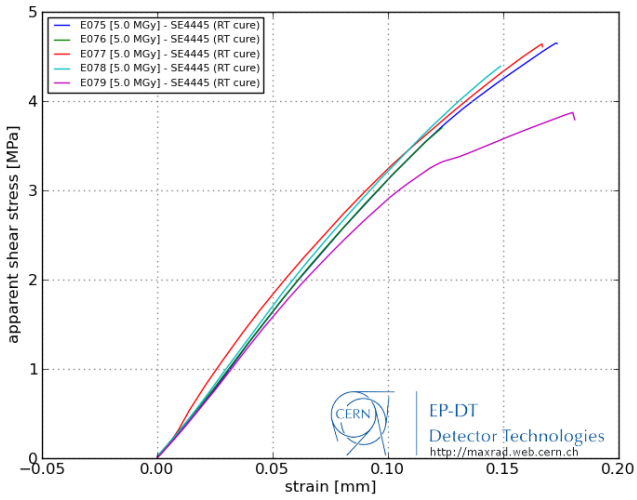


Figure 4.8: Apparent stress versus strain of SE4445 samples irradiated with a dose of 5 MGy [77].

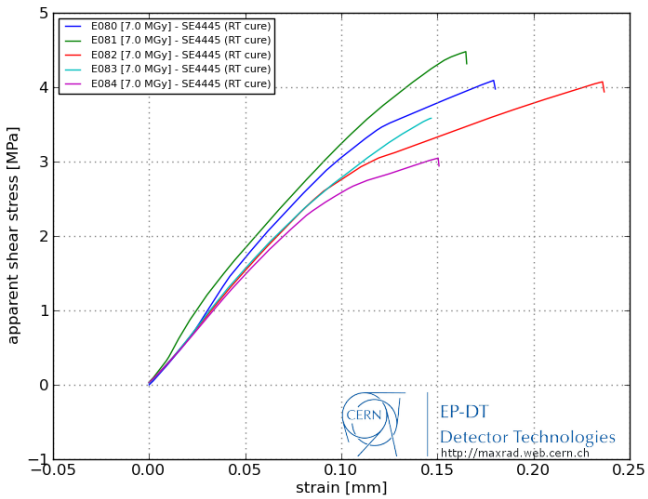


Figure 4.9: Apparent stress versus strain of SE4445 samples irradiated with a dose of 7 MGy [77].

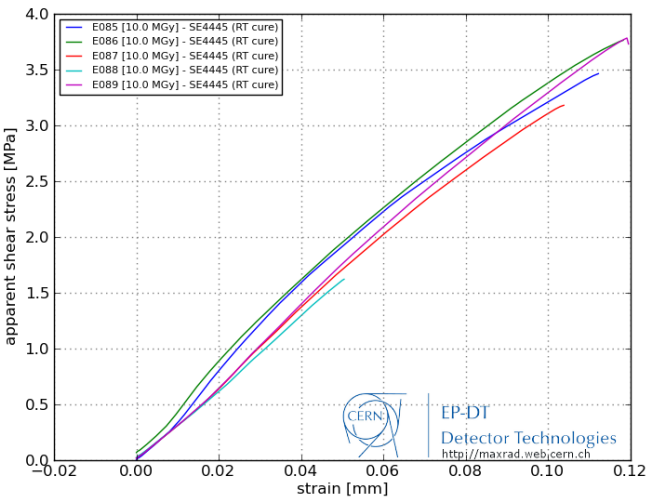


Figure 4.10: Apparent stress versus strain of SE4445 samples irradiated with a dose of 10 MGy [77].

4.5 Adhesive Mixing

Both SE4445 and Araldite 2011 are two-part adhesives and proper mixing of the parts is critical to the final strength of the bond between the modules and the carbon fiber supports. SE4445 is a two-part encapsulant gel and requires the two parts to be mixed with a volume ratio of one to one. Araldite is a two-part epoxy that also requires a volume ratio of one to one when mixed. The quality of an adhesive batch depends on the technique used for mixing and the parameters of the technique including speed and duration of the mixing process. Several methods of mixing have been investigated and are described here.

One method is to deposit each adhesive part into separate disposable containers and control the volume by measuring the mass prior to combining the two parts. The parts can be combined by use of a stirring rod and fine control of the rod can lead to decent results of the mix. The process is slow and prone to variable results.

The default method recommended by the adhesive manufacturers is to use a helical mixing tube and a caulking gun. The equipment for such a process is shown in Figure 4.11. The Araldite packaging container is loaded into a caulking gun and a helical mixing tube is attached to the open end of the container. The open end of the container has a locking mechanism to which the helical tube is attached. When the helical mixing tube is attached, the caulking gun applies pressure to the two parts of the adhesive container simultaneously, and the two parts are guided into the helical tube and mixed as they move through the helical tube. The mixed Araldite is deposited directly into a syringe that will in turn be used for precision dispensing. Before the Araldite is deposited into the syringe, some of the Araldite needs to be deposited into a disposable cup until the mix is a solid color. To fill the syringe with Araldite, the syringe is held vertically and the helical tube is inserted into the large open end of the syringe and a syringe tip is attached to the other end. A technique

of pulling the caulking gun plunger slowly to avoid air bubble build up in the syringe and raising the end of the helical tube as the syringe is filled is implemented.



Figure 4.11: Materials for mixing Araldite 2011 into a 5 ml syringe.

The default process, as has been described, produced quality results for the Araldite mixing. The mixing of SE4445 is more variable and prone to poor results. This is likely due to the low viscosity of the SE4445 and shorter pot life. The viscosity of SE4445 was found to change gradually. The best results are obtained if the SE4445 is used before one hour has elapsed since it was mixed. The pot life after mixing can be extended if the mixture is placed in a freezer and stored below -40 °C. Due to the complicated nature of mixing the SE4445, it is prudent to mix and freeze large batches of SE4445 at a time. The SE4445 is mixed into 5 ml (or 10 ml) syringes and stored in a freezer indefinitely. The protocol of freezing the SE4445 to prolong the pot life is not a recommendation from the materials data sheet but was discussed with an expert at the manufacturing facility (Dow Corning). The SE4445 from the freezer was tested periodically for six months and similar results were achieved throughout this period.

SE4445 undergoes a process of sedimentation in each of the two parts before mixing if it is stored for too long in one orientation or at too high of a temperature.

The manufacturer's recommendations suggest storing the two-part cartridge between 0 °C and 32 °C but do not comment on the orientation during storage. To avoid sedimentation, a daily schedule of rotating the SE4445 cartridges is implemented and they are kept in a refrigerator at 12 °C. Before mixing the cartridges are shaken with a paint shaker. The cartridges are shaken in two orientations for 5 minutes in each orientation.

A stabilizing setup was constructed to improve repeatability of mixing the SE4445 and can be seen in Figure 4.12. The caulking gun is held in place such that the two-



Figure 4.12: Setup for manual mixing of SE4445.

part container is face down and the helical tube is extended toward the ground. A metal rod is used to prop up the SE4445 caulking gun. Vertical application was preferable and provided the most consistent results. The caulking gun handle is squeezed to push the two SE4445 parts through the helical tube, which is made of translucent plastic. The quality of the mixture of the two parts can be observed by noting the change in color throughout the helical tube. The two parts begin to mix

1/3 of the way through the helical tube. The color changes from distinct white and dark parts to a light gray color as the SE4445 travels through the helical tube. The quality of the mix is again assessed after the SE4445 is pushed through the end of the helical tube. The initial mixture, of the material first pushed through, is poor and streaks of light and dark are visible. The SE4445 is expelled into a disposable cup in the amount of about 100 ml before the color becomes uniform. Subsequently 5 ml syringes are filled from the spout of the helical tube. With practice, air bubbles can be eliminated during the syringe-filling procedure. The pressure applied to the handle of the caulking gun must be uniform to avoid streaks of light and dark in the mixture inside the syringe.

Extending the helical mixing tube was investigated to see the impact on the quality of the mix of SE4445. The extension was made by attaching two helical mixing tubes together. The large bell connector on one helical mixing tube and the spout of the other were cut and the outer edges of both tubes were reshaped using a lathe and a lathe file, pictured in Figure 4.13. The two tubes were connected with a Yor-Lok fitting. One extended helical tube is compared to a commercially available longer helical tube. The commercially available option has a larger inner diameter that is not ideal for mixing the low viscosity SE4445. The quality of the mix was marginally improved by the extended mixing tube. A drawback of the extended tube was the increased difficulty to keep the spout steady during delivery to the syringe. This led to the increased possibility of capturing air in the SE4445.

A record of each syringe of SE4445 is kept in a log book attached to the freezer. Each syringe is marked with an identification code and records of the time the syringe was inserted into the freezer and the quality of the mixture in the syringe (i.e. notes on white or dark streaks visible through the syringe) are kept for reference when at a later time the syringe will be used for deposition tests. The syringe barrels are assembled with an on/off valve that allows SE4445 to flow only when the valve



Figure 4.13: (Left) Extension of the helical SE4445 mixing tube was investigated, using a lathe. (Right) the extended tube is longer and has a smaller inner diameter compared to the commercially available option.

is open. A cap is inserted in the end of the valve to prevent ice or other material from contaminating the opening when the syringe is in storage. The syringe barrel is marked with a fill line to measure the volume of SE4445 in each syringe and all syringes are consistently filled to 4 ml. After the syringe is filled with SE4445 a cap is inserted to block other materials from contaminating the mix before use. A set of assembled syringes is shown in Figure 4.14, and the freezer used for storing the SE4445 below -40 °C after mixing is shown in the background of Figure 4.14.

A study of the warm-up time for the freezer is shown in Figure 4.15. The power was turned off and the temperature of the freezer was recorded for the next three hours. The black points are the recorded temperature of the empty freezer during the warm up. The freezer was operating at a steady temperature below -50 °C before the study began.

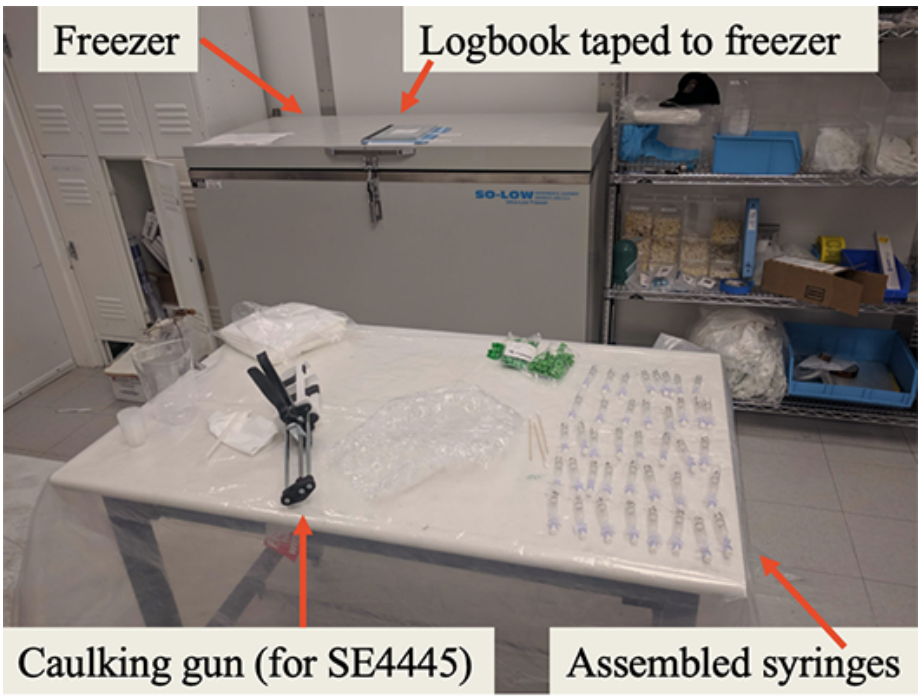


Figure 4.14: The SE4445 mixing station.

SE4445 syringes were stored in the freezer after the warm-up study had been performed and the freezer had reached its low temperature again. Repeated studies of the full warm-up curves after the storage of SE4445 in the freezer began were not practical due to the expected loss of SE4445 material.

Four aluminum blocks, approximately one inch thick, three feet long and one foot wide, were inserted into the freezer to prolong the cold temperature in the event of a power failure. The blue points in Figure 4.15 are obtained when the power to the freezer remained on and the second aluminum block was added to the freezer. At this point the second aluminum block was in the freezer and in equilibrium with the freezer temperature. The temperature rise due to inserting the room temperature aluminum block to the system is expected. A third aluminum block was inserted, with the power remaining on, to the freezer and the warm-up curve is shown in the red points in Figure 4.15. The warm-up curve of the red points has a lower slope

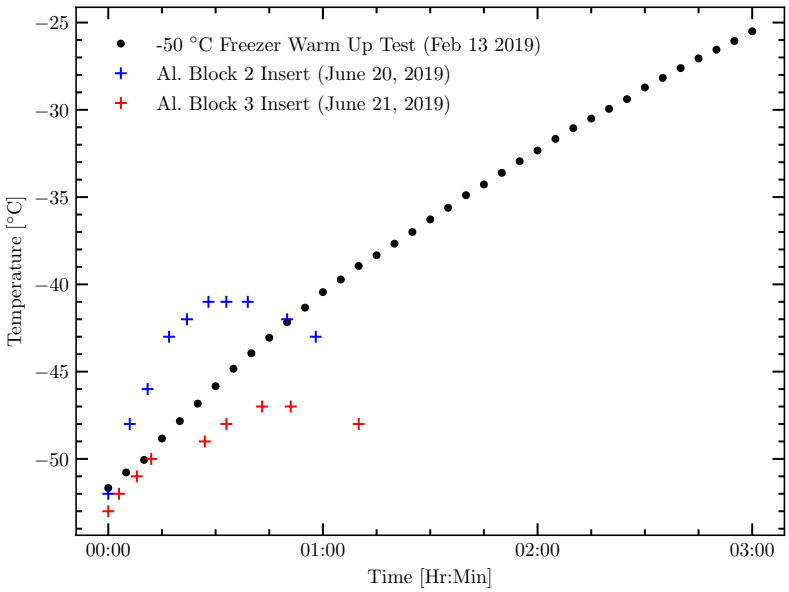


Figure 4.15: The warm-up curve of the freezer after a power cut is represented by the black data points. Two warm-up curves after aluminum blocks were inserted into the freezer, while the power was still on, are represented in the red and blue crosses.

than the blue points, because the temperature of the freezer system is maintained by the aluminum blocks already in the freezer. As a result of the insertion of the aluminum blocks, the warm-up curve of the freezer is expected to have a lower slope than was measured for the empty freezer.

During mixing of SE4445, air voids can be introduced into the mix. Air is not a good thermal conductor compared to SE4445 and a quality mixing process should minimize air in the final product. A vacuum de-airing step was investigated while developing the mixing procedures for the SE4445. Two syringes of mixed SE4445 inside of the vacuum chamber can be seen in Figure 4.16. The chamber has to be sealed after the syringes are placed inside. The vacuum pump can achieve 28 inHg in the chamber and air bubbles pulled through the SE4445 are observable. Two

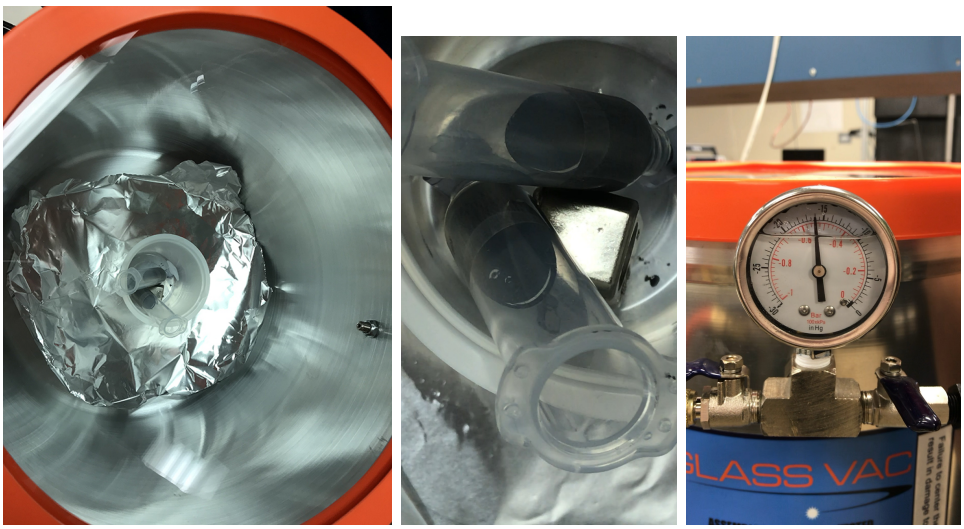


Figure 4.16: Vacuum chamber used for de-airing the SE4445 syringes. (Left) The contents of the vacuum chamber are visible through the the top view of the vacuum chamber. (Middle) Two syringes of SE4445 are de-aired at a time. (Right) The vacuum pressure of 28 inHg is applied to the chamber.

syringes of SE4445 are placed in the vacuum chamber before the vacuum pressure is applied. Air bubbles can be seen as the vacuum is applied, coming through the top. After about 5 minutes the air bubbles stop. The amount of time that the de-airing took away from the workable time (the time before curing) resulted in the removal of this process from the mixing procedures of many syringes.

An alternative solution for adhesive mixing is to use a centrifugal planetary mixer. This mixing process can include de-airing into the mixing step, if the mixer has a vacuum option. A uniform mixture is repeatable because computer controlled mixing is introduced. The mixing concept is shown on the left of Figure 4.17 [134]. The material is mixed in a container that is rotated about two axes simultaneously. Several industrial companies manufacture centrifugal planetary mixers, one of which is FlakTech SpeedMixer. An image of the SpeedMixer machine is shown on the right of Figure 4.17.

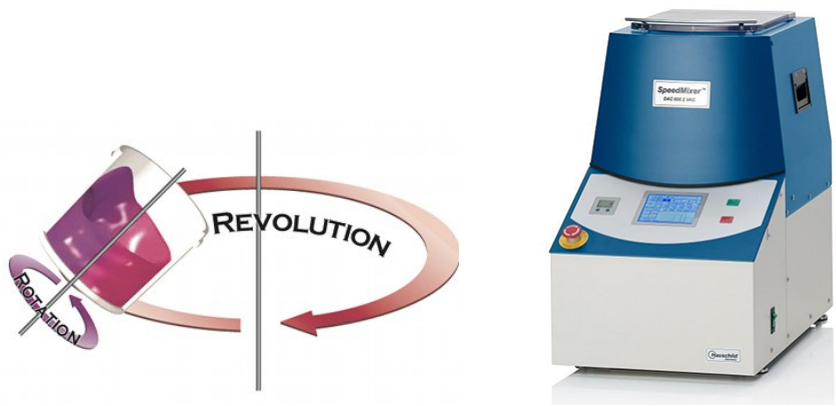


Figure 4.17: (Left) The concept of the planetary, centrifugal mixer involves rotation of the mixing material around two axes [134]. (Right) The SpeedMixer allows for streamlined use with display screen controls and programmable settings.

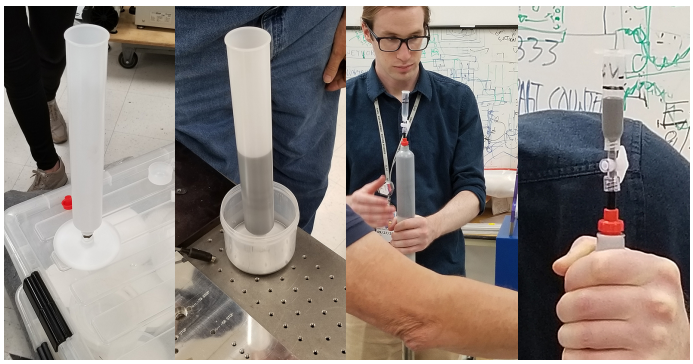
A demonstration was arranged to mix and test a cartridge of SE4445 using a SpeedMixer DAC 600.2 VAC model. The mixing process took under one minute. The contents of the SE4445 are delivered to a mixing cup, (4.18a). The cup is placed into the planetary mixer, (4.18b). The cup is mixed in the planetary mixer, (4.18c). The planetary mixer is stopped, (4.18d) and the temperature is measured. The mixed contents of the cup have a very uniform color, (4.18e).



(a) (b) (c) (d) (e)

Figure 4.18: Illustration of the sequence of mixing SE4445 with a centrifugal, planetary mixer.

The temperature of the contents of the cup was measured with a handheld infrared temperature meter before and after mixing. The temperature before mixing was 22.8 °C and the temperature after mixing was 27.4 °C. The mixed SE4445 was delivered to 5 ml syringes using a transfer tube shown in Figure 4.19. The transfer tube is shown, with the sealed fitting designed for the mixing cup (4.19a). The contents of the mixing cup are delivered to the transfer tube by applying downward pressure on the sealed fitting (4.19b). A cap is inserted in the large open end of the transfer tube until it makes contact with the SE4445 (a thin wire is inserted with the cap to allow air to flow past the cap until contact with the SE4445 is made), and the filled transfer tube is removed from the sealed fitting and turned upside down (4.19c). Mixed SE4445 is delivered to a syringe by applying pressure to the cap (4.19d). When the syringe is filled, the valve on the syringe is closed and another syringe is attached for filling.



(a) (b) (c) (d)

Figure 4.19: Illustration of the sequence involved in transfer of SE4445 from the mixing cup to syringe, demonstration.

The mixing and transfer process could be optimized with further tests. Improvements would include mixing the contents at a lower temperature and speeding up the delivery from the mixing cup syringes by filling multiple syringes simultaneously directly from the mixing cup.

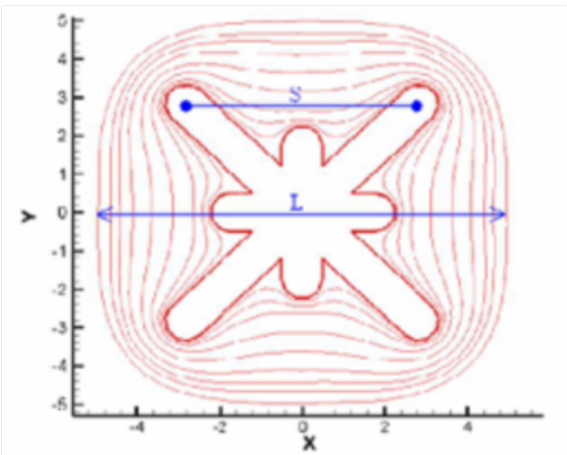


Figure 4.20: Simulation of liquid pattern spreading in two dimensions. Full coverage of the rectangular surface is achievable with such an initial dispensed pattern. Image was originally published in [117].

4.6 Adhesive Deposition Patterns

Several deposition patterns are investigated. These included application from a single point centered on the module location, a rectangle, a circle, and a "star" pattern (see the dark red pattern in Figure 4.20). The patterns are investigated using an experimental setup as follows. A Nordson EFD fluid dispenser is connected to an air supply and allows air to be applied at a user-defined pressure. A syringe is filled with adhesive using a helical tube mixer. The open end of the syringe is connected to the fluid dispenser with a flexible plastic tube; a syringe tip is connected to the other end. The adhesive is applied through the syringe tip by controlling the pressure and duration of air supplied by the fluid dispenser. The syringe is held by hand and an adhesive pattern is deposited on a glass plate. When the pattern is complete, a 22 mm $\times$ 22 mm microscope cover glass is placed on top of the adhesive. Adhesives spread between the two glass surfaces on the order of minutes and cure on the order of hours. Two samples between glass, and a third without a cover glass, made with

the star pattern deposition of SE4445 and Araldite dots in the corners are shown in Figure 4.21. The samples shown in Figure 4.21 are made through controlling the syringes by hand. Too much variability is introduced when depositing the adhesives

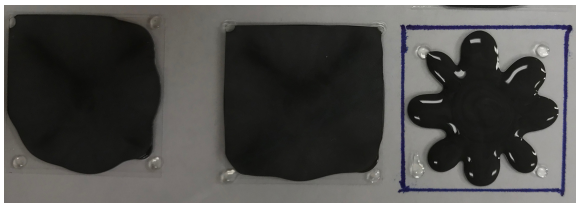


Figure 4.21: SE4445 adhesive samples using the star pattern. Samples spread between the two surfaces.

by hand, and an important conclusion from the early samples is that a computer controlled robot is needed to obtain repeatable results. Nevertheless, the deposition pattern could be experimented with quickly when depositing the adhesives from the syringe by hand and this technique is used to determine the optimal deposition pattern.

The adhesive samples can be judged based on a few observations. Ensuring that the sample has cured is a first step, and can be determined by applying pressure to the sample in several directions, most importantly parallel to the glass surface. Typically the samples will strongly resist movement if cured; thick SE4445 samples can have a slight spring behavior like a rubber band.

Using glass allows the samples to be visually inspected. Full coverage of the surface is optimal, although lower coverage of the module surface may be sufficient. Some adhesive patterns lead to larger air voids in the cured samples. The number of these voids is significantly decreased in the star pattern. These voids can be observed by placing a lamp behind the samples. Finally, the thickness and the levelness of the samples can be measured using a height gauge or an automated programmable tool like a coordinate measuring machine (see Section 4.13). The star pattern is selected

as the optimal pattern for depositing the adhesives, because it resulted in the best surface coverage and smallest air voids.

The deposition when controlling the syringe by hand leads to variable results in the thickness of the lines. Careful inspection of the sample on the far right in Figure 4.21 (no cover glass is applied to this sample) reveals that the width of each line is variable. The thickness (in the direction into the page) of the SE4445 is correlated with the width of the line and has a large impact on the cover glass that is placed above the deposition. Precise placement of the Araldite 2011 dots is also highly variable.

4.7 Robot-Controlled Adhesive Deposition

Using computer numeric control of the adhesive deposition allows for precision tuning and repeatability of results. A Nordson Robot Machine is used to control the deposition patterns of Araldite 2011 and SE4445. It has three axes of control and a specialized computer program can be used for giving commands. The computer program can control the on-off state of the EFD air dispenser when it is connected into the system. The Nordson Robot Machine pictured in Figure 4.22 is equipped with a pressure-activated height measurement along one of the three axes of control.

A custom fitted syringe holder was designed and fabricated for the Nordson Robot Machine and is pictured in Figure 4.23. The custom syringe holder is crucial for allowing quick insertion and removal of syringes and avoiding an open spout of a syringe filled with adhesive. The head acts as a clamp to hold a syringe in place and allows a user to easily switch syringe heads. A Luer lock connector is used between the spout of the syringe and the syringe tip to allow different sized syringes to fit in the custom syringe holder. The Nordson Robot Machine has a pre-made syringe



Figure 4.22: Adhesive testing station in the clean room at SLAC, including a Nordson Robot Machine and a fluid dispenser. The computer used for controlling these instruments is to the left of the image (not pictured).



Figure 4.23: The custom syringe holder for the Nordson Robot, (left) top view and (right) front view.

holder, but it is designed such that the Luer lock and the syringe spout must be inserted through opposite ends of the syringe holder to connect them.

In Figure 4.24, the adhesive samples are made with SE4445 and Araldite 2011

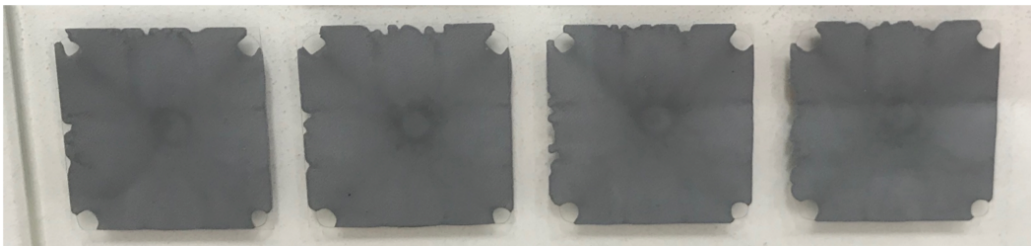


Figure 4.24: Image of four adhesive samples between two glass plates.

adhesives. The samples are shown between two glass surfaces. In Figure 4.25 (left), the sample on the top does not have a cover glass placed on top and the sample on the bottom shows the result of a cover glass placed by the robot on the deposited adhesive. The same adhesive pattern is used for both the top sample and the bottom sample. The image on the right is of the same two samples, viewed through the other side of the base glass plate.

Back-lighting the samples, as in Figure 4.26, is used to inspect air voids in the

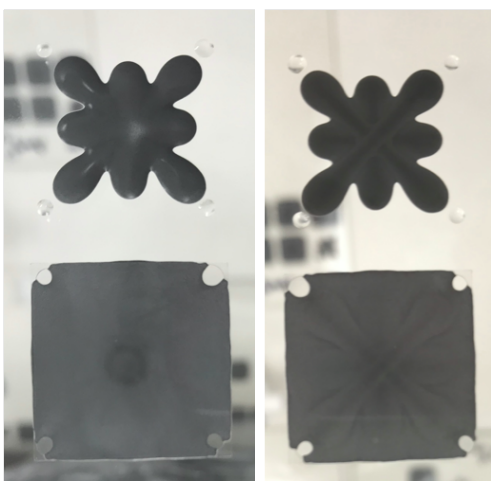


Figure 4.25: Adhesive samples deposited on a glass base plate. The (left) view from the front of glass and (right) through the back of the glass are important for characterizing the SE4445 spread. The adhesive pattern is investigated (top samples) without a cover glass placed on the pattern and (bottom samples) with a cover glass placed on top of the pattern.

sample. The air voids can be minimized through the mixing process and by dedicated cleaning of the bonding surfaces immediately prior to the bonding. Several carbon fiber surfaces were used to investigate the impact on the SE4445 spread (Figure 4.27). The carbon fiber samples with smoother finishes resulted in a more uniform coverage of the SE4445. The carbon fiber shown in the image has a smooth finish.

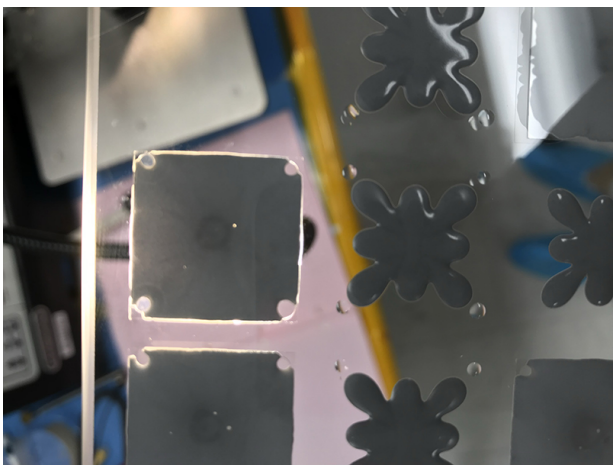


Figure 4.26: Image of a back-lit adhesive sample.

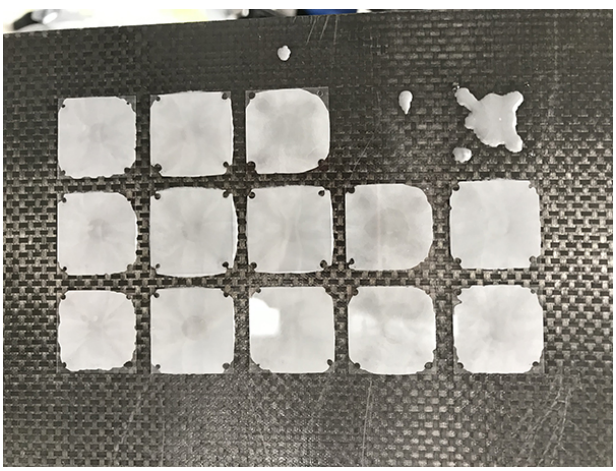


Figure 4.27: SE4445 samples on carbon fiber.

4.8 Module Placement Fixture

The cover glass needs to be placed down slowly and parallel with the glass base plate for optimal results. A vacuum suction device operated by hand is used for testing, but leads to non-level and misaligned placements. For the final loading process a fixture must be designed for placing modules on the adhesive. A prototype for this fixture is designed and tested for the samples. This fixture can be seen in Figure 4.28. It is fabricated with Lexan plastic in order to utilize the transparent properties and allow for visual observation of the sample preparations. A vacuum channel is drilled through the Lexan and allows for attachment of a cover glass. When a vacuum pump is connected and turned on, the cover glass remains in place. The attachment of the cover glass can be seen on the left of Figure 4.28. Screws are used in the corners to set the resting height and can be calibrated with a metal wire of known thickness. The micrometer control setup seen in Figure 4.28 (right) is implemented to allow controlled, level lowering to a specified height. Some success is achieved with the Lexan prototype, but the application of the cover glass with the prototype is not fast enough for a streamlined loading process. In the preparation of ten samples, the placement of a few slides with the Lexan fixture is possible. After this, the SE4445 starts to cure and the cover glass placement no longer results in adequate spreading.

For production, three modules will be placed in parallel. They will be held by vacuum with the pads shown in Figure 4.29. Micrometer control from three points in the fixture is planned.

4.9 Robot Module Placement

As shown in Figure 4.30 (left), a cover glass is picked up from a holding fixture. The robot is programmed to come in contact with the cover glass, wait for the vacuum to

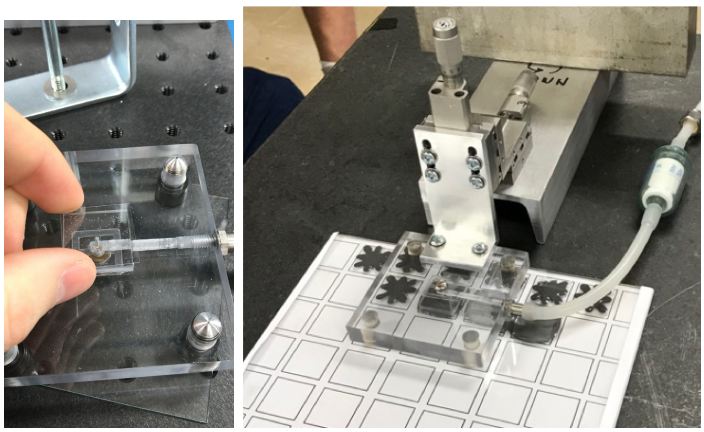


Figure 4.28: The placement fixture fabricated with Lexan is used for testing of cover glass placements.

be turned on, and then lift the cover glass out of the holding position. In Figure 4.30 (middle) a cover glass is placed onto an adhesive deposit. A pressure application device was built to investigate the impact of prolonged pressure on the samples, Figure 4.30 (right). The device surrounds a sample and pressure is applied to the sample in the vertical direction. Different pressures were investigated by applying

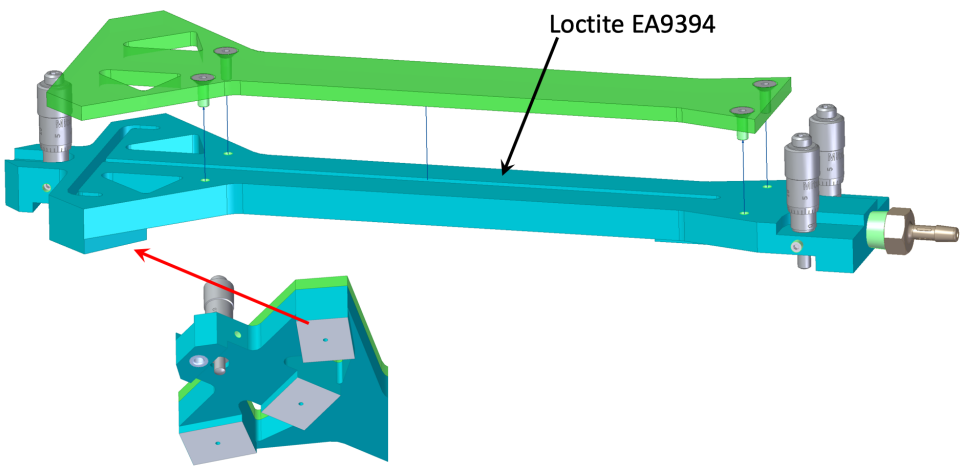


Figure 4.29: Design of a production single module fixture [139].

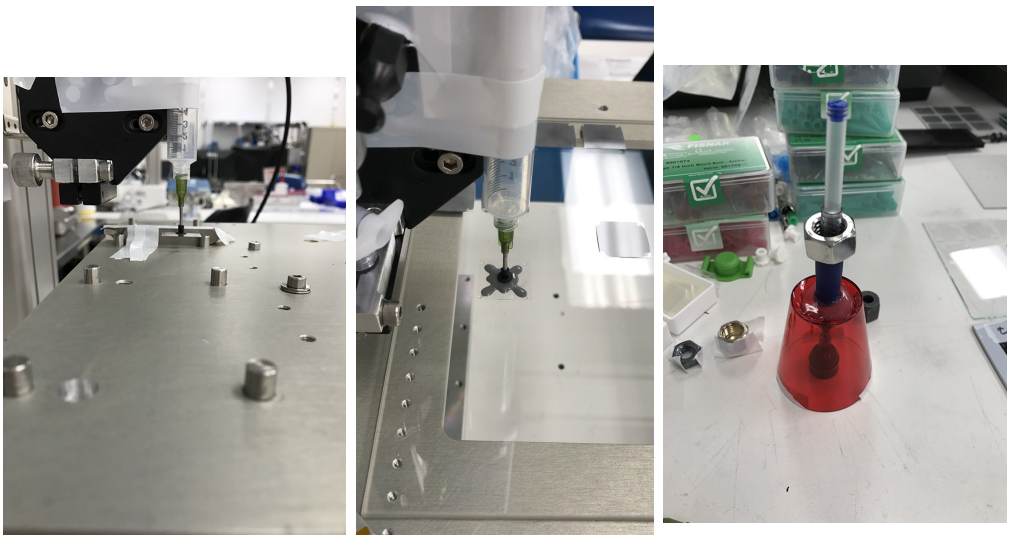


Figure 4.30: (Left) A cover-glass slide is picked up using the robot arm and (middle) placed on an adhesive sample. (Right) A pressure application device prototype.

weights ranging from 5 g to 20 g, by adding steel threaded nuts to the center column of the device.

4.10 Module-to-Framework Loading Strategy

A strategy for loading a coupled disk is presented in this section. The limitations on the loading are due to the pot life and cure times of SE4445 and Araldite 2011. It is determined empirically that SE4445 remains usable in a syringe after removal from the freezer for up to one hour, and after one hour the results are sufficiently compromised to warrant the disposal of the syringe. There is also a time limit on the usefulness of the SE4445 after deposition to the bonding surface. This time is referred to as the air time and is much shorter than the syringe pot life The maximum allowable air time for SE4445 is 5 minutes. For best results the module should be placed on the dispensed SE4445 before the maximum allowable air time has elapsed. The syringe pot life of Araldite 2011 is 50 min and the maximum allowable air time

is 20 minutes. In order to meet these time constraints a strategy for the loading procedures is necessary.

A breakdown of the times for each step of the loading process is reported here. The amount of time to mount the Araldite 2011 syringe on the robot and expel an initial amount from the syringe is about 25 seconds, and is extended to 1 minute to include a safety factor. The amount of time for the user to remove the Araldite syringe from the robot and mount the SE4445 syringe is about 1 minute 40 seconds, and is expanded to 2 minutes to include a safety factor. The robot program takes 26.96 seconds to deposit one SE4445 star pattern (for one FEI4 chip) and 1 minute 48 seconds to deposit four star patterns (for one quad module). The time to deposit 4 Araldite dots for 1 chip is 41 seconds. Another notable time is the room temperature curing time of SE4445, after the modules have been placed on the adhesive depositions, about 24 hours.

Before the loading procedures begin, all surfaces should be cleaned, the holders that keep syringes vertical when they are not in use should be cleared, and the mixing materials for Araldite should be prepared. These materials include the syringe tip, Luer lock, 3 cc syringe, helical mixing tube, Araldite cartridge (checking that it is not expired), and the Araldite caulking gun (all pictured in Figure 4.11).

Th robot calibration should be performed with the assembled Araldite syringe prior to delivering the Araldite to the syringe. The calibration requires the user to manually control the robot and record the Araldite tip height when it is touching the loading surface. This information is then passed to the robot loading program by the user.

The contents of the SE4445 freezer should be checked by referencing the freezer logbook, and a choice of which syringe will be used should be made prior to starting the procedures. Clean wipes should be made available at the loading station.

Figure 4.31a shows the inner ring of a coupled disk and an outline of where the nine modules will be placed. The following procedures can be used to load the inner ring. Notes on timing are included to ensure that the air time and syringe pot life times are not exceeded for either SE4445 or Araldite 2011 during the process.

1. Load Araldite syringe into robot. Takes 1 min.
2. Remove SE4445 syringe from freezer and place in syringe holder next to robot.
3. Wait 4 minutes before starting step 4 to allow enough time for SE4445 to thaw.
4. Figure 4.31b: Deposit Araldite dots for the nine modules on the inner ring. This takes 6 min 9 sec to complete in the robot program. The maximum Araldite syringe time is 11 min 9 sec from, and including, step 1.
5. Switch from Araldite syringe to SE4445 syringe, takes 2 min.
6. Figure 4.31c: Deposit SE4445 for 3 sequential modules, takes 1 min 30 sec.

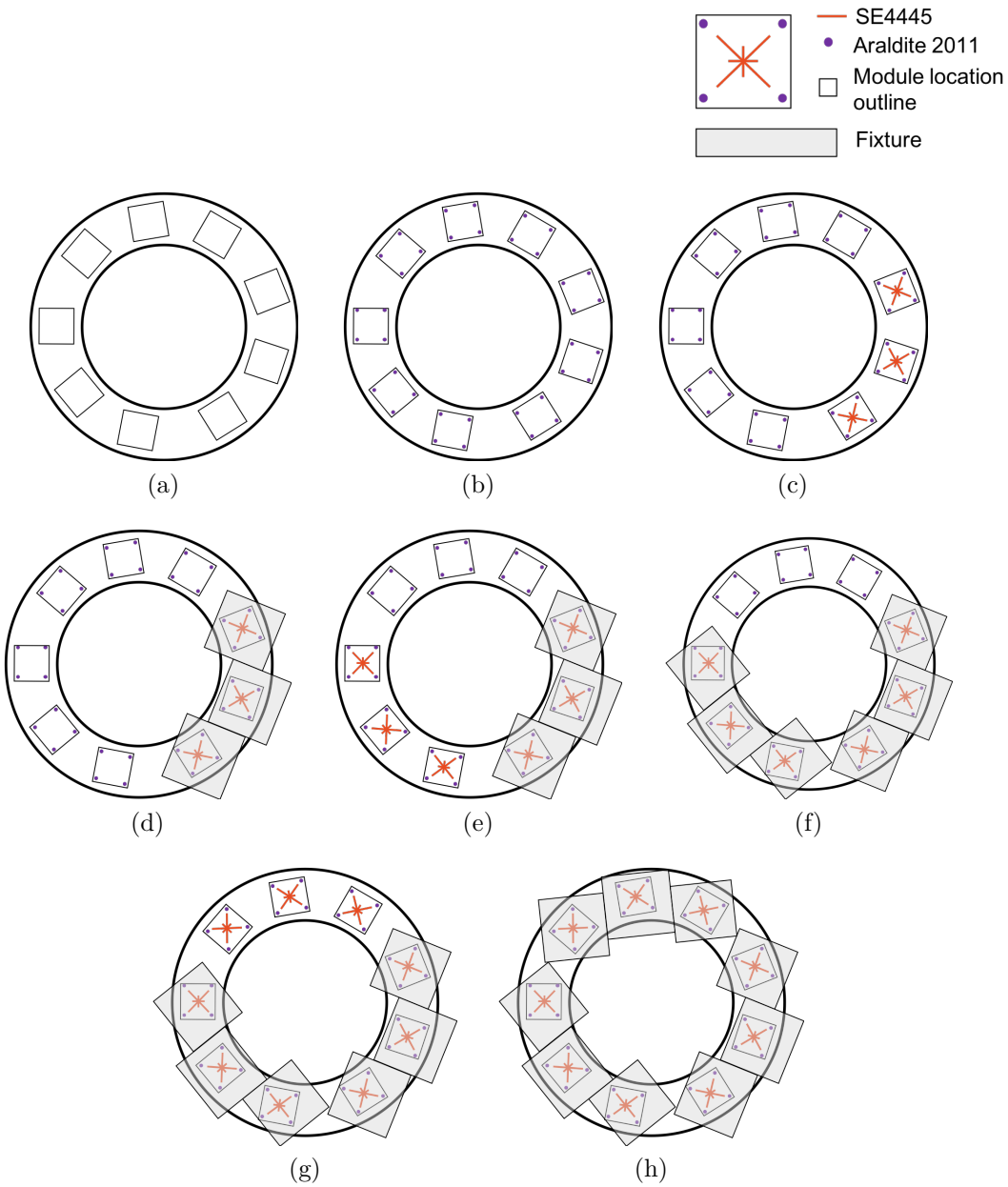


Figure 4.31: Loading strategy for the inner ring of a coupled disk. The procedures are described in the text. The Araldite is applied first, then sets of three SE4445 adhesive patterns are applied and the modules are placed with the placement fixture. Dispensed Araldite and SE4445 are represented by the purple and orange patterns, the future and present module locations are outlined, and the applied fixture is represented by the semi-transparent boxes. The figures and patterns are not drawn to scale and are for illustrative purposes only.

7. Figure 4.31d: Place fixture for 3 modules, takes 1 min. Note - the maximum air times for the group of placements is 11 min for Araldite and 3 min for SE4445. The fixture is left in place while the next procedures are undertaken.

8. Figure 4.31e: Deposit SE4445 for 3 sequential modules, takes 1 min 30 sec.

9. Figure 4.31f: Place fixture for 3 modules, takes 1 min. Note - the maximum air times for the group of placements is 12 min for Araldite and 3 min for SE4445. The fixture is left in place while the next procedures are undertaken.

10. Figure 4.31g: Deposit SE4445 for 3 sequential modules, takes 1 min 30 sec.

11. Figure 4.31h: Place fixture for 3 modules, takes 1 min. Note - the maximum air times for the group of placements is 13 min for Araldite and 3 min for SE4445. The fixture is left in place while the next procedures are undertaken. The maximum SE4445 syringe time is 19 min 39 sec.

Similar to that for the inner ring of the coupled disk, a loading strategy for the outer ring is prepared. The outer ring holds ten quad modules. Each quad module is made of four front end chips, and the quad modules will be attached to the disk with four of the developed adhesive patterns - one for each front end chip. The placement fixtures for the quad modules will place two quad modules at a time. The placement fixtures will remain in the loading position until the adhesive is cured. Figures 4.32, 4.33, and 4.34 illustrate the loading procedures for the outer ring. Figure 4.32a shows the intended locations of the ASICs of the quad modules on the outer ring, before loading. The loading procedures are detailed here, and the syringe air time and syringe pot life are noted for reference.

1. Load Araldite syringe into robot. Hook into air supply, expel small amount of Araldite through the tip and clean the tip. This takes 1 min.

2. Remove SE4445 syringe from freezer and place in syringe holder next to robot, will be thawed after step 3.

3. Figure 4.32b: Deposit Araldite dots for 4 quads (corresponding to 16 chips). This takes 10 min 56 sec in total and 5 min 28 sec for the second two quads.

4. Switch from Araldite syringe to SE syringe, takes 2 min.

5. Figure 4.32c: Deposit SE4445 for 2 quads (corresponding to 8 chips). This takes 4 min.

6. Figure 4.32d: Place fixture to load two quads. This takes 1 min. The maximum Araldite air time for these two quads is 18 min. The maximum SE4445 air time for these quads is 5 min.

7. Dispense SE4445 into throwaway cup (to maintain flow). This takes 1 min.

8. Figure 4.32e: Deposit SE4445 for 2 quads (corresponding to 8 chips). This takes 4 min.

9. Figure 4.32f: Place fixture to load two quads. This takes 1 min. The maximum Araldite air time: 18 min. The maximum SE4445 air time: 5 min.

10. Load Araldite Syringe. Takes 1 min.

11. Figure 4.33a: Deposit Araldite dots for 4 quads (corresponding to 16 chips). This takes 10 min 56 sec in total and 5 min 28 sec for the second two quads.

12. Switch from Araldite syringe to SE syringe, takes 2 min.

13. Figure 4.33b: Deposit SE4445 for 2 quads (corresponding to 8 chips). This takes 4 min.

14. Figure 4.33c: Place fixture to load two quads. This takes 1 min. The maximum Araldite air time for these two quads is 18 min. The maximum SE4445 air time for these quads is 5 min.

15. Figure 4.33d: Deposit SE4445 for 2 quads (corresponding to 8 chips). This takes 4 min.

16. Figure 4.33e: Place fixture to load two quads. This takes 1 min. The maximum Araldite air time: 18 min. The maximum SE4445 air time: 5 min

17. Load Araldite Syringe. Takes 1 min.

18. Figure 4.34a: Deposit Araldite dots for 2 quads (corresponding to 8 chips). This takes 5 min 28 sec. This is the last time the Araldite is used in the the outer ring loading procedures. Syringe time is 49 min, starting from, and including, step 1 of these procedures.

19. Switch from Araldite syringe to SE syringe, takes 2 min.

20. Figure 4.34b: Deposit SE4445 for 2 quads (corresponding to 8 chips). This takes 4 min.

21. Figure 4.34c: Place fixture to load two quads. This takes 1 min. The maximum Araldite air time for these two quads is 13 min. The maximum SE4445 air time for these quads is 5 min. SE4445 syringe time is 55 min, starting from, and including, step 2 of these procedures.

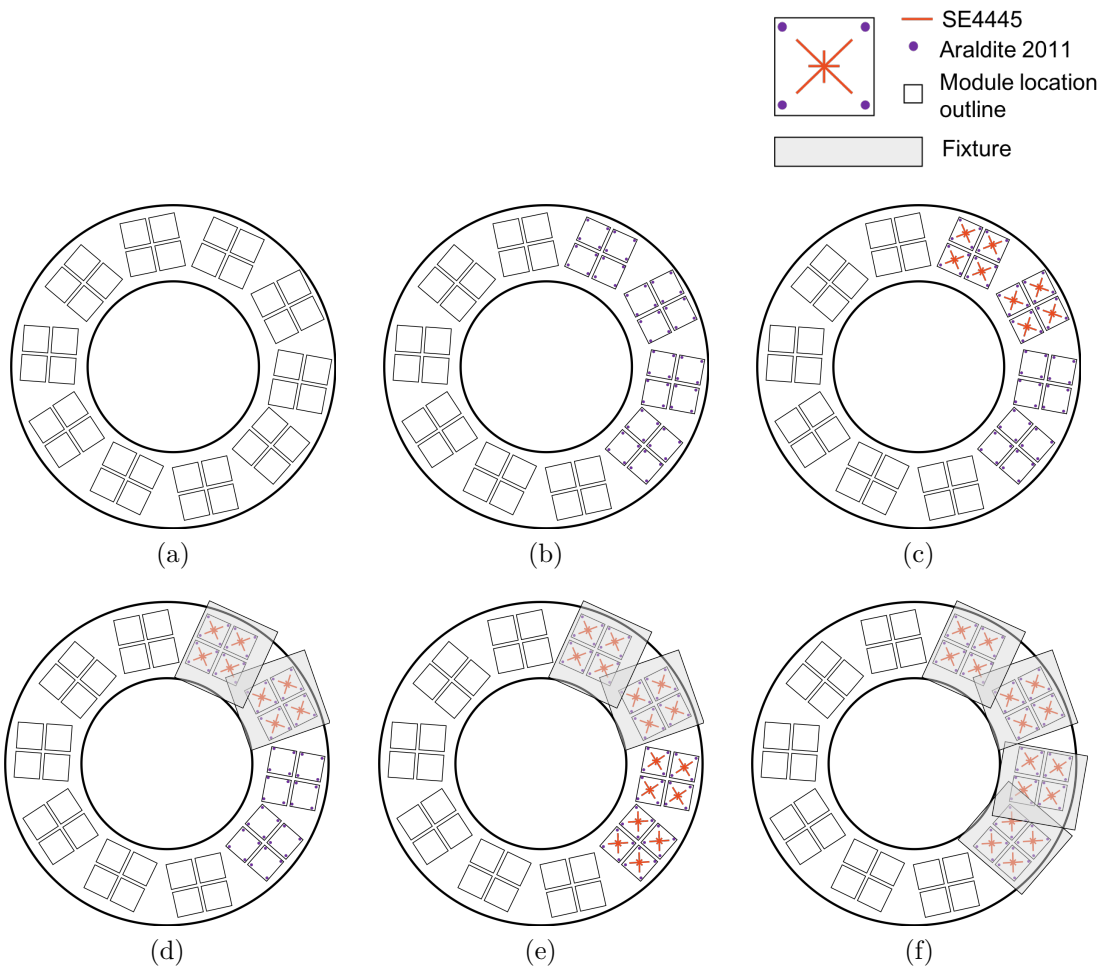


Figure 4.32: Loading strategy for the first four quad modules in the outer ring of the disk. The procedures are described in the text. The Araldite is applied first, then the SE4445 adhesive patterns are applied and the modules are placed with the placement fixture in sets of two modules at a time. Dispensed Araldite and SE4445 are represented by the purple and orange patterns, the future and present module locations are outlined, and the applied fixture is represented by the semi-transparent boxes. The figures and patterns are not drawn to scale and are for illustrative purposes only.

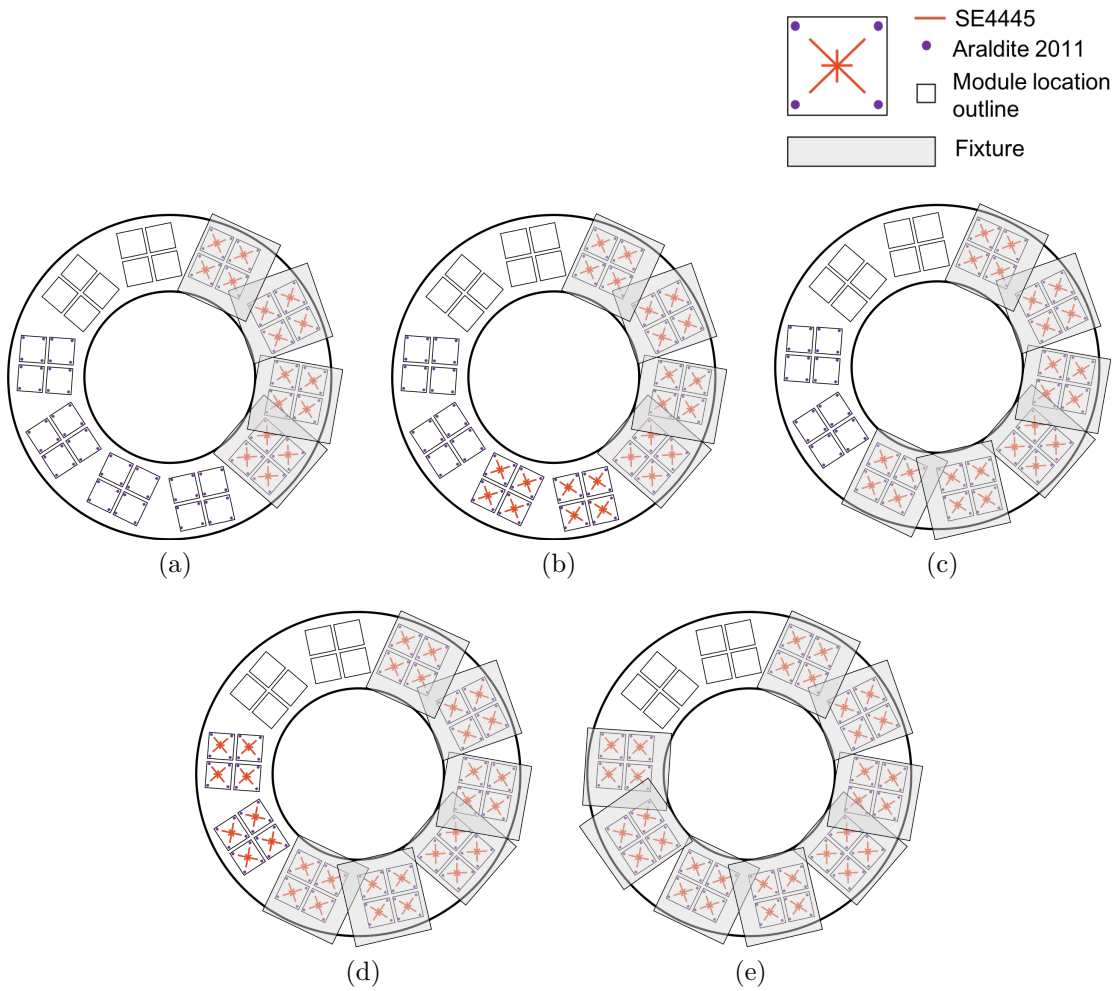


Figure 4.33: Loading strategy for the second four quad modules in the outer ring of the disk. The procedures are described in the text. The Araldite is applied first, then the SE4445 adhesive patterns are applied and the modules are placed with the placement fixture in sets of two modules at a time. Dispensed Araldite and SE4445 are represented by the purple and orange patterns, the future and present module locations are outlined, and the applied fixture is represented by the semi-transparent boxes. The figures and patterns are not drawn to scale and are for illustrative purposes only.

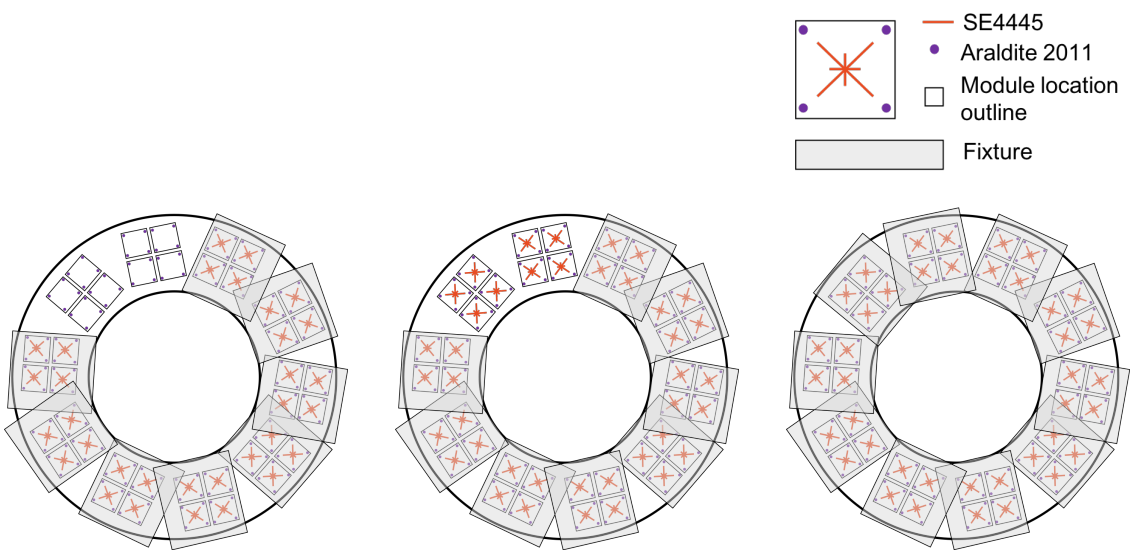


Figure 4.34: Loading strategy for the last two quad modules in the outer ring of the disk. The procedures are described in the text. The Araldite is applied first, then the SE4445 adhesive patterns are applied and the modules are placed with the placement fixture. Dispensed Araldite and SE4445 are represented by the purple and orange patterns, the future and present module locations are outlined, and the applied fixture is represented by the semi-transparent boxes. The figures and patterns are not drawn to scale and are for illustrative purposes only.

4.11 Prototype Assembly

A demonstration of the loading procedures was designed and executed in the construction of four stavelets. A stavelet is a miniature version of a stave.

A model module, called a heater, is used to mimic the heat load of a module. The process of assembling the heaters was developed and is depicted in Figure 4.35. A spare heater with one corner missing is shown. The platinum coated silicon heater is placed in a custom designed and fabricated aluminum fixture, with the platinum side up. Solder wick is cut to length and held in place by aluminum bars that are screwed down to apply pressure. Once the heater and wicks are assembled in the aluminum fixture, as shown in the middle image, the fixture is placed on a hot plate and brought to 220 °C. The temperature is monitored with a thermocouple fastened to an aluminum block, of the same thickness as the fixture, also placed on the hot plate. Solder is applied to the space between the wick and the heater, for both wicks. The fixture and heater are carefully removed from the hot plate and allowed to cool. Figure 4.36 shows an assembled heater the size of a quad module.

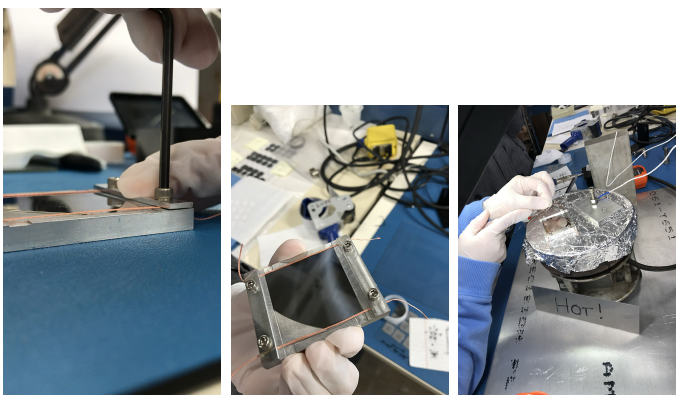


Figure 4.35: (Left and middle) Solder wicks and a silicon heater are held in place with a custom aluminum fixture. (Middle) The fixture is placed on a hot plate, where solder is applied between the heater and the solder wick.

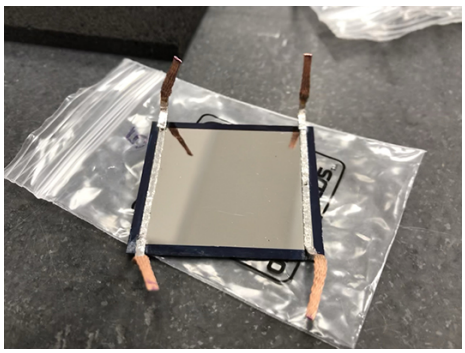


Figure 4.36: A fully assembled platinum coated silicon heater with solder-attached leads.

Eight platinum coated silicon heaters with dimensions of a quad sized module are prepared for attachment to four unloaded carbon fiber stavelets. Electrical leads are soldered to two parallel edges of the heaters. The unusually large application of solder required for this job led to the development of a specialized aluminum fixture for holding the heaters and electrical leads steady on a hot plate. The heaters reach the melting point of solder when resting on the hot plate. No soldering iron is required as a result. The solder is applied between the solder wick and the heater and then removed from the hot plate and allowed to cool.

A program was developed to deposit four Araldite 2011 dots in the corners of the eventual heater location and then a star pattern of SE4445 centered on the heater location. This program is developed to be applied to any horizontal surface in the robot volume. The adhesive design for the stavelets is based on the design of single sized modules but scaled to the size of a quad module. An exact scaling relation of all parameters of the deposition is not possible given time constraints resulting in the requirement of additional testing with large glass samples. In order to perform tests of larger samples a technique of cutting large microscope cover glass to the quad size dimension is developed. This technique involves a diamond tip pen tool and a piece of thin sheet metal to guide the cut. With many quad sized glass modules the

development of quad module sized adhesive depositions that result in a 150 μm thick adhesive connection is achieved.

A fixture is developed for holding the empty stavelets in place during loading. The fixture is shown in Figure 4.37 (left). Another fixture is developed for holding the heaters in place prior to their being picked up by the robot arm. Movement of the stavelet is constrained in three directions to counterbalance the movement of the robot. An empty stavelet is placed in the fixture, shown in Figure 4.37 (right). The complete setup of the stavelet loading station is shown in Figure 4.38.

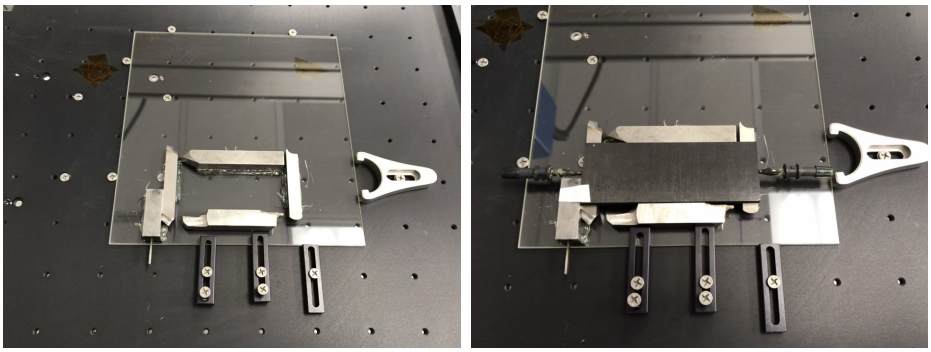


Figure 4.37: A holding fixture used for loading a stavelet.

Prior to loading, an empty stavelet is placed in the loading fixture. When the robot program is executed, it compensates for the height of the stavelet, then it applies the Araldite dot pattern to the stavelet surface. After applying the Araldite dots the robot waits in a holding position while the user exchanges the Araldite syringe for the SE4445 syringe. At the user's direction (after the syringes are switched) the robot applies the SE4445 star pattern to the stavelet surface. Once the deposition process is complete, a heater is placed in its holding fixture. The electrical leads must be positioned so that they will not interfere with the robot pickup tool. When the heater is in position, at the user's direction, the robot proceeds to pick up the heater and then performs the placement operations. The robot program is designed to lower the heater into the placement position slowly (a parameter that is finely

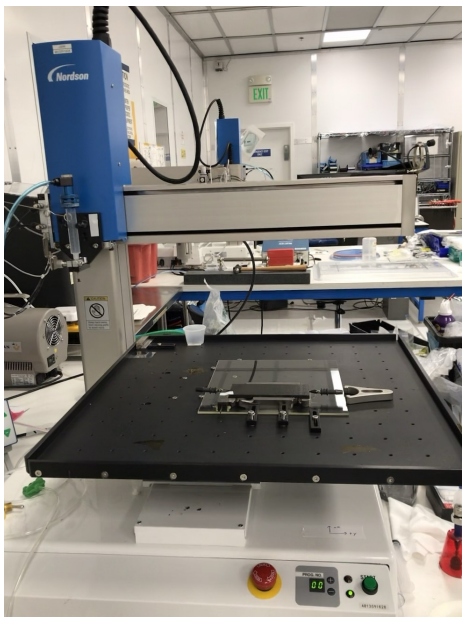


Figure 4.38: The robot module loading station. An empty stavelet held in the loading fixture is being prepared for the loading demonstration.

tuned). After the first heater is loaded to the stavelet the operations are repeated for the second heater in a position next to the first.

The loading of one quad sized heater is depicted in Figure 4.39. On the upper left, the Araldite dots are applied to the surface of the stavelet. On the upper right, SE4445 is deposited on the stavelet. In the lower left, the robot picks up an assembled heater, through a suction cup. On the lower right, the robot places the heater on the adhesive pattern for attachment to the stavelet.

Two of the four stavelets had heaters that were loaded without Araldite dots in the pattern. This is done by design to aid in further irradiation and testing qualifications. The four loaded stavelets are shown in Figure 4.40. Residual white tape is seen on the corners of the stavelets. This provided stability in the fixture during the loading process - when the heaters were attached to the stavelets.

A demonstration of the adhesive deposition in the pattern of a coupled ring disk is

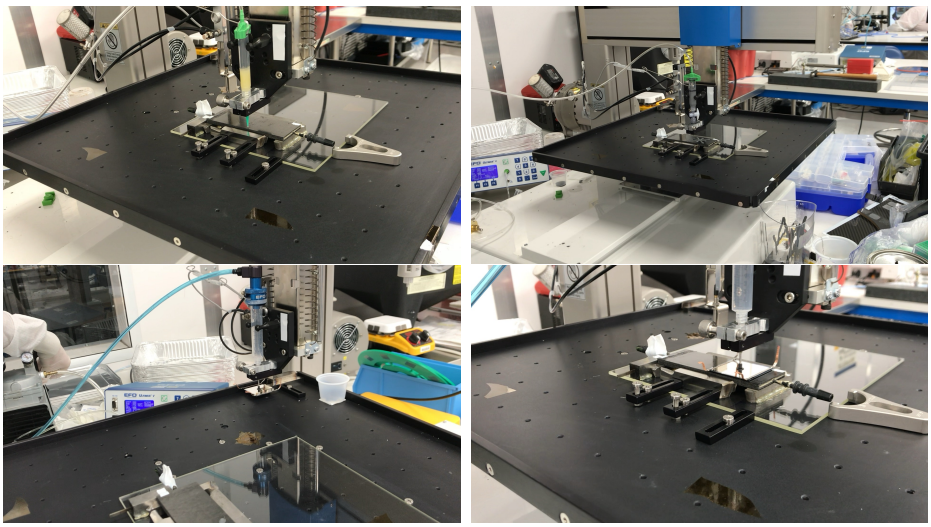


Figure 4.39: The stavelet loading procedures are to (upper left) apply Araldite 2011 pattern for one sensor, (upper right) apply SE4445 adhesive pattern for one sensor, (lower left) pick up the sensor from the holding fixture, and (lower right) place the sensor on the adhesive pattern.

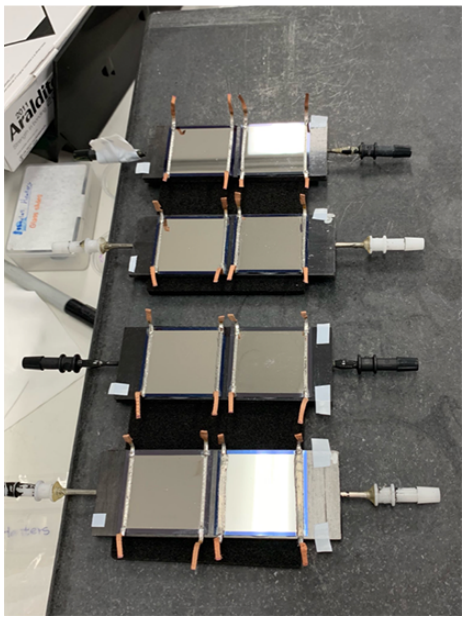


Figure 4.40: Four fully assembled stavelet prototypes.

shown in Figure 4.41. The adhesives (Araldite 2011 and SE4445) are deposited using a Nordson Robot machine. The program implements the rotations and translations, such that the disk does not need to be removed from the robot machine during loading.



Figure 4.41: Adhesive deposition in the pattern of a coupled ring disk.

Coupled disk adhesive application is demonstrated in Figure 4.41. Circular pattern design and pattern rotations are introduced to the robot program and are demonstrated in the test on a single large glass plate. This test verifies the ability of the robot to deposit adhesive for a full coupled ring with re-positioning of the ring - an advantage for precision loading.

4.12 Preparations for Correcting Loading Mistakes

Contingency preparations for loading mistakes are prudent given the experience of previous experiments. Figure 4.42 shows the number of production IBL modules that required corrections due to loading mistakes. The module loading procedures should be developed so that they reflect the lessons learned from the past. However, it is

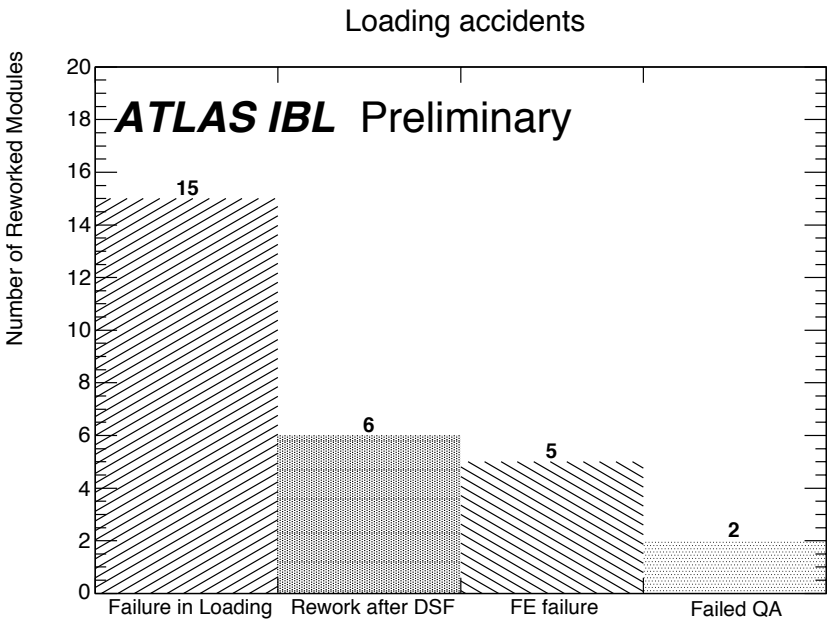


Figure 4.42: ATLAS IBL loading mistakes [14].

not possible to predict what will happen in a new environment with the intrinsically different parameters of a new detector. Investigation of possible recourse in the event of a loading failure has been undertaken. It is found that SE4445 bonds can be broken with the use of isopropyl alcohol and a large gauge wire. Figure 4.43 shows the practice of threading the thin wire below the module and pulling it back and forth (towards one hand and then the next) to cut the SE4445 bond. Isopropyl alcohol should be applied as needed during the process of cutting the bond. It serves

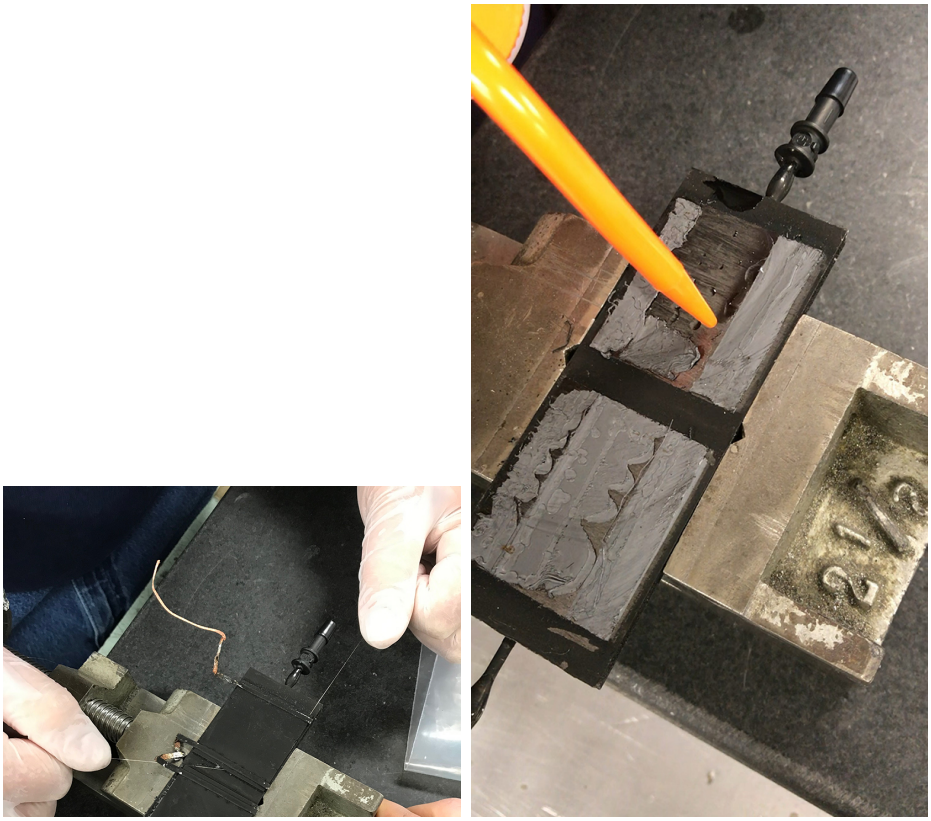


Figure 4.43: Modules can be (left) removed from the carbon fiber framework using a thin metal wire and (right) the adhesive residue can be cleaned with isopropyl alcohol.

as a lubricant and helps weaken the bond. Once the module is removed, isopropyl alcohol and a clean wipe can be used to remove any residual SE4445. Araldite 2011 can be cleaned in the same way as SE4445 before it has cured (within a matter of hours after application). Araldite 2011 is more difficult to clean if it has cured, but implementation of a heat source such as a soldering iron and thin wire is a potential solution.

4.13 Coordinate Measuring Machine

A coordinate measuring machine (CMM) is a sophisticated tool for making measurements with precision of 1 micrometer over a large volume of space. A CMM will be used for measurements of ATLAS parts throughout the assembly process of the ITk. The CMM can be operated manually as well as through a program from a connected computer through Computer Numeric Control (CNC). The CMM measurement setup can be seen in Figure 4.44.

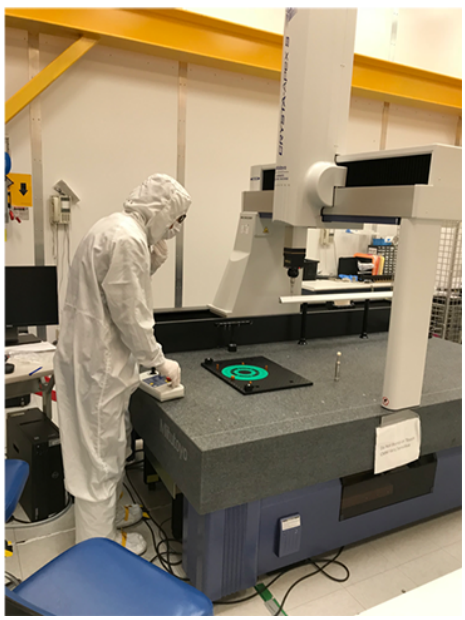


Figure 4.44: The CMM measurement setup.

When measuring a new part the first step is to define a coordinate system attributed to that part. This is important for user interpretation of subsequent measurements. Once the coordinate system of a part is set the following CNC measurements are possible (among others): point, plane, circle, and cylinder. Additionally, comparative measurements can be made – including: circularity, how well do the point measurements match a circle, concentricity, how concentric are 2 circles and

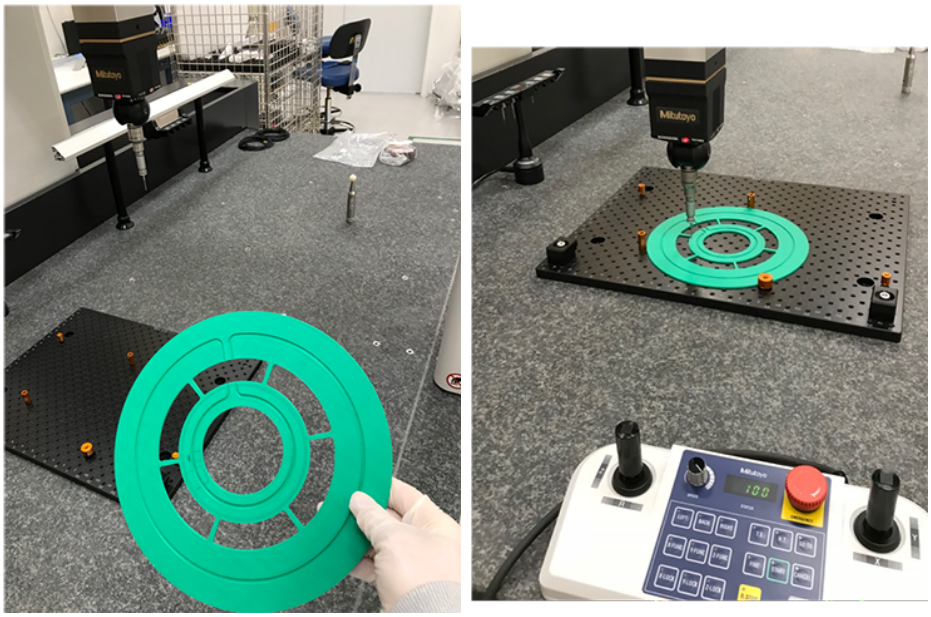


Figure 4.45: (Left) A three-dimensional printed model of a coupled disk, in front of the CMM. The model disk is used for preparing the CMM measurements code that will be used during the production of the ITk parts. (Right) The CMM can be controlled with the hand-held controls or through computer numeric control.

flatness, how well do the point measurements fit to a plane.

A preliminary test of the CMM machinery was designed around the measurement of the three-dimensional printed disk shown in Figure 4.45. A custom program was written for the CMM to make three measurements on the model disk - the innermost circle, outermost circle and the plane of the disk.

A coordinate system is fully determined by setting the position of the origin and orienting the axes. Defining a coordinate system requires a set of three data. The measurements made to orient the coordinate system of the model disk are shown in Figure 4.46. The measurements include a plane, whose normal vector determines the z axis, a circle, whose center determines the origin of the coordinate system, and a point measurement, which breaks the x-y axes degeneracy.

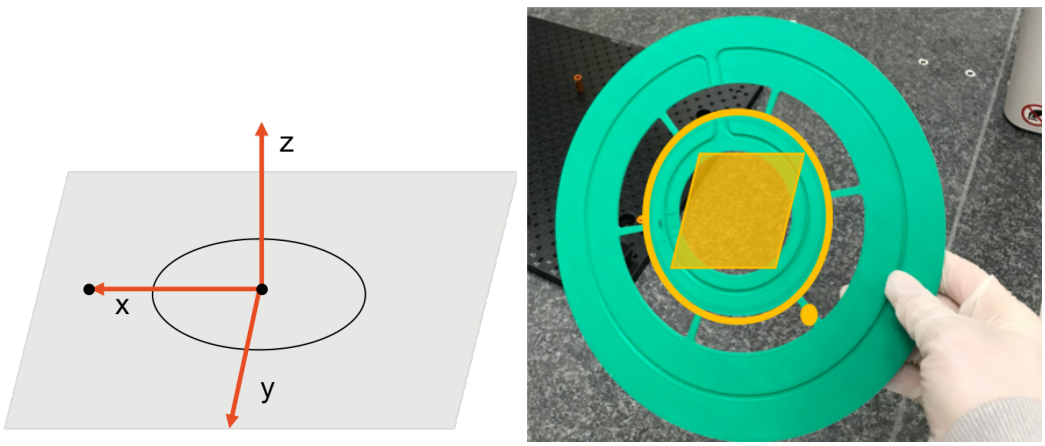


Figure 4.46: The coordinate system of a disk is set with three measurements on the disk.

The goal is reproducibility of the CMM measurements. The bottom line is a "Green light/Red light" or a "Good/Not good" for quality control. Various measurements are performed of the disk three times without moving the part (Position 1). Additionally, a fourth trial with double the number of points of each measurement is made for comparison. Finally, the disk is removed and replaced in the fixture and the measurements are repeated (in Position 2).

The measurements of the disk in Position 1 are summarized in Table 4.2. The measurements of the disk in Position 2 are summarized in Table 4.3.

A set of circularity measurements with the CMM optical probe were made. The computer screen video panel and the corresponding CMM probe position can be seen in Figure 4.48. A series of circularity measurements were performed in sequence without moving the disk position and the values produced were: 0.238, 0.237, and 0.223. The optical probe provides a measurement through an automation system that triggers on the edges of objects in the field of view. Optimization of the lighting in the field of view (controlled through the CMM optical probe) has to be performed to produce repeatable results. The final measurement listed above is different from the

two previous measurements due to the automated program triggering on a different edge in the field of view.

Parameter under test		Position 1 Trial 1	Trial 2	Trial 3	Trial 4*
Inner circle	Diameter [mm]	71.943	71.943	71.943	71.945
	Circularity	0.139	0.139	0.138	0.145
Outer circle	Diameter [mm]	243.897	243.897	243.896	243.904
	Circularity	0.296	0.297	0.297	0.338
Concentricity (inner and outer circle)		0.049	0.049	0.049	0.080
Disk Flatness		0.096	0.096	0.096	0.108

Table 4.2: Measurements of a model of a disk performed with the CMM. Trials 1 to 3 are performed using the same program, one after another, to check the repeatability of the measurements. The same measurements of the model disk in Trial 4, marked with an asterisk, are performed with twice as many points per measurement.

The CMM software can produce customized detailed graphics of the measurements. A set of graphics, for a circle measurement and for a plane measurement are shown in Figure 4.47. These graphics will be useful during ITk loading and assembly production by providing an easily accessible green light or red light display for each measurement. As such, these graphics can be used for a quality control review.

Some adhesive sample thickness measurements were performed with the CMM, shown in Figure 4.49. These measurements can be made with the touch probe or with the optical probe, if the measurement surface is non-reflective. Due to the variable nature of the positioning of the adhesive samples during development of the procedures, most height measurements of the samples were performed manually with a height gauge.

Parameter under test		Position 2 Trial 1	Trial 2	Trial 3	Trial 4*
Inner circle	Diameter [mm]	71.936	71.937	71.938	71.943
	Circularity	0.128	0.130	0.130	0.136
Outer circle	Diameter [mm]	243.252	243.256	243.251	243.911
	Circularity	0.296	0.297	0.297	0.342
Concentricity (inner and outer circle)		0.042	0.043	0.043	0.082
Disk Flatness		0.072	0.073	0.073	0.095

Table 4.3: Measurements of a model of a Disk performed with the CMM. The same measurements as in Table 4.2 are performed after removing and re-placing the Disk in the holding position. Measurements in Trial 4, marked with an asterisk, are performed with twice as many points per measurement.

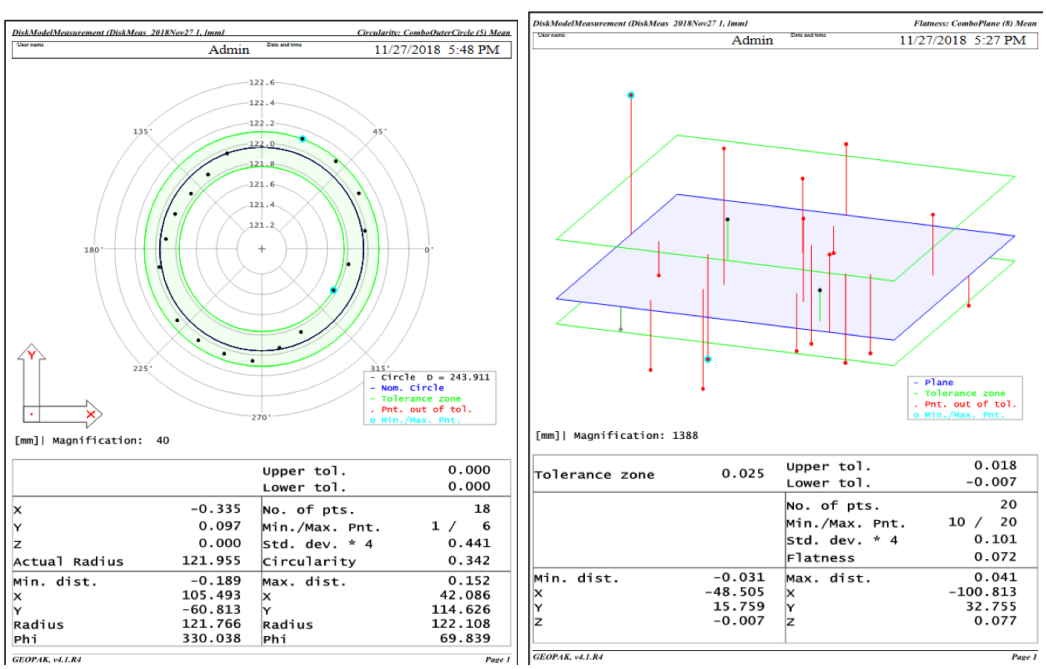


Figure 4.47: Measurement graphics generated by the CMM software can be customized to provide information to a parts database and allow for in-situ quality control (go or no-go) information to the user during production.

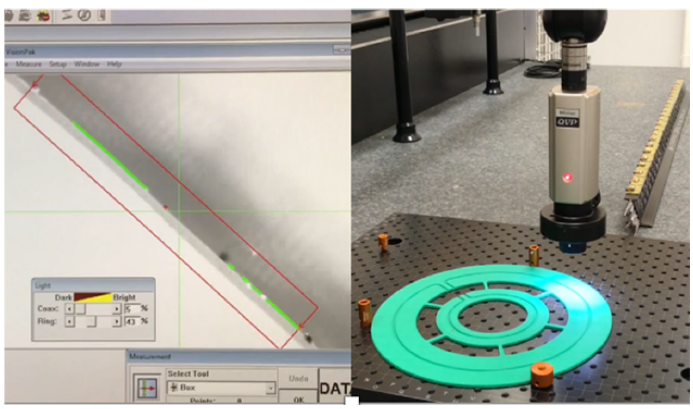


Figure 4.48: A measurement with the CMM optical probe. (Right) The optical probe camera takes an image from a precisely known position and (left) transfers the image to a computer for viewing and processing.

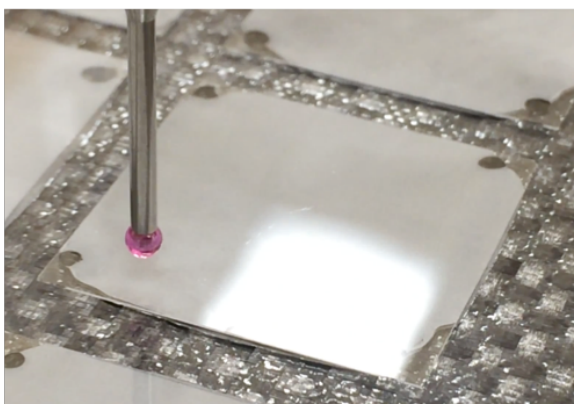


Figure 4.49: The touch probe is used for some thickness measurements of the adhesive samples between glass and carbon fiber.

4.14 Thermal Conductivity

Thermal conductivity of the adhesive samples is the ultimate quality assurance test of the procedures. Development work on the infrared camera imaging of the samples and environmental control chamber has been performed in preparation for this test. The test should be designed with an IR camera with frame rate fast enough to view the temperature change in real time.

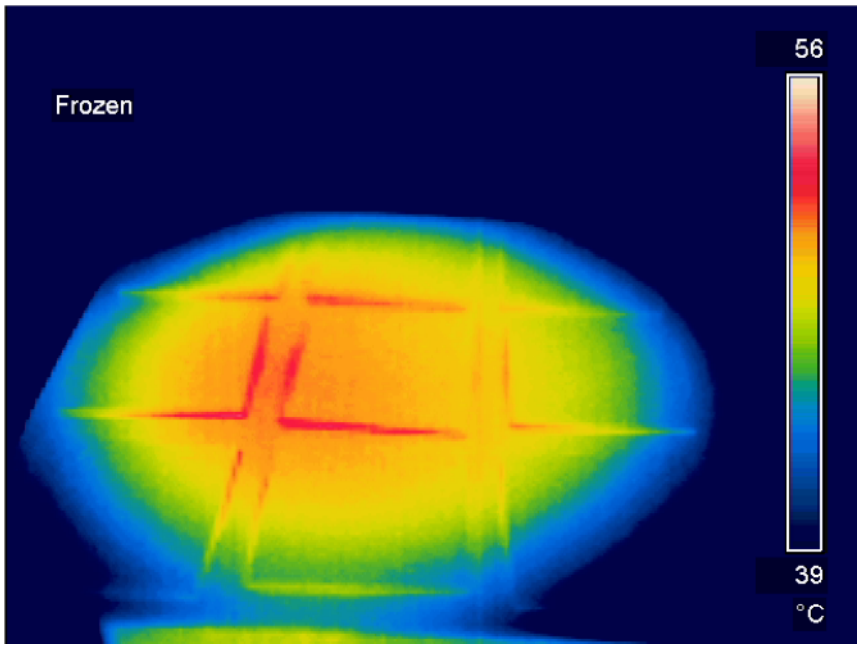


Figure 4.50: Infrared image of samples over a heat source.

Chapter 5

New Technologies for Particle Physics Applications

This chapter presents a series of projects aimed at advancing the technological capabilities of the hardware and software used in high energy physics experiments. In the following sections a description of a novel device for calibrating high energy particle sensors (Section 5.1), two projects aimed at pushing the boundaries of device irradiation and characterization (Sections 5.2 and 5.3), and a simulation project of irradiated n-type and p-type silicon sensors is discussed. The formalism for the simulation is developed (Section 5.4) and applied in the temperature and radiation conditions in space (Section 5.5). Each of these projects provides new insight into the hardware development needed for the HL-LHC era. The development of new technologies, such as those described herein, is essential for continued discovery in fundamental physics.

5.1 A Radiation Tolerant Light Pulser for Particle Physics Applications

A radiation tolerant light pulser is developed for calibration of particle physics detectors. Particle physics experiments are frequently operated in high irradiation environments and new tools for calibration of the detectors are required for the safety of the experimenters.

Optical pulsers are frequently needed as in-situ time and amplitude calibrators in particle physics experiments. In applications with no significant radiation field, approaches ([43, 78, 86, 112, 115, 159, 172, 183], and references therein), to calibration based on radioluminescence sources, optoelectronics with LEDs or lasers, and gas-discharge (lamps) have been employed. A circuit has been developed on the model of Kapustinsky [131] and has been implemented in the design of a pulser for use in radiation fields, for example during commissioning of systems that provide precision timing of particle transit near an interaction point at a hadron collider.

5.1.1 Pulser Design

The circuit, see Figure 5.1, uses eight off-the-shelf components plus (at Output) the Thorlabs LED465E, which has a 465 nm wavelength (blue) output. Light pulse intensity is varied by setting the V_{IN} which charges a 100 pF capacitor. Fast discharge of the capacitor through the LED is achieved with a low impedance transistor switch (complementary pair of RF bipolar junction transistors) which is triggered by an externally generated trigger pulse. The circuit was implemented in pairs on laminated glass epoxy boards with finished thickness $0.06''$, dimensions $1.5''\times\ 1.95''$, surface mount components, and 1-oz. copper trace layers.

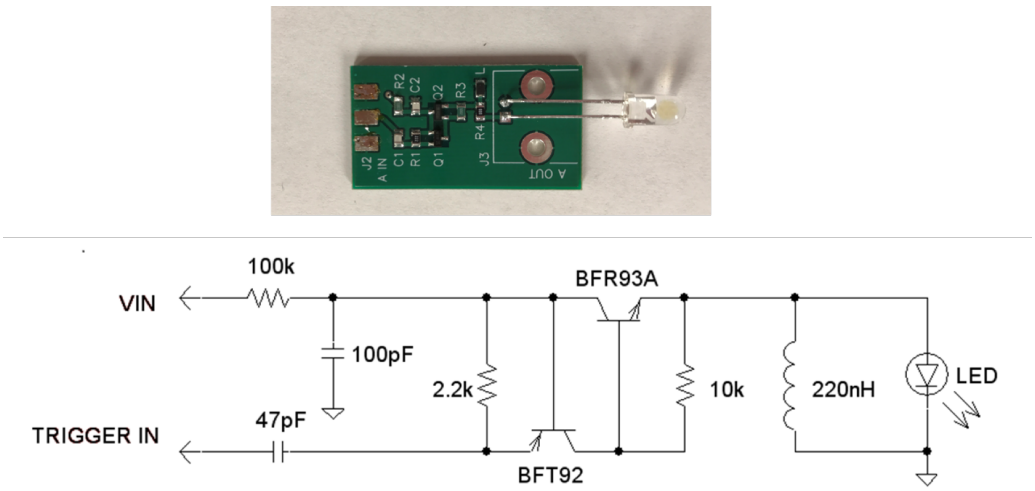


Figure 5.1: Pulser circuit design and fabricated board. Images originally published in [88].

5.1.2 Characterization

Pulsers were characterized before and after exposure to a proton beam or to cobalt-60 gammas. Signals from a photomultiplier tube (PMT) were read by a Tektronix TDS7354B 2.5 GHz oscilloscope. Figure 5.2 shows the experimental setup. The distance from LED to PMT is 60 cm. The PMT used for measurements before and after gamma irradiation is a Hamamatsu R7400U. The PMT used for measurements before and after proton irradiation is a Photonis 85001-501. The effects of the R7400U PMT and the TDS7354B oscilloscope on the full width at half maximum of the signal from the pulser range from 0.3% at $V_{\mathrm{IN}} = 4$ V to 0.03% at $V_{\mathrm{IN}} = 24$ V; these values are calculated using the transient time spread (TTS) of the PMT (230 ps) and the effect of the oscilloscope bandwidth (176 ps). The same values were assumed for the Photonis 85001-501 PMT. The standard deviation of the pulse width of a typical non-irradiated LED ranges from 6.2% at $V_{\mathrm{IN}} = 4$ V to 7% at $V_{\mathrm{IN}} = 24$ V. In Figure 5.3 a typical measurement of a normalized pulse width at two different values of V_{IN} is shown. This measurement technique is sufficient for comparative

measurements. An absolute timing measurement [111] would require single photon counting using a constant fraction discriminator (CFD).

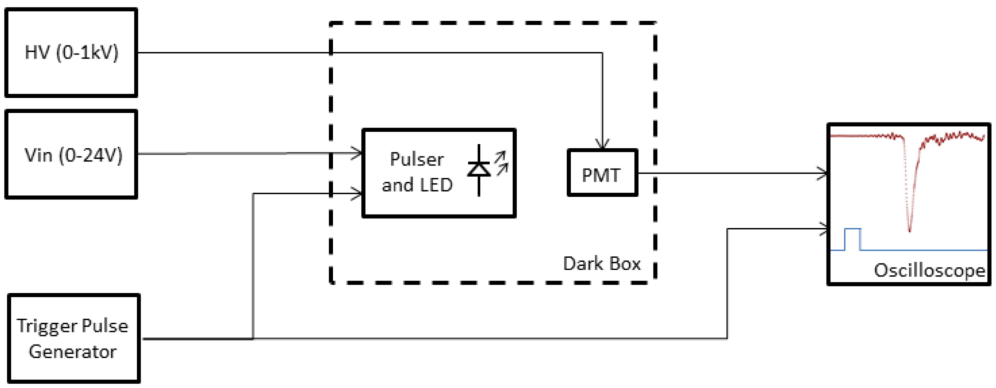


Figure 5.2: Experimental setup. This image was originally published in [88].

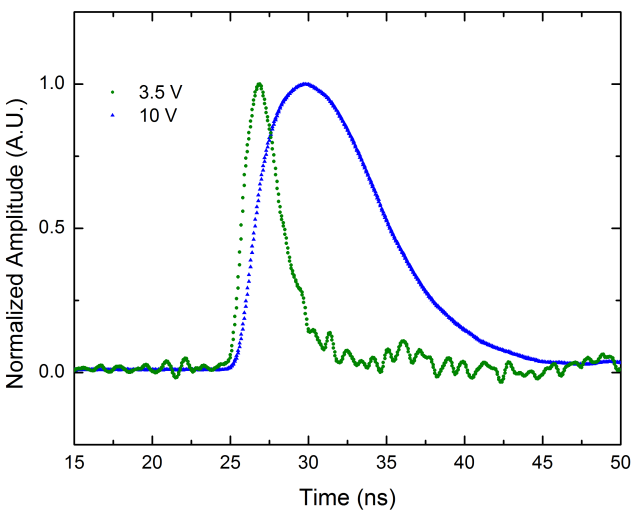


Figure 5.3: Pulse width output using input voltages of $V_{\mathrm{IN}} = 3.5$ V and $V_{\mathrm{IN}} = 10$ V.

5.1.3 Proton Irradiations

Three pulser boards, including all their components, were exposed to 800 MeV protons at the Los Alamos LANSCE facility in 2013. The protons were applied at room temperature over a period of less than an hour. Two boards received 1.5 $\times$ 10^{13} p/cm^2 and one received 6.7 $\times$ 10^{13} p/cm^2. Figure 5.4 indicates the effect of the proton fluences upon the pulse width, as a function of input voltage. The error bars shown reflect variations of the V_{IN} (0.5%), angle and distance of the LED with respect to the PMT (0.03%), and oscilloscope precision (1%), as well as the PMT TTS and oscilloscope bandwidth. Also included in the error is the statistical variation in the typical pulse width of an LED465E previously mentioned. After irradiation with 1.5 $\times$ 10^{13} p/cm^2, the pulse shape and minimum width are similar to the pre-irradiated values. The minimum pulse width rises from 5 to 8 ns after application of 6.7 $\times$ 10^{13} p/cm^2. The minimum V_{IN} at which signal output is achievable increases with dose. Pulse width increases as V_{IN} increases in each set of data. Figure 5.5 shows the pulse amplitude (V_{OUT}) as a function of input voltage for the same devices. Contributing factors to the error are variations of the V_{IN} (ranging from 12% at V_{IN} = 7 V to 0.3% at V_{IN} = 24 V), angle and distance of the LED with respect to the PMT (0.1%), and oscilloscope precision (1%). Although the amplitude is diminished in the proton-irradiated devices, over 50% of the light output is retained in the upper half of the input voltage range.

5.1.4 Gamma Irradiations

Ten pulsers were exposed to gammas at the Sandia Gamma Irradiation Facility in 2017, with two each receiving doses of 100 krad, 500 krad, 1 Mrad, 3 Mrad, and 5 Mrad. Figure 5.6 shows the output pulse amplitude as a function of input voltage, before and after irradiation for all doses. The LED light diminishes incrementally

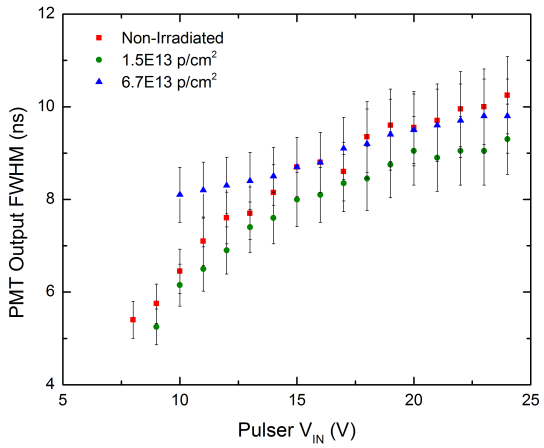


Figure 5.4: Pulse width of pulser before and after proton irradiation to fluences of 1.5×10^{13} and 6.7×10^{13} 800-MeV p/cm^2.

with increasing gamma dose, reaching a minimum of 80% for the 5 Mrad case. Figure 5.7 shows the output pulse width as a function of input voltage, before and after irradiation for all doses. The pulse width increases monotonically with increasing V_{IN}

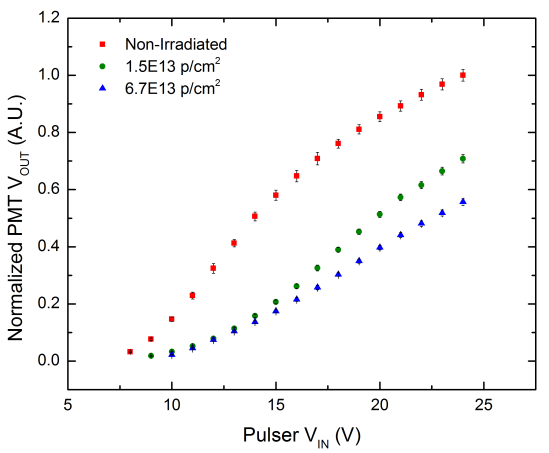


Figure 5.5: Pulse amplitude of pulser before and after proton irradiation to fluences of 1.5×10^{13} and 6.7×10^{13} 800-MeV p/cm^2.

and the gamma dose applied does not affect the FWHM significantly. The error bars shown are calculated in the same way as mentioned previously. The pulser circuit is robust to this gamma dose.

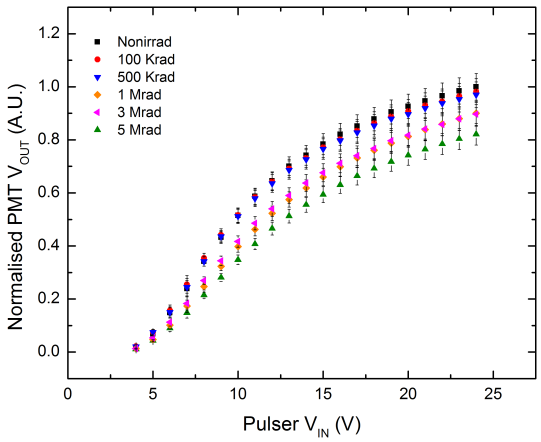


Figure 5.6: Pulse amplitude of pulser before and after gamma irradiation to doses up to 5 MGy.

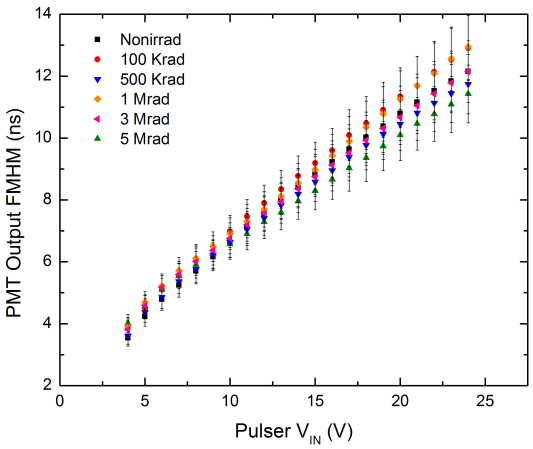


Figure 5.7: Pulse width of pulser before and after gamma irradiation to doses up to 5 MGy.

5.1.5 Pulser Operational Results

The gamma and proton irradiated components were removed from the pulser boards after irradiation. The LEDs' current versus voltage (IV) characteristics were measured (see Figure 5.8). The IV curves of the gamma irradiated LEDs overlap the IV curves of the non-irradiated ones. In the proton irradiated devices the forward threshold voltage is increased and for any given forward voltage the output current (and thus the output light) is diminished in proportion to the applied proton fluence. Figure 5.9 examines the effect of the radiation on the transistors' gain; an example of the I_{C} vs V_{BE} of the BFR93A NPN transistor is shown. Data from the gamma-irradiated devices again overlap the data from the non-irradiated transistors. The proton irradiated transistors exhibit a higher shift in V_{BE} threshold voltage and a decrease in transistor gain. Similar results are measured on the BFT92 PNP transistor. All other components (thick film resistors, ceramic capacitors, and a wirewound ferrite core inductor) were found to have been unaffected by both the gamma and the proton exposures. Visual inspection shows the LED to be discolored by both gamma and proton exposure. The reduction of the PMT output amplitude of the gamma irradiated devices is due to discoloration of the clear LED casing. The reduction of the PMT output amplitude seen in the proton irradiated devices is due to the effects on the semiconductor material in the LEDs and transistors as well as the LED casing discoloration.

A pulser circuit suitable for operation in radiation fields up to at least 6.7×10^{13} 800-MeV-protons/cm^2 and 5 Mrad gammas has been developed. Pulse widths are largely unchanged due to the irradiations and remain in the 4-12 ns range depending upon input voltage. Output amplitude and thus the light output decreases proportionally to the proton and gamma exposure but preserves 80% (in the case of gammas) and 50% (in the case of hadrons) at the highest exposure. The affected components of the pulser board are the RF transistors and the LEDs. The LED cases

are sensitive to both species, while the semiconductors are changed by the hadrons only. The device is compact, economical, and applicable to a variety of particle physics experimental environments.

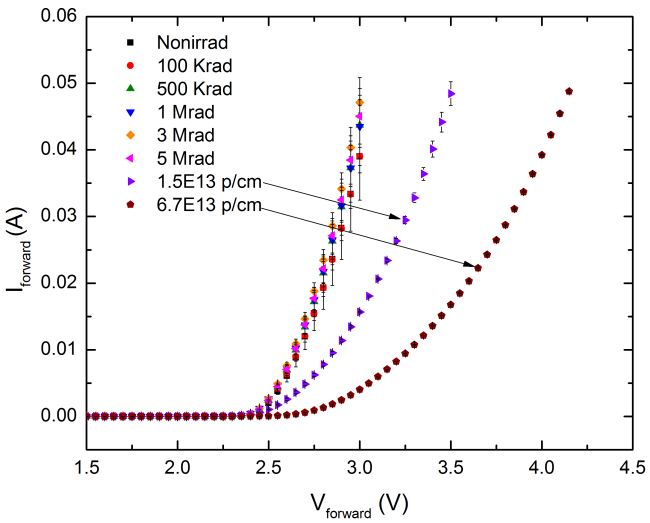


Figure 5.8: Forward current versus forward voltage measurements of LED465E components, with and without applied irradiations.

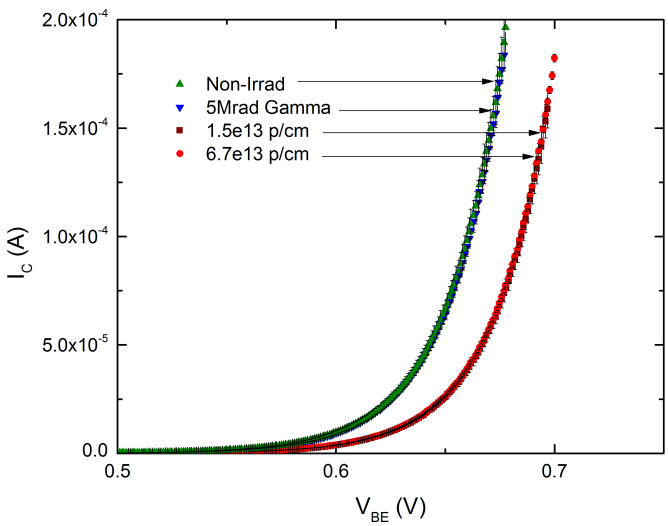


Figure 5.9: Measured I_{C} versus applied V_{BE} of NPN Transistor BFR93A with constant $V_{\mathrm{CE}} = 2$ V, with and without applied irradiations.

5.2 Application of p-i-n Photodiodes to Charged Particle Fluence Measurements Beyond 10^{15} n_{eq}/cm^2

5.2.1 Introduction to Beam Fluence Monitoring with p-i-n Photodiodes

Some detectors planned for use in the HL-LHC will need to operate at fluences twenty times the LHC specifications or higher. The LHC Radiation Monitoring System (RadMon) [168] was developed to monitor and measure radiation levels in order to avert equipment failures. Several device types were characterized and found to be appropriate for use as radiation monitors [156]. The commercially available OSRAM BPW34F p-i-n diodes have been used in this study and have the following characteristics: (1) they are fabricated with n-type silicon of resistivity approximately 2.5 kΩ-cm, (2) they have a base length of 210 μm and cross section of 2.65 mm^2, and (3) they are sensitive only to damage produced by fast hadrons (E > 100 keV) and almost insensitive to photons. Forward voltage across the diode has been shown to increase linearly with fluence when supplied with a constant forward current [155]. The study described in this section seeks to extend the linear regime of forward voltage versus fluence for real time measurements [101]. This will facilitate radiation campaigns involving new particle tracking detectors where the goal is optimal performance at high fluences. The linearity range has been observed to extend from about 2×10^{12} to about 2×10^{14} n_{eq} / cm^2, see Figure 5.10. The goal of this study is to extend the region of linearity to beyond 10^{15} in response to the higher fluences of present and future particle physics experiments.

An assembly of 49 diodes, arranged as a 7 × 7 matrix, has been used for real-

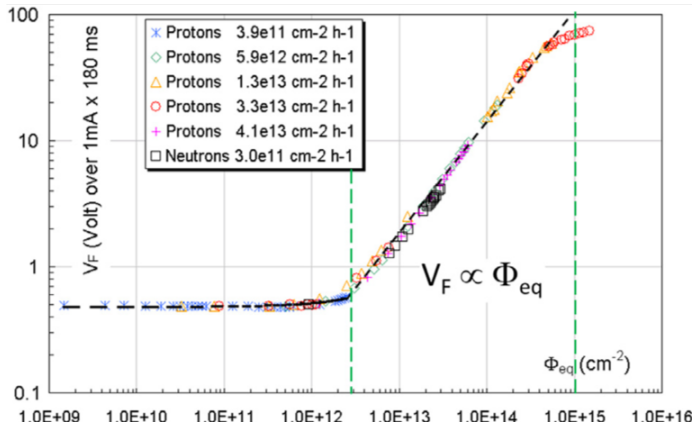


Figure 5.10: Linear relation between forward voltage and applied particle fluence [155].

time monitoring of the fluence applied by a charged particle beam to a target. The diode arrangement has been developed [151] and is shown in Figure 5.11. The pitch between diode centers is 3.8 mm and the resolution is 1.1 mm.

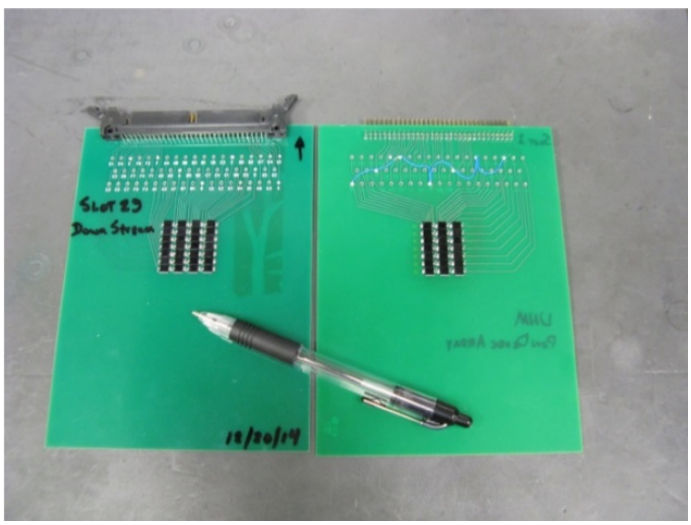


Figure 5.11: Front and back sides of the p-i-n diode array used for real time fluence measurements.

5.2.2 Irradiation of the Diodes

The diodes are irradiated at the Los Alamos Neutron Science Center (LANSCE) up to fluences of 3.8×10^{15} $n_{\mathrm{eq}}/\mathrm{cm}^2$ with an 800 MeV proton beam. Aluminum dosimeters are irradiated to the same fluences as the diodes; each piece of aluminum is placed right on top of a diode so the same high energy particles traverse both. After the irradiation, the sensors are stored in a freezer to minimize annealing effects.

The diodes are irradiated in the LANSCE Irradiation Hall in a custom Lexan support box. Many samples are irradiated along the beam line. Real-time forward voltage measurements are made with the diode array including transverse plane spatial resolution. The aluminum foil activation is used to calibrate the diode response to fluence.

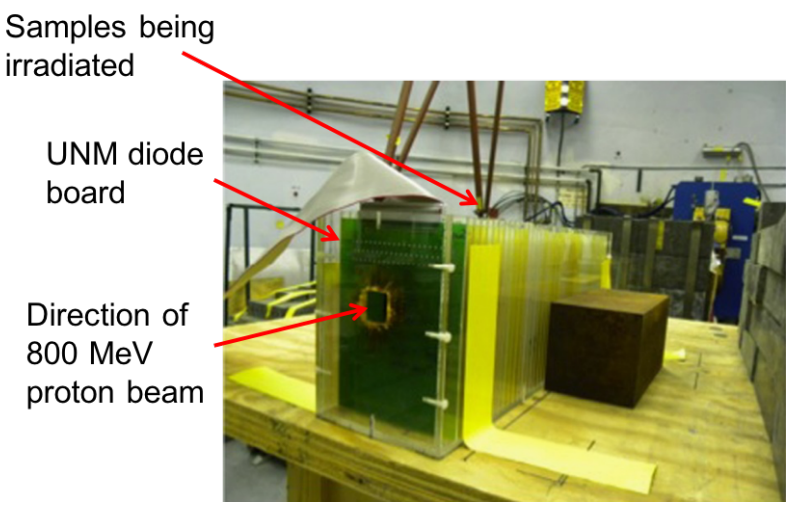


Figure 5.12: The experimental setup inside the LANSCE Irradiation Hall is shown here. The p-i-n diode board arrays together with other samples to be irradiated, included aluminum foil dosimeters, are placed in the Lexan holding box. The 800 MeV proton beam is directed through the center of the box and the diodes arrays and other samples are aligned to intersect the beam.

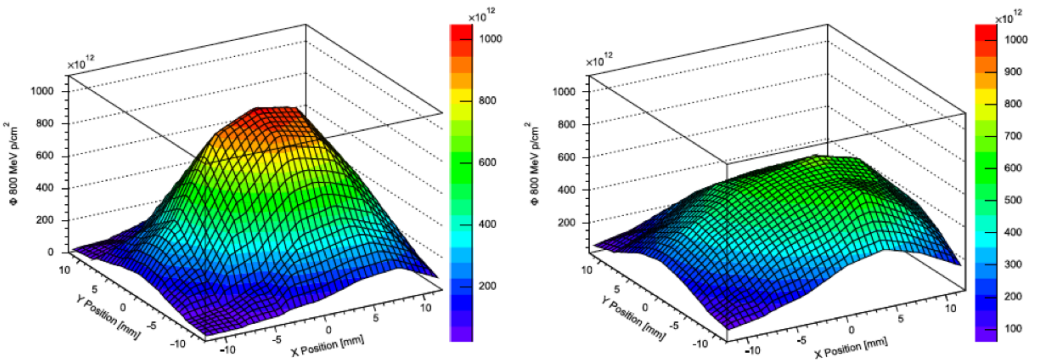


Figure 5.13: Real time fluence measurements are made with the p-i-n diode board arrays in the LANSCE proton beam. The fluence contours accumulated with the p-i-n diode arrays reflect the areas in the proton beam that received higher or lower total dose. Displayed together, the fluence measurements from the diodes in the array can reconstruct a profile of the beam. The upstream beam profile is shown on the left and a downstream beam profile is shown on the right.

5.2.3 Pulse Width Optimization

In the lab at UNM, optimization of the diode measurements is done. Diodes are temporarily brought to room temperature with the use of a thermal chamber. Current is applied to the sensors in the diode arrays individually. A circuit is used to modulate the pulse width of the source current. This setup allows for a variety of combinations of measurement conditions. The aluminum foils are analyzed with a gamma spectrometer and the decay of Na-22 is used to obtain the fluence. The calibration of forward voltage of the diode array at 1 mA versus fluence is performed using the results from [151]. The linear coefficient of the fitted line in Figure 5.14 is $9.558 \pm 1.536 \times 10^{-14}$ $n_{\mathrm{eq}}/\mathrm{cm}^2$ for the 800 MeV proton beam.

The measurement setup is shown in Figure 5.15. The pulse width can be varied with an adjustable timer. The magnitude of the pulsed forward current can be set with the high voltage power supply and the diode temperature is controlled with a thermal chamber. Finally, measurements are read out with an oscilloscope.

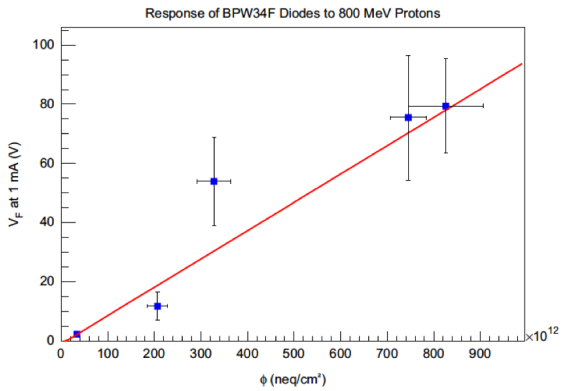


Figure 5.14: Forward voltage versus fluence data and linear fit [151]. The fitted line is used for calibration of the p-i-n diode array real time fluence measurements.

A decrease in amplitude is observed with increasing pulse width. The forward voltage versus time for varying pulse widths (372 ms, 50 ms, and 5 ms) is shown in Figure 5.16. Accuracy of the measurement is compromised with larger pulse widths so the shortest achievable width is used.

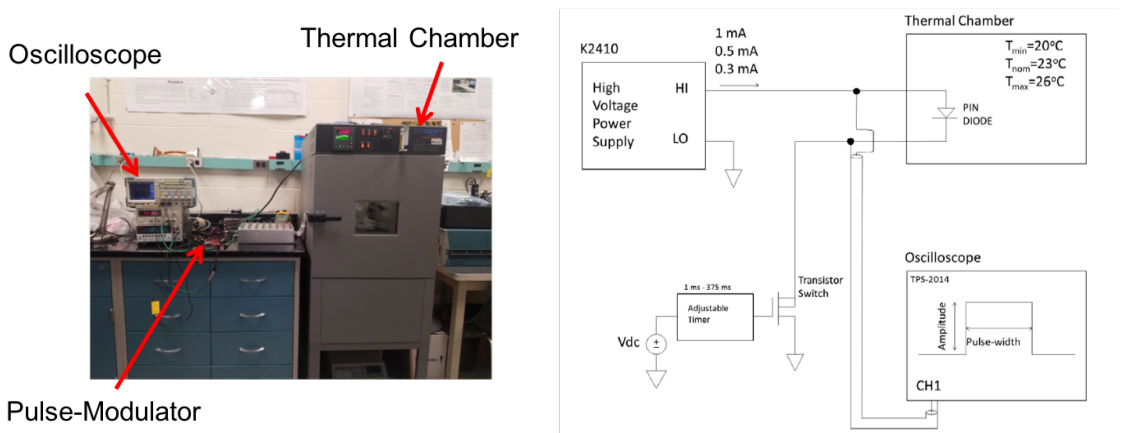


Figure 5.15: (Left) Measurement setup in the UNM laboratory. (Right) Measurement setup diagram. The diagram was originally published in [101].

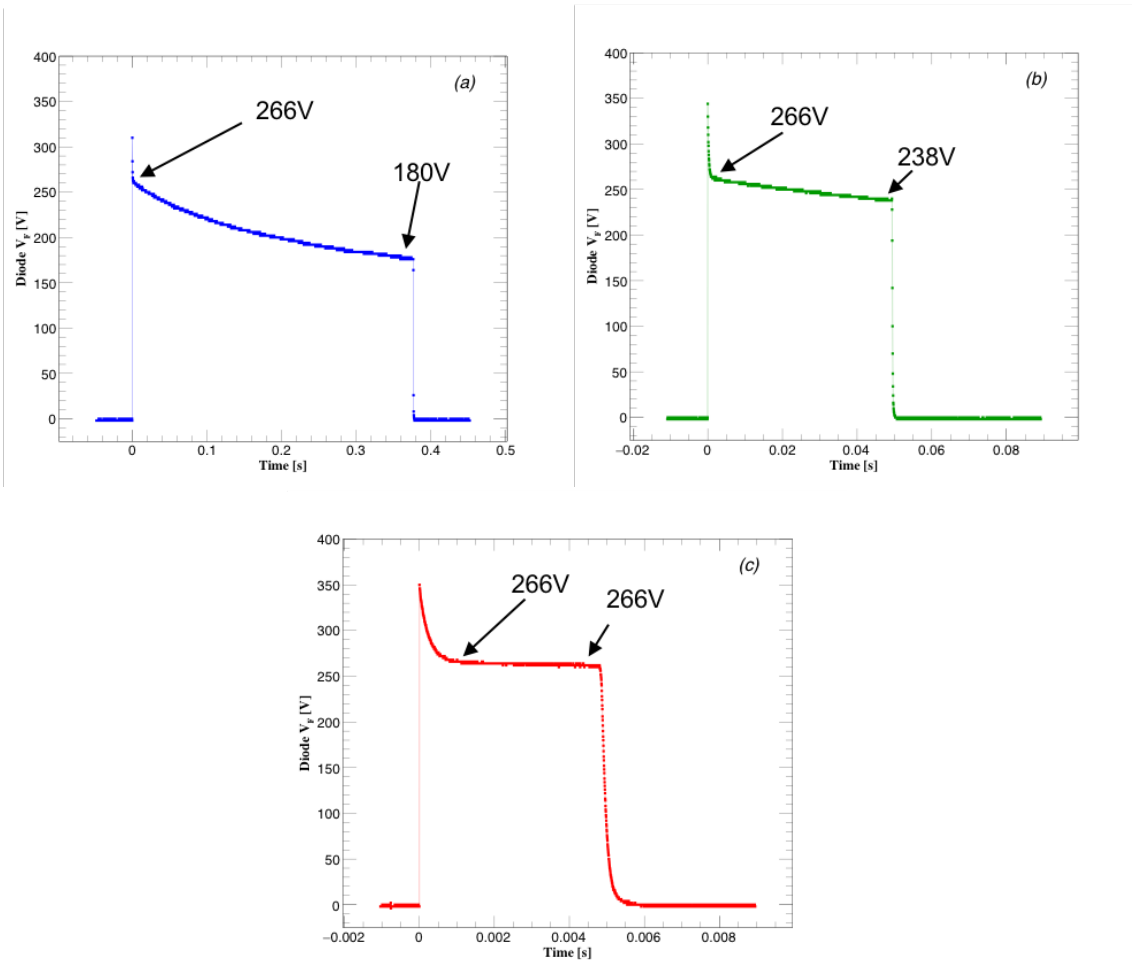


Figure 5.16: Diode forward voltage versus time, for a p–i–n diode irradiated to a fluence of 2.1×10^{15} $n_{\mathrm{eq}}/\mathrm{cm}^2$ at 20 °C, observed for pulse widths of 372 ms (a), 50 ms (b), and 5 ms (c).

5.2.4 Systematic Uncertainties

The forward voltage error is calculated by the combined uncertainties related to temperature variation during the irradiation process, current pulse width, and source meter precision. The applied fluence error is determined from the uncertainty deriving from counting statistics on calibration foils in a gamma spectrometer

5.2.5 Amplitude of the Pulsed Current

Diode forward voltage as a function of applied fluence, for three choices (1.0 mA, 0.5 mA, and 0.3 mA) of forward current amplitude is shown in Figure 5.17. The fluences are independently measured using gamma spectrometry of the aluminum dosimeters. A linear relationship is realized for 1.0 mA of forward current amplitude up to 4×10^{15} $n_{\mathrm{eq}}/\mathrm{cm}^2$.

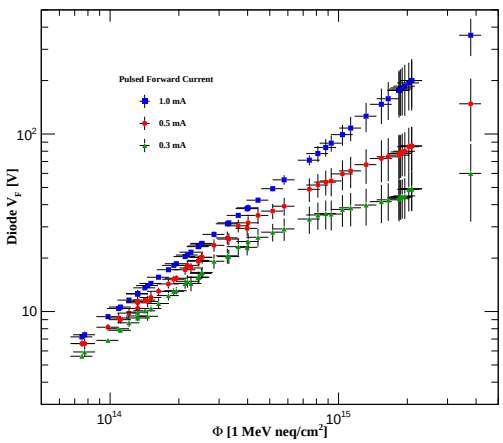


Figure 5.17: Diode forward voltage as a function of applied fluence, for three choices of applied current amplitude. The vertical error bars indicate the combined uncertainties related to temperature variation during the irradiation process, current pulse width, and sourcemeter precision. The horizontal error bars indicate the uncertainty deriving from counting statistics on calibration foils in the gamma spectrometer.

5.2.6 Conclusions From the p-i-n Photodiode Irradiation Studies

A linear characteristic in forward voltage versus fluence can be obtained with OSRAM BPW34F pin diodes for fluences up to approximately 4×10^{15} $n_{\mathrm{eq}}/\mathrm{cm}^2$ using applied current amplitude 1.0 mA and pulse width 5 ms at temperature 23 °C. This represents a twenty-fold extension of the linear region of applicability of these diodes relative to previous operational guidelines.

Reducing the instantaneous measurement temperature down to 20 °C, and/or decreasing the applied current as low as 0.3 mA, increases the voltage-fluence regime over which measurements can be made. Functional forms for the voltage-fluence characteristic curves are provided for several combinations of current and temperature.

5.3 Application of 3D Diodes to Charged Beam Profile Measurement

An instrument has been developed for precision controlled exposures of electronic devices and material samples in particle beams. The instrument provides simultaneously a real time record of the profile of the beam and the fluence received. The system is capable of treating devices with dimensional scales ranging from millimeters to extended objects of cross sections measured in tens of square centimeters. The instrument has been demonstrated to operate effectively in integrated fluences ranging up to a few times 10^{16} n_{eq} / cm^2. The positioner portion of the system comprises a set of remotely controllable sample holders incorporating cooling and interfaces for sample power and readout, all constructed from low activation technologies. The monitoring component of the system samples the current or voltage

of radiation tolerant silicon diodes placed directly in the path of the beam.

5.3.1 Introduction to Beam Monitoring with 3D Diodes

A custom instrument has been developed to facilitate remote control and monitoring of samples in a particle beam. One purpose of this study is to describe the device in sufficient detail to permit replication of it. A second goal is to describe the branch points in the design process, so that an investigator with goals that are related but not identical could build upon this experience to optimize differently.

This is a portable instrument that provides remote control of the position and environment of experimental samples in a radiation zone for use by experimenters who are outside of the radiation enclosure. Being portable and robust for transportation, this instrument can be used at a variety of beamlines worldwide. The capability of real-time measurement of beam profile and fluence can be used both to prepare the beam prior to exposure and to monitor the beam during exposure. On the order of one hundred distinct samples can be served by this instrument simultaneously.

5.3.2 The Positioners

The horizontal positioning system is shown in the upper half of Figure 5.18. Several translation stages are mounted to an acrylic platform of dimensions 51 cm $\times$ 86 cm $\times$ 1.3 cm. The translation arms are perpendicular to the axis to which the beam is aligned. Upon each stage is affixed one sample box using non-activating (plastic) screws except at one position, where a metal screw is required for rigidity. Each stage provides a 10 cm travel distance. Translation is achieved by pneumatic pressure applied differentially, through a manifold (lower half of Figure 5.18) to the near or far end of a PVC cylinder of length 14 cm and diameter 5.7 cm, displacing a PVC

piston internal to the cylinder and attached to its stage by a PVC rod. The exposed and the internal O-rings of the cylinder are EPDM for which the elastic seal integrity has been demonstrated up to 10^6 Gy or 10^8 rad. The two ends of each pneumatic tube are attached to 6.4 mm plastic tubing that runs 30 m to the manifold where the application of a simple hand-operated air pump translates a selected sample remotely and practically without delay.

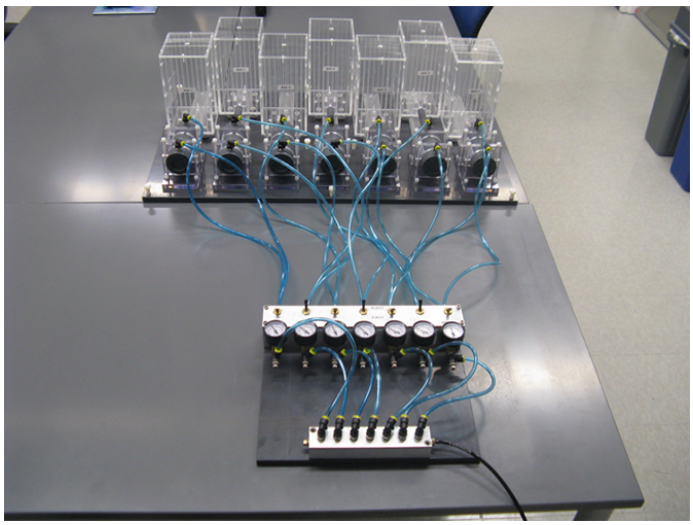


Figure 5.18: The positioning system, showing seven horizontal translation stages with attached sample boxes and a manifold that allows differential air pressure to be applied selectively to either end of each translation piston. During operation, the actual length of the plastic tubing between manifold and stages would be much greater - typically tens of meters, in order to allow personnel to operate the manifold outside of a radiation zone in which the translation stages are enclosed. This image was originally published in [102].

A typical sample box (see Figure 5.19) has dimensions 13.5 cm $\times$ 11.4 cm $\times$ 21.9 cm and is fabricated from acrylic and assembled with plastic screws. The beam enters and exits each box sequentially through a Kapton-covered square aperture of dimensions 2.5 cm $\times$ 2.5 cm. Boxes have lids through which power, readout, and cooling gas flow connections can be made. Precision machined slots at 1 cm intervals on opposing interior walls of the box have depth 2 mm. These hold G-10 boards onto

which samples are affixed, typically with Kapton tape. Using these precision slots, samples whose dimension is small compared to the width of the beam are positioned perpendicular to the beam.

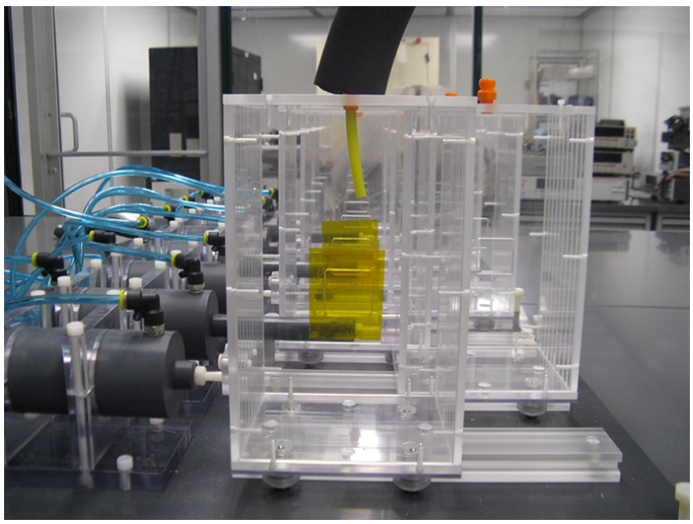


Figure 5.19: A sample box with gas flow port in the lid. This image was originally published in [102].

Samples significantly larger than the beam can be oriented at an angle of 60° with respect to the beam, to reduce their effective cross section by half and thereby permit more uniform exposure in one of their dimensions; for these samples, larger G-10 boards are held in position by slotted inserts positioned at the floor of their box (see Figure 5.20).

The positioning system also includes a stage that combines vertical and horizontal translation (Figure 5.21). The vertical translation system has a resolution of 1 μm and can scan through a vertical distance of 12 cm. A separate horizontal stabilizing rod that slides through a linear sleeve bearing is needed to achieve stability and repeatability of the sample box placement and scanning motion. The electronics that control the motor that activates the vertical motion are protected by a lead shield.

The number of sample boxes that can be included is limited only by available space in the beamline.

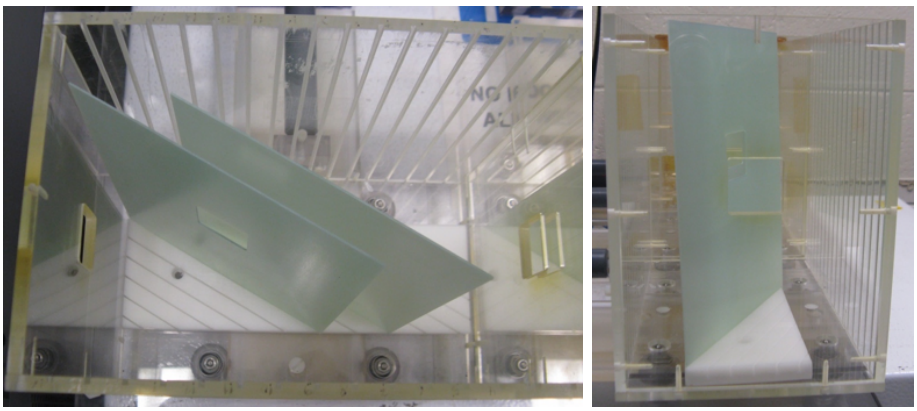


Figure 5.20: (left) Top view and (right) side view of the removable slotted insert that can be positioned at the base of a sample box to allow the sample to be oriented at an angle with respect to the beam axis. This image was originally published in [102].

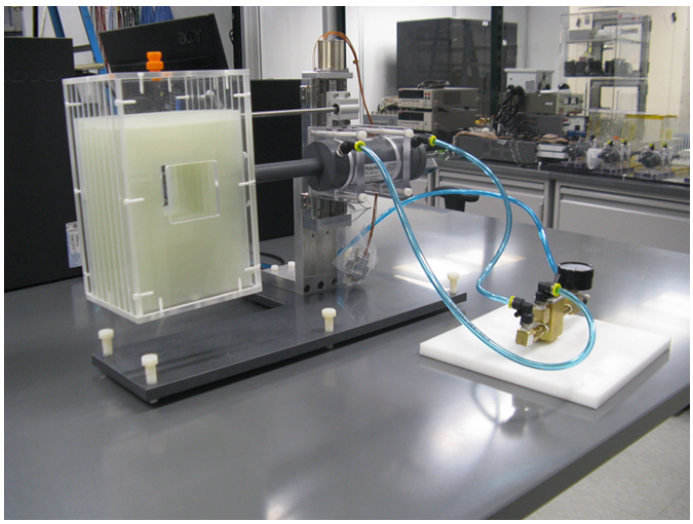


Figure 5.21: The combined vertical-horizontal translation stage. This image was originally published in [102].

5.3.3 The Beam Monitor

The beam profile and fluence are measured in real time at one or more points by custom electronics boards. Each of these boards carries a rectangular array of diodes through which the beam passes. Two diode technologies were investigated; both were found to be suitable for particular goals of the experimenter. Both are described here. In both cases, the multiple identical arrays are operated simultaneously in the beam, typically with one placed at each end of the stack of devices under test, permitting some redundancy as well as interpolation of fluences in the spatial interval between them.

5.3.4 P-i-n diodes

P-i-n diodes of the type BPW34F by OSRAM have the property that their forward voltage increases linearly with fluence when supplied by a constant forward current. For current amplitude 1 mA and pulse width 50 ms or less, the linear regime in forward voltage versus fluence spans the range from approximately 2×10^{12} n_{eq} / cm^2 to approximately 4×10^{15} n_{eq} / cm^2 [101]. The default configuration is a 7×7 array of 49 diodes on a pitch of 3.8 mm, covering an area of 2.5 square centimeters. The diodes are assembled into the array (see Figure 5.19 in [151]) using standard lead-free solder.

5.3.5 3D diodes

Diodes of the 3D geometry, like other silicon sensors, manifest a linear relationship between their leakage current and hadronic fluence given by $I_{leak} = \alpha \mathrm{V} \Phi_{\mathrm{neq}}$, where is the current-related damage coefficient [145], V is the depleted volume, and neq is the 1 MeV neutron equivalent fluence. A 7×4 array of 28 diodes was constructed

(see Figure 5.22) with pitch 3.8 mm × 7.6 mm. Because this array is constituted by discrete points, the resolution, given by pitch/$\sqrt{12}$ [132], is 1.1 mm × 2.2 mm. The array incorporates diodes of types 2E and 3E (which have respectively 2 and 3 n^+ columns per pixel cell), some with and some without guard rings, as variation among these features was found not to influence the array's operation. The nominal thickness of every diode is 130 microns. These diodes are very uniform in their characteristics, having been taken from a common wafer and pre-screened for similar electrical characteristics. Prior to irradiation, the leakage current and breakdown voltage of every diode in the batch were measured. Those used for this instrument were selected on the basis of their having pre-irradiation leakage current in the range 30 to 300 pA and pre-irradiation breakdown voltage above 100 V. The pre-irradiation depletion voltages of the diodes were also measured prior to assembly, and all diodes showed full depletion below 2 V. The diodes are held in place with silver conductive epoxy and connected to the readout lines of the array with wire bonds.

5.3.6 Diode Array Readout

Each diode array is connected by ribbon cable to a converter box that maps each channel to a coaxial cable.

In the case of the 3D diodes, the coaxial outputs are connected to Keithley 3761 Low Current Multiplexer cards in a Keithley 3706A scanner (Figure 5.23). A Keithley 6487 picoammeter supplies voltage and measures the current of each diode through the scanner. The measurement is automated with LabView. The diodes are unpowered except during operator-initiated readout. A complete scan of the 28 diodes requires 3.64 seconds.

The mode of operation of the p-i-n diode array has been described previously [145]. A Keithley 2410 sourcemeter sources a pulse of current and reads out the forward

voltage across the pn junction. The sourcemeter is interfaced to the array through the Keithley 3706 scanner for rapid automated data collection via LabView.

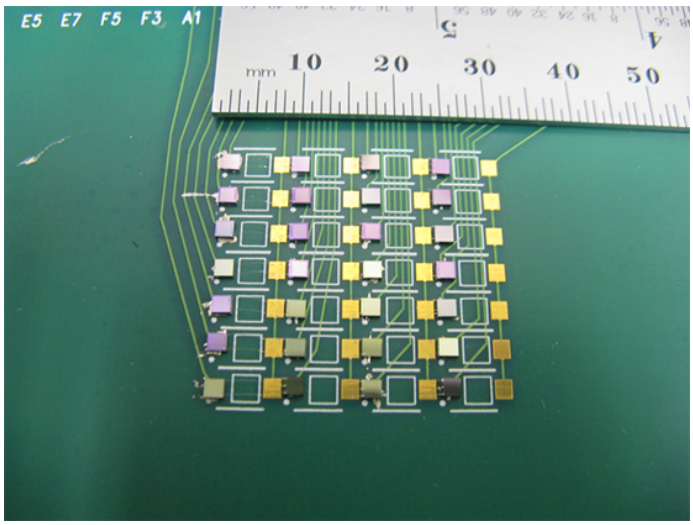


Figure 5.22: The 3D diode array on a printed circuit board. This image was originally published in [102].

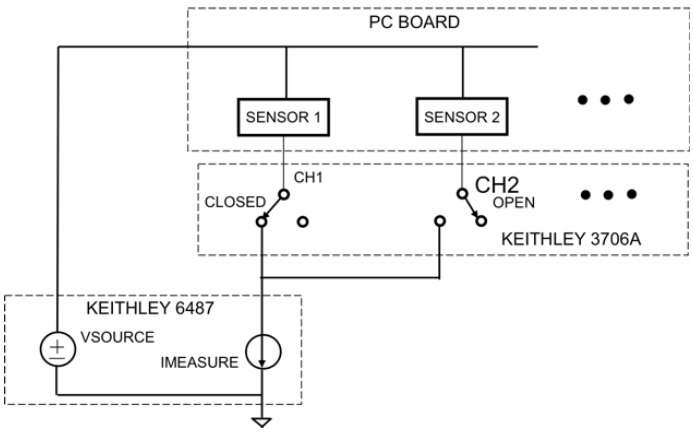


Figure 5.23: Electrical circuit for the 3D diode array readout. This image was originally published in [102].

Figure 5.24 shows the beam profile obtained using forward voltage data from a p-i-n diode array. An interpolation function supplied by ROOT is used to reconstruct the shape of the beam.

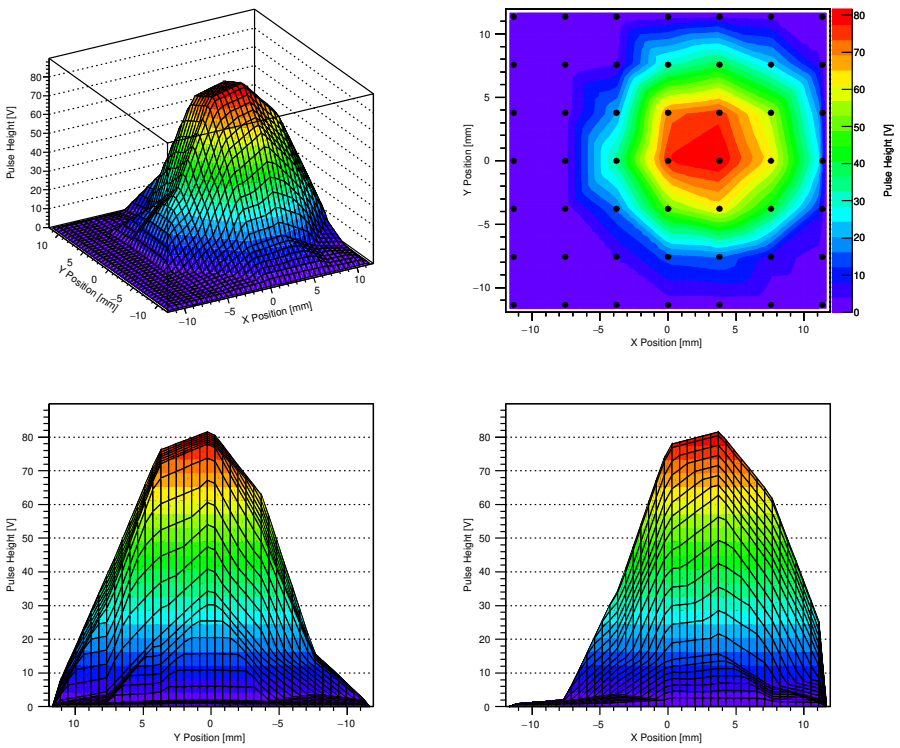


Figure 5.24: The 800 MeV proton beam profile, imaged using the p-i-n diode array. (Lower left) The recorded pulse height (or voltage) versus position, projected in the y-direction; (Lower right) The recorded pulse height versus position, projected in the x-direction; (Upper right) three-dimensional reconstruction of the pulse height recorded as a function of x- and y-positions; (Upper left) contour plot of pulse height in the x-y plane, with black dots indicating the locations of the centers of the diodes.

The beam profile, recorded with a different beam using leakage current data of 3D diodes, is shown in Figure 5.25 An interpolation function supplied by ROOT is used to reconstruct the shape of the beam. Three of the twenty-eight 3D diodes are excluded from the analysis due to broken wirebonds. Table 5.1 summarizes the sources of uncertainty on the 3D leakage current data. An uncertainty of 8.2% is associated with the effects of packaging (epoxy, wirebonds, and light-tight enclosure) upon the 3D diodes in the array; this is obtained by comparing pre-irradiation leakage current data acquired with bare diodes on the probe station to data acquired

after assembly of the array in the printed circuit board. The data are transferred to the computer through a 30 m long ribbon cable, which introduces an uncertainty of 11.7%. This uncertainty arises from the data acquisition procedure, which reads out bias current in response to pulsed bias voltage; RLC characteristics of the cable modify the pulse shape. This uncertainty was measured by comparing data for several nominally identical cables of length 30 m, and for several cables of length 30 cm, for three different diode arrays, each measured multiple times. The temperature uncertainty is determined from the estimated difference in temperature between diodes in the array (2 °C uncertainty) and the thermocouple temperature reading on the PC board (0.3 °C uncertainty). The temperature uncertainty is determined to be 17.8% and includes leakage current temperature scaling according to Equation 3.2 with a reference temperature T_R =25 °C. The standard deviation of three measurements of leakage current per diode is collected, producing a statistical uncertainty given by the standard deviation on all diodes in the array, 0.4%. The total uncertainty is the quadrature sum of the four contributors.

Contributors to the uncertainty	Packaging	Readout Cable	Temperature	Statistics	Total
Uncertainty [%]	8.2	11.7	17.8	0.4	22.8

Table 5.1: Sources of uncertainty in the 3D diode array measurement.

5.3.7 The Cooling System

Cooling is provided to several points in the instrument. A Norhof liquid nitrogen (LN2) microdose dewar system is positioned externally to the radiation enclosure. Techflex vacuum-insulated stainless steel transfer lines of inner diameter 6.4 mm extend 30 meters from the dewar into the radiation enclosure where they adapt to

the sample boxes. Optionally, to limit activation of transfer line material within a meter of the beamline, the stainless tubing can be interfaced with conventional plastic tubing insulated with Aerocel (EPDM) foam over the last few feet before the sample boxes. While the sample box construction is not designed to be hermetic, this nitrogen vapor inhibits condensation on the samples which may be powered.

The cooling system uses LN2 at -196 °C as a cooling medium. A microprocessor-controlled pump on the dewar is attached to a heating element. The element heats the LN2 slightly, producing an overpressure in the dewar that drives LN2 into the transfer line. The system uses Proportional Integral Derivative (PID) temperature control. Figure 5.26 shows the elements of this system. The set-point is the desired temperature of the sample box. The Resistance Temperature Detector (RTD) measures the temperature inside the sample box and compares that with the set point. The difference between the two values is the Error_Value. This value is used in calculating Proportional, Integral, and Derivative terms which produce a signal which either increases or decreases the LN2 flow by controlling the heater. The RTD measures the new temperature (the New_Feedback_Value) and this feedback loop iterates.

The rate at which the Norhof system equilibrates the samples to the desired temperature depends upon the P, I, and D parameters, two time constants (Td_S, the delay time constant during steady state operation, and Td_B, the delay time constant during boost), and the height of the maximum point of the fill line to the exhaust valve at the dewar. We have operated this 30-meter line in an experimental hall of nominal temperature 25 °C and, for a single cooling branch, lowered the temperature in a sample box of a few liters' volume to -10 °C and maintained the atmosphere at that temperature indefinitely. Table 5.2 shows a sample set of the Norhof parameters that when applied with a transfer line of length 30 m, achieve -10 °C at the destination in 140 minutes.

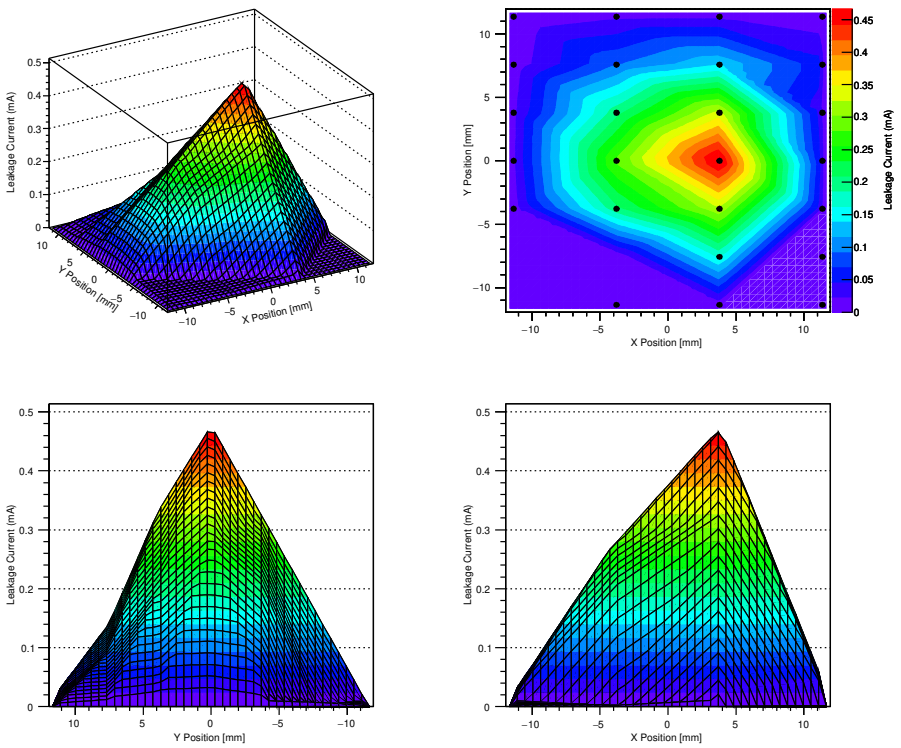


Figure 5.25: The 800 MeV proton beam profile, imaged using the 3D diode array. (Lower left) the recorded leakage current versus position, projected in the y-direction; (Lower right) the recorded leakage current versus position, projected in the x-direction; (Upper left) three-dimensional reconstruction of the leakage current recorded as a function of x- and y-positions; (Upper right) contour plot of leakage current in the x-y plane, with black dots indicating the locations of the centers of the active diodes.

The Norhof drip rate varies from a few drops per minute to 1 liter per minute throughout the cooling process in order to reach the set temperature and maintain a constant temperature afterwards. During operation, the temperature measurements by the RTD in the Norhof system are validated by a thermocouple connected externally. Figure 5.27 shows both measurements as a function of time, for a trial that required a sample temperature of -5 °C.

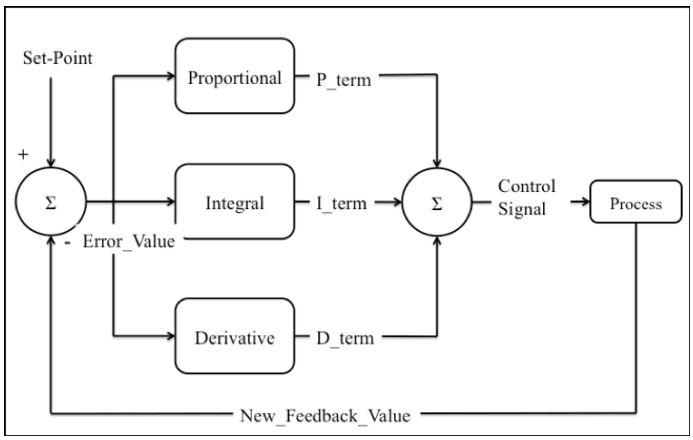


Figure 5.26: The PID temperature control system. This image was originally published in [102].

Parameter	Value
Proportional	9
Integral	8
Derivative	8
Td_B [seconds]	7
Td_S [seconds]	8
Fill line height [cm]	76

Table 5.2: Norhof parameters applied to achieve a -10 °C atmosphere in a few-liter sample box served by a 30 m insulated transfer hose, in a nominally 25 °C experimental hall.

5.3.8 Operational Experience and Conclusions

Several versions of this instrument have been operated successfully in the 800 MeV proton beam at the Los Alamos Neutron Science Center during roughly annual radiation campaigns from 2014 to the present; each exposure lasted approximately 48 to 72 hours. All elements of the instrument work reliably. Some images of the instrument in situ at LANSCE are shown in Figure 5.28.

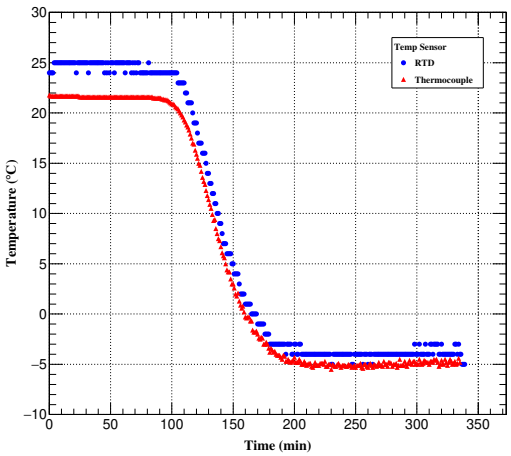


Figure 5.27: Temperature recorded in the sample box located 30 m from the Norhof dewar, as a function of time after the cooling process was started. Temperature was measured with two sensors, a thermocouple and an RTD.

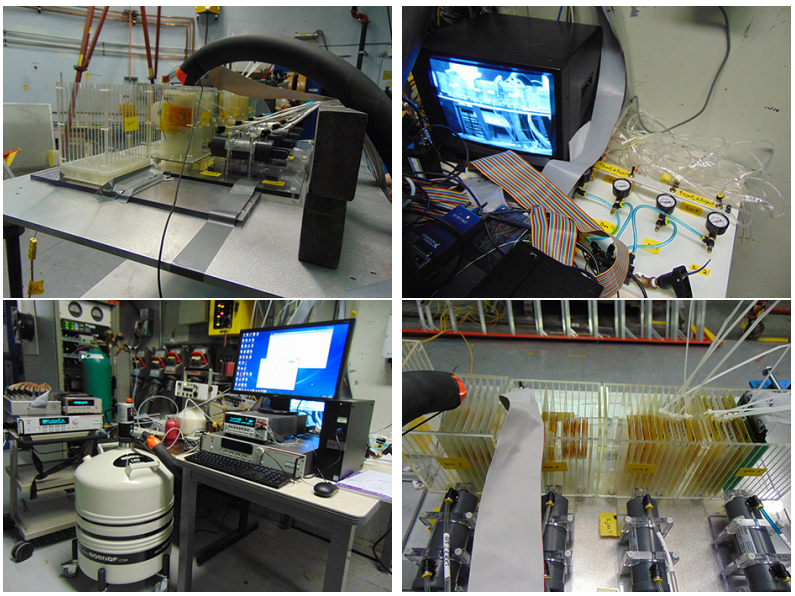


Figure 5.28: A composite of images of the instrument, including prototypes, photographed over several years during irradiation campaigns at LANSCE.

Both the p-i-n diode array and the 3D diode array are effective tools for measuring particle beam profile and fluence. The 3D diodes have the benefit that they can operate above fluences on the order of 1.7×10^{16} n_{eq} / cm^2. This fluence, and those recorded by p-i-n diode arrays, are confirmed by post-irradiation gamma spectrometry of ultrapure aluminum foils. These segmented foils are placed directly atop 3D arrays during each run, and thus each foil receives exactly the same fluence as the diodes beneath it.

The p-i-n diode arrays, on the other hand, must be replaced after each approximately 4×10^{15} n_{eq} / cm^2. As is described in Reference [101], above fluences of 4×10^{15} n_{eq} / cm^2, the linear relationship between applied fluence and measured forwarded voltage ceases to hold for the p-i-n diodes.

Drawbacks of using the 3D arrays include the facts that (1) they are photosensitive, which necessitates radiation resistant light shielding directly in the path of the particle beam, (2) they require cooling to suppress leakage current as radiation and annealing progress, and (3) conversion of their signal to an absolute fluence requires an accurate thermal history for them, which may be difficult to assure in the conditions of the active beamline.

While all of these drawbacks to the 3D implementation could be overcome through advanced packaging, the p-i-n diode array suffers from none of them, and its lower radiation tolerance can be overcome by sequential use of multiple p-i-n arrays inserted and removed remotely via the translation system described here. For example, during a 48-hour campaign, if the target fluence is 10^{16} n_{eq}, three sets of p-i-n arrays need to be cycled sequentially into and then out of the beamline.

The cooling system is able to operate over substantial distances to achieve and maintain temperatures as low as those typically used in particle physics experiments. Limitations on the circulation pattern of coolant in the sample boxes might be over-

come by incorporation of a vacuum port at the opposite end of the box from the coolant inflow.

5.4 The Hamburg Model of Depletion Voltage

The next generation of particle physics experiments will make much greater use of p-type silicon detectors, an evolution from n-type sensors that improves radiation hardness and simplifies fabrication. This motivated extension of the Hamburg Model simulation to describe p-type devices. It is expected that the new Hamburg Model software will be widely used in LHC applications and beyond. To demonstrate its broad applicability, the new simulation code was used in an application related to extra-terrestrial science. This is reported in Section 5.5.

The Hamburg Model can be used for predicting the change in the silicon sensor characteristics leakage current and depletion voltage in response to temperature and applied particle fluence conditions. The mathematical application of the depletion voltage sector of the Hamburg Model [128, 144, 145] is presented in this section. The extension of the Hamburg Model to make it applicable to p-type silicon sensors is also discussed.

5.4.1 The Hamburg Model: Depletion Voltage in n-type Sensors

The Hamburg Model proposes that radiation damage introduces defects in the silicon bulk that change the effective space charge density N_{eff} and that the depletion voltage V_{dep} is proportional to the N_{eff} as:

$$V_{\text{dep}} = \frac{qd^2}{2\epsilon\epsilon_0} \times |N_{\text{eff}}| \tag{5.1}$$

where q is the electric charge, d is the thickness of a planar silicon device, and ϵ and ϵ_0 are the permittivity of silicon and the vacuum, respectively. The space charge density N_{eff} is initially defined by the doping concentration of the silicon bulk, which is to say, the concentration of donors (Group VII atoms such as phosphorus) in n-type silicon or the concentration of acceptors (Group III atoms such as boron) in p-type sensors. Irradiation will introduce further defects in the silicon at a rate that is proportional to the fluence. Once irradiated the silicon will undergo annealing effects. Both reverse and beneficial annealing are possible and are described by the impact on the space charge density. The space charge density can be written as: $N_{\text{eff}} = N_{\text{donor}} - N_{\text{acceptor}}$, where N_{donor} and N_{acceptor} are the effective donor and acceptor concentrations, respectively. For beneficial annealing, if N_{eff} is positive (meaning the bulk has more donors than acceptors) it will become more positive and if N_{eff} is negative (meaning there are more acceptors than donors) then it will become less negative. The opposite is true for the reverse annealing.

The change in effective doping concentration due to irradiation is written as:

$$\Delta N_{\text{eff}} = N_{\text{eff},0} - N_{\text{eff, final}} \tag{5.2}$$

where $N_{\text{eff},0}$ is the doping concentration before irradiation and $N_{\text{eff, final}}$ is the doping concentration after irradiation. The main results of the Hamburg Model are summarized in [143]:

$$\Delta N_{\text{eff}} = N_{\text{C}} + N_{\text{A}} + N_{\text{Y}} \tag{5.3}$$

$$N_{\text{A}} = g_{\text{A}} \Phi_{\text{eq}} e^{-t/\tau_{\text{a}}} \tag{5.4}$$

$$N_{\text{C}} = N_{\text{C},0}(1 - c_{\text{D}} \Phi_{\text{eq}}) + g_{\text{C}} \Phi_{\text{eq}} \tag{5.5}$$

$$N_{\text{Y}} = g_{\text{Y}} \Phi_{\text{eq}} (1 - e^{t/\tau_{\text{Y}}}). \tag{5.6}$$

where N_{C} is the stable damage term and is independent of time after irradiation, N_{A} is the beneficial annealing term, and N_{Y} is the reverse annealing term.

These results can be written as the impact on the effective donors and acceptors in the form of differential equations, as in [20]:

$$\frac{d}{dt}N_{\text{donor}}^{\text{removable}}(t) = -c_{\text{D}}\Phi_{\text{eq}}(t)N_{\text{donor}}^{\text{removable}} \tag{5.7}$$

$$\frac{d}{dt}N_{\text{acceptor}}^{\text{stable}}(t) = g_{\text{C}}\Phi_{\text{eq}}(t) \tag{5.8}$$

$$\frac{d}{dt}N_{\text{acceptor}}^{\text{beneficial}}(t) = g_{\text{A}}\Phi_{\text{eq}}(t) - k_{\text{A}}N_{\text{acceptor}}^{\text{beneficial}}(t) \tag{5.9}$$

$$\frac{d}{dt}N_{\text{neutral}}^{\text{reverse}}(t) = g_{\text{Y}}\Phi_{\text{eq}}(t) - k_{\text{Y}}N_{\text{neutral}}^{\text{reverse}}(t) \tag{5.10}$$

$$\frac{d}{dt}N_{\text{acceptor}}^{\text{reverse}}(t) = k_{\text{Y}}N_{\text{neutral}}^{\text{reverse}}(t). \tag{5.11}$$

A parameterized set of equations (as solved for in [47]) can be used to describe this change in doping concentration. They depend on time and temperature and take into account the defects introduced by the irradiation, and the resulting beneficial and reverse annealing. (In the literature, beneficial annealing is sometimes referred to as short-term annealing. Reverse annealing can also be referred to as long-term annealing or anti-annealing.) These equations are listed here:

$$N_{\text{donor}}^{\text{removable}} = N_{\text{donor,0}}^{\text{removable}}(1 - e^{-c_{\text{D}}\Phi_{\text{eq}}^{\text{rate}}t}) \tag{5.12}$$

$$N_{\text{acceptor}}^{\text{stable}} = g_{\text{C}}\Phi_{\text{eq}}^{\text{rate}}t \tag{5.13}$$

$$N_{\text{acceptor}}^{\text{beneficial}} = \frac{g_{\text{A}}}{k_{\text{A}}}\Phi_{\text{eq}}^{\text{rate}}(1 - e^{-k_{\text{A}}t}) + N_{\text{acceptor,0}}^{\text{beneficial}}e^{-k_{\text{A}}t} \tag{5.14}$$

$$N_{\text{neutral}}^{\text{reverse}} = \frac{g_{\text{Y}}}{k_{\text{Y}}}\Phi_{\text{eq}}^{\text{rate}}(1 - e^{-k_{\text{Y}}t}) + N_{\text{neutral,0}}^{\text{reverse}}e^{-k_{\text{Y}}t} \tag{5.15}$$

$$N_{\text{acceptor}}^{\text{reverse}} = \frac{g_{\text{Y}}}{k_{\text{Y}}}\Phi_{\text{eq}}^{\text{rate}}(k_{\text{Y}}t + e^{-k_{\text{Y}}t} - 1) + N_{\text{neutral,0}}^{\text{reverse}}(1 - e^{-k_{\text{Y}}t}) \tag{5.16}$$

and the Hamburg Model is given as:

$$\begin{aligned}\Delta N_{\text{eff}} &= N_{\text{donor}} - N_{\text{acceptor}} \\ &= N_{\text{donor}}^{\text{non-removable}} + N_{\text{donor}}^{\text{removable}} - N_{\text{acceptor}}^{\text{stable}} - N_{\text{acceptor}}^{\text{beneficial}} - N_{\text{acceptor}}^{\text{reverse}}.\end{aligned} \tag{5.17}$$

Equation 5.12 represents initial dopant concentration removal due to applied fluence, which for n-type sensors means the removal of donors. Equation 5.13 represents

the stable damage introduced by applied fluence. $N_{\mathrm{C},0}$ is the number of removable dopants (this fraction is frequently found to be less than one [143]) and c_{D} is the donor removal coefficient, dependent on the initial doping concentration as:

$$c_{\mathrm{D}} = 10.9 \times 10^{-2}\,\mathrm{cm}^{-1}/N_{\mathrm{eff},0}. \tag{5.18}$$

For the sensors simulated in this study, $c_{\mathrm{D}} = 6.4 \times 10^{-14}\,\mathrm{cm}^2$. Equation 5.14 describes the short-term beneficial annealing and Equations 5.15 and 5.16 describes reverse annealing.

The parameters k_i where $i = \mathrm{A}$ or Y follow an Arrhenius equation:

$$k_i = k_{i,0} e^{-E_i/k_{\mathrm{B}}T} \tag{5.19}$$

where E_i are the activation energies ($E_{\mathrm{A}} = 1.09 \pm 0.03$ eV, $E_{\mathrm{Y}} = 1.33 \pm 0.03$ eV) and the amplitudes $k_{i,0}$ are $k_{\mathrm{A},0} = 2.4^{+1.2}_{-0.8} \times 10^{13}$/s and $k_{\mathrm{Y},0} = 1.5^{+3.4}_{-1.1} \times 10^{15}$/s [144].

Finally, the introduction rates g_i, where $i = \mathrm{C}$, A or Y, are determined using the ATLAS data from the B-Layer [25] as: $g_{\mathrm{C}} = 0.43 \times 10^{-2}$/cm, $g_{\mathrm{A}} = 0.6 \times 10^{-2}$/cm, and $g_{\mathrm{Y}} = 6.0 \times 10^{-2}$/cm.

5.4.2 The Hamburg Model for p-type Sensors

For p-type silicon sensors, fewer studies have been performed and so less is understood regarding the impact of radiation on N_{eff} [143]. One idea behind the use of p-type sensors is to engineer the sensors for improved radiation hardness (foreseen in [144]). There is also a benefit from a simplified single-sided processing of the silicon wafer during fabrication. The effective doping concentration as a result of hadron irradiation for p-type silicon sensors can be written as [99, 116]:

$$N_{\mathrm{eff}} = N_{\mathrm{eff},0} - N_{\mathrm{C}}(1 - \exp(-c_{\mathrm{A}}\Phi_{\mathrm{eq}})) + g_{\mathrm{C}}\Phi_{\mathrm{eq}}, \tag{5.20}$$

where $N_{\text{eff},0}$ is the initial doping concentration, c_{A} is the initial acceptor removal constant, N_{C} is the number of removable initial acceptors, and g_{C} is the introduction rate of effective acceptors. Substantial short-term annealing of acceptors has not been observed [179] and does not appear in the equation above. The long-term annealing in p-type sensors has not been as widely studied as for n-type sensors, and does not appear in Equation 5.20. Initial results are presented here neglecting any impact of long-term annealing, followed by an introduction of the long-term annealing based on n-type characterizations.

In the context of the previous section, Equation 5.20 can be implemented using the following two equations (analogous to Equations 5.12 and 5.13) for performing a simulation of irradiated p-type sensors:

$$N_{\text{acceptor}}^{\text{removable}} = N_{\text{acceptor},0}^{\text{removable}}(1 - e^{-c_{\text{A}}\Phi_{\text{eq}}^{\text{rate}}t}) \tag{5.21}$$

$$N_{\text{acceptor}}^{\text{stable}} = g_{\text{C}}\Phi_{\text{eq}}^{\text{rate}}t. \tag{5.22}$$

The constant $c_{\text{A}} = 1.98\times10^{13}\,\text{cm}^2$ is taken from [179], consistent with the summary of recent results presented in [143] where the parameter has been shown to be dependent on initial doping concentration. The simulation of p-type sensors is an area of open research. Several values for the parameters $N_{\text{acceptor}}^{\text{removable}}$ and g_{C} are available in the literature. The extremes of the ranges of these values are investigated and presented in the next section. Simulations including and excluding long-term annealing are investigated; the long-term annealing is introduced using the same introduction rate $g_{\text{Y}} = 6.0 \times 10^{-2}\text{cm}^{-1}$ as is used in the n-type simulation, to reflect that acceptor increase observed during the long-term annealing is likely due to restoration of initial acceptors from a radiation induced interstitial site to a pre-irradiation substitutional site [179].

5.5 Simulation of Silicon Sensor Characteristics Under Extra-Terrestrial Radiation Conditions

Silicon detection is a mature technology for registering the passage of charged particles. At the same time it continues to evolve toward increasing radiation tolerance as well as precision and adaptability. For these reasons it is likely to remain a critical element of detection systems associated with extra-terrestrial exploration. Silicon sensor leakage current and depletion voltage depend upon the integrated fluence received by the sensor, and upon its thermal history during and after the irradiation process. For minimal assumptions on shielding and hence on particle energy spectrum, and using published data on Martian ground temperature, the leakage current density and depletion voltage are predicted, as a function of time, of silicon sensors in transit to, and subsequently deployed continuously on, the Mars surface for a duration of up to 28 Earth-years, for several sensor geometries and a worst-case temperature scenario.

5.5.1 Simulation Model and Sensor Types

The response of silicon detectors to non-ionizing energy loss (NIEL) by through-going particles has been parameterized, see Figure 5.29. The resulting Hamburg Model [128, 144, 145] has been widely used to predict changes in the effective dopant concentration - and consequently, in device leakage current and depletion voltage - due to radiation-induced bulk defects that evolve with temperature and time. Previous applications of this model have centered on, and been validated [18] using data such as those presented in Chapter 3, from experiments such as those at the CERN Large Hadron Collider. The implementation of the Hamburg Model can be found in [13].

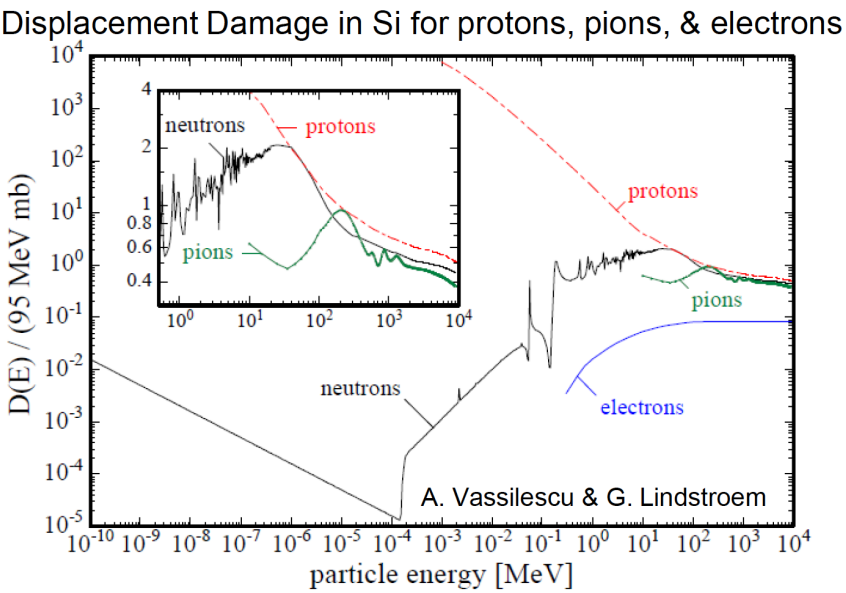


Figure 5.29: The NIEL scaling hypothesis [176].

The simulations herein examine the characteristics of sensors processed with two technologies: One uses the ATLAS design [33], based on oxygenated n-type bulk of depleted thickness 250 μm (representative of planar processed sensors). The other uses p-type bulk and sensor depletion distance 40 μm; this is taken to be approximately representative of 3D processed sensors. The initial donor concentration for the n-type sensors is taken to be 1.7×10^{12} cm^{-3}. The initial acceptor concentration for the p-type sensors is taken to be 2×10^{12}cm^{-3}. Both of these are typical values that are currently used in fabrications.

A simulation of the change in leakage current ΔI due to particle irradiation is discussed in Chapter 3, where the damage constant, α, describes both short- and long-term annealing [144]. A similar treatment is performed in this study of extra-terrestrial environmental conditions discussed in Section 5.5.2. The model of change in depletion voltage in planar silicon sensors due to irradiation is distinct from the model of leakage current. Details of the depletion voltage Hamburg Model were

described in Section 5.4. Finally the results of each simulation are compared in Section 5.5.3, including an investigation of several model-specific parameters. A discussion of the results and uncertainties is presented in Section 5.5.4.

5.5.2 Environmental Conditions for the Simulation

This section presents the conditions, such as temperature and radiation, used for making predictions of the silicon sensor bulk characteristics, leakage current density and depletion voltage. Each simulation produces a prediction of the sensor characteristics for a period corresponding to approximately 28.2 Earth-years, combined with the time associated with transit from the Earth to Mars, a period of about 250 days. The effects of the continuous flux of solar protons and galactic cosmic rays as well as occasional solar energetic particle (SEP) events are included.

Silicon detectors of moderate radiation tolerance are deployed already for numerous space applications, for example:

- Human dosimetry of charged particles is accomplished on the International Space Station/ISS through thick and thin silicon diodes [75].

- Particle radiation at the surface of Mars is measured by a suite of devices including three silicon p-i-n diodes, in the Radiation Assessment Detector (RAD) on the Mars Space Laboratory [94].

- The Cosmic Ray Telescope for the Effects of Radiation (CRaTER), an instrument on the Lunar Reconnaissance Orbiter spacecraft designed to characterize the lunar radiation environment, uses six silicon disks [167]; its records of intense SEPs are input to human organ dose projection code to assess risks to space travelers due to SEP exposure.

The primary motivation for this study is interest in the level of radiation hardness needed for a mission to Mars for the duration indicated above. Such a mission could additionally be interpreted as a proxy for extended intervals of space travel, possibly involving shielded human explorers at new frontiers, and including transport through regions susceptible to SEPs. A second motivation is presented by the resource-limited environment of such a mission (which has analogs in the environments of particle physics experiments), and a desire to investigate what parameters might permit best usage of resources. The RAD system provides examples of choices made in the resource limited environment: 4.2W are needed to power the full RAD detector, and due to power constraints it is powered for only 15 of every 60 minutes [135].

The simulation of silicon detector leakage current and depletion voltage takes as input fluence Φ_{eq} (in 1-MeV-neutron-equivalent ($\mathrm{n_{eq}}$) per area), temperature, and duration (which incorporates both duration of radiation exposure and of subsequent annealing). Four separate contributions to Φ are estimated: chronic radiation on the Mars surface; chronic radiation during transit; radiation due to SEPs that reach the Mars surface; and radiation due to SEPs that occur during the transit. To estimate the chronic charged particle fluence at the Martian surface, due to solar protons and galactic cosmic rays, the average charged particle dose rate D of (0.210 ± 0.040) mGy/day as recorded [95] by the Curiosity Rover during the period 2012-2013 serves as the starting point.

Radiation that reaches the Martian surface includes approximately 11%-14% alpha particles and heavier nuclei, and about 1% electrons, with the remaining 85% - 90% being protons [95]. Simulations of the effect of alpha particles on silicon bulk damage indicate that their contribution to NIEL in the silicon is 0.18% that of protons [110], under the conditions of a thin layer of shielding and including the effects of secondary particles. Accordingly, the fluence considered in this simulation is restricted to that of protons. To accomplish this, in calculations below, the

dose rate associated with the full charged particle spectrum is scaled by 0.9. Thus $D_{\mathrm{p}} = 0.9 \cdot 0.210$ mGy/day $= 0.189$ mGy/day is used. This dose rate is applied for a period $\tau = 28.2$ Earth-years (15 Martian-years), which is 10293 Earth-days; this time frame is chosen because it is approximately a factor of two greater than the operational span of the Opportunity Mars Exploration Rover, which holds the record for longevity. Thus the baseline lifetime proton dose is $0.000189 \times 10293 = 1.95$ Gy.

To convert this dose to fluence Φ, effects associated with production of high energy electrons in the silicon are neglected, as these have no significant impact on bulk damage. With the neglect of electron production, linear energy transfer (LET) can be replaced by rate of energy loss per unit length (dE/dx). With this approximation,

$$\Phi = D_{\mathrm{p}} \cdot \tau \cdot \frac{6.24 \times 10^9 \left[\mathrm{MeVg^{-1}Gy^{-1}}\right]}{dE/dx} \tag{5.23}$$

where dE/dx is measured in units of $\mathrm{MeVg^{-1}cm^2}$ [137, 182].

The rate of energy loss per unit length (dE/dx) for proton kinetic energies ranging from 1 keV to 10 GeV is shown in Figure 5.30, using data taken from [46].

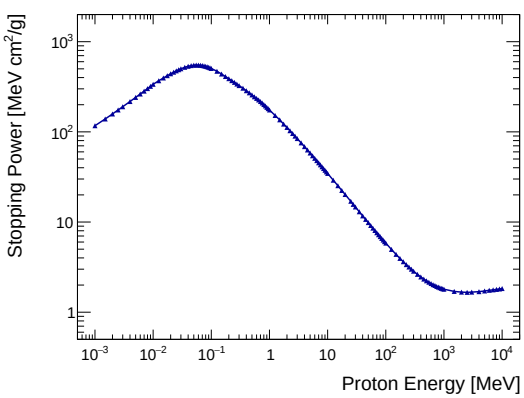


Figure 5.30: Stopping power for protons applied to silicon, from [46].

Applying Equation 5.23 to each point of Figure 5.30, for $D_{\mathrm{p}} = 0.189$ mGy/day,

yields Figure 5.31, proton fluence applied per day as a function of proton kinetic energy.

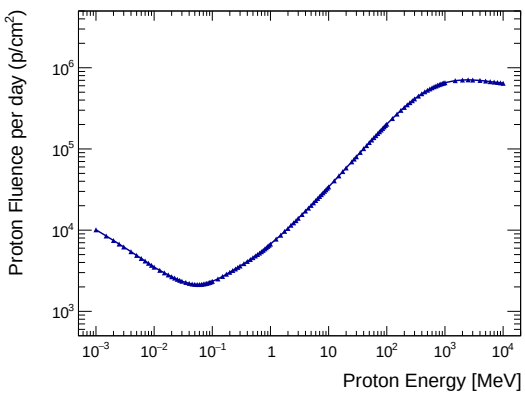


Figure 5.31: Proton fluence applied per day as a function of proton kinetic energy.

The information in Figure 5.31 can be converted from protons/cm^2 to n_{eq}/cm^2 using the NIEL scale factors, taken from Reference [177], at each proton kinetic energy. The outcome is shown in Figure 5.32, the conversion between proton energy and fluence Φ_{eq}, in n_{eq}/cm^2, per day.

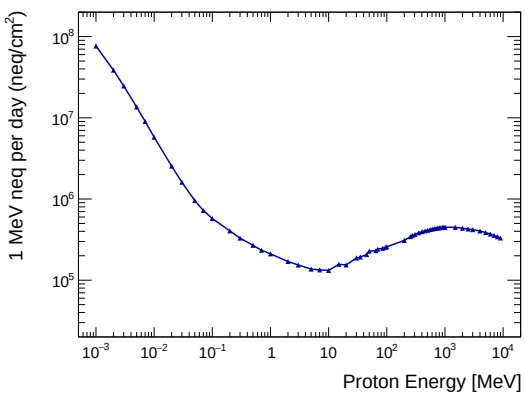


Figure 5.32: Average daily proton fluence, in 1-MeV-neutron equivalent per area, as a function of proton kinetic energy.

The energy spectrum to which silicon detectors operating on Mars will be exposed

depends on their shielding. In the absence of knowledge of what that shielding (and hence spectrum) will be, Figure 5.32 is used to identify the worst-case baseline proton fluence scenario for the region of the Martian surface explored by the Curiosity Rover. Neglecting protons of kinetic energies below 1 MeV (as it is assumed [149] that these will not penetrate to the experimental apparatus), the worst-case maximum fluence rate would be observed for a spectrum dominated by protons of kinetic energy 1.005 GeV, the local maximum of Figure 5.32. The associated proton fluence rate is 4.49×10^5 $n_{\mathrm{eq}}/\mathrm{cm}^2/\mathrm{day}$ or 5.2 $n_{\mathrm{eq}}/\mathrm{cm}^2/\mathrm{sec}$. This is rounded up to 6 $n_{\mathrm{eq}}/\mathrm{cm}^2/\mathrm{sec}$ and applied to the Hamburg Model simulation at 60 second intervals for a duration of 28.2 Earth-years to predict an integrated fluence of 4.6×10^9 $n_{\mathrm{eq}}/\mathrm{cm}^2$ for chronic solar protons and galactic cosmic ray protons of energies greater than or equal to 1 MeV.

A similar calculation is used to estimate the chronic fluence during transit, with the modification that the surface dose rate of 0.210 mGy/day is replaced by the measured [184] value for transit conditions, (higher in transit due to absence of protection by the Mars magnetosphere) of 0.481 mGy/day. The simulation applies this dose rate for 250 days, a period consistent with the length of time that was used to transport the Curiosity Rover to Mars.

In addition to the ambient flux of solar protons and galactic cosmic rays, silicon detectors at the Mars surface and in transit will be subjected to solar energetic particle (SEP) events. Two classes of SEPs have been reported [71], as categorized by their duration: the impulsive (1-20 hours) class, and the gradual (1-3 days) class. In this simulation they are not distinguished: SEPs in this simulation are applied to the silicon for a duration of one Mars-day, 24 hours, 40 minutes.

The Curiosity Rover detected 1 SEP event in the first 300 sols (each of duration 24 hours 40 minutes) at the Martian surface [95]. On this basis, the simulation of conditions at the surface includes 2 SEPs per Mars-year, which is 30 SEPs in

total. At the Mars surface, the observed [95] SEP dose is 0.025 mGy per event, which is 5.94×10^4 $n_{\mathrm{eq}}/\mathrm{cm}^2$/event. This is applied in the case of 27 of the simulated SEPs. The authors of Reference [140] have noted, however, that "extreme" SEPs, which occur approximately once per solar cycle, should be considered separately due to their exceptional potential for damage. To incorporate extreme SEP radiation, 3 such events are applied over the 15 Mars-year duration. Each is applied for the duration of one Mars-day. Simulation of their effect uses a flux for them of 1.88×10^{10} p/cm^2, corresponding to the maximum in the range reported in [140] for protons with energy greater than 30 MeV, equivalently 4.97×10^5 $n_{\mathrm{eq}}/\mathrm{cm}^2$/sec. Converted from protons to 1-MeV-neutron equivalent fluence, this predicts 4.41×10^{10} $n_{\mathrm{eq}}/\mathrm{cm}^2$/event for each of these three cases. In the simulation, SEPs are applied to the Martian surface once in each Martian summer and once in each Martian winter. The extreme SEPs are applied during the Martian summer 2, 8, and 14 Mars-years after the sensor has reached the Mars surface, so there is one year of chronic fluence before the first extreme SEP and one year of chronic fluence after the third one.

The Curiosity Rover detected 5 SEPs during the 250 day transit [184]. Accordingly, to simulate a high impact scenario of SEP effects during the transit, a total of 5 events are assumed, each with a dose (from Table 2 in [95]) of 19.5 mGy. A similar calculation to the one described above for computing chronic fluence on the surface is used to convert this dose rate to a fluence rate, corresponding to 4.63 $n_{\mathrm{eq}}/\mathrm{cm}^2$/event, or 12 $n_{\mathrm{eq}}/\mathrm{cm}^2$/sec.

This is sufficient as a fluence input to the Hamburg Model. The other inputs to the model include the depletion depth of the silicon sensor, the temperature, and the duration of exposure.

Temperatures of the Martian soil and atmosphere have been sampled at a variety of locations. Data reported [136] by the Rover Environmental Monitoring Station indicate an approximately sinusoidal variation in ambient air temperature over the

course of one sol with the minimum at about 205 K and the maximum at about 270 K. Information from the Mars Pathfinder instrument indicates that surface temperature within 0.25 m of the ground can exceed the air temperature 1.5 m above the ground by 20 Kelvin degrees. Earlier measurements by Viking instruments estimated maximum summer surface temperatures at the equator to be about 293 K. During the winter, the temperature near the Martian poles diminishes to 248 K. To cover the worst case scenario, the simulation reported here uses ground temperature that varies sinusoidally with amplitude 40 K over the course of each sol. This cycle is modulated for seasonal variations during the Mars year: the mean temperature is set to 235.5 K with annual sinusoidal variation of amplitude 22.5 K. Thus the Martian-yearly maximum temperature is taken to be 298 K, and the Martian-yearly minimum is 173 K. This thermal profile is applied for 15 Martian years (28.2 Earth-years). The temperature during transit is conservatively taken to be 283 K, for consistency with the maximum temperature recorded [154] for the silicon detectors in the AMS experiment. AMS is used as a concrete example of a silicon detector functioning in the extra-terrestrial environment, whose thermal profile and operating characteristics are available in the literature. The maximum AMS temperature is used because leakage current and annealing rate both depend upon temperature, and the maximum permits a conservatively high prediction of leakage current.

The simulation examines the characteristics of sensors processed with two technologies: One uses the ATLAS design [33], based on oxygenated n-type bulk of depleted thickness 250 μm (representative of planar processed sensors). The other uses p-type bulk and sensor depletion distance 40 μm; this is taken to be approximately representative of 3D processed sensors [152], although the cylindrical shape of the electrodes, and correspondingly convergent pattern of the electric fields lines reaching them, is neglected.

The details of the model used for the simulations are provided in Sections 3.5

(leakage current) and 5.4 (depletion voltage).

5.5.3 Simulation Results

Figure 5.33 (left) shows the change in leakage current density as a function of fluence in a sensor whose response is normalized to that at 294 K. Figure 5.33 (right) shows the same change in leakage current density, but as a function of the time, in Earth-years, from the beginning of the mission. The leakage current is clearly dominated by the extreme SEPs. The vertical drops represent annealing that dominates after the cessation of each extreme SEP. The curvature of the function in Figure 5.33 (left) in the fluence regime during application of each extreme SEP reflects the silicon's response to the temperature cycle over the course of a single Martian day. The step-like structure in Figure 5.33 (right) shows the response to the periodic non-extreme SEPs. The final value of ΔI_{leak}, after 15 Mars-years, is $4.03\mu\mathrm{A/cm}^3$. The peak leakage current, immediately after application of the final extreme SEP event, is $6.26\mu\mathrm{A/cm}^3$.

To predict the response of silicon devices being operated in other Martian thermal environments T, the current at temperature $T_{\mathrm{R}} = 294$ K can be translated according to Equation 3.2 (using E_{eff}, the effective silicon bandgap energy, = 1.21 eV). Figure 5.34 shows the change in depletion voltage during the same interval, for a device with depletion depth 250 μm and oxygenated n-type bulk. Figure 5.34 (left) shows the predicted full depletion voltage as a function of fluence, while Figure 5.34 (right) shows the same information versus time in Earth-years. The discontinuities reflect the effects of reverse annealing after cessation of extreme SEPs. The final value is 67 V. The negative slope on the n-type device indicates that the sensors will not have undergone type inversion at this stage. After inversion, the depletion voltage will rise; sensors of these geometries can continue to operate fully depleted up to several hundred volts.

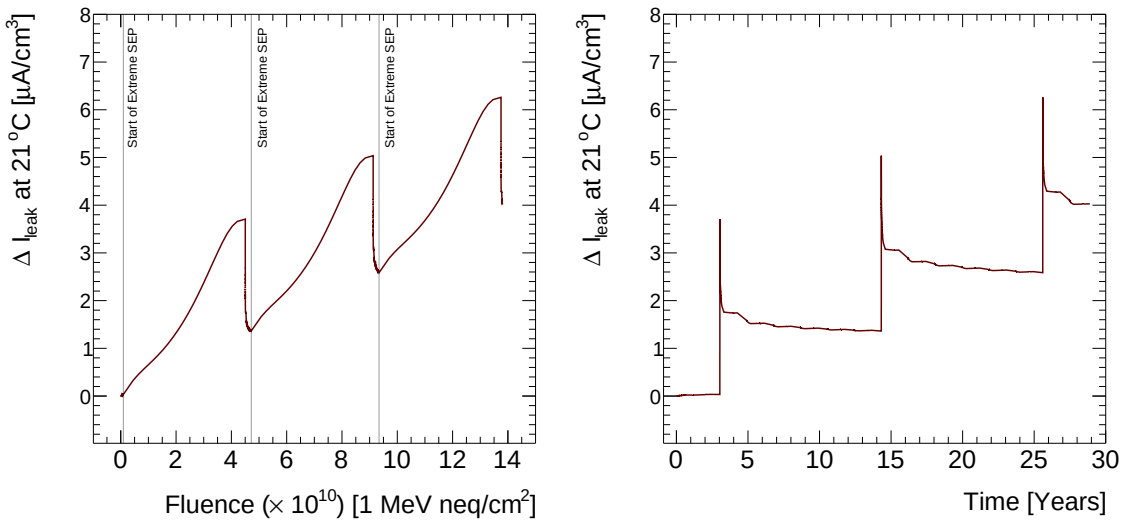


Figure 5.33: Predicted change in leakage current density as a function of (left) integrated charged hadron fluence and (right) time in Earth-years, in both the n-type and p-type silicon sensors, normalized to 294 K.

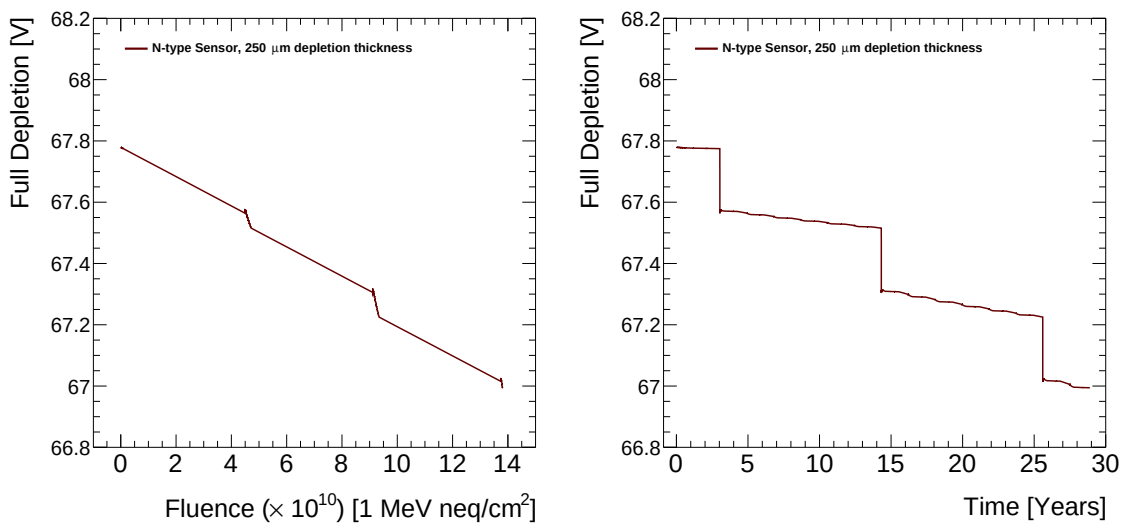


Figure 5.34: Depletion voltage as a function of (left) integrated charged particle fluence, and (right) time in Earth-years, for an oxygenated n-type silicon sensor of depletion depth 250 μm.

Four simulations of a p-type sensor with depletion depth 40 μm, representative of 3D, are shown in Figure 5.35. For three of the simulations, the effective acceptor introduction rate g_C has been fixed to $0.02\,\mathrm{cm}^{-1}$, consistent with [59, 128]. Nominally, complete initial acceptor removal, $N_{\mathrm{acceptor}}^{\mathrm{removable}}/N_{\mathrm{eff},0} = 1$, has been assumed. The result of the simulation requiring incomplete acceptor removal, $N_{\mathrm{acceptor}}^{\mathrm{removable}} = 0.1 \times N_{\mathrm{eff},0}$, consistent with the low initial acceptor removal results in [59, 116] is shown in Figure 5.35. The result of another simulation, excluding reverse annealing, is also shown. Finally these simulations are compared to a simulation using $g_C = 4.3 \times 10^{-3}/\mathrm{cm}$, matching the nominal n-type introduction rate. For the simulation with $g_C = 4.3 \times 10^{-3}/\mathrm{cm}$, complete initial acceptor removal is assumed and reverse annealing is included. The alternative choices yield similar results to those shown for the $g_C = 0.02\ \mathrm{cm}^{-1}$ simulations.

For the p-type case, the final value is approximately 2.4 V when full initial acceptor removal is simulated. (The final voltage is about 2.5 V for 10% initial acceptor removal.) In the case of the p-type sensor, once the initial acceptor removal is exhausted, the effective acceptor introduction term will dominate subsequent behavior, and the slope will become positive (this behavior can be seen in Figure 8 of [3]).

5.5.4 Results, Uncertainties, and Discussion

In comparisons of silicon sensor leakage current data to predictions by this model, the model was found to under-predict the observed current by 15% to 47% [18] depending on the detailed conditions of the sensor. Accordingly the leakage currents predicted for silicon sensors in the Mars environment are conservatively scaled by a safety factor of 1.5. Including this safety factor, the predicted leakage current density and depletion voltages after 28.2 years are shown in Table 5.3 for the two sensor geometries considered. The current per volume is the most natural unit for indicating the leakage, because devices such as those considered here are operated in reverse-

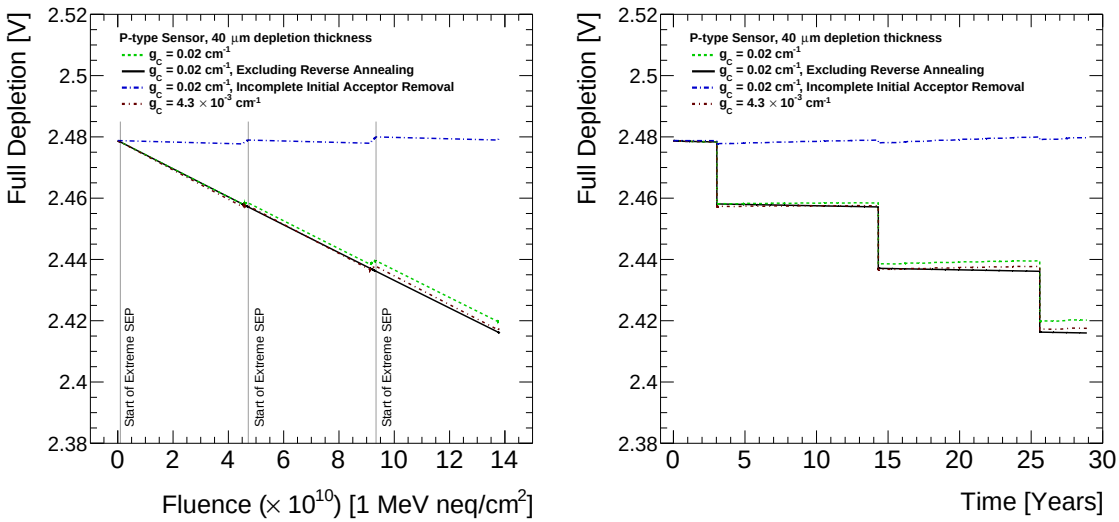


Figure 5.35: Several simulations of depletion voltage as a function of (left) integrated charged particle fluence, and (right) time in Earth-years, for a p-type silicon sensor of depletion depth 40 μm.

bias mode, in which the leakage current scales directly with volume; additionally the signal generated in the depleted region scales with depth. As a point of reference, the volume of a planar ATLAS pixel sensor (to which the data of [18] apply) is 0.25 cm^3.

The uncertainty on the predicted leakage current density is 10.5%, corresponding to contributions from the scale factor fit and the precision by which the temperature is known [18]. The contributions of uncertainties on the Hamburg Model parameters - approximately 20% - are not shown in the leakage current prediction. The uncertainty on the depletion voltage, due to uncertainties on the Hamburg Model parameters, is approximately 20%.

The relevant fluence due to space radiation conditions over the duration of a rover mission to Mars is significantly lower than the fluence received by the silicon detectors in ATLAS [4,19]. Consistent with expected lower fluences, the leakage current predictions presented here are lower than in ATLAS. Similarly, the magnitude of the change in depletion voltage in planar sensors is smaller than in the ATLAS

Sensor Type	n-type (planar)	p-type (approximation to 3D)
Depletion Depth (μm)	250	40
Leakage Current density (μA/cm^3)	9.4±1.0	9.4±1.0
Depletion Voltage (V)	67±13	2.4±0.5 (2.5)

Table 5.3: Predicted peak leakage current density and final depletion voltage for silicon sensors operating in the Martian environment for a duration of 28.2 Earth-years, including a safety factor of 1.5 applied to current. The predicted depletion voltage for p-type sensors assuming incomplete initial acceptor removal is shown in parentheses. The 10.5% uncertainty on the leakage current corresponds to contributions from the scale factor fit and the precision by which the temperature is known. The uncertainty on the depletion voltage, due to uncertainties on the Hamburg Model parameters, is taken to be 20%.

simulations. Depletion voltage predictions for 3D sensors in ATLAS have not been published, so no comparison may be made at this time to them. (Measurements of leakage current evolution in p-type bulk sensors are available in [21].). The simulation results presented here reflect the same expected annealing responses to temperature changes and received particle fluence as those in ATLAS simulations.

This work is restricted to the study of bulk silicon damage. Effects of surface damage by ionizing particles have not been included in the simulations reported here. The main surface effect is the increase of positive charge trapped in the surface oxide layer, which in turn can cause loss of isolation between electrodes, increased parasitic capacitance between adjacent regions, and variation in the distribution of the electric field at the Si-SiO_2 interface, affecting the breakdown voltage. Some of this can be mitigated by, for example, doping design in the inter-electrode region. A rough calculation predicts that these electronic devices in a space environment will be exposed to a gamma dose on the order of tens of krad from chronic sources. This modifies the above result by less than 1%, an amount that is unobservable within

the uncertainty of the prediction. Gammas induced by SEPs contribute negligible additional dose [85]. The present authors have studied the effect of gamma irradiation on 3D silicon sensor operating current [68]; exposure to a 5 Mrad dose increased the operating current by approximately a factor of two.

The Perugia Model [67, 146] incorporates surface effects, and it will provide an important foundation for follow-up studies to this one. Effective annealing behavior can be adapted from the Hamburg Model to the Perugia Model as is done in [21].

In the resources-limited environment of space, decreased power consumption can be realized with the 3D sensor technology. When possible, silicon sensors used for particle detection are typically operated above the estimated full depletion voltage to achieve optimal charge collection efficiency. In the case of 3D, these predictions indicate that an applied bias voltage as low as 10V may be sufficient for optimal operation.

In conclusion, Hamburg Model simulation of bulk electrical characteristics of silicon sensors using contemporary 3D and planar processing technology, fabricated with high resistivity n-type and p-type bulk, predicts that these devices' leakage current and depletion voltage will not pose restrictions for operation in Martian radiation and thermal conditions, including conditions associated with extreme Solar Energetic Particle events, through transit and for 28.2 Earth-years. These simulations may be used for insight and interpretation of measurements made with the Perseverance Rover [147]. The data collected by Perseverance may provide useful input and cross-checks of these simulations in the future.

Appendix A

$B^0_{(s)} \to \mu^+\mu^-$ Analysis - Variable Distributions in the Signal Channel

A set of variable distributions in the signal channel datasets discussed in Chapter 2 is provided in this appendix. The variable distributions are determined from three datasets: the sideband data, the $b\bar{b} \to \mu^+\mu^- X$ MC sample and the signal MC. These figures represent the set from which the comparisons shown in Figure 2.18 in the main text were selected. The figures in this appendix are organized roughly in the categories presented in Table 2.2. Additional analysis variables are included beyond those defined in Table 2.2. The plots shown in Figure 2.18 are repeated here for completeness.

As discussed in the main text, there is fair agreement between the $b\bar{b} \to \mu^+\mu^- X$ MC and the sideband data distributions. The $b\bar{b} \to \mu^+\mu^- X$ sample is not used for BDT training. The differences between the signal MC and the sideband data distributions are of particular interest: greater differences translate to larger separation power and are therefore useful to the BDT for signal discrimination.

The variables in category (a) of Table 2.2 are presented first, in Figures A.1, A.2, and A.3. These correspond to the B meson variables, related to the reconstruction of the decay vertex and to the collinearity between $\overrightarrow{p}^B$ and the flight vector between the production and decay vertices $\overrightarrow{\Delta x}$.

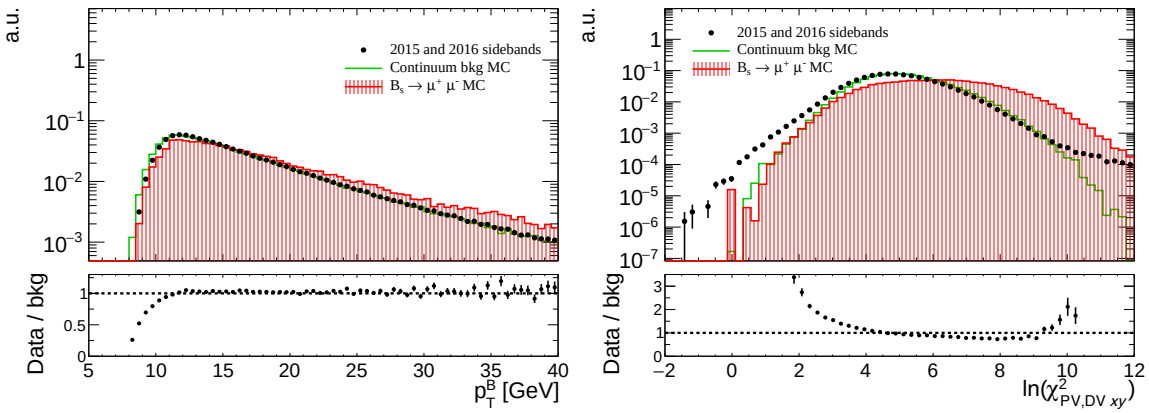


Figure A.1: Distributions of the variables (left) p_T^B and (right) $\ln(\chi^2_{\mathrm{PV,DV}\ xy})$ in the sideband data, the $b\bar{b} \to \mu^+\mu^- X$ MC sample and the signal MC sample. For each comparison the ratio of the distributions in the sideband data and the $b\bar{b} \to \mu^+\mu^- X$ MC sample is shown in the lower panel.

The variables ΔR_{flight} and $|\alpha_{\text{2D}}|$ are two of the most important variables in the BDT training due to the differences observed in the signal and background distributions, shown in Figure A.2

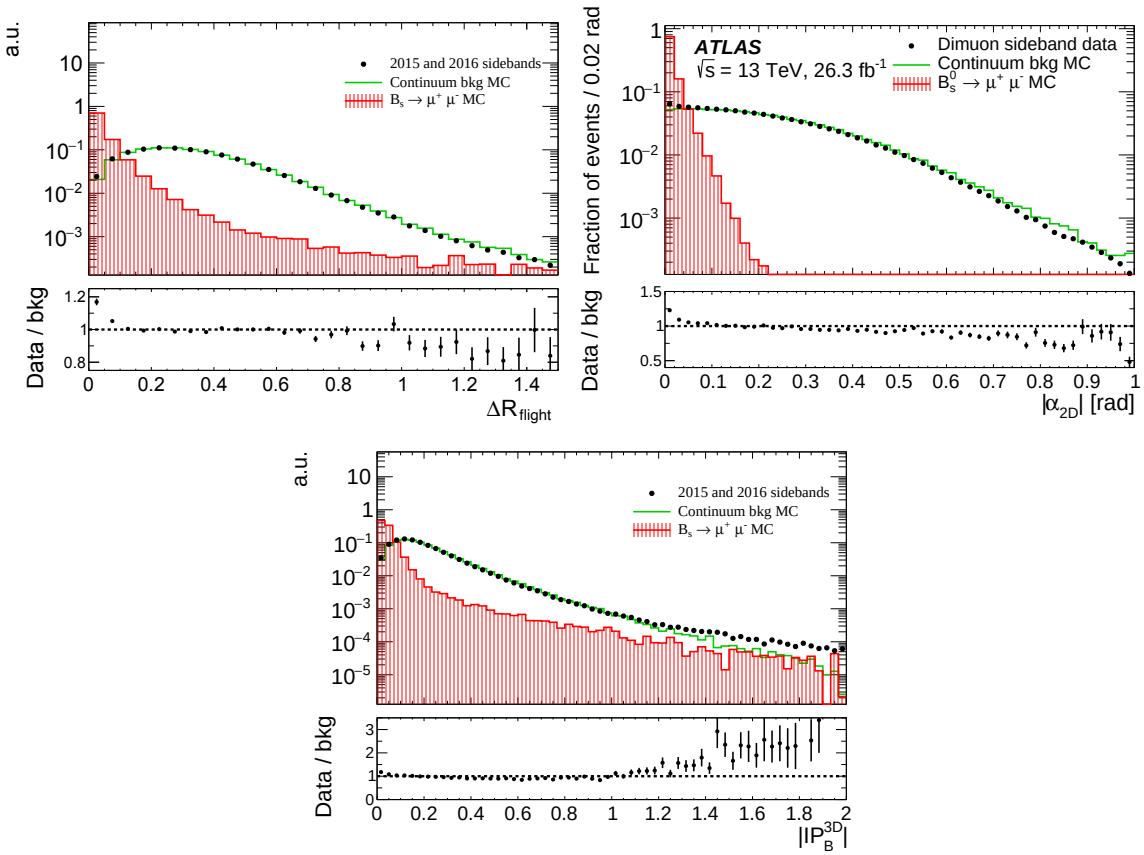


Figure A.2: Distributions of the variables (top left) ΔR_{flight} and (top right) $|\alpha_{\text{2D}}|$ and (bottom) IP_B^{3D} in the sideband data, the $b\bar{b} \to \mu^+\mu^- X$ MC sample and the signal MC sample. For each comparison the ratio of the distributions in the sideband data and the $b\bar{b} \to \mu^+\mu^- X$ MC sample is shown in the lower panel.

The variable L_{xy} is used as an input for the BDT training. It is shown together with the corresponding L_{xy} error and significance in Figure A.3.

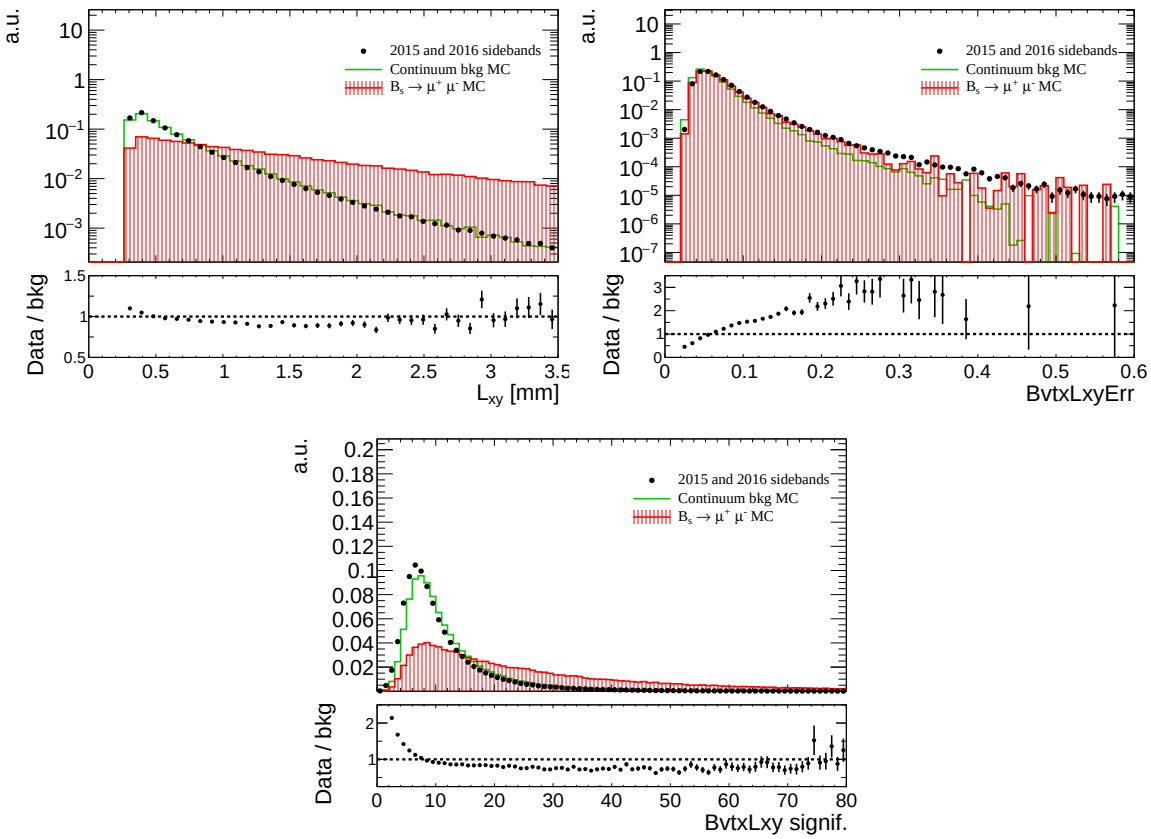


Figure A.3: Distributions of the variables (top left) L_{xy} and (top right) the respective error and (bottom) significance in the sideband data, the $b\bar{b} \to \mu^+\mu^- X$ MC sample and the signal MC sample. For each comparison the ratio of the distributions in the sideband data and the $b\bar{b} \to \mu^+\mu^- X$ MC sample is shown in the lower panel.

The category (b) variables describing the muons that form the B meson candidate are now presented.

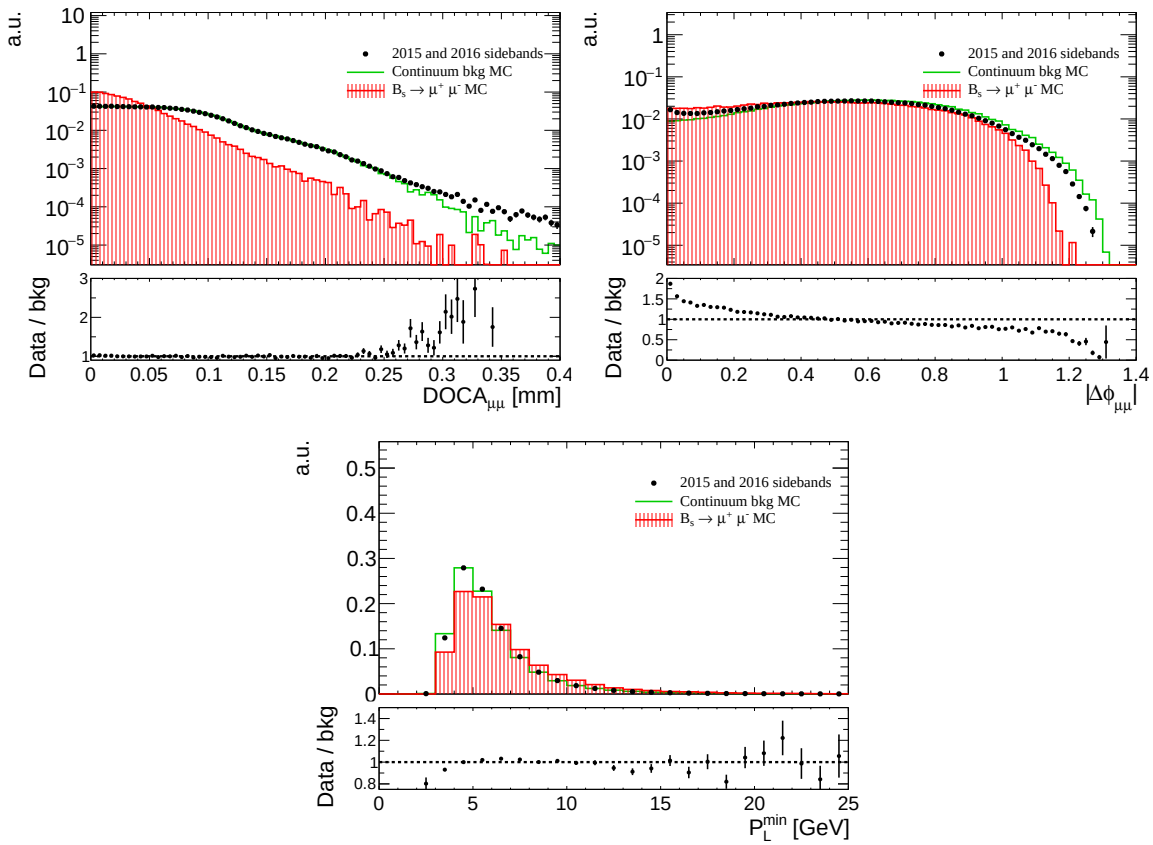


Figure A.4: Distributions of the variables (top left) $\mathrm{DOCA}_{\mu\mu}$, (top right) $|\Delta\phi_{\mu\mu}|$, and (bottom) $P_{\mathrm{L}}^{\mathrm{min}}$ in the sideband data, the $b\bar{b} \to \mu^+\mu^- X$ MC sample and the signal MC sample. For each comparison the ratio of the distributions in the sideband data and the $b\bar{b} \to \mu^+\mu^- X$ MC sample is shown in the lower panel.

The $|d_0|^{\min}$ significance and $|d_0|^{\max}$ significance are computed with $|d_0|^{\min}$ and $|d_0|^{\max}$ variables and their corresponding errors. The significances, which are used as input to the BDT are shown in Figure A.5.

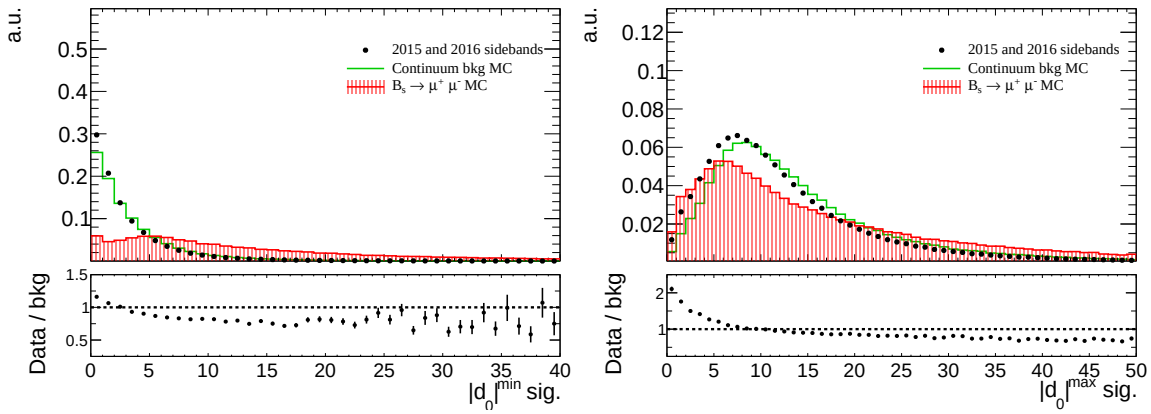


Figure A.5: Distributions of the variables (left) $|d_0|^{\min}$-sig. and (right) $|d_0|^{\max}$-sig. in the sideband data, the $b\bar{b} \to \mu^+\mu^- X$ MC sample and the signal MC sample. For each comparison the ratio of the distributions in the sideband data and the $b\bar{b} \to \mu^+\mu^- X$ MC sample is shown in the lower panel.

The components of the $|d_0|^{\min}$ significance and $|d_0|^{\max}$ significance are shown in Figure A.6.

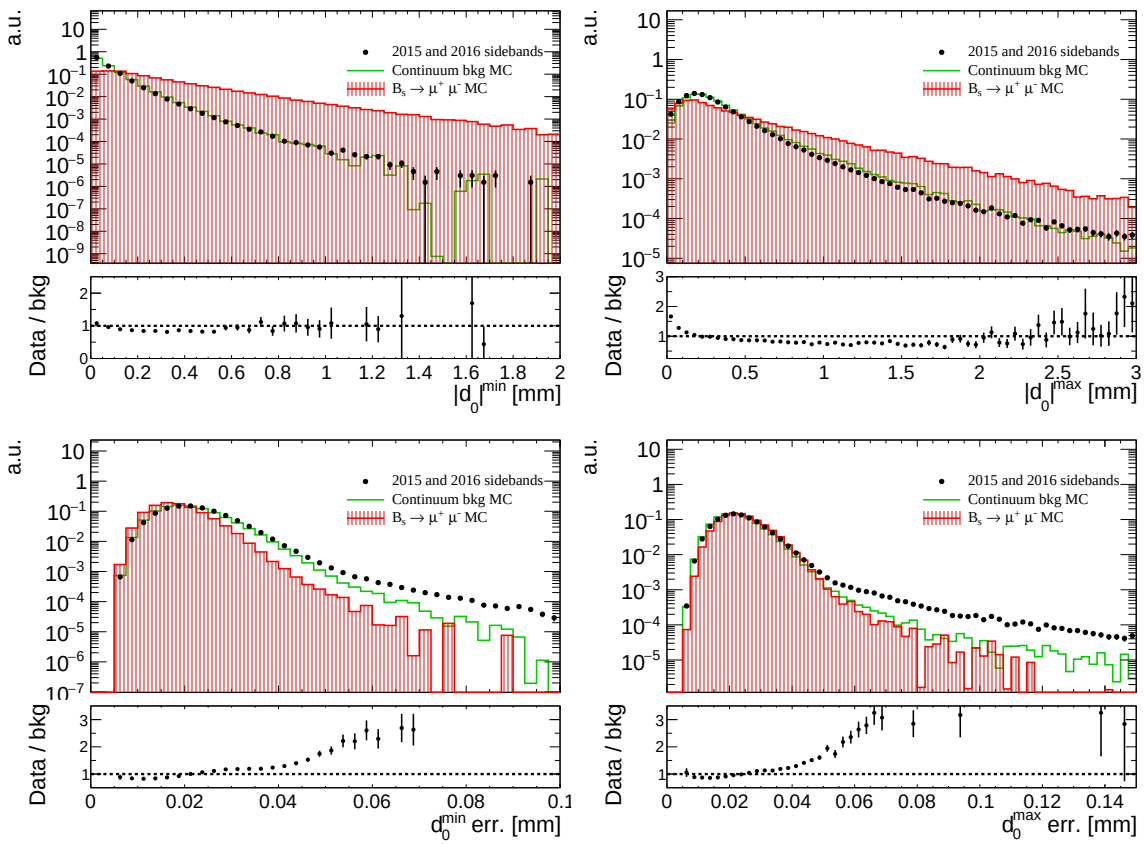


Figure A.6: Distributions of the variables (top left) $|d_0|^{\min}$, (top right) $|d_0|^{\max}$, (bottom left) $|d_0|^{\min}$ error and (bottom right) $|d_0|^{\max}$ error in the sideband data, the $b\bar{b} \to \mu^+\mu^- X$ MC sample and the signal MC sample. For each comparison the ratio of the distributions in the sideband data and the $b\bar{b} \to \mu^+\mu^- X$ MC sample is shown in the lower panel.

In addition to the other variables listed in Table 2.2 category (b), the individual muon $|\eta|$ and p_{T} distributions are shown in Figure A.7.

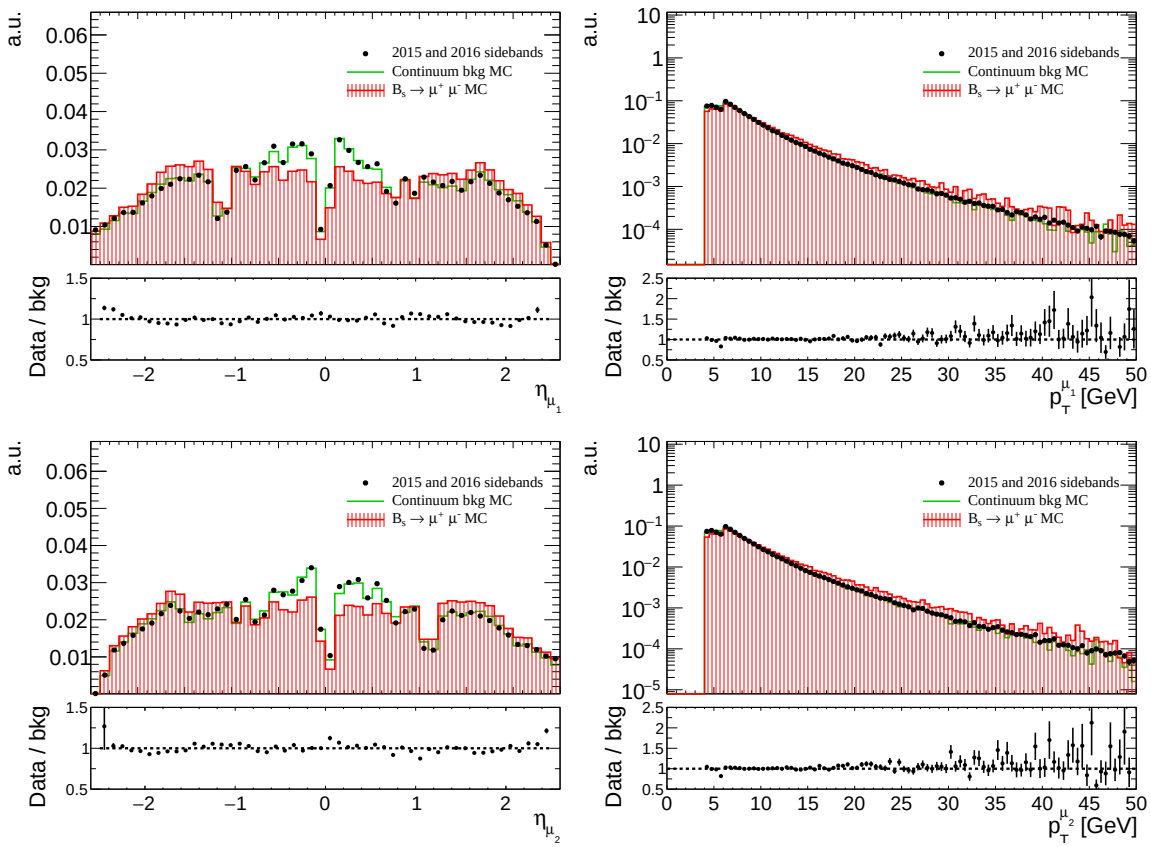


Figure A.7: Distributions of the variables (top left) η_{μ_1} error, (top right) $p_{\mathrm{T}}^{\mu_1}$, (bottom left) η_{μ_2} and (bottom right) $p_{\mathrm{T}}^{\mu_2}$ in the sideband data, the $b\bar{b} \to \mu^+\mu^- X$ MC sample and the signal MC sample. For each comparison the ratio of the distributions in the sideband data and the $b\bar{b} \to \mu^+\mu^- X$ MC sample is shown in the lower panel.

The category (c) variables of Table 2.2 related to the isolation of the B candidate within the event are shown in Figure A.8. The definitions of the variables shown in these distributions correspond to those presented in Table 2.2, before the explicit studies, presented in Chapter 2, were performed to optimize these definitions.

The distribution of the number of tracks (excluding the B candidate's muon tracks) contained within a cone of size $\Delta R = \sqrt{(\Delta\phi)^2 + (\Delta\eta)^2} = 0.7$ around the B direction, and used in the computation of B_{iso}, is shown in Figure A.8. This variable is not included in the BDT training.

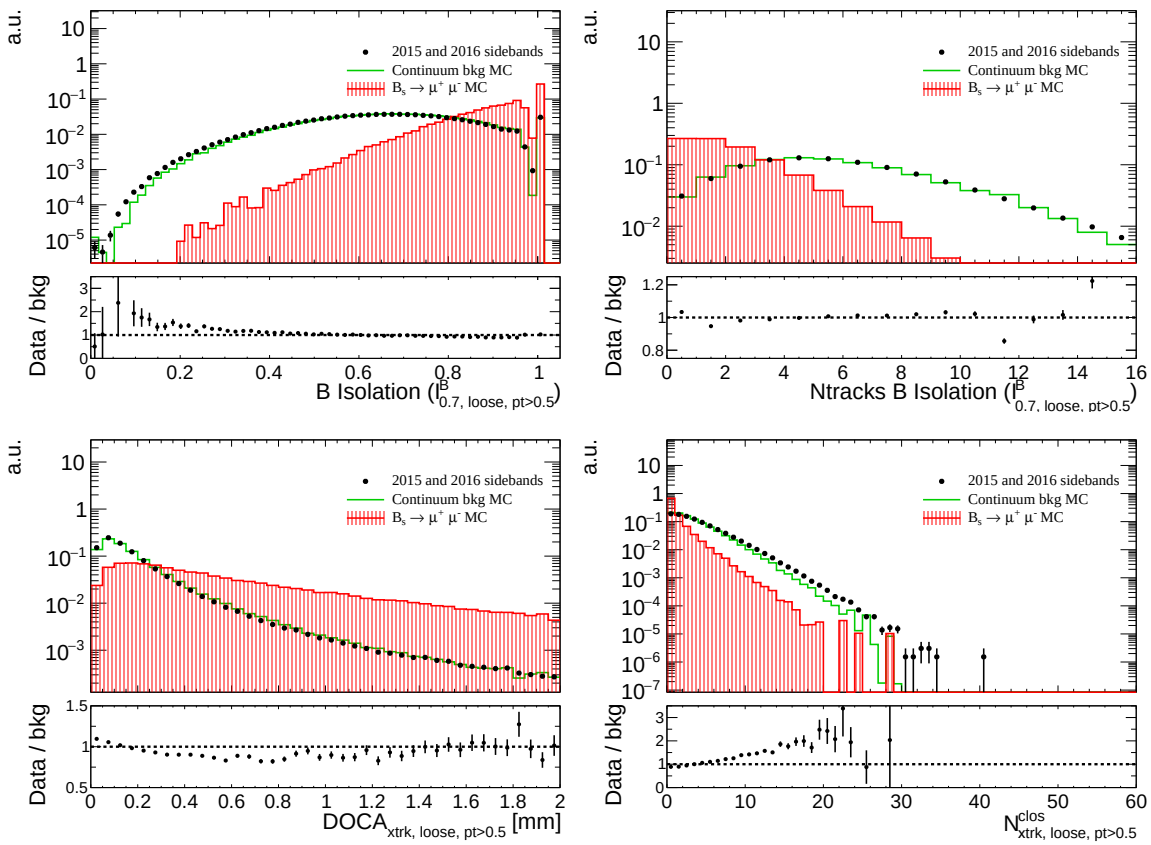


Figure A.8: Distributions of the variables (top left) B_{iso}, (top right) number of tracks in the B_{iso} cone, (bottom left) $\text{DOCA}_{\text{xtrk}}$ and (bottom right) $N^{\text{close}}_{\text{xtrk}}$ in the sideband data, the $b\bar{b} \to \mu^+\mu^- X$ MC sample and the signal MC sample. For each comparison the ratio of the distributions in the sideband data and the $b\bar{b} \to \mu^+\mu^- X$ MC sample is shown in the lower panel.

The distributions of the variable in category (d) of Table 2.2 are shown in Figure A.9. The variable is used to indicate the degree of compatibility of a muon in the B candidate originating at a point inconsistent with the primary vertex. There is a striking difference between the signal and background distributions which leads to the BDT using this variable frequently during training.

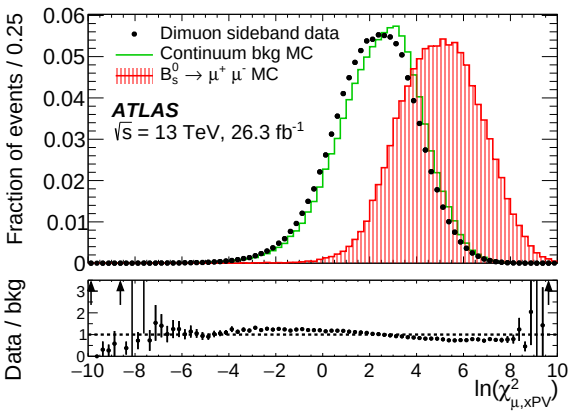


Figure A.9: Distributions of the variable $\chi^2_{\mu,\mathrm{xPV}}$ in the sideband data, the $b\bar{b} \to \mu^+\mu^- X$ MC sample and the signal MC sample. For each comparison the ratio of the distributions in the sideband data and the $b\bar{b} \to \mu^+\mu^- X$ MC sample is shown in the lower panel.

The distributions for two pileup variables are shown in Figure A.10. The signal MC is reweighted on the pileup variable $\langle\mu\rangle$.

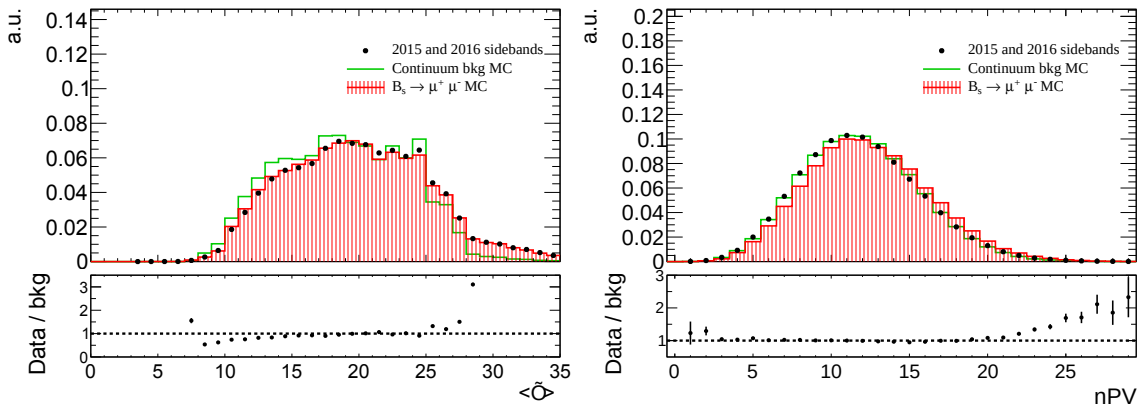


Figure A.10: Distributions of the variables (left) $\langle\mu\rangle$ and (right) nPV in the sideband data, the $b\bar{b} \to \mu^+\mu^- X$ MC sample and the signal MC sample. For each comparison the ratio of the distributions in the sideband data and the $b\bar{b} \to \mu^+\mu^- X$ MC sample is shown in the lower panel.

Two variables related to the position of the B candidate in the detector are shown in Figure A.11.

Two variables related to the position of the two muons with respect to one another are presented in Figure A.12.

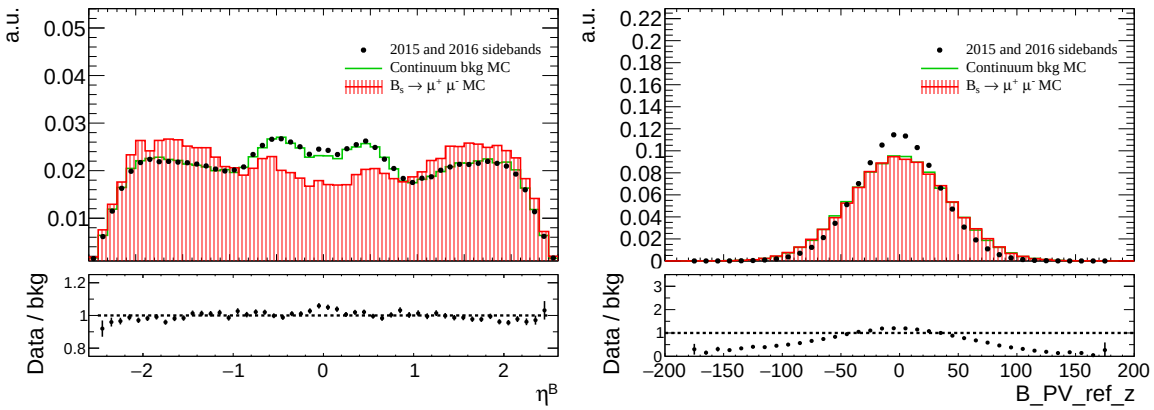


Figure A.11: Distributions of the variables (left) η^B and (right) the z position of the B primary vertex in the sideband data, the $b\bar{b} \to \mu^+\mu^- X$ MC sample and the signal MC sample. For each comparison the ratio of the distributions in the sideband data and the $b\bar{b} \to \mu^+\mu^- X$ MC sample is shown in the lower panel.

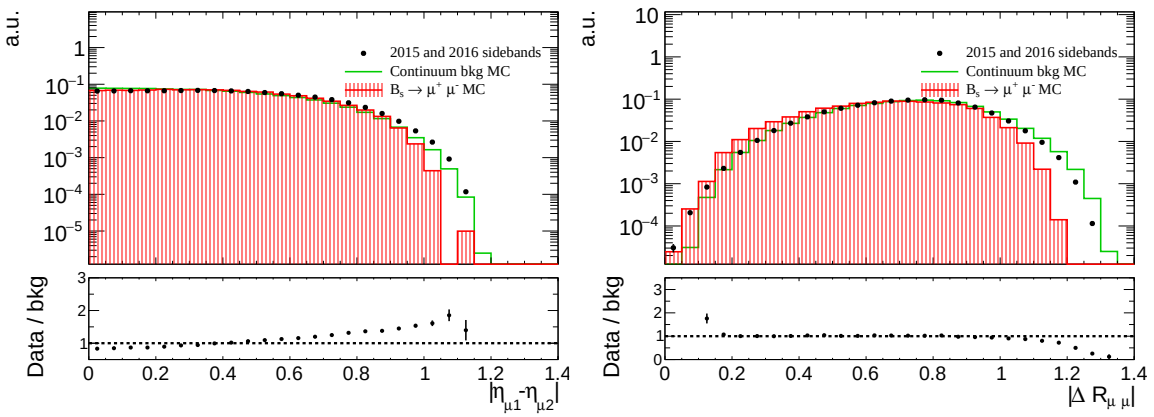


Figure A.12: Distributions of the variables (left) the difference in η of the two muons in the B candidate and (right) the opening angle $\Delta R_{\mu\mu}$ between the two muons in the B candidate in the sideband data, the $b\bar{b} \to \mu^+\mu^- X$ MC sample and the signal MC sample. For each comparison the ratio of the distributions in the sideband data and the $b\bar{b} \to \mu^+\mu^- X$ MC sample is shown in the lower panel.

The B candidate mass and the corresponding error are shown in Figure A.13. In these figures, the blinded window is excluded in the background samples.

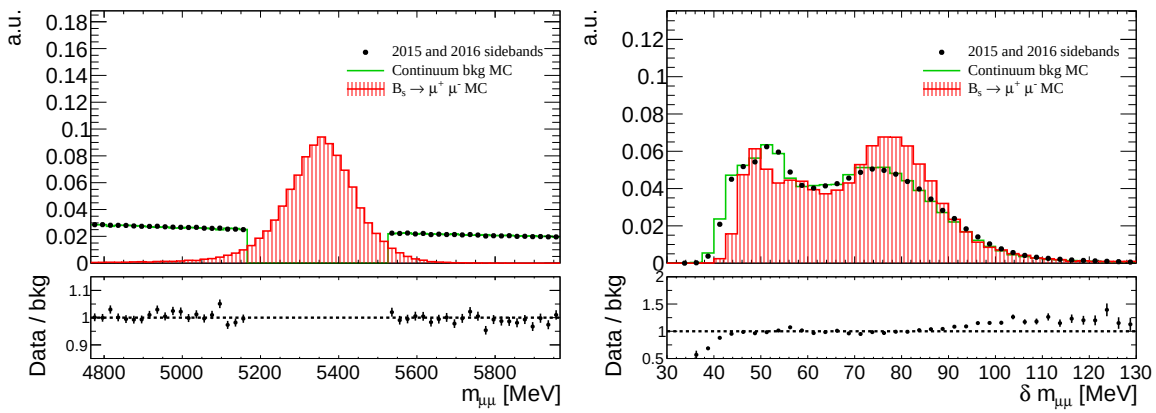


Figure A.13: Distributions of the variables (left) B invariant mass and (right) corresponding error in the sideband data, the $b\bar{b} \to \mu^+\mu^- X$ MC sample and the signal MC sample. For each comparison the ratio of the distributions in the sideband data and the $b\bar{b} \to \mu^+\mu^- X$ MC sample is shown in the lower panel.

The lifetime of the B candidates is probed in the distribution of the proper decay time ($c\tau$) and the corresponding significance in Figure A.14.

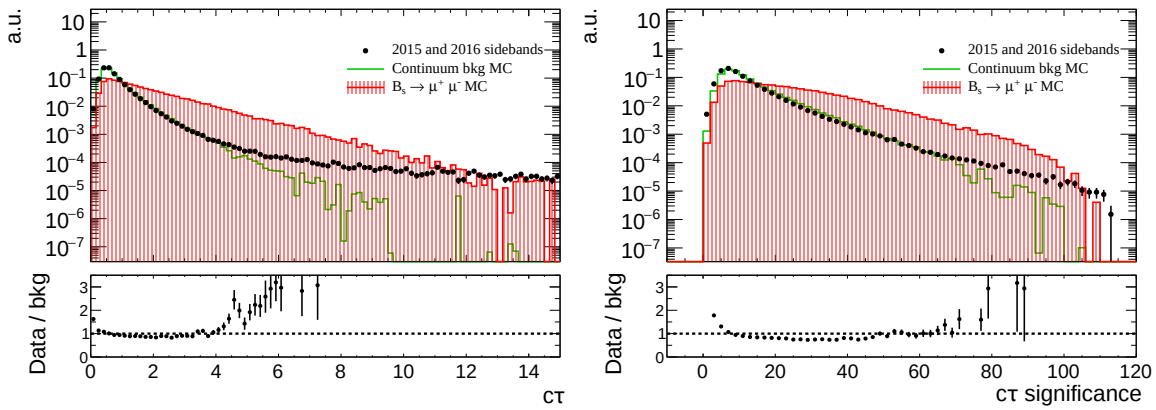


Figure A.14: Distributions of the variables (left) proper decay time of the B candidate and (right) corresponding significance in the sideband data, the $b\bar{b} \to \mu^+\mu^- X$ MC sample and the signal MC sample. For each comparison the ratio of the distributions in the sideband data and the $b\bar{b} \to \mu^+\mu^- X$ MC sample is shown in the lower panel.

References

[1] G. Aad et al., *ATLAS Pixel Detector Electronics and Sensors*, J. Instrum. **3** (2008) P07007. [pages 10, 14, 117]

[2] B. Abbott et al., *Production and integration of the ATLAS Insertable B-Layer*, J. Instrum. **13** (2018) T05008. [page 14]

[3] A. Affolder et al., *Radiation damage in the LHCb vertex locator*, J. Instrum. **8** (2013) P08002. [page 259]

[4] S. Agostinelli et al., *GEANT4 – A simulation toolkit*, Nucl. Instrum. Methods A **506** (2003) 250–303. [pages 25, 36, 119]

[5] ALICE Collaboration, *The ALICE experiment at the CERN LHC*, J. Instrum. **3** (2008) S08002. [page 5]

[6] Y. Amhis et al., *Averages of b-hadron, c-hadron, and τ-lepton properties as of summer 2016*, Eur. Phys. J. C **77** (2017) 895. [pages 59, 71, 79]

[7] C. D. Anderson, *The Positive Electron*, Phys. Rev. **43** (1933) 491–494. [page 4]

[8] ATLAS Collaboration, *A Leakage Current-Based Measurement of the Radiation Damage in the ATLAS Pixel Detector*, ATL-INDET-PUB-2014-004 (2014), https://cds.cern.ch/record/1752122. [pages 14, 121]

[9] ATLAS Collaboration, *ATLAS Luminosity Public Results: Delivered Luminosity versus time for 2011-2018*, 2020, https://twiki.cern.ch/twiki/bin/view/AtlasPublic/LuminosityPublicResultsRun2. [page 123]

[10] ATLAS Collaboration, *ATLAS Luminosity Public Results: Pileup Interactions and Data Taking Efficiency*, 2020, https://twiki.cern.ch/twiki/bin/view/AtlasPublic/LuminosityPublicResultsRun2#Pileup_Interactions_and_Data_Tak. [pages 86, 87]

[11] ATLAS Collaboration, *Determination of the Ratio of b-quark Fragmentation Fractions f_s/f_d in pp Collisions at $\sqrt{s} = 7$ TeV with the ATLAS Detector*, Phys. Rev. Lett. **115** (2015) 262001. [page 79]

[12] ATLAS Collaboration, *Expected Tracking Performance of the ATLAS Inner Tracker at the HL-LHC*, ATL-PHYS-PUB-2019-014 (2019), https://cds.cern.ch/record/2669540. [page 17]

[13] ATLAS Collaboration, *Hamburg Model Simulation Code*, 2019, https://gitlab.cern.ch/atlas/athena/tree/master/InnerDetector/InDetCalibAlgs/PixelCalibAlgs/RadDamage/HamburgModel. [pages 126, 248]

[14] ATLAS Collaboration, *IBL Module Loading onto Stave and Quality Check*, ATL-INDET-PUB-2015-003 (2015), https://cds.cern.ch/record/2110639. [page 203]

[15] ATLAS Collaboration, *Luminosity determination in pp collisions at $\sqrt{s} = 8$ TeV using the ATLAS detector at the LHC*, Eur. Phys. J. C **76** (2016) 653. [pages 123, 130]

[16] ATLAS Collaboration, *Luminosity Determination in pp Collisions at $\sqrt{s} = 13$ TeV using the ATLAS Detector at the LHC*, ATLAS-CONF-2019-021 (2019), https://cds.cern.ch/record/2677054. [pages 8, 31]

[17] ATLAS Collaboration, *Measurement of quarkonium production in proton–lead and proton–proton collisions at* 5.02 TeV *with the ATLAS detector*, Eur. Phys. J. C **78** (2018) 171. [page 25]

[18] ATLAS Collaboration, *Measurement of radiation damage through leakage current monitoring of the ATLAS Pixel Detector*, ATL-INDET-PUB-2019-001 (2019), https://cds.cern.ch/record/2699903/. [pages 2, 13, 127, 248, 259, 260]

[19] ATLAS Collaboration, *Measurement of the muon reconstruction performance of the ATLAS detector using 2011 and 2012 LHC proton–proton collision data*, Eur. Phys. J. C **74** (2014) 3130. [page 28]

[20] ATLAS Collaboration, *Modeling Radiation Damage to Pixel Sensors in the ATLAS Detector*, J. Instrum. **14** (2019) P06012. [pages 126, 245]

[21] ATLAS Collaboration, *Modelling radiation damage to pixel sensors in the ATLAS detector*, J. Instrum. **14** (2019) P06012. [pages 261, 262]

[22] ATLAS Collaboration, *Muon reconstruction performance of the ATLAS detector in proton–proton collision data at* $\sqrt{s} = 13$ *TeV*, Eur. Phys. J. C **76** (2016) 292. [pages 28, 36]

[23] ATLAS Collaboration, *Operation and performance of the ATLAS semiconductor tracker*, J. Instrum. **9** (2014) P08009. [page 10]

[24] ATLAS Collaboration, *Performance of the ATLAS trigger system in 2015*, Eur. Phys. J. C **77** (2017) 317. [page 27]

[25] ATLAS Collaboration, *Radiation damage in 2015-2017, Figure 8*, 2018, https://atlas.web.cern.ch/Atlas/GROUPS/PHYSICS/PLOTS/PIX-2018-005/. [page 246]

[26] ATLAS Collaboration, *Search for the decay* $B_s^0 \to \mu^+\mu^-$ *with the ATLAS detector*, Phys. Lett. B **713** (2012) 387. [pages 25, 60]

[27] ATLAS Collaboration, *Sensor Radiation Damage in the ATLAS Inner Detector using Leakage Currents*, 2020, https://atlas.web.cern.ch/Atlas/GROUPS/PHYSICS/PLOTS/IDET-2020-001/. [pages 151, 154, 155]

[28] ATLAS Collaboration, *Study of the rare decays of B_s^0 and B^0 into muon pairs from data collected during the LHC Run 1 with the ATLAS detector*, Eur. Phys. J. C **76** (2016) 513. [pages 22, 23, 38, 74]

[29] ATLAS Collaboration, *Study of the rare decays of B_s^0 and B^0 mesons into muon pairs using data collected during 2015 and 2016 with the ATLAS detector*, J. High Energ. Phys. **4** (2019) 98. [pages 2, 20, 35, 55, 57, 61, 64, 67, 69, 72, 73, 75–77, 80–82]

[30] ATLAS Collaboration, *Study of the rare decays of B_s^0 and B^0 into muon pairs from data collected during the LHC Run 1 with the ATLAS detector*, Eur. Phys. J. C (2016). [page 46]

[31] ATLAS Collaboration, *Summary of ATLAS Pythia 8 Tunes*, ATL-PHYS-PUB-2012-003 (2012), https://cds.cern.ch/record/1474107. [pages 124, 128]

[32] ATLAS Collaboration, *Technical Design Report for the ATLAS Inner Tracker Pixel Detector*, CERN-LHCC-2017-021 (2017), https://cds.cern.ch/record/2285585. [pages 14, 15, 117, 162, 164]

[33] ATLAS Collaboration, *The ATLAS Experiment at the CERN Large Hadron Collider*, J. Instrum. **3** (2008) S08003. [pages 5, 9–13, 125, 249, 256]

[34] ATLAS Collaboration, *The ATLAS Simulation Infrastructure*, Eur. Phys. J. C **70** (2010) 823. [page 25]

[35] ATLAS Tracking Group, Kaon Reconstruction Recommendations (Private Communications), (2018). [page 60]

[36] ATLAS TRT Collaboration, *The ATLAS Transition Radiation Tracker (TRT) proportional drift tube: design and performance*, J. Instrum. **3** (2008) P02013–P02013. [page 10]

[37] ATLAS Vertexing Group, Selection Recommendations (Private Communications), (2020). [page 92]

[38] ATLAS, CMS, and LHCb Collaborations, *Combination of the ATLAS, CMS and LHCb results on the $B^0_{(s)} \to \mu^+\mu^-$ decays*, CERN CDS (2020), https://cds.cern.ch/record/2727216. [pages 2, 77, 80–82]

[39] G. Avoni et al., *The new LUCID-2 detector for luminosity measurement and monitoring in ATLAS*, J. Instrum. **13** (2018) P07017. [page 31]

[40] K. Babu and C. Kolda, *Higgs mediated $B^0 \to \mu^+\mu^-$ in minimal supersymmetry*, Phys. Rev. Lett. **84** (2000) 228–231. [page 5]

[41] S. Baranov et al., *Estimation of Radiation Background, Impact on Detectors, Activation and Shielding Optimization in ATLAS*, ATL-GEN-2005-001 (2005), https://cds.cern.ch/record/814823. [pages 118, 124]

[42] G. Battistoni et al., *The FLUKA code: Description and benchmarking*, AIP Conf. Proc. **896** (2007) 31–49. [pages 119, 124]

[43] R. Becker-Szendy et al., *Calibration of the IMB detector*, Nucl. Instrum. Methods A **352** (1995) 629–639. [page 213]

[44] Belle Collaboration, *Observation of a Narrow Charmoniumlike State in Exclusive $B^\pm \to K^\pm\pi^+\pi^- J/\psi$ Decays*, Phys. Rev. Lett. **91** (2003) 262001. [page 4]

[45] M. Beneke, C. Bobeth, and R. Szafron, *Power-enhanced leading-logarithmic QED corrections to $B_q \to \mu^+\mu^-$*, J. High Energ. Phys. **10** (2019) 232. [page 22]

[46] M. Berger et al., *Stopping-Power & Range Tables for Electrons, Protons, and Helium Ions*, 2017, https://www.nist.gov/pml/stopping-power-range-tables-electrons-protons-and-helium-ions. [page 252]

[47] J.-C. Beyer, "Optimisation of pixel modules for the ATLAS inner tracker at the high-luminosity LHC," Doctoral dissertation: Ludwig-Maximilians-Universität München, 2019, http://nbn-resolving.de/urn:nbn:de:bvb:19-239390. [page 245]

[48] C. Bobeth, M. Gorbahn, and E. Stamou, *Electroweak corrections to* $B_{s,d} \to l^+l^-$, Physi. Rev. D **89** (2014) 034023. [page 21]

[49] T. E. Browder and K. Honscheid, *B mesons*, Progress in Particle and Nuclear Physics **35** (1995) 81–219. [page 21]

[50] A. J. Buras, *Relations between* $\Delta M_{s,d}$ *and* $B_{s,d} \to \mu^+\mu^-$ *in models with minimal flavour violation*, Phys. Lett. B **566** (2003) 115–119. [page 5]

[51] A. J. Buras, R. Fleischer, J. Girrbach, and R. Knegjens, *Probing new physics with the* $B_s \to \mu^+\mu^-$ *time-dependent rate*, J. High Energ. Phys. **07** (2013) 77. [pages 24, 61]

[52] C. Bobeth et al., $B_{s,d} \to l^+l^-$ *in the Standard Model with Reduced Theoretical Uncertainty*, Phys. Rev. Lett. **112** (2014) 101801. [pages 22, 61]

[53] CERN, *LHC Design Report*, CERN Yellow Report (2004), https://cds.cern.ch/record/782076. [page 5]

[54] CERN, *LHC Project Schedule*, https://project-hl-lhc-industry.web.cern.ch/content/project-schedule. [page 16]

[55] O. Chamberlain, E. Segrè, C. Wiegand, and T. Ypsilantis, *Observation of Antiprotons*, Phys. Rev. **100** (1955) 947–950. [page 4]

[56] A. Chilingarov, *Temperature Dependence of the Current Generated in Si Bulk*, J. Instrum. **8** (2013) P10003. [pages 119, 122, 143]

[57] S. R. Choudhury, A. S. Cornell, N. Gaur, and G. C. Joshi, *Signatures of new physics in dileptonic B-decays*, Int. J. Mod. Phys. A **21** (2006) 2617–2634. [page 5]

[58] S. R. Choudhury and N. Gaur, *Dileptonic decay of B_s meson in SUSY models with large tan β*, Phys. Lett. B **451** (1999) 86–92. [page 5]

[59] V. Cindro et al., *Radiation damage in p-type silicon irradiated with neutrons and protons*, Nucl. Instrum. Methods A **599** (2009) 60–65. [page 259]

[60] CMS and LHCb Collaborations, *Observation of the rare $B_s^0 \to \mu^+\mu^-$ decay from the combined analysis of CMS and LHCb data*, Nature **522** (2015) 68. [pages 21, 22]

[61] CMS Collaboration, *Measurement of properties of $B_s^0 \to \mu^+\mu^-$ decays and search for $B^0 \to \mu^+\mu^-$ with the CMS experiment*, J. High Energ. Phys. **4** (2020) 188, ISSN: 1029-8479. [pages 76, 77, 79–82]

[62] CMS Collaboration, *Measurement of the $B_s^0 \to \mu^+\mu^-$ Branching Fraction and Search for $B^0 \to \mu^+\mu^-$ with the CMS Experiment*, Phys. Rev. Lett. **111** (2013) 101804. [page 22]

[63] CMS Collaboration, *The CMS experiment at the CERN LHC*, J. Instrum. **3** (2008) S08004. [page 5]

[64] W. D. Cooper and H. B. Weisbecker, *Solid State Devices and Integrated Circuits*, Reston Publishing, 1982. [page 118]

[65] G. D'Ambrosio, G. Giudice, G. Isidori, and A. Strumia, *Minimal flavor violation: an effective field theory approach*, Nucl. Phys. B **645** (2002) 155–187. [page 5]

[66] C. da Via et al., *3D silicon sensors: Design, large area production and quality assurance for the ATLAS IBL pixel detector upgrade*, Nucl. Instrum. Methods A **694** (2012) 321–330. [page 14]

[67] R. Dalal, A. Bhardwaj, K. Ranjan, M. Moll, and A. Elliott-Peisert, *Combined effect of bulk and surface damage on strip insulation properties of proton irradiated n^+-p silicon strip sensors*, J. Instrum. **9** (2014) P04007. [page 262]

[68] G.-F. Dalla Betta et al., *Electrical characterization of FBK small-pitch 3D sensors after γ-ray, neutron and proton irradiations*, J. Instrum. **12** (2017) C11028. [page 262]

[69] S. Davidson and S. Descotes-Genon, *"Minimal Flavour Violation" for lepto-quarks*, J. High Energ. Phys. **11** (2010) 73. [page 5]

[70] K. De Bruyn et al., *Probing New Physics via the $B_s^0 \to \mu^+\mu^-$ Effective Lifetime*, Phys. Rev. Lett. **109** (2012) 41801. [pages 24, 61]

[71] M. Desai and J. Giacalone, *Large gradual solar energetic particle events*, Living Rev. in Sol. Phys. **13** (2016) 3. [page 254]

[72] P. A. M. Dirac, *The quantum theory of the electron*, Proc. R. Soc. A (1928). [page 4]

[73] P. A. M. Dirac, *On the theory of quantum mechanics*, Proc. R. Soc. A (1926). [page 57]

[74] F. Englert and R. Brout, *Broken Symmetry and the Mass of Gauge Vector Mesons*, Phys. Rev. Lett. **13** (1964) 321–323. [page 3]

[75] Erasmus Experiment Archive, Experimental Record No. 9502, *European Crew Personal Active Dosimeter*, `https://eea.spaceflight.esa.int/portal/exp/?id=9502`. [page 250]

[76] ETM Collaboration, *Mass of the b quark and B-meson decay constants from $N_f = 2+1+1$ twisted-mass lattice QCD*, Phys. Rev. D **93** (2016) 114505. [page 21]

[77] Experimental Physics Detector Technology (EP-DT) Technology and Physics group, MaxRad Project, 2020, `https://ep-dep.web.cern.ch/organisation/dt`. [pages 166–168]

[78] A. Fedorov, A. Lopatik, Q. Missevitch, J.-P. Peigneux, and A. Singovski, "High Stability LED Pulser for the Electromagnetic Calorimeter Monitoring," *2000 IEEE NSS-MIC Conf. Rec. (Cat. No.00CH37149)*, IEEE, 2000 6–251, https://doi.org/10.1109/nssmic.2000.949191. [page 213]

[79] E. Fermi, *On the Quantization of the Monoatomic Ideal Gas*, Trans. by A. Zannoni (1999), https://arxiv.org/abs/cond-mat/9912229. [page 57]

[80] Fermilab Lattice and MILC Collaborations, *B- and D-meson leptonic decay constants from four-flavor lattice QCD*, Phys. Rev. D **98** (2018) 074512. [page 21]

[81] A. Ferrari, P. Sala, A. Fassò, and J. Ranft, *FLUKA: A multi-particle transport code (program version 2005)*, CERN, 2005, https://cds.cern.ch/record/898301. [pages 119, 124]

[82] Flavour Lattice Averaging Group, *FLAG Review 2019: Flavour Lattice Averaging Group (FLAG)*, Eur. Phys. J. C **80** (2020) 113. [page 21]

[83] K. C. Freeman, *On the Disks of Spiral and S0 Galaxies*, Astrophys. J. **160** (1970) 811, https://ui.adsabs.harvard.edu/abs/1970ApJ...160..811F. [page 5]

[84] S. L. Glashow, *Partial-symmetries of weak interactions*, Nucl. Phys. **22** (1961) 579–588. [page 3]

[85] C. S. Gorguinpour, "The Impact of Solar Particle Events on Radiation Risk for Human Explorers of Mars," Doctoral dissertation: Univ. of California, San Francisco and Univ. of California, Berkeley, 2010, https://digitalassets.lib.berkeley.edu/etd/ucb/text/Gorguinpour_berkeley_0028E_10415.pdf. [page 262]

[86] D. Green, *A LED system to test scintillation counter hodoscopes*, Nucl. Instrum. Methods **151** (1978) 307–312. [page 213]

[87] P. Griffin, J. Kelly, T. Luera, and J. VanDenburg, *SNL RML recommended dosimetry cross section compendium*, 1993, https://www.osti.gov/biblio/10115441/. [pages 124, 129]

[88] A. Grummer, M. Hoeferkamp, and S. Seidel, *A radiation tolerant light pulser for particle physics applications*, Nucl. Instrum. Methods A **883** (2018) 29–32. [pages 2, 214, 215]

[89] D. Guadagnoli and G. Isidori, *$B(B_s \to \mu^+\mu^-)$ as an electroweak precision test*, Phys. Lett. B **724** (2013) 63–67. [page 5]

[90] G. S. Guralnik, C. R. Hagen, and T. W. B. Kibble, *Global Conservation Laws and Massless Particles*, Phys. Rev. Lett. **13** (1964) 585–587. [page 3]

[91] F. Halzen and A. Martin, *Quarks & Leptons: An Introductory Course in Modern Particle Physics*, Wiley, 1984, https://www.wiley.com/en-us/Quarks%20and%20Leptones:%20An%20Introductory%20Course%20in%20Modern%20Particle%20Physics-p-9780471887416. [page 7]

[92] C. Hamzaoui, M. Pospelov, and M. Toharia, *Higgs-boson-mediated FCNC in supersymmetric models with large tan β*, Phys. Rev. D **59** (1999) 095005. [page 5]

[93] P. F. Harrison and H. R. Quinn, eds., *The BABAR Physics Book: Physics at an Asymmetric B Factory*, Stanford Linear Accelerator Center (1998), https://www-public.slac.stanford.edu/SciDoc/docMeta.aspx?slacPubNumber=SLAC-R-504. [page 44]

[94] D. M. Hassler et al., *The Radiation Assessment Detector (RAD) Investigation*, Space Sci. Rev. **170** (2012) 503–558. [page 250]

[95] D. M. Hassler et al., *Mars' Surface Radiation Environment Measured with the Mars Science Laboratory's Curiosity Rover*, Science **343** (2014) 1244797, ed. by O. Kemppinen et al. [pages 251, 254, 255]

[96] T. Hermann, M. Misiak, and M. Steinhauser, *Three-loop QCD corrections to* $B_s^0 \to \mu^+\mu^-$, J. High Energ. Phys. **12** (2013) 97. [page 21]

[97] W. Herr and B. Muratori, *Concept of Luminosity*, CERN Yellow Report (2006), https://cds.cern.ch/record/941318. [pages 7, 8]

[98] P. W. Higgs, *Broken Symmetries and the Masses of Gauge Bosons*, Phys. Rev. Lett. **13** (16 1964) 508–509. [page 3]

[99] B. Hiti et al., *Charge collection in irradiated HV-CMOS detectors*, Nucl. Instrum. Methods A **924** (2019) 214–218. [page 246]

[100] A. Hoecker et al., *TMVA 4, Toolkit for Multivariate Data Analysis with ROOT Users Guide*, (2020), https://root.cern.ch/root/htmldoc/guides/tmva/TMVAUsersGuide.pdf. [pages 38, 43, 44]

[101] M. Hoeferkamp, A. Grummer, I. Rajen, and S. Seidel, *Application of p–i–n photodiodes to charged particle fluence measurements beyond* 10^{15} *1-MeV neutron-equivalent/cm*^{2}, Nucl. Instrum. Methods A **890** (2018) 108–111. [pages 2, 221, 225, 233, 242]

[102] M. Hoeferkamp, J. Wickramasinghe, A. Grummer, I. Rajen, and S. Seidel, *An instrument for precision controlled radiation exposures, charged beam profile measurement, and real-time fluence monitoring beyond* 10^{16} n_{eq}/cm^2, J. Instrum. **15** (2020) P05024. [pages 2, 230–232, 235, 240]

[103] HPQCD Collaboration, *B-Meson Decay Constants from Improved Lattice Nonrelativistic QCD with physical u, d, s, and c quarks*, Phys. Rev. Lett. **110** (2013) 222003. [page 21]

[104] C. Huang, W. Liao, and Q. Yan, *Promising process to distinguish supersymmetric models with large tanβ from the standard model:* $B \to X_s\mu^+\mu^-$, Phys. Rev. D **59** (1998) 11701. [page 5]

[105] C. Hughes, C. H. Davies, and C. J. Monahan, *New methods for B meson decay constants and form factors from lattice NRQCD*, Phys. Rev. D **97** (2018) 054509. [page 21]

[106] M. Huhtinen and P. Aarnio, *Pion induced displacement damage in silicon devices*, Nucl. Instrum. Methods A **335** (1993) 580–582. [pages 124, 129]

[107] Iseg Spezialelektronik GmbH, *High Voltage Power Supply EHQ F607n-F , Operators Manual.* www.iseg-hv.com. [pages 121, 128]

[108] N. L. Johnson, *Systems of frequency curves generated by methods of translation*, Biometrika **36** (1949) 149–176. [page 56]

[109] M. C. Jones and A. Pewsey, *Sinh-arcsinh distributions*, Biometrika **96** (2009) 761–780. [page 56]

[110] I. Jun, M. Xapsos, and E. Burke, *Alpha particle nonionizing energy loss (NIEL)*, IEEE Trans. on Nucl. Sci. **51** (2004) 3207–3210. [page 251]

[111] J. Kapustinsky et al., *A fast timing light pulser for scintillation detectors*, Nucl. Instrum. Methods A **241** (1985) 612–613. [page 215]

[112] M. Khan et al., *The monitoring system for the aerogel Cherenkov counter of the BELLE detector*, Nucl. Instrum. Methods A **413** (1998) 201–212. [page 213]

[113] A. N. Kolmogorov, *Sulla determinazione empirica di una legge di distribuzione*, G. Ist. Ital. Attuari **4** (1933) 83–91. [pages 43, 70]

[114] A. Y. Konobeyev, Y. A. Korovin, and V. N. Sosnin, *Neutron displacement cross-sections for structural materials below 800 MeV*, J. Nucl. Mater. **186** (1992) 117–130. [pages 124, 129]

[115] M. V. Korzhik, A. P. Lopatic, O. V. Misevich, and A. A. Fedorov, *A source of reference light pulses for stabilization of the energy scale of fast multichannel scintillation detectors*, Instr. Exper. Tech. **44** (2001) 485–490. [page 213]

[116] G. Kramberger et al., *Initial acceptor removal in p-type silicon*, Trento Workshop (2015), https://indico.cern.ch/event/351695/contributions/828342/attachments/695856/955483/Kramberger-AcceptorRemoval-Trento2015.pdf. [pages 246, 259]

[117] M. Lee, "The squeezing process of complex epoxy patterns in the die-attaching of large IC-chip," *2006 Int. Conf. on Electron. Mater. and Packag.* IEEE, 2006, https://doi.org/10.1109/EMAP.2006.4430590. [page 179]

[118] C. Lefèvre, *LHC Complex*, https://cds.cern.ch/record/1260465. [page 6]

[119] LHCb Collaboration, *Measurement of b hadron fractions in 13 TeV pp collisions*, Phys. Rev. D **100** (2019) 031102. [page 79]

[120] LHCb Collaboration, *Measurement of f_s/f_u Variation with Proton-Proton Collision Energy and B-Meson Kinematics*, Phys. Rev. Lett. **124** (2020) 122002. [page 79]

[121] LHCb Collaboration, *Measurement of the $B^0_s \to \mu^+\mu^-$ Branching Fraction and Search for $B^0 \to \mu^+\mu^-$ Decays at the LHCb Experiment*, Phys. Rev. Lett. **111** (2013) 101805. [page 22]

[122] LHCb Collaboration, *Measurement of the $B^0_s \to \mu^+\mu^-$ Branching Fraction and Effective Lifetime and Search for $B^0 \to \mu^+\mu^-$ Decays*, Phys. Rev. Lett. **118** (2017) 191801. [pages 22, 76, 77, 80–82]

[123] LHCb Collaboration, *Measurement of the fragmentation fraction ratio f_s/f_d and its dependence on B meson kinematics*, J. High Energ. Phys. **04** (2013) 1. [pages 78, 79]

[124] LHCb Collaboration, *Observation of $J/\psi p$ Resonances Consistent with Pentaquark States in $\Lambda^0_b \to J/\psi K^- p$ Decays*, Phys. Rev. Lett. **115** (2015) 072001. [page 4]

[125] LHCb Collaboration, *The LHCb Detector at the LHC*, J. Instrum. **3** (2008) S08005. [page 5]

[126] LHCb collaboration, *Observation of structure in the J/ψ-pair mass spectrum*, Sci. Bull. **65** (2020) 1983–1993. [page 4]

[127] LHCf Collaboration, *The LHCf detector at the CERN Large Hadron Collider*, J. Instrum. **3** (2008) S08006. [page 5]

[128] G. Lindström et al., *Radiation hard silicon detectors – developments by the RD48 (ROSE) Collaboration*, Nucl. Instrum. Methods A **466** (2001) 308–326. [pages 118, 243, 248, 259]

[129] B. List, *Statistical error from weighted events*, 2015, https://www.desy.de/~blist/. [page 113]

[130] Los Alamos National Laboratory, *Flight paths and facilities at Los Alamos Neutron Science Center*, 2020, https://lansce.lanl.gov/facilities/index.php. [page 18]

[131] B. Lubsandorzhiev and Y. Vyatchin, *Studies of "Kapustinsky's" light pulser timing characteristics*, J. Instrum. **1** (2006) T06001. [page 213]

[132] G. Lutz, *Semiconductor Radiation Detectors: Device Physics*, Springer-Verlag, 1999. [page 234]

[133] S. Mandelstam, *Determination of the Pion-Nucleon Scattering Amplitude from Dispersion Relations and Unitarity. General Theory*, Phys. Rev. **112** (4 1958) 1344–1360. [page 7]

[134] Manufacturing Chemist, *Mixing on a mini scale*, 2010, https://www.manufacturingchemist.com/news/article_page/Mixing_on_a_mini_scale/46649. [pages 176, 177]

[135] *Mars Curiosity Rover: RAD for Scientists*, https://mars.nasa.gov/msl/spacecraft/instruments/rad/for-scientists/. [page 251]

[136] *Mars Science Laboratory Archive*, https://atmos.nmsu.edu/data_and_services/atmospheres_data/MARS/curiosity/rems_temperature.html. [page 255]

[137] P. Marshall and C. Marshall, *Proton effects and test issues for satellite designers - Part A: Ionization effects*, Nucl. Space and Radiat. Eff. Conf. Short Course (1999), Norfolk, VA, https://ntrs.nasa.gov/citations/19990110691. [page 252]

[138] A. D. Martin, W. J. Stirling, R. S. Thorne, and G. Watt, *Parton Distributions for the LHC*, Eur. Phys. J. C **63** (2009) 189–285. [pages 124, 128]

[139] S. J. Metcalfe, SLAC National Accelerator Laboratory, private communication (2019). [page 186]

[140] L. Miroshnichenko and R. Nymmik, *Extreme fluxes in solar energetic particle events: Methodological and physical limitations*, Radiation Measurements **61** (2014) 6–15. [page 255]

[141] MoEDAL Collaboration, *Technical Design Report of the MoEDAL Experiment*, CERN-LHCC-2009-006 (2009), http://cds.cern.ch/record/1181486. [page 5]

[142] MoEDAL Collaboration, *The physics programme of the MoEDAL experiment at the LHC*, Int. J. Mod. Phys. A **29** (2014). [page 5]

[143] M. Moll, *Displacement Damage in Silicon Detectors for High Energy Physics*, IEEE Trans. Nucl. Sci. **65** (2018) 1561–1582. [pages 244, 246, 247]

[144] M. Moll, "Radiation damage in silicon particle detectors: Microscopic defects and macroscopic properties," Doctoral dissertation: University of Hamburg, 1999, http://www-library.desy.de/cgi-bin/showprep.pl?desy-thesis99-040. [pages 118, 243, 246, 248, 249]

[145] M. Moll, E. Fretwurst, and G. Lindström, *Leakage Current of Hadron Irradiated Silicon Detectors – Material Dependence*, Nucl. Instrum. Methods A **426** (1999) 87–93. [pages 118, 121, 125, 126, 233, 234, 243, 248]

[146] F. Moscatelli et al., *Combined Bulk and Surface Radiation Damage Effects at Very High Fluences in Silicon Detectors: Measurements and TCAD Simulations*, IEEE Trans. Nucl. Sci. **63** (2016) 2716–2723. [page 262]

[147] NASA, *Mars 2020/Perseverance*, 2020, `https://mars.nasa.gov/files/mars2020/Mars2020_Fact_Sheet.pdf`. [page 262]

[148] J. Neyman, *Outline of a Theory of Statistical Estimation Based on the Classical Theory of Probability*, Phil. Trans. R. Soc. London A **236** (1937) 767. [page 72]

[149] J. W. Norbury et al., *Galactic cosmic ray simulation at the NASA Space Radiation Laboratory*, Life Sciences in Space Research **8** (2016) 38–51. [page 254]

[150] S. L. Olsen, T. Skwarnicki, and D. Zieminska, *Nonstandard heavy mesons and baryons: Experimental evidence*, Rev. Mod. Phys. **90** (2018) 015003. [page 4]

[151] P. Palni et al., *A method for real time monitoring of charged particle beam profile and fluence*, Nucl. Instrum. Methods A **735** (2014) 213–217. [pages 222, 224, 225, 233]

[152] S. Parker, C. Kenney, and J. Segal, *3D – A proposed new architecture for solid-state radiation detectors*, Nucl. Instrum. Meth. A **395** (1997) 328–343. [page 256]

[153] S. Perlmutter et al., *Measurements of* Ω *and* Λ *from 42 High-Redshift Supernovae*, Astrophys. J. **517** (1999) 565–586. [page 5]

[154] M. Pohl, "AMS tracking in-orbit performance," *Proc. Sci.(VERTEX2015)*, Sissa Medialab, 2015 022, `https://pos.sissa.it/254/022`. [page 256]

[155] F. Ravotti, "Development and Characterization of Radiation Monitoring Sensors for the High Energy Physics Experiments of the CERN LHC Accelerator," Doctoral dissertation: Université Montpellier II, 2006 123–124, https://cds.cern.ch/record/1014776. [pages 221, 222]

[156] F. Ravotti, M. Glaser, and M. Moll, *Sensor Catalogue for Radiation Monitoring*, https://ep-dep-dt.web.cern.ch/irradiation-facilities/radmon. [page 221]

[157] RD53 Collaboration, *RD53B Manual*, CERN-RD53-PUB-19-002 (2019), https://cds.cern.ch/record/2665301. [page 16]

[158] RD53 Collaboration, *The RD53A Integrated Circuit*, CERN-RD53-PUB-17-001 (2017), https://cds.cern.ch/record/2287593. [page 16]

[159] W. Reiter and G. Stengl, *A blue light emitting diode used as a reference element in scintillation spectrometers*, Nucl. Instrum. Methods **180** (1981) 105–107. [page 213]

[160] A. G. Riess et al., *Observational Evidence from Supernovae for an Accelerating Universe and a Cosmological Constant*, Astron. J. **116** (1998) 1009–1038, https://doi.org/10.1086/300499. [page 5]

[161] A. Rogozhnikov, *Reweighting with Boosted Decision Trees*, J. Phys. Conf. Ser. **762** (2016) 12036. [page 54]

[162] L. Rossi and O. Brüning, "Introduction to the HL-LHC Project," *The High Luminosity Large Hadron Collider*, World Scientific, 2015 1–17, https://cds.cern.ch/record/2130736. [page 15]

[163] V. C. Rubin and W. K. Ford, Jr., *Rotation of the Andromeda Nebula from a Spectroscopic Survey of Emission Regions*, Astrophys. J. **159** (1970) 379. [page 5]

[164] A. Salam, *Gauge unification of fundamental forces*, Rev. Mod. Phys. **52** (1980) 525–538. [page 3]

[165] T. Sjöstrand, S. Mrenna, and P. Z. Skands, *A brief introduction to PYTHIA 8.1*, Comput. Phys. Commun. **178** (2008) 852–867. [page 25]

[166] T. Sjöstrand et al., *An Introduction to PYTHIA 8.2*, Comput. Phys. Commun. **191** (2015) 159. [pages 119, 124]

[167] H. E. Spence et al., *CRaTER: The Cosmic Ray Telescope for the Effects of Radiation Experiment on the Lunar Reconnaissance Orbiter Mission*, Space Sci. Rev. **150** (2010) 243–284. [page 250]

[168] G. Spiezia et al., "The LHC Radiation Monitoring System - RadMon," *Proc. Sci. RD11*, Sissa Medialab, 2011 24, `https://pos.sissa.it/143/024`. [page 221]

[169] G. P. Summers, E. A. Burke, P. Shapiro, S. R. Messenger, and R. J. Walters, *Damage correlations in semiconductors exposed to gamma, electron and proton radiations*, IEEE Trans. Nucl. Sci. **40** (1993) 1372–1379. [pages 124, 129]

[170] S. M. Sze, *Physics of Semiconductor Devices*, 2nd Edition, Wiley, 1984. [page 121]

[171] M. Tanabashi et al., *Review of Particle Physics*, Phys. Rev. D **98** (2018) 30001. [pages 21, 28, 37, 58, 59, 61, 71, 77, 79]

[172] H. Tanaka et al., *A gain monitoring system with a Nd:YAG laser for the photomultipliers of the HERMES experiment*, Nucl. Instrum. Methods A **515** (2003) 725–732. [page 213]

[173] TOTEM Collaboration, *The TOTEM Experiment at the CERN Large Hadron Collider*, J. Instrum. **3** (2008) S08007. [page 5]

[174] A. Valassi et al., *COOL, LCG conditions database for the LHC experiments: Development and deployment status*, IEEE Nucl. Sci. Symp. Conf. Rec. (2008). [page 121]

[175] S. van der Meer, *Calibration of the effective beam height in the ISR*, 1968, https://cds.cern.ch/record/296752. [pages 86, 123]

[176] A. Vasilescu, *The NIEL scaling hypothesis applied to neutron spectra of irradiation facilities and in the ATLAS and CMS SCT*, tech. rep. ROSE/TN/97-2, CERN, 1997, http://cern.ch/rd48. [page 249]

[177] A. Vasilescu and G. Lindström, *Displacement damage in silicon, on-line compilation*, 2000, http://rd50.web.cern.ch/rd50/NIEL/. [pages 119, 124, 129, 253]

[178] S. Weinberg, *A Model of Leptons*, Phys. Rev. Lett. **19** (1967) 1264–1266. [page 3]

[179] R. Wunstorf, W. M. Bugg, J. Walter, F. W. Garber, and D. Larson, *Investigations of donor and acceptor removal and long term annealing in silicon with different boron/phosphorus ratios*, Nucl. Instrum. Methods A **377** (1996) 228–233. [page 247]

[180] A. Yamamoto et al., *The ATLAS central solenoid*, Nucl. Instrum. Methods A **584** (2008) 53–74. [page 13]

[181] C. N. Yang and R. L. Mills, *Conservation of Isotopic Spin and Isotopic Gauge Invariance*, Phys. Rev. **96** (1954) 191–195. [page 3]

[182] W.-M. Yao et al., *Review of Particle Physics*, J. Phys. G **33** (2006) 1, Chapter 29, http://pdg.lbl.gov. [page 252]

[183] J. Zabierowski and J. Rachowski, *The Light-Pulser Monitoring System for the WASA detector facility*, Nucl. Instrum. Methods A **606** (2009) 411–418. [page 213]

[184] C. Zeitlin et al., *Measurements of Energetic Particle Radiation in Transit to Mars on the Mars Science Laboratory*, Science **340** (2013) 1080–1084. [pages 254, 255]

[185] F. Zwicky, *On the Masses of Nebulae and of Clusters of Nebulae*, Astrophys. J. **86** (1937) 217, https://ui.adsabs.harvard.edu/abs/1937ApJ....86..217Z. [page 5]